Volume 98, Number 2, March–April 1993
Journal of Research of the National Institute of Standards and Technology

Contents

Articles

Conference Reports

News Briefs

Volume 98, Number 2, March–April 1993
Journal of Research of the National Institute of Standards and Technology

Volume 98, Number 2, March–April 1993
Journal of Research of the National Institute of Standards and Technology

Volume 98, Number 2, March-April 1993
Journal of Research of the National Institute of Standards and Technology

[J. Res. Natl. Inst. Stand. Technol. 98, 159 (1993)]

Absolute Spatially- and Temporally-Resolved Optical Emission Measurements of rf Glow Discharges in Argon

Volume 98 | Number 2 | March-April 1993

S. Djurović[1], J. R. Roberts, M. A. Sobolewski, and J. K. Olthoff

National Institute of Standards and Technology,
Gaithersburg, MD 20899-0001

Spatially- and temporally-resolved measurements of optical emission intensities are presented from rf discharges in argon over a wide range of pressures (6.7 to 133 Pa) and applied rf voltages (75 to 200 V). Results of measurements of emission intensities are presented for both an atomic transition (Ar I, 750.4 nm) and an ionic transition (Ar II, 434.8 nm). The absolute scale of these optical emissions has been determined by comparison with the optical emission from a calibrated standard lamp. All measurements were made in a well-defined rf reactor. They provide detailed characterization of local time-resolved plasma conditions suitable for the comparison with results from other experiments and theoretical models. These measurements represent a new level of detail in diagnostic measurements of rf plasmas, and provide insight into the electron transport properties of rf discharges.

Key words: argon; discharge; gaseous electronics; optical emission; plasma; rf; spatial profile; temporal dependence.

Accepted: November 5, 1992

1. Introduction

A fuller understanding of the rf glow discharges utilized for the etching of semiconductor materials requires knowledge of the microscopic gas-phase collision processes that occur in the plasma. Optical emission spectroscopy is a non-intrusive technique that allows the detection of atoms, molecules, and ions in excited states within the plasma. Analysis of the spatial and temporal distributions of the optical emission from an rf glow discharge also provides information concerning electron transport properties and the electron-energy distributions in the plasma.

The number of studies investigating the time-varying optical emission from rf plasmas at frequencies near 13.56 MHz are limited. De Rosny et al. [1] have observed the time-dependent emission from a short-lived state of Si in a pure SiH_4 rf plasma. Donnelly and coworkers [2] reported the effects of frequency on the time-varying optical emission from chlorine-containing rf discharges. Bletzinger and De Joseph [3] investigated the temporally-resolved optical emission from a nitrogen plasma as a function of position between the rf electrodes. More recently Tochikubo et al. [4] and Köhler et al. [5] reported spatially- and temporally-resolved optical emission data for neutral and ionic transitions that occur in argon plasmas. Tochikubo et al. [4] calculated the relative net excitation rates by deconvoluting the optical emission profile, while Köhler et al. [5] performed Boltzmann calculations to derive excited state populations for comparison with the time-modulated emission intensity.

[1] Permanent address: Institute of Physics, Novi Sad, Trg Dositja Obradovica 4, 21000 Novi Sad, Yugoslavia.

Recent modeling of low-pressure rf glow discharges has begun to predict many of the time-varying aspects of high-frequency rf plasmas [6–10]. However, the presently available time-resolved optical emission data is insufficient to fully validate the conclusions derived by plasma modeling; either because the data do not cover an adequate range of experimental conditions or because the experimental conditions are not adequately defined. Additionally, the time-resolved optical emission data presently in the literature consist only of relative emission intensities which do not allow for comparison with calculations of absolute excitation rates or absolute population densities.

The emphasis of the present work is therefore to measure the absolute, time-resolved and spatially-resolved optical emission intensities from "well-defined" argon plasmas over a wide range of pressures and voltages. All experiments were performed on a Gaseous Electronics Conference (GEC) rf reference cell [11,12]. Ostensibly identical copies of this cell have been assembled and characterized in several laboratories. For each rf voltage and pressure setting, the time-varying optical emission intensity was measured absolutely for an Ar I (750.4 nm) and Ar II (434.8 nm) line as a function of observation location along the central axis between the parallel-plate electrodes by using a calibrated monochromator. No radial emission profiles were taken. Voltage and current waveforms were also measured for each set of plasma conditions, and analyzed to determine the time-dependent voltage and current signals at the surface of the powered electrode in contact with the plasma.

2. Experimental Details

2.1 GEC rf Reference Cell

All experiments were performed using a GEC rf reference cell. The GEC rf reference cell is an rf plasma research reactor whose design was initiated at the 1988 Gaseous Electronics Conference (Oct. 18–22, Minneapolis, MN). The reference cell was designed to provide a standard experimental platform for rf plasma research that was physically identical from laboratory to laboratory, so that experimental results, theoretical models, and various plasma diagnostics could be more easily compared.

The details of the design of the GEC rf reference cell are given in Refs. [11] and [12]. Briefly, the cell is a parallel-plate discharge chamber with 102 mm diameter electrodes separated by 25 mm. The electrodes are cylindrically symmetric and their surfaces are horizontal. The top electrode contains 169 holes (380 μm diameter) to provide a showerhead gas inlet and is grounded to the outer wall of the vacuum chamber. The bottom electrode is powered by an ENI[2] 13.56 MHz rf power supply isolated with a 0.1 μF blocking capacitor. For the data presented here, flow rates were 20 standard cubic centimeters per minute (sccm), pressures were varied from 6.7 to 133.3 Pa, and peak-to-peak rf voltages ranged from 75–200 V. The cylindrical vacuum chamber is constructed of stainless steel and has eight radial copper-gasket flanges at the chamber midplane. Two 203 mm diameter flanges are fitted with 136 mm diameter quartz windows for spectroscopic observations. Two 152 mm flanges are orthogonal to these, one of which accommodates a turbomolecular pump for establishing a base pressure of $<10^{-5}$ Pa. Four 70 mm diameter flanges at 45° with respect to the four larger flanges are also mounted at the cell midplane. The bottom of the vacuum chamber is constructed so the pumpout of the gas is accomplished by four symmetrically placed 70 mm diameter ports piped into a single exhaust line to a mechanical vacuum pump.

On the GEC rf reference cell at NIST, a mass spectrometer with an ion energy analyzer has been mounted on one of the 152 mm diameter side ports and an electrical plasma probe has been attached to one of the 70 mm diameter ports (see Fig. 1). Detailed discussions of these diagnostics are presented elsewhere [13–15].

2.2 Electrical Measurements

Voltage and current waveforms were measured on the powered electrode lead using a voltage probe and a Pearson current probe with upper 3 dB frequencies of 300 and 200 MHz, respectively. The probe signals were digitized by a Phillips PM3323 oscilloscope and then transferred to a computer for Fourier analysis. To extract the amplitude and phase of the significant Fourier components, an iterative least squares curve fitting algorithm was used instead of discrete Fourier transform techniques, which only provide Fourier coefficients at frequencies commensurate with the sampling

[2] Certain commercial equipment, instruments, or materials are identified in this paper to specify adequately the experimental procedure. Such identification does not imply recommendation or endorsement by the National Institute of Standards and Technology, nor does it imply that the materials or equipment identified are necessarily the best available for the purpose.

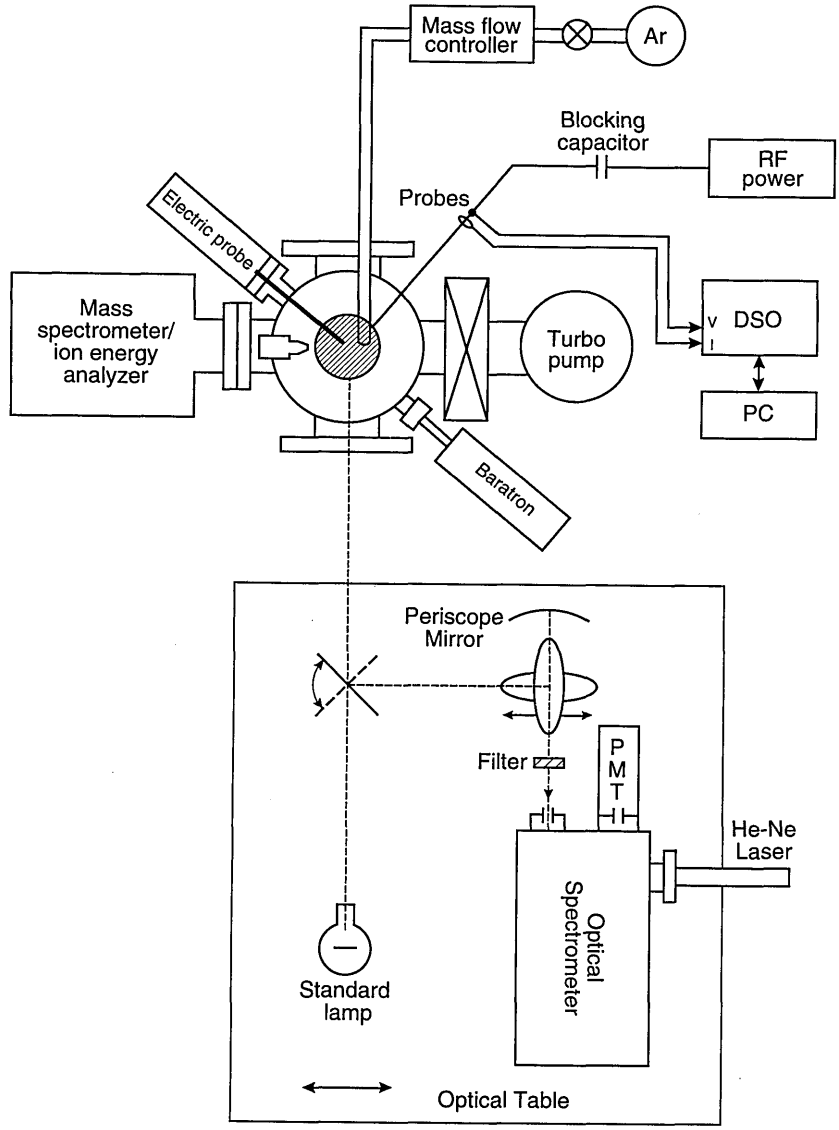

Fig. 1. Diagram of the NIST GEC rf reference cell, optical setup, and other diagnostics; where PMT is the photomuliplier tube, DSO is the digital storage oscilloscope, and PC is a personal computer. The mass spectrometer/ion energy analyzer and electrical probe are discussed elsewhere [13–15].

frequency. The curve-fitting algorithm, which operates very efficiently, is described elsewhere [16]. The fits included a dc component, the fundamental (13.56 MHz) component and the second through fifth harmonics. The signals at the harmonic frequencies, which arise because the impedance of the plasma is nonlinear, contain additional information not present in the fundamental components.

Phases obtained from the fits were corrected to account for propagation delays in the cables connecting the probes to the oscilloscope. Current and voltage values were subsequently corrected for the effects of stray impedance. Due to the stray impedance of the cell, the current and voltage waveforms at the point outside the cell where the probes are located, $I_m(t)$ and $V_m(t)$, will differ from the waveforms actually present at the powered electrode, $I_p(t)$ and $V_p(t)$. For example, some of the measured current $I_m(t)$ is drawn not by the plasma but by parasitic capacitances in the electrode assembly and in the probes. Also, $V_m(t)$ will differ from $V_p(t)$ due to a voltage drop along the power lead, as its inductance is significant at radio frequencies. To correct for these effects we use a technique described previously [11]. A set of measurements made in the absence of a plasma fully

determines the cascade matrix of the network of parasitics between the measurement point and the surface of the powered electrode. This matrix then serves to convert the waveforms measured when plasma is present, $I_m(t)$ and $V_m(t)$, into the waveforms $I_p(t)$ and $V_p(t)$.

When parasitic currents are large, the corrected values are extremely sensitive to small errors in the measured values [17]. To avoid this problem, a shunt circuit consisting of a coil and an air variable capacitor, was connected between the power lead and the chamber ground at a point between the current probe and the chamber [11]. The shunt is designed to have a net inductive impedance at 13.56 MHz that will cancel, at that frequency, the net capacitive reactance of parasitics in the cell. The variable capacitor allows fine tuning of the impedance of the shunt and also maintains capacitive coupling to the cell so as not to short out the dc bias of the powered electrode. With the cell evacuated below 10^{-5} Pa and excited at 13.56 MHz, the capacitor was adjusted until the measured current was nulled. When nulled, the cell still draws parasitic current, but the shunt draws an equal and opposite current. Later, when gas is introduced and a plasma is generated, this is still approximately true; the current drawn by cell parasitics is still roughly canceled by the current drawn by the shunt. Excluding the large parasitic currents from the measurement branch results in increased precision, and also alleviates some concerns about rf interference and current probe overload. The characterization of cell parasitics is performed with the shunt in place and tuned, so that the correction for the effects of the parasitics includes the effects of the shunt as well.

2.3 Optical Emission Measurement System

The experimental setup for spectroscopic measurements is shown schematically in Fig. 1. The spectroscopic apparatus consists of a 2/3 m Czerny-Turner type grating monochromator with a 1200 lines/mm grating. This monochromator is equipped with a cooled Burle C31034A photomultiplier for pulse detection of the optical emission signal. The monochromator is equipped with a retractable mirror near its exit slit so a He-Ne laser may be substituted for the detector for alignment purposes. The vertical entrance and exit slits of the monochromator are typically 100 μm wide and 2 mm high. The slit widths and photomultiplier voltage were kept constant (100 μm and 1700 V, respectively) for all measurements, and metallic film neutral density filters were used, when necessary, to reduce the photon signals to suitable count rates for the pulse counting electronics used for data acquisition. Calibration of these filters is discussed in the next section.

The optics to image the plasma onto the monochromator slit are front surface mirrors with coatings to efficiently reflect the plasma emission at wavelengths from 200 nm to 1500 nm. There are three flat mirrors and one concave mirror, each 152 mm in diameter. The concave mirror (650 mm focal length) is positioned so that the plasma image is demagnified onto the entrance slit by approximately a factor of 2. These mirrors are arranged to act as a periscope bringing the level of the plasma emission to the same height as the monochromator, as well as rotating the image of the plasma by 90°. By this rotation, the electrode surfaces are imaged parallel to the long dimension of the entrance slit, thus permitting observations close to the electrode surface and providing higher spatial resolution of the plasma along the vertical axis. The spatial resolution was 0.5 mm vertically and 4 mm horizontally. Because of the periscope, scanning of the plasma emission between the electrodes can be accomplished by translating one of the mirrors (see Fig. 1).

2.4 Calibration of the Optical System

A tungsten ribbon filament lamp calibrated for spectral radiance (±2%) by the Radiometric Physics Division, NIST [18] is mounted on the optics table and is substituted for the plasma source by rotating one of the flat mirrors to image the lamp filament onto the slit (see Fig. 1). This lamp is used to calibrate the optics/monochromator system to obtain absolute spectral radiance measurements. The calibration measurements were made with the same slit width and photomultiplier voltage as used in the plasma measurements. The standard lamp had to be mounted with the long dimension of its filament in a horizontal position to accommodate the 90° rotation of the optical system. This is not a conventional configuration for a radiance calibrated standard lamp; therefore an estimate of the effects of this configuration had to be made. It was determined from a separate experiment that this rotation amounted to an additional uncertainty of ± 2% in the absolute radiance calibration at the wavelengths of the observed spectral lines.

An additional uncertainty in the calibration procedure arose because the intensity of the standard

lamp signal was stronger than the observed spectral lines by approximately a factor of 10^3. To prevent the measurement from saturating, metallic film neutral density filters were placed in the optical path in front of the monochromator slit for measurement of the lamp signals. For measurements at longer wavelengths, second order radiation from the lamp had to be blocked. On the other hand, for measurements at shorter wavelengths, the strong lamp radiation at longer wavelengths also had to be blocked to avoid a significant contribution to the signal from scattered light. Bandpass interference filters were incorporated into the optical path to serve both of these requirements. The bandpass filters were used only in the standard lamp calibration procedure, and not in the plasma experiments. Interference filters were used in the above procedure, since the use of color glass filters to perform the same functions created additional problems due to their fluorescence at certain wavelengths and changing transmission characteristics as a function of incident light flux. The metallic film neutral density filters and the bandpass filters could not be characterized using this optical monochromator system, and were therefore individually calibrated for transmission over the wavelength region of interest by a double monochromator system at NIST used for spectral radiance calibrations. The uncertainty associated with the calibration of these filters is estimated to be $\pm 5\%$. The total uncertainty ($1\,\sigma$) in the measurement of a spectral line radiance is therefore estimated to be $\pm 6\%$.

2.5 Time-Resolved Optical Detection System

The time-varying output from the photomultiplier was recorded with a system utilizing a time-to-amplitude converter (TAC) and a multi-channel analyzer (MCA). A detailed schematic diagram is shown in Fig. 2. The timing cycle of the TAC is initiated by a fast pulse derived by a 200 MHz discriminator from a 10:1 voltage probe attached to the bottom of the powered electrode. The timing cycle is stopped by a photon-initiated pulse from the photomultiplier system, or by the ending of the preset TAC timing period. For the data presented here, the maximum time measured by the TAC was set to 200 ns (slightly less than 3 rf cycles). As mentioned previously, photon count rates were kept low ($< 10^5$ counts/s) by placing calibrated neutral density filters in the optical path for the measurement of the most intense optical signals. Because much less than one photon is detected, on the average, for each timing cycle, there is no discrimination against photons detected later in the timing cycle.

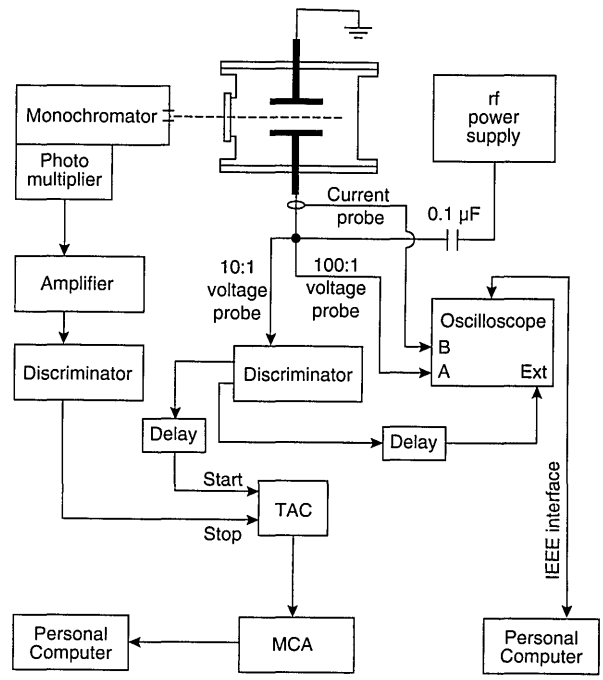

Fig. 2. Schematic diagram of the timing electronics utilized to measure the temporal variation of the optical emission signal from argon plasmas for comparison with the applied rf voltage waveform. The TAC is a time-to-amplitude converter, the MCA is a multichannel analyzer, and Ext refers to the external trigger of the digital storage oscilloscope.

The output pulses from the TAC, whose magnitudes are proportional to the time between the trigger from the voltage waveform and the detection of the photon, are sorted into channels by the MCA. This accumulated spectrum represents the time-resolved optical emission signal for a single spatial location. Observation times at each position were 3 min for the Ar I line and 5 min for the less intense Ar II line. Measurements were made at 10–15 different positions between the electrodes, depending upon the degree of spatial variation in the signal intensity.

The MCA was set to record 256 channels providing a timing resolution of 0.78 ns/channel (200 ns/256 channels). More channels could have been utilized, thereby providing a smaller time increment. However, the uncertainty in timing measurements (discussed in the next section) and the broad distribution in time of the optical signal eliminate any inherent advantage to a finer time increment. Also, using more channels in the MCA would have significantly increased the data-taking time at each observation position.

2.6 Calibration of Timing Circuit

In order to correlate the time-varying optical emission signal with the applied rf voltage, it is necessary to calibrate the time delays of the entire optical/detector/electronics system. The voltage waveform is actually measured approximately 20 cm from the bottom of the powered electrode. The transit time from this point to the electrode surface is ~0.3 ns; which is nearly insignificant. In contrast, the time delays inherent in the voltage probe, cables, discriminator, amplifier, TAC, MCA, and oscilloscope are not insignificant, and were determined by simultaneously applying fast pulses to the external trigger of the dual trace digital oscilloscope, to the 100:1 voltage probe attached to oscilloscope channel A, to the start of the TAC, and to the input cable of the amplifier following the photomultiplier. The time delay units in the electrical circuit were then adjusted so that signals on the scope and MCA both appeared in the zero channel.

The time delay between the emission signal and the output of the photomultiplier was determined in the following way. A fast avalanche photo-diode, the 300 MHz oscilloscope, and a fast pulse generator were used to calibrate the delay time of a pulsed diode laser (Hamamatsu Picosecond Light Pulser). This laser was then positioned near the standard lamp at the focal point of the optical system. The time delay between triggering the pulsed laser and detection of the output pulse from the photomultiplier was measured using the oscilloscope and fast pulse generator. The time delay in the optical system (adjusted for the time delay of the laser) was 47 ns and was accounted for by adding this time to the time delay unit located prior to the start input of the TAC. The estimated uncertainty in the timing measurements is ±3 ns, and is primarily due to the finite rise time (~2 ns) of the fast electrical pulses used for calibration.

3. Results

The time-dependent emission intensities of a neutral argon line (750.4 nm) and an ionic argon line (434.8 nm) were measured at each observation point between the electrodes. The upper level of the Ar I transition has an atomic lifetime of approximately 20 ns [19] while the upper level of the Ar II transition has an atomic lifetime of approximately 7 ns [19]. These lines were chosen for study because: 1) they are well separated from possible interfering lines; 2) they are of sufficient intensity to allow for reasonable data acquisition times; 3) they have atomic lifetimes that are less than the 13.56 MHz period (73.7 ns); and 4) some previously published data exists in the literature for comparison [4,5].

Examples of correlations between the measured time-dependent optical emission signals and the voltage and current waveforms are shown in Fig. 3 for argon plasmas with uncorrected peak-to-peak rf voltages of 200 V and gas pressures of 133.3 Pa (Figs. 3a–3d) and 13.3 Pa (Figs. 3e–3h). Figure 3a shows the raw Ar I optical emission signal as recorded by the MCA at a point where the emission signal was a maximum (21 mm from the grounded electrode). The observation time was 3 min and a filter with 0.6% transmission was used to reduce the count rate to acceptable levels. The raw data for the Ar II line are shown in Fig. 3b for the same plasma at an observation point 22.5 mm from the grounded electrode (also the location of the maximum emission intensity). The observation time was 5 min and no transmission filters were used. The dotted curves in Fig. 3c and 3d show the voltage and current waveforms, $V_m(t)$ and $I_m(t)$ acquired simultaneously by the digital oscilloscope with the data shown in Figs. 3a and 3b. The solid curves represent the voltage and current waveforms, $V_p(t)$ and $I_p(t)$, at the surface of the powered electrode as calculated by the equivalent circuit model discussed in Sec. 2.2. The presence of higher harmonics in the electrical waveforms is indicated by the nonsinusoidal character of the curves.

Similar data obtained for a lower pressure plasma (13.3 Pa) are shown in Figs. 3e–3h. The Ar I optical emission data in Fig. 3e were obtained at a point 17 mm from the surface of the grounded electrode with a 2.9% transmission filter. The Ar II data in Fig. 3f were obtained at a point 18.5 mm from grounded electrode, and no transmission filters were used.

The optical emission profiles for the Ar I and Ar II lines, as shown in Fig. 3, are quite different. For the plasma at 133.3 Pa, the peaks in the time-varying Ar I optical emission signal are broader than in the Ar II profile and exhibit an assymmetry on the right hand side of the temporal peaks. These characteristics are due to the relatively long atomic lifetime (20 ns) of the neutral excited state. This also contributes to the significant "background" or non-time-dependent portion of the Ar I signal observed in Fig. 3a. For other transitions whose excited-state lifetimes are even longer (approaching the rf period), the fraction of the optical

signal exhibiting a time-dependence is very small due to the "smearing-out" effect of the long atomic lifetimes [5]. In contrast, the Ar II signal profile at 133.3 Pa exhibits narrow temporal peaks and a large time-dependent signal due to the short lifetime of the excited state (~7 ns) as compared with the rf period. At 13.3 Pa, the Ar I profile is very similar to that observed at 133.3 Pa, however, the peaks in the Ar II profiles are much broader than at higher pressures. This indicates a change in the excitation of the Ar II transition as the pressure changes.

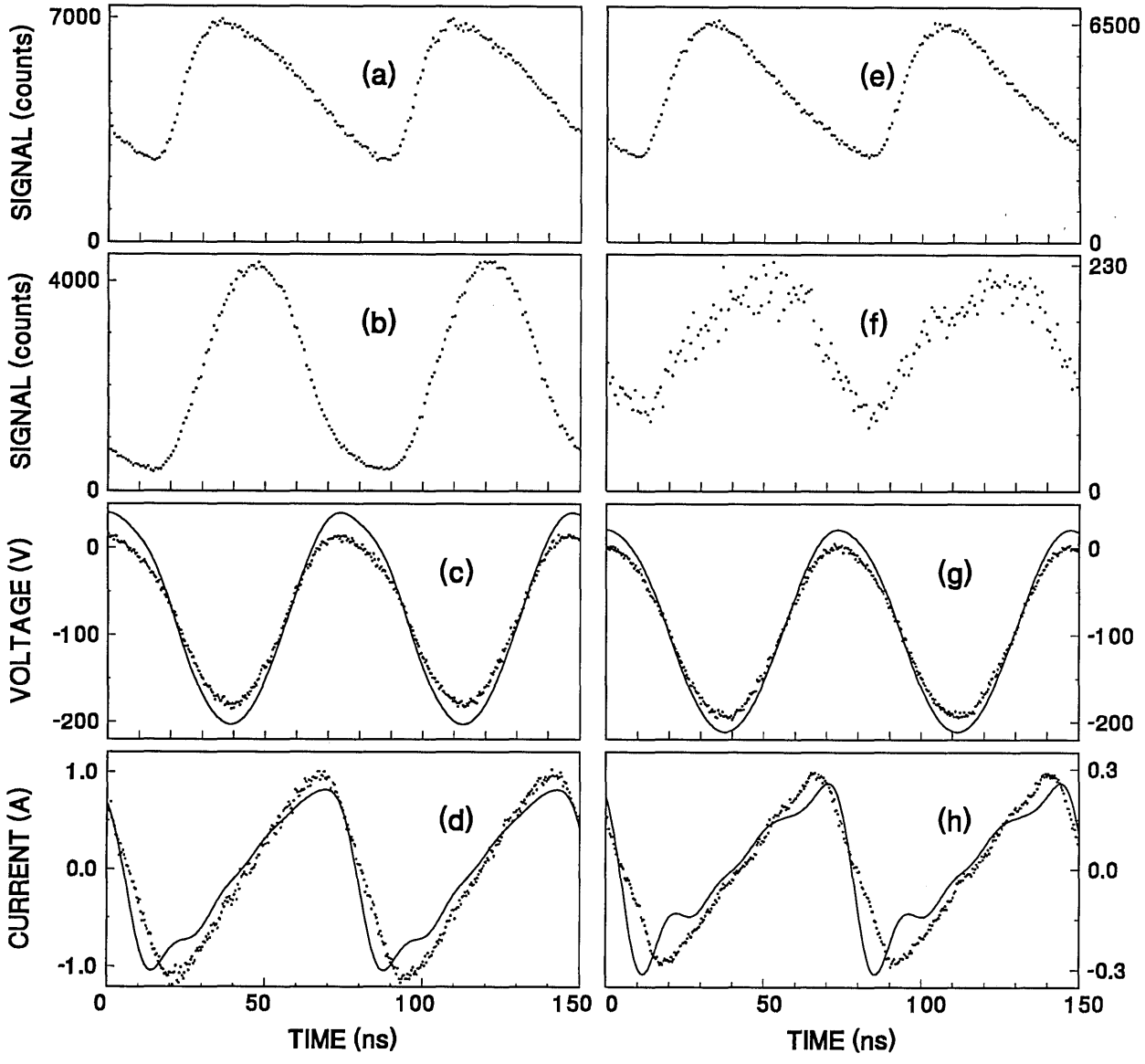

Fig. 3. Measured time-dependent optical emission signals, and the corresponding voltage and current waveforms from argon plasmas with applied rf voltages of 200 V and pressures of 133.3 Pa (a–d) and 13.3 Pa (e–h). (a) noncalibrated optical emission Ar I signal at 750.4 nm from an observation point 21 mm from the grounded electrode; (b) noncalibrated Ar II optical signal at 434.8 nm from an observation point 22.5 mm from the grounded electrode; (c) ··· measured voltage waveform obtained simultaneously with the optical emission data in 3a and 3b, — calculated voltage waveform at the surface of the powered electrode; (d) ··· measured current waveform corresponding to the voltage waveforms in 3c, — calculated current waveform at the surface of powered electrode; (e) noncalibrated optical emission Ar I signal at 750.4 nm from an observation point 17 mm from the surface of the grounded electrode; (f) noncalibrated Ar II signal at 434.8 nm from an observation point 18.5 mm from the grounded electrode; (g) ··· measured voltage waveform obtained simultaneously with the optical emission data in 3e and 3f, — calculated voltage waveform at the surface of the powered electrode; (h) ··· measured current waveform corresponding to the voltage waveform in 3g, — calculated current waveform at the surface of the powered electrode.

Comparison of the optical-emission data in Fig. 3 also indicates that the Ar I and Ar II profiles are not in phase with each other, with the Ar I profile leading the Ar II profile. The Ar II time-dependence at 133.3 Pa is observed to be nearly 180° out-of-phase with the applied voltage, as was previously reported by Tochikubo et al. [4]. Due to the non-sinusoidal nature of the current waveform, it is difficult to draw correlations between the current and the optical emission signals.

The optical emission signals as a function of observation point and time are shown for a range of plasma conditions in Figs. 4–8 for the Ar I line (750.4 nm) and in Figs. 9–13 for the Ar II line

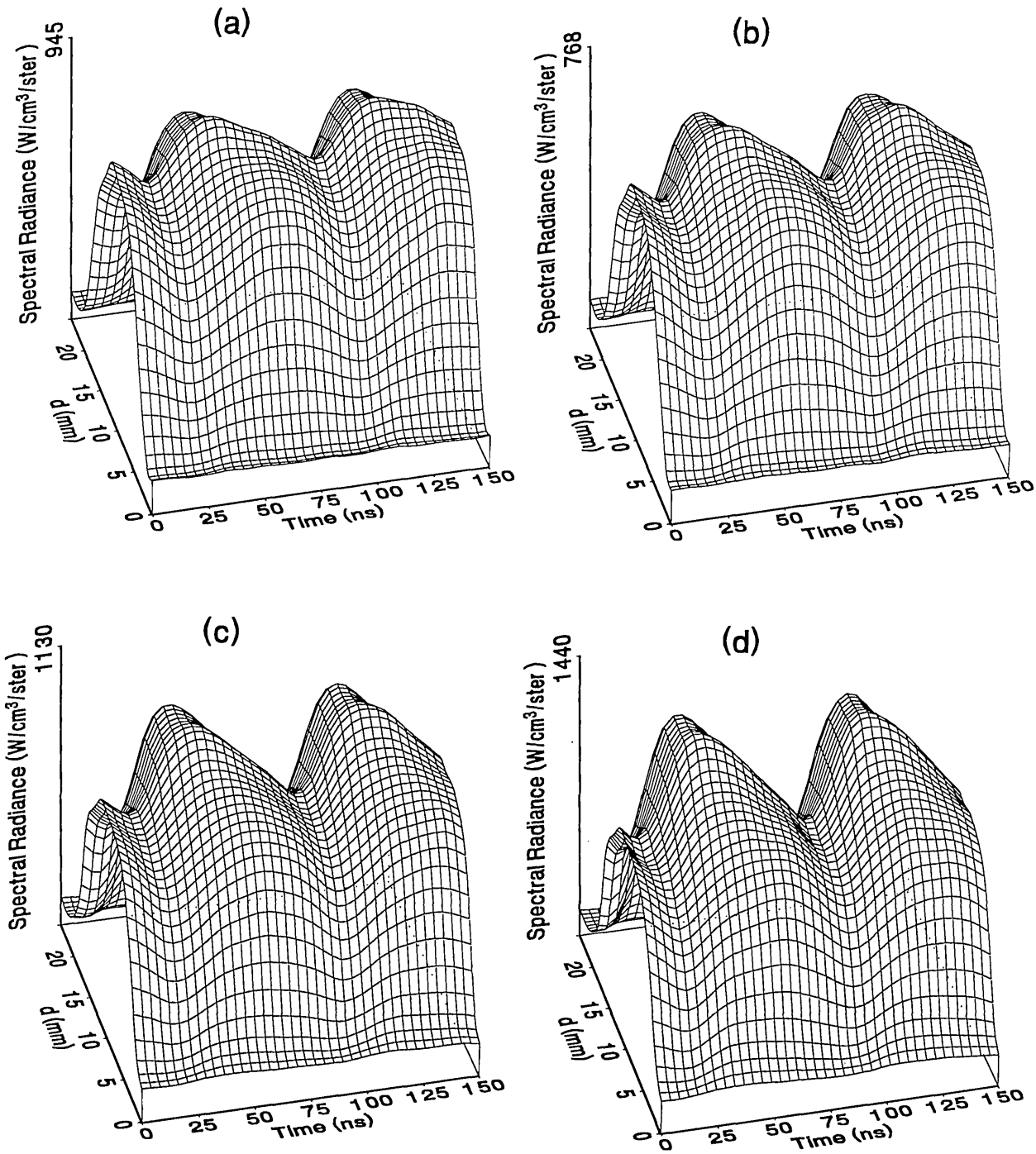

Fig. 4. Optical emission measurements of the spatial profile and temporal evolution of the Ar I 750.4 nm emission line from a 6.7 Pa argon plasma at (a) 75 V, (b) 100 V, (c) 150 V, and (d) 200 V applied rf voltages.

(434.8 nm). Data was taken for argon pressures of 6.7, 13.3, 33.3, 66.7, and 133.3 Pa (50, 100, 250, 500, and 1000 mTorr), and uncorrected applied peak-to-peak rf voltages of 75, 100, 150, and 200 V. Figures 4–13 are plots of surface fits to the calibrated optical emission time profiles taken at many observation points between the electrodes. A time range of 150 ns is shown (~2 complete rf cycles),

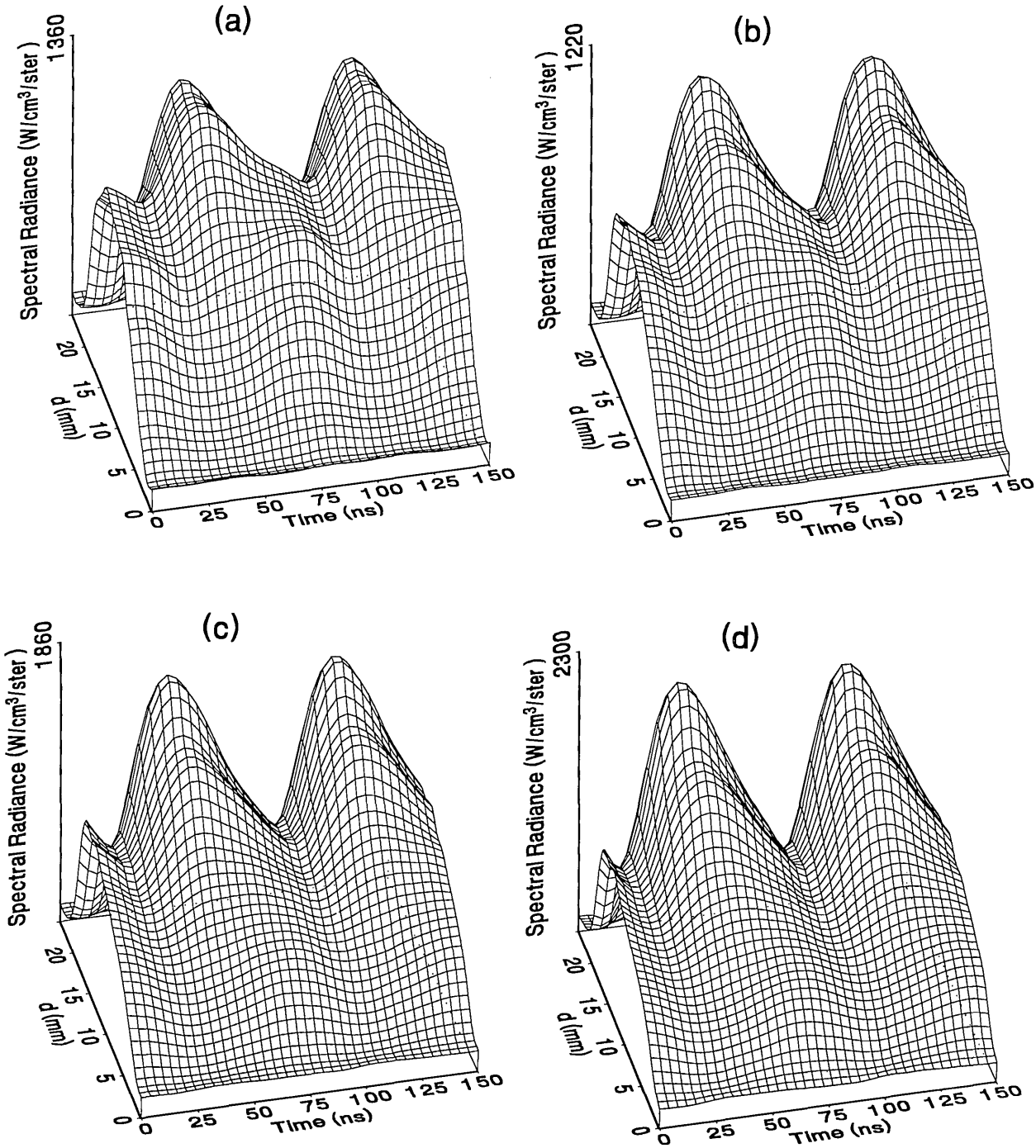

Fig. 5. Optical emission measurements of the spatial profile and temporal evolution of the Ar I 750.4 nm emission line from a 13.3 Pa argon plasma at (a) 75 V, (b) 100 V, (c) 150 V, and (d) 200 V applied rf voltages.

with each square of the grid corresponding to approximately 4 ns on the time axis and 0.5 mm on the d axis. The time $t = 0$ was chosen to correspond to the maximum of the voltage waveform. For these figures and for the remainder of this paper d is defined as the position of the observation point as measured from the grounded electrode along an axis through the center of the rf electrodes. The

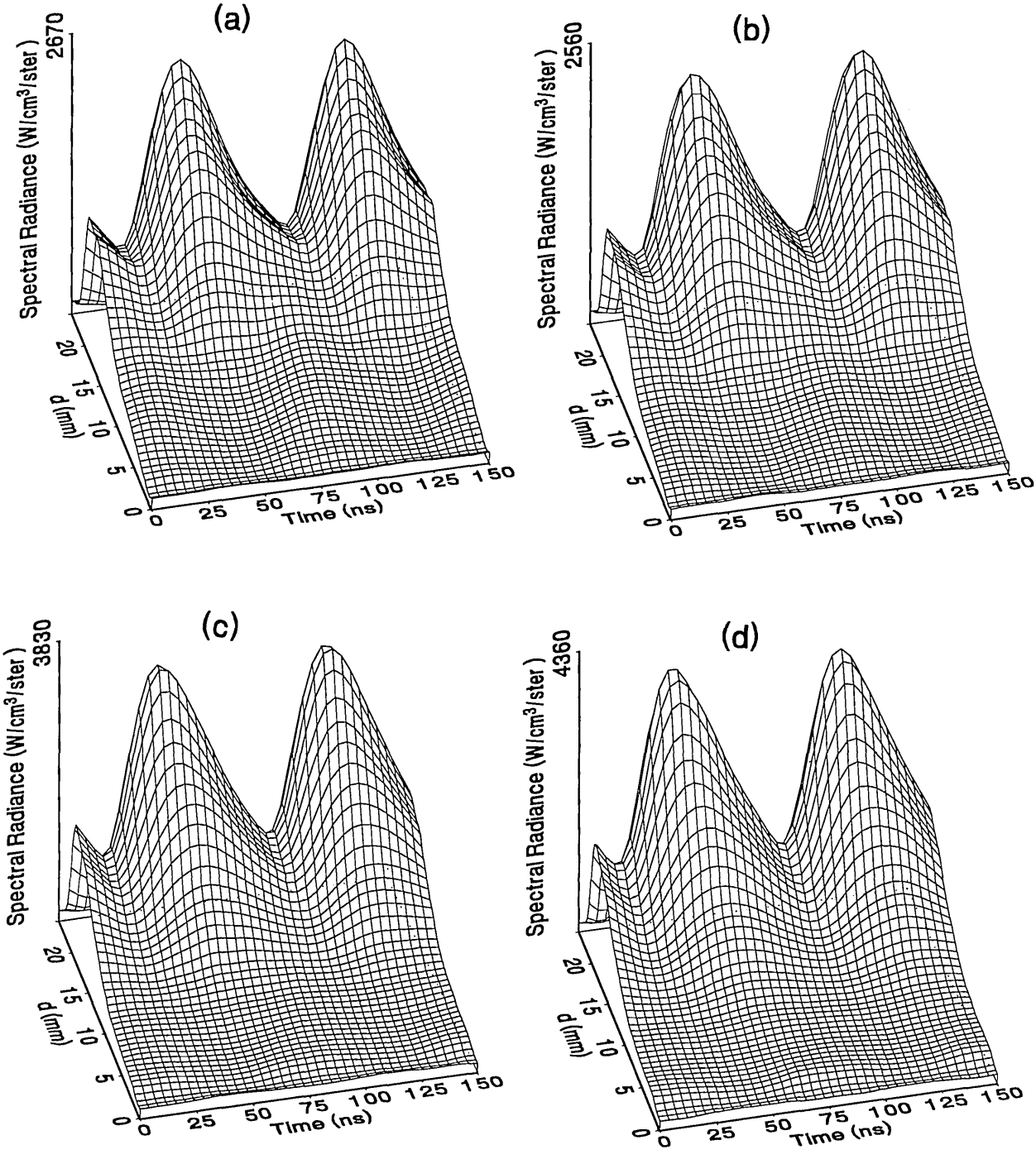

Fig. 6. Optical emission measurements of the spatial profile and temporal evolution of the Ar I 750.4 nm emission line from a 33.3 Pa argon plasma at (a) 75 V, (b) 100 V, (c) 150 V, and (d) 200 V applied rf voltages.

vertical axis on each plot is the absolute spectral radiance measured from the discharge. The number at the top of the vertical axis is the magnitude of the maximum observed signal.

Two complete cycles are shown in each plot to help in determining the significance of minor features in the surface plots. If a feature is not repeated in both cycles, then it is not reproducible and should not be considered to be real. This is particularly evident for the low-pressure Ar II data shown in Figs. 9 and 10 where the signal levels were low, resulting in noisy data.

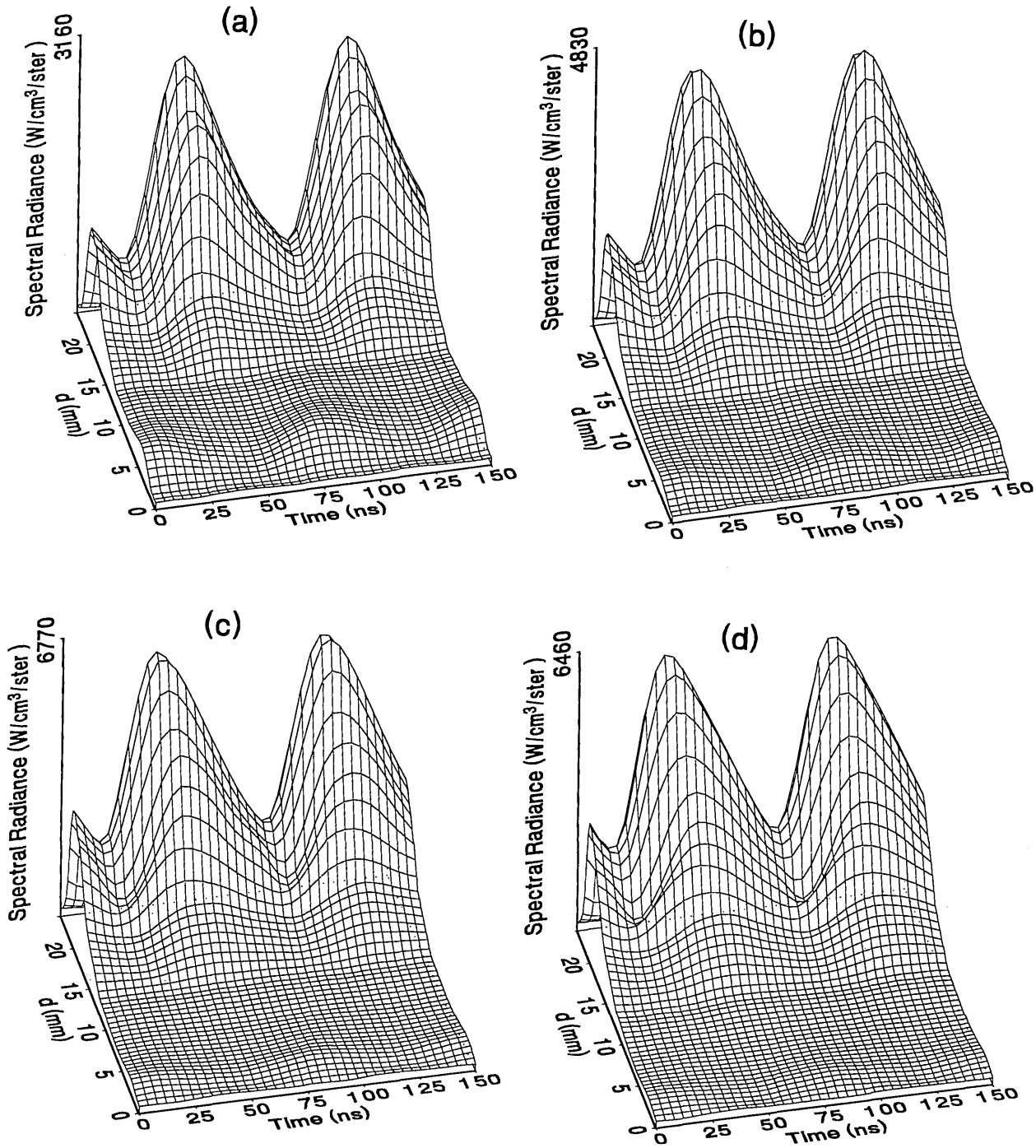

Fig. 7. Optical emission measurements of the spatial profile and temporal evolution of the Ar I 750.4 nm emission line from a 66.7 Pa argon plasma at (a) 75 V, (b) 100 V, (c) 150 V, and (d) 200 V applied rf voltages.

In order to characterize the conditions of the plasmas for which the data in Figs. 4–13 were obtained, data from the measurements of the current and voltage waveforms are presented in Table 1. Listed are the magnitudes and relative phases of the first three Fourier components of the voltage and current waveforms at the surface of the powered electrode, $V_p(t)$ and $I_p(t)$. Higher order

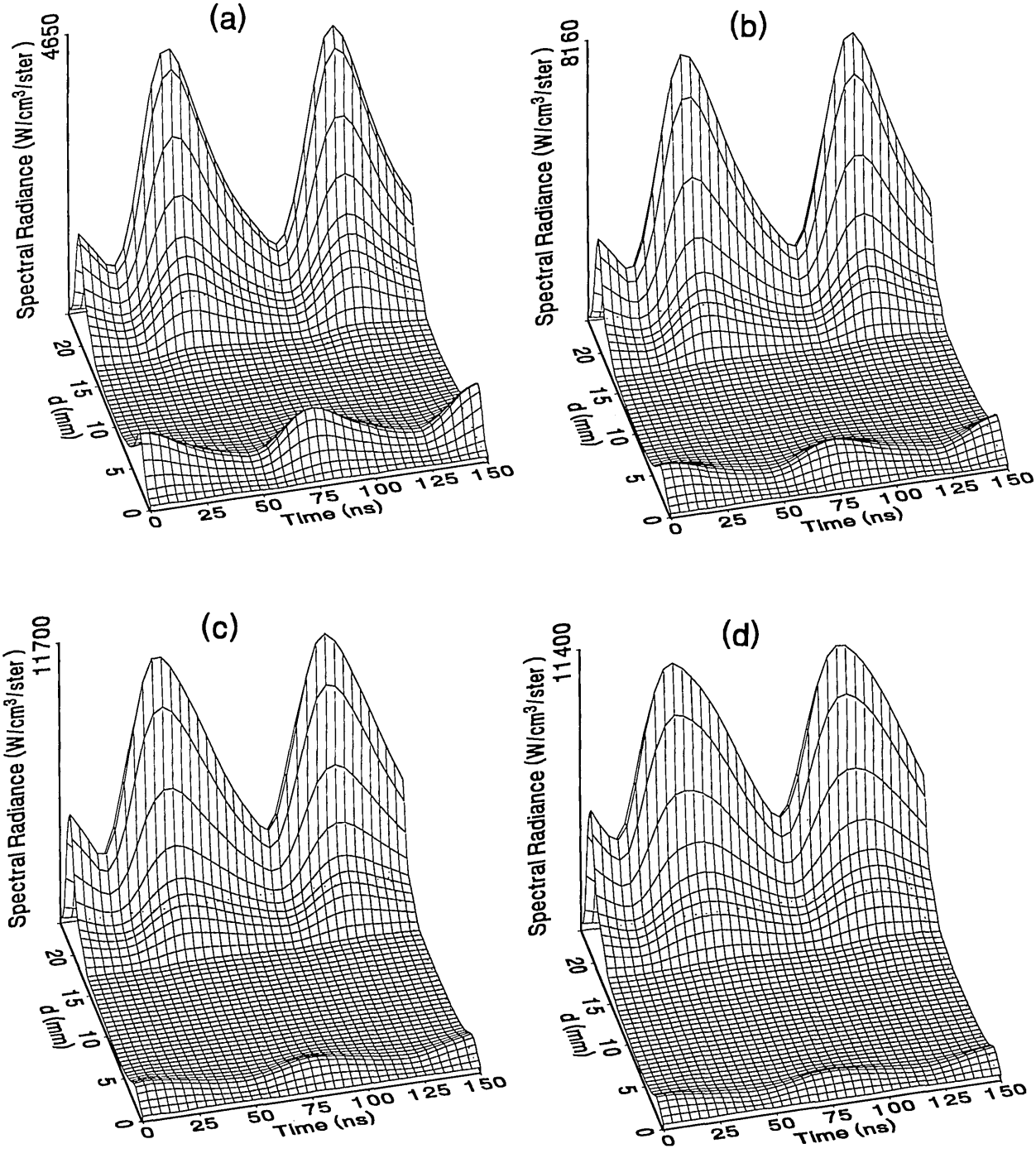

Fig. 8. Optical emission measurements of the spatial profile and temporal evolution of the Ar I 750.4 nm emission line from a 133.3 Pa argon plasma at (a) 75 V, (b) 100 V, (c) 150 V, and (d) 200 V applied rf voltages.

components were too small to be reproducibly measured. For ease of comparison, the time origin of the waveforms was shifted so that in each case the phase of the fundamental current component ($n = 1$) was equal to zero.

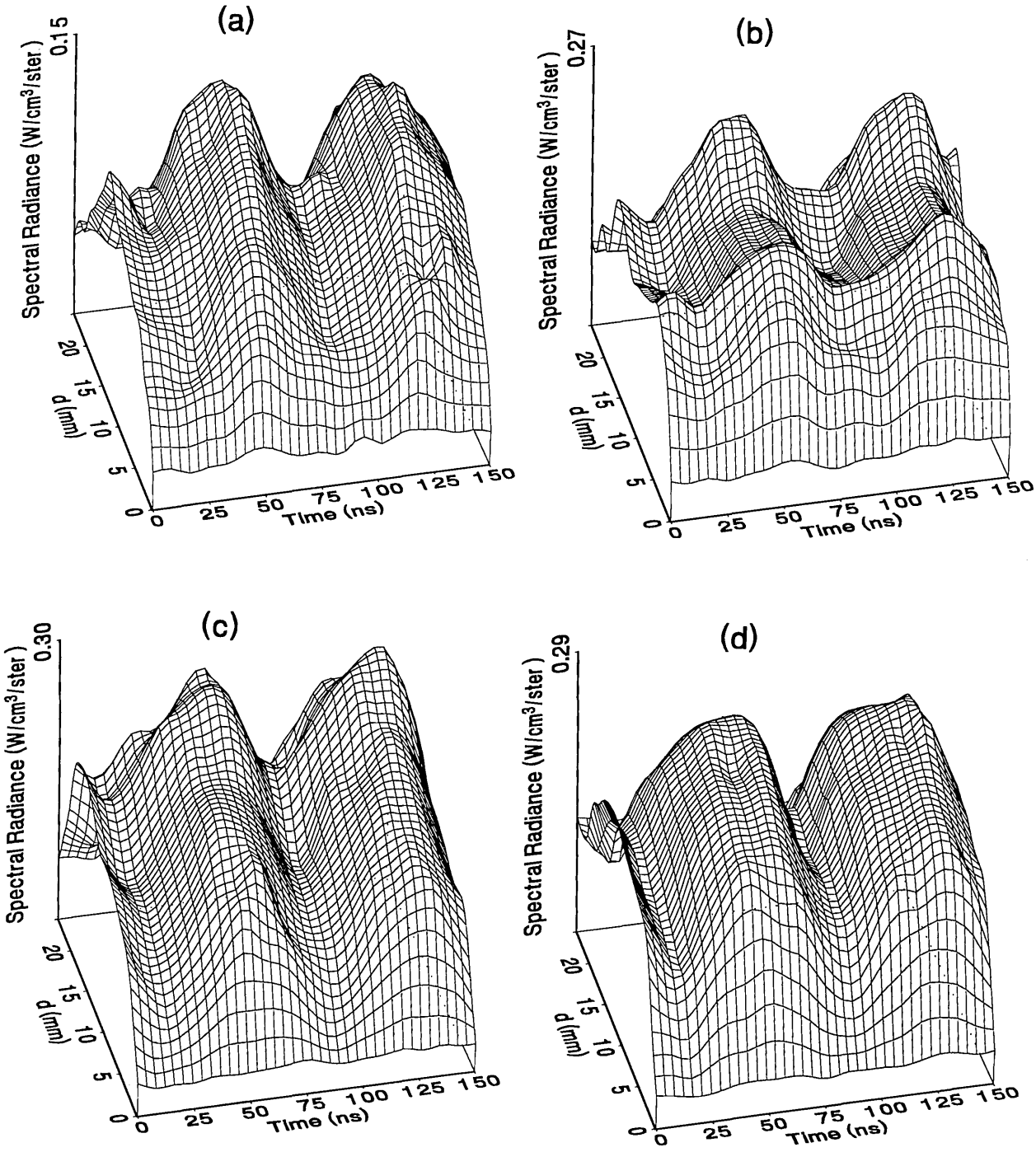

Fig. 9. Optical emission measurements of the spatial profile and temporal evolution of the Ar II 434.8 nm emission line from a 6.7 Pa argon plasma at (a) 75 V, (b) 100 V, (c) 150 V, and (d) 200 V applied rf voltages.

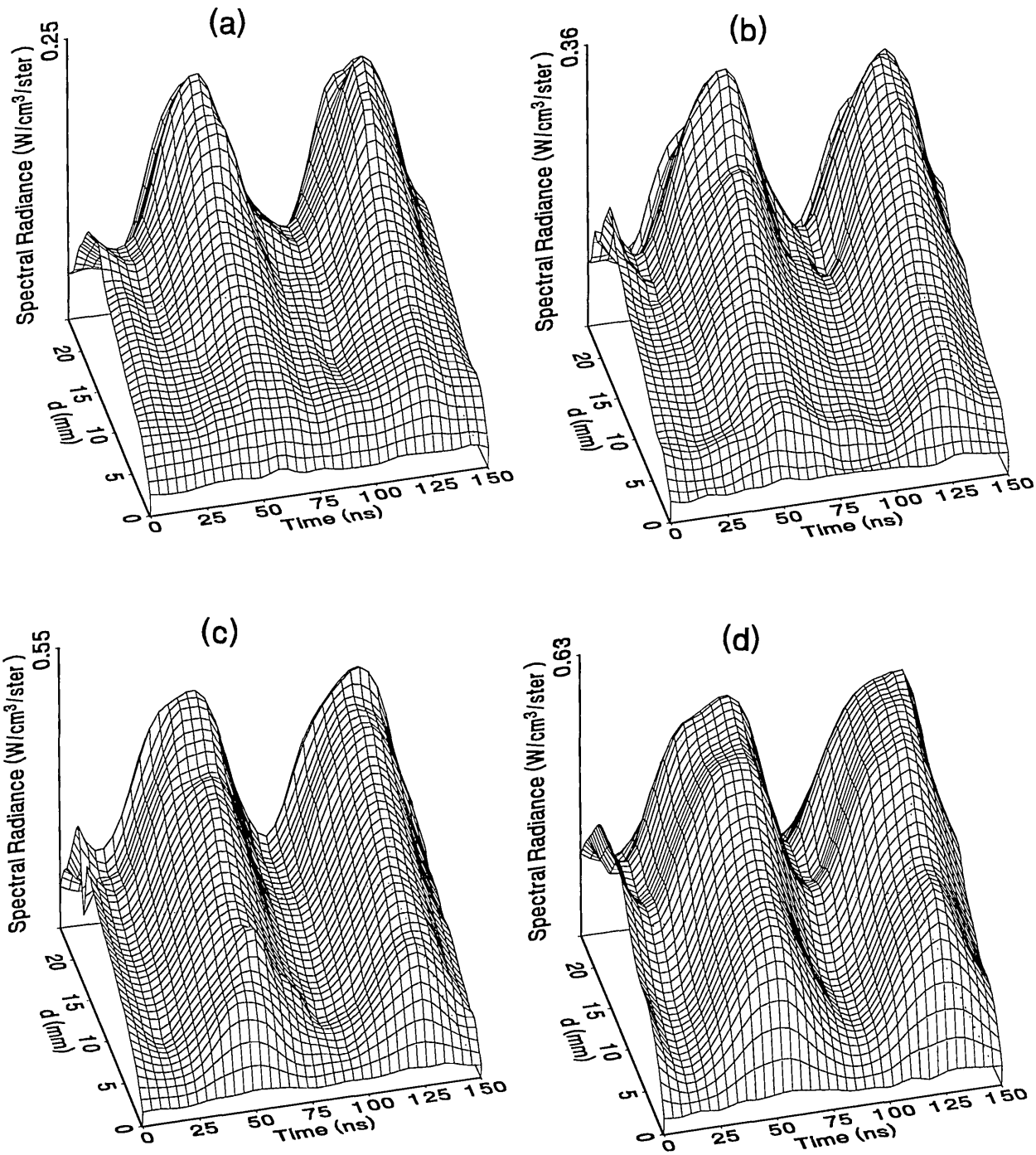

Fig. 10. Optical emission measurements of the spatial profile and temporal evolution of the Ar II 434.8 nm emission line from a 13.3 Pa argon plasma at (a) 75 V, (b) 100 V, (c) 150 V, and (d) 200 V applied rf voltages.

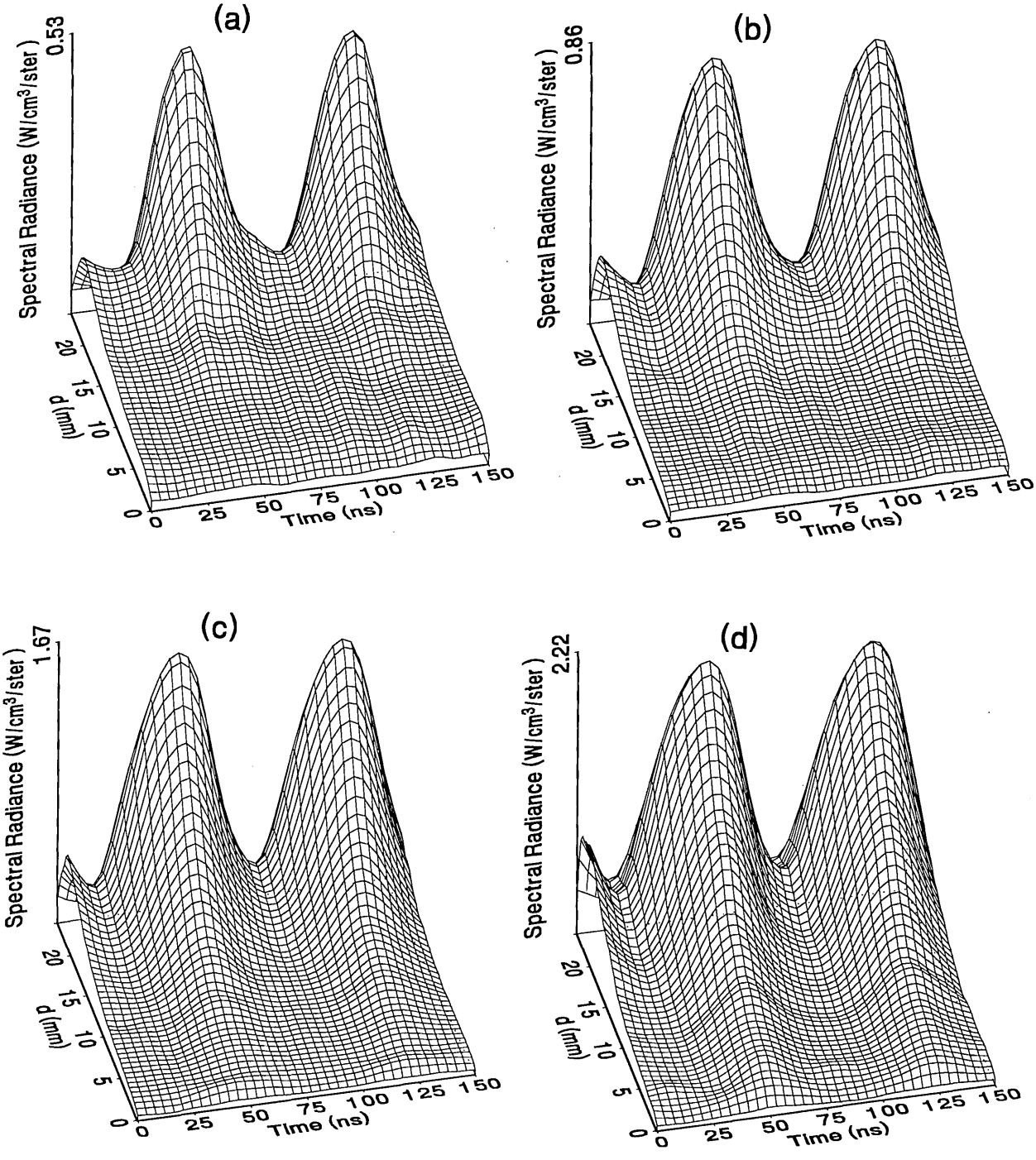

Fig. 11. Optical emission measurements of the spatial profile and temporal evolution of the Ar II 434.8 nm emission line from a 33.3 Pa argon plasma at (a) 75 V, (b) 100 V, (c) 150 V, and (d) 200 V applied rf voltages.

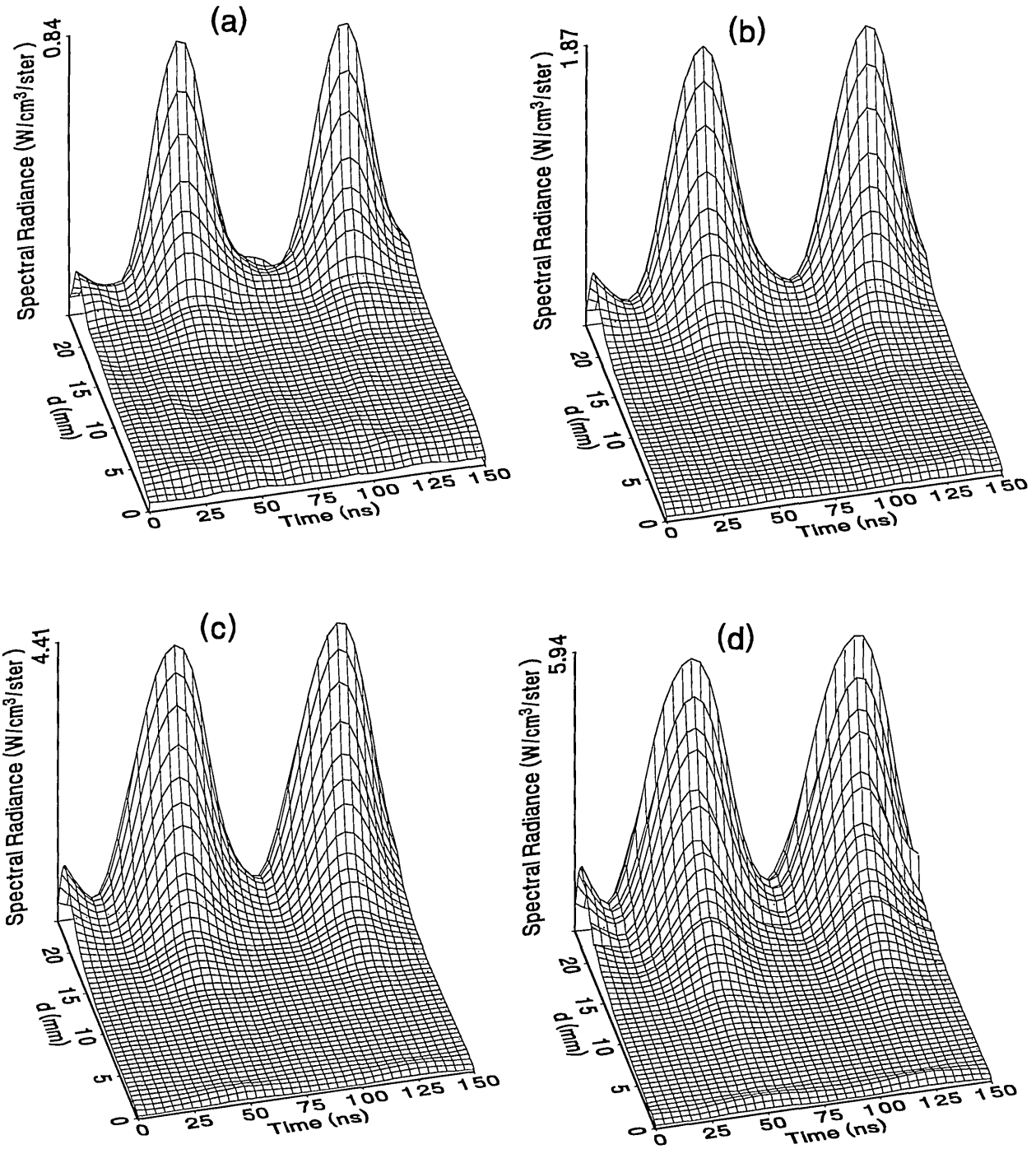

Fig. 12. Optical emission measurements of the spatial profile and temporal evolution of the Ar II 434.8 nm emission line from a 66.7 Pa argon plasma at (a) 75 V, (b) 100 V, (c) 150 V, and (d) 200 V applied rf voltages.

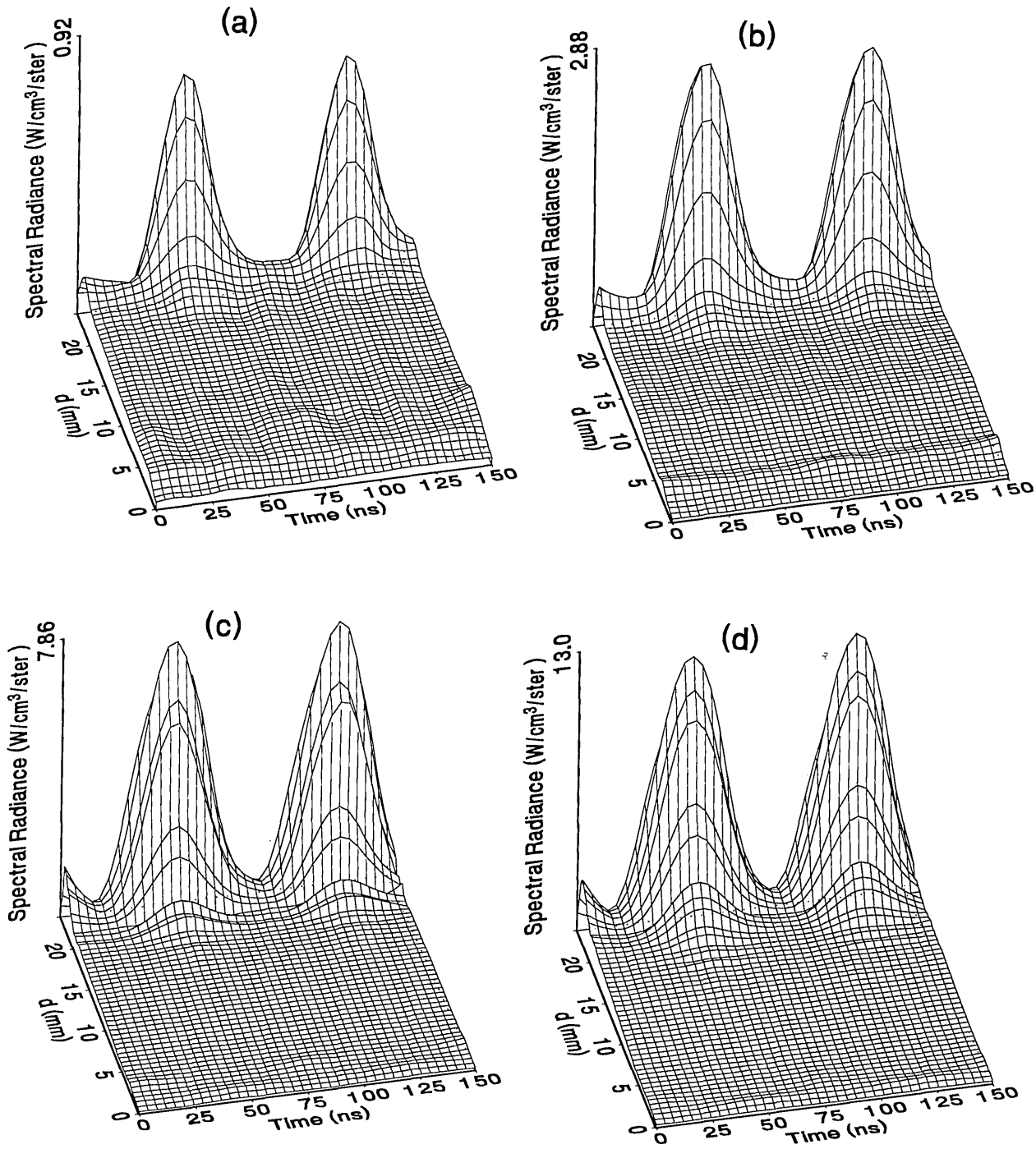

Fig. 13. Optical emission measurements of the spatial profile and temporal evolution of the Ar II 434.8 nm emission line from a 133.3 Pa argon plasma at (a) 75 V, (b) 100 V, (c) 150 V, and (d) 200 V applied rf voltages.

Table 1. Voltage and current parameters for the voltage and current waveforms at the surface of the powered electrode for all plasma conditions used in this paper[a]

Pressure (Pa)	V_{rf} (V)	V_{dc} (V)	V_1 (V)	V_2 (V)	V_3 (V)	I_1 (mA)	I_2 (mA)	I_3 (mA)	ϕ_{i1} (deg)	ϕ_{i2} (deg)	ϕ_{i3} (deg)	ϕ_{v1} (deg)	ϕ_{v2} (deg)	ϕ_{v3} (deg)	Power (W)
6.7	75	−22.4	42.8	0.3	0.3	65	21	14	0	−104.4	159.2	−67.6	−14.7	−107.8	0.5
	100	−36.0	57.5	0.5	0.6	88	31	25	0	−104.2	174.3	−71.2	−20.0	−93.1	0.8
	150	−65.1	85.1	1.0	1.1	126	57	46	0	−93.9	162.8	−74.4	2.4	−106.7	1.4
	200	−95.0	114.8	0.9	1.5	159	65	61	0	−95.6	−179.3	−76.3	−6.6	−89.3	2.2
13.3	75	−19.0	43.2	0.4	0.4	83	26	17	0	−103.2	146.7	−68.8	−10.0	−119.8	0.7
	100	−35.8	59.3	0.6	0.8	121	41	32	0	−101.2	162.8	−73.2	−8.4	−105.3	1.0
	150	−62.7	85.8	0.9	0.9	172	64	40	0	−89.4	162.0	−76.0	18.6	−106.8	1.8
	200	−94.4	116.6	1.2	1.5	208	84	65	0	−93.5	166.7	−77.5	−3.0	−104.0	2.6
33.3	75	−15.8	43.9	0.4	0.3	124	29	13	0	−107.4	136.1	−68.9	−4.3	−131.1	1.0
	100	−28.1	58.9	0.8	0.6	176	54	26	0	−105.5	144.9	−72.5	−11.1	−122.0	1.6
	150	−58.6	87.5	1.5	1.4	288	103	59	0	−97.7	162.3	−76.8	−1.5	−106.2	2.9
	200	−82.8	119.7	2.9	2.5	558	197	108	0	−94.4	171.0	−78.6	−1.1	−99.1	7.2
66.7	75	−13.5	44.0	0.5	0.4	153	34	14	0	−117.8	126.5	−67.2	−25.5	−141.0	1.3
	100	−26.2	60.6	1.0	0.7	251	66	29	0	−104.2	142.0	−71.4	−2.0	−127.4	2.4
	150	−55.2	89.0	2.2	1.9	429	144	81	0	−97.2	156.1	−75.7	0.9	−113.5	4.7
	200	−82.8	119.7	2.9	2.5	558	197	108	0	−94.3	160.1	−77.6	0.2	−109.1	7.2
133.3	75	−11.9	44.5	0.5	0.2	184	33	10	0	−122.2	130.2	−65.9	−28.2	−138.5	1.7
	100	−25.1	60.5	1.1	0.7	315	77	28	0	−110.9	141.9	−70.4	−18.5	−127.6	3.2
	150	−49.4	89.0	1.8	1.7	524	144	70	0	−102.3	160.7	−73.3	−4.9	−108.4	6.7
	200	−75.2	119.5	3.1	3.0	754	232	125	0	−97.2	163.8	−74.4	−1.9	−106.7	12.1

[a] V_{rf} is the applied peak-to-peak rf voltage, V_{dc} is the self-bias potential, V_n is the magnitude of the nth Fourier component of the voltage waveform, I_n is the magnitude of the nth Fourier component of the current waveform, ϕ_{in} and ϕ_{vn} are the phases of the nth Fourier current and voltage components with respect to I_1, and the power is the power dissipated in the plasma as calculated from the measured waveforms. Therefore the nth voltage component is defined by $V_n \cos(n\omega t + \phi_{vn})$ and the nth current components is $I_n \cos(n\omega t + \phi_{in})$ where ω is the fundamental angular frequency. The time origin of each waveform has been shifted so that $\phi_{i1} = 0$.

4. Discussion

As is evident from Figs. 4–13, the temporal and spatial profiles of the optical emission are highly dependent upon the discharge pressure. At 6.7 Pa (Figs. 4 and 9) the spatial profiles are broad with the emission essentially extending across the entire region between the electrodes. Only a small fraction of the optical emission signal exhibits time-dependent behavior at these lower pressures. As the pressure increases to 133.3 Pa the absolute intensity of the optical emission signals increase by a factor 8 for the Ar I line and a factor of 45 for the Ar II line for an applied voltage of 200 V. At these higher pressures a larger fraction of the optical signal exhibits a time dependence, which is in agreement with previous results by Seeböck and Köhler [20] for lower frequency discharges.

As the pressure is increased from 6.7 to 133.3 Pa, the most intense regions of emission shift toward the powered electrode and the formation of well-defined sheaths (dark zones near the electrode surfaces) are observed. The formation of sheaths and a bright band of emission near the powered electrode is not due solely to an increase in signal intensity in that region, but also to a decrease in emission intensity in the central regions of the plasma. Careful analysis of the spatial variation in the optical signals indicates that for a given pressure and voltage, this bright band of emission peaks significantly closer to the powered electrode in the Ar II data than for the Ar I emission. This is more evident in Fig. 14 where the time-averaged spatial dependence of the Ar I and Ar II lines are shown for a 200 V plasma. Figure 14 also indicates that for most plasma conditions the Ar II emission is spatially broader than the Ar I profile, with the Ar II emission extending closer to both electrodes.

Formation of bright bands near the grounded electrode is observed for only a few sets of plasma conditions. For the Ar I transition, a weak sheath is observed at 66.7 Pa with well defined sheaths present at 133.3 Pa (see Figs. 7 and 8). As expected, the time dependence of the bright bands in front of the grounded electrode is 180° out of phase with the emission signal near the powered electrode. Interestingly, as the applied voltage increases (see Fig. 8) the amplitude of the emission near the grounded electrode remains nearly constant while the emission near the powered electrode increases by a factor of 2.5. This may be related to the fact that the voltage across the sheath near the grounded electrode is nearly independent of the applied rf voltage as shown by

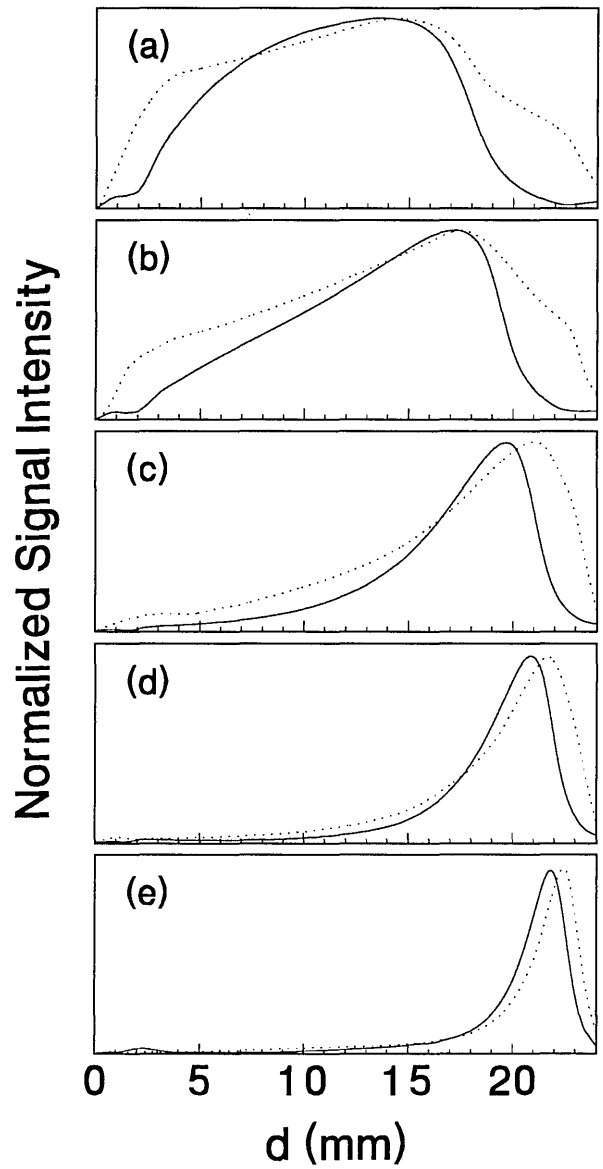

Fig. 14. Normalized, time-averaged optical emission spatial profiles taken along the central axis of the electrodes for Ar I 750.4 nm (−) and Ar II 434.8 nm (...) lines from argon plasmas. The applied rf voltage was 200 V and the gas pressures were (a) 6.7 Pa, (b) 13.3 Pa, (c) 33.3 Pa, (d) 66.7 Pa, and (e) 133.3 Pa. The position $d = 0$ corresponds to the surface of the grounded electrode.

electrical measurements [16] and ion kinetic-energy measurements [14].

The existence of a bright band of Ar II emission near the grounded electrode was only observed for high-pressure, high-voltage plasmas (e.g., 200 V, 66.7 Pa). For these conditions a weak increase in the optical signal is detected near the grounded electrode. Unlike the Ar I signal this bright band

increases in intensity with increasing voltage, and the time dependence is in phase with the optical signal near the powered electrode.

The changes in the temporal and spatial distributions with applied rf voltage are less dramatic than those observed with changing pressure. As the applied voltage increases, the peak emission intensity increases, particularly at the higher pressures. Additionally, the widths of the peaks in the time dependent signal increase with increasing voltage. This indicates that conditions are favorable for the excitation of the required transitions for emission during a greater portion of the rf cycle at higher applied voltages.

The time-dependent optical emission signals exhibit very strong spatial dependences near the powered electrode. Figures 15 and 16 show examples of how the shape of the temporal evolution for the Ar I line changes with position in the sheath region of 200 V argon plasmas with pressures of 133.3 and 13.3 Pa, respectively. This type of variance is not observable in Figs. 4-13 due to the viewing angle chosen for the 3-dimensional surface plots, but exists for many of the plasma conditions. The dependence of these temporal distributions on position in the sheath may provide a powerful diagnostic technique for the investigation of sheath dynamics.

5. Conclusions

Spatially- and temporally-resolved optical emission profiles have been measured for argon plasmas with pressures ranging from 6.7 to 133.3 Pa, and applied rf voltages from 75 to 200 V. These data include the entire set of "standard" GEC reference cell operating conditions [11] in order to allow for easy comparison with other reference cell measurements. A tabulated set of the optical emission data is available on diskette upon request [21].

The magnitude of the plasma emission for two lines has been put on an absolute scale by comparison with emission from a standard lamp. This allows for a complete characterization of the optical emission signal from the rf plasma, and provides a more comprehensive data set for comparison with theoretical modeling results. A complete set of electrical measurements for all plasma conditions is also provided in order to more fully characterize the discharge.

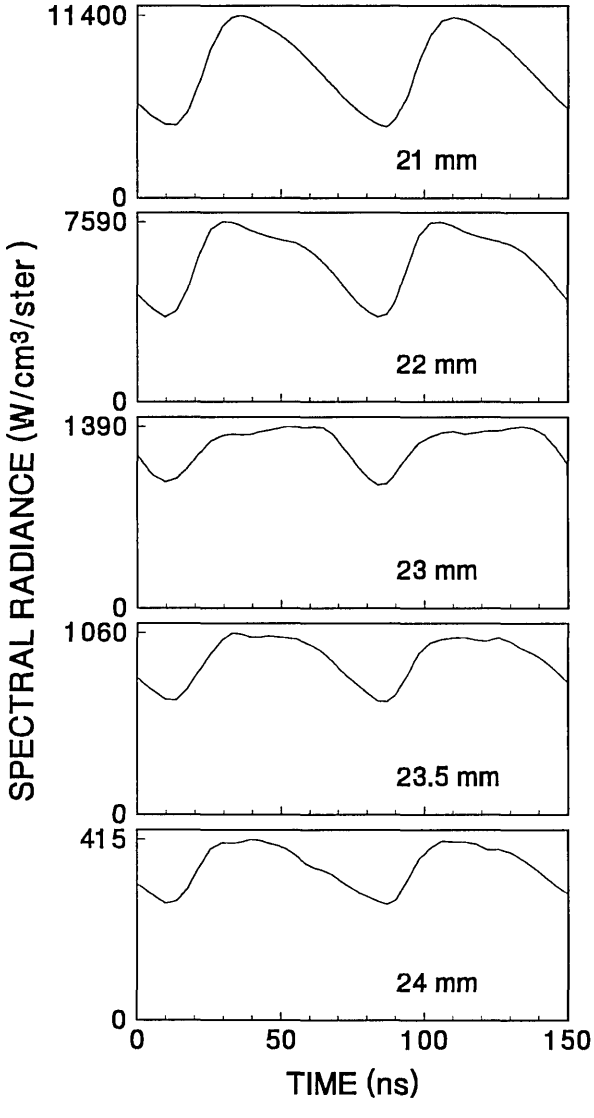

Fig. 15. Temporal distributions of the optical emission for the Ar I 750.4 nm line for locations near the powered electrode in a 200 V, 133.3 Pa argon plasma. Distances are given from the grounded electrode.

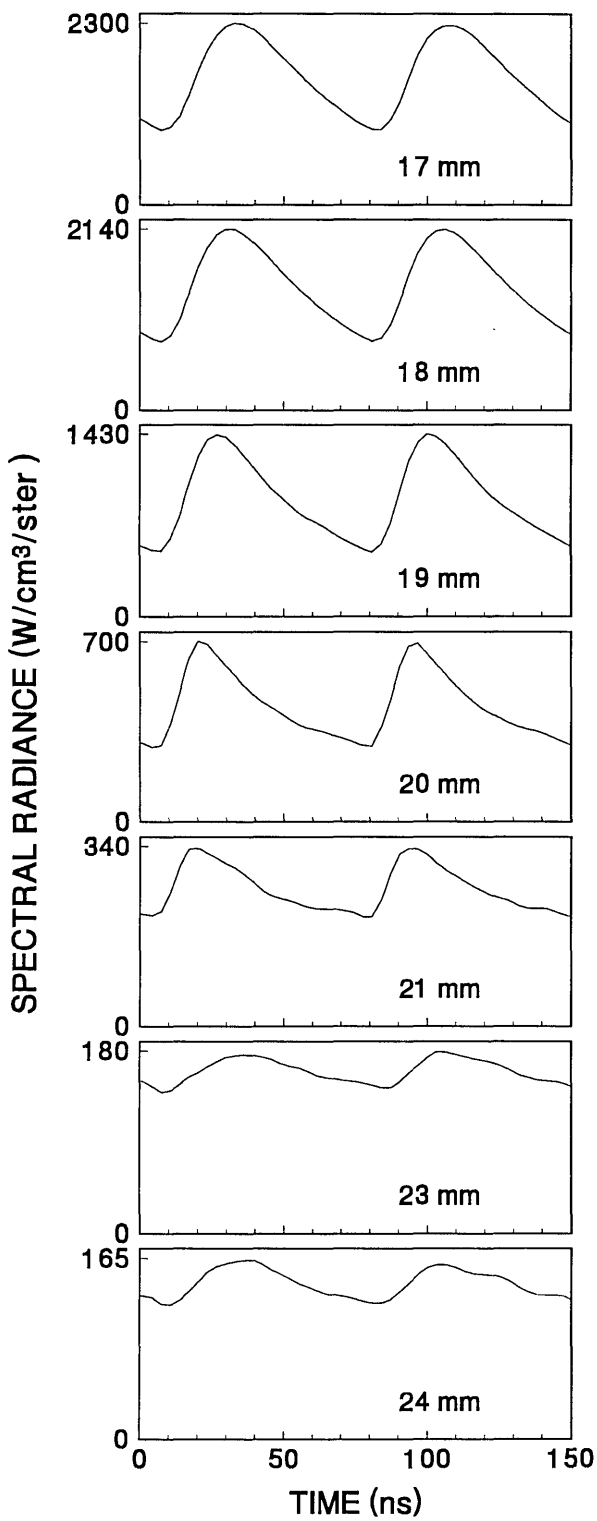

Fig. 16. Temporal distributions of the optical emission for the Ar I 750.4 nm line for locations near the powered electrode in a 200 V, 13.3 Pa argon plasma. Distances are given from the grounded electrode.

6. References

[1] G. de Rosny, E. R. Mosburg, J. R. Abelson, G. Devaud, and R. C. Kerns, J. Appl. Phys. **54**, 2272 (1983).
[2] V. M. Donnelly, D. L. Flamm, and R. H. Bruce, J. Appl. Phys. **58**, 2135 (1985).
[3] P. Bletzinger and C. A. De Joseph, IEEE Trans. Plasma Sci. **PS-14**, 124 (1986).
[4] F. Tochikubo, T. Kokubo, S. Kakuta, A. Suguki, and T. Makabe, J. Phys. D **23**, 1184 (1990).
[5] W. E. Köhler, R. J. Seeböck, and F. Rebentrost, J. Phys. D **24**, 252 (1991).
[6] T. J. Sommerer, W. N. G. Hitchon, R. E. P. Harvey, and J. E. Lawler, Phys. Rev. A **43**, 4452 (1991).
[7] M. Surendra and D. B. Graves, IEEE Trans. Plasma Sci. **19**, 144 (1991).
[8] H. W. Trombley, F. L. Terry, and M. Elta, IEEE Trans. Plasma Sci. **19**, 158 (1991).
[9] S. K. Park and D. J. Economou, J. Appl. Phys. **68**, 3904 (1990).
[10] M. Meyyappan, J. Appl. Phys. **69**, 8047 (1991).
[11] P. J. Hargis, K. E. Greenberg, P. A. Miller, J. B. Gerardo, J. R. Torcznski, M. E. Riley, G. A. Hebner, J. R. Roberts, J. K. Olthoff, J. R. Whetstone, R. J. Van Brunt, M. A. Sobolewski, H. M. Anderson, M. Splichal, J. L. Mock, P. Bletzinger, A. Garscadden, R. A. Gottscho, G. Selwyn, M. Dalvie, J. E. Heidenreich, J. W. Butterbaugh, M. L. Brake, M. L. Passow, J. Pender, A. Lujan, M. E. Elta, D. B. Graves, H. H. Sawin, M. J. Kushner, J. T. Verdeyen, R. Horwath, and T. R. Turner, Rev. Sci. Instrum., in press.
[12] J. R. Roberts, J. K. Olthoff, R. J. Van Brunt, and J. R. Whetstone, Advanced Techniques for Integrated Circuit Processing, Vol. 1392, pp. 428–436, Society of Photo-Optical Instrumentation Engineers, Bellingham, WA (1990).
[13] J. K. Olthoff, J. R. Roberts, R. J. Van Brunt, J. R. Whetstone, M. A. Sobolewski, and S. Djurović, Process Module Metrology, Control, and Clustering, Vol. 1594, pp. 168–178, Society of Photo-Optical Instrumentation Engineers, Bellingham, WA (1991).
[14] J. K. Olthoff, R. J. Van Brunt, and S. B. Radovanov, J. Appl. Phys. **72**, 4566 (1992).
[15] M. A. Sobolewski, J. R. Whetstone, and J. R. Roberts, unpublished.
[16] M. A. Sobolewski and J. R. Whetstone, Advanced Techniques for Integrated Circuit Processing II, Vol. 1803, pp. 309–320, Society of Photo-Optical Instrumentation Engineers, Bellingham, WA (1993).
[17] M. A. Sobolewski, J. Vac. Sci. Technol. **10**, 3550 (1992).
[18] J. H. Walker, R. D. Saunders, A. T. Hattenburg, Spectral Radiance Calibrations, NBS Spec. Publ. 250-1 (January 1987).
[19] W. L. Wiese, M. W. Smith, and B. M. Miles, Atomic Transition Probabilities, Natl. Stand. Ref. Data Ser., Natl. Bur. Stand. (U.S.) 22, Vol. II (1969).
[20] R. J. Seeböck and W. E. Köhler, J. Appl. Phys. **64**, 3855 (1988).
[21] Send requests to J. R. Roberts, NIST, A167, Building 221, Gaithersburg, MD 20899-0001.

About the authors: *Stevica Djurović was a visiting guest scientist in the Atomic Physics Division of the Physics Laboratory. He has since returned to his permanent position as a physicist at the Institute of Physics, Novi Sad, Yugoslavia. James R. Roberts is the group leader of the Plasma Radiation Group in the Atomic Physics Division of the Physics Laboratory. Mark A. Sobolewski is an electrical engineer in the Process Measurement Division of the Chemical Science and Technology Laboratory, and James K. Olthoff is a physicist in the Electricity Division of the Electronics and Electrical Engineering Laboratory. The National Institute of Standards and Technology is an agency of the Technology Administration, U.S. Department of Commerce.*

Volume 98, Number 2, March-April 1993
Journal of Research of the National Institute of Standards and Technology

[J. Res. Natl. Inst. Stand. Technol. 98, 181 (1993)]

Optimizing Complex Kinetics Experiments Using Least-Squares Methods

Volume 98 | Number 2 | March-April 1993

A. Fahr, W. Braun, and M. J. Kurylo

National Institute of Standards and Technology,
Gaithersburg, MD 20899-0001

Complex kinetic problems are generally modeled employing numerical integration routines. Our kinetics modeling program, Acuchem, has been modified to fit rate constants and absorption coefficients generically to real or synthesized "laboratory data" via a least-squares iterative procedure written for personal computers. To test the model and method of analysis the self- and cross-combination reactions of HO_2 and CH_3O_2 radicals of importance in atmospheric chemistry are examined. These radicals as well as other species absorb ultraviolet radiation. The resultant absorption signal is measured in the laboratory and compared with a modeled signal to obtain the best-fit to various kinetic parameters. The modified program generates synthetic data with added random noise. An analysis of the synthetic data leads to an optimization of the experimental design and best-values for certain rate constants and absorption coefficients.

Key words: CH_3O_3; computer modeling; complex gas phase kinetics; free radicals; HO_2; least squares; optimization; simulated data.

Accepted: October 22, 1992

1. Introduction

Many rate constant determinations, particularly for radical-radical reactions, are obtained in complex kinetic systems in which more than one rate process and more than two species concentrations are involved. The kinetic processes can be first or second order or can be mixed. In such cases, an analytic relationship involving species concentrations and rate constants is often impossible to attain and numerical integration is required. If the measurements involve optical absorption, for example, an added complication of contributions to the signal from more than one species may arise. There are a number of modeling programs available to handle such complex systems but most are written for main-frame computers and few are capable of optimizing the fit of a given model to laboratory data by simultaneously adjusting a number of parameters [1]. To obtain a "best-fit" of the data to the kinetic parameters the least squares procedure can be applied. While there is in principle only one least squares method [2,3], its application requires consideration of the conditional constraints relevant to each problem. These are sometimes referred to as the condition or adjustment equation(s).

We describe in this paper the application of a computer program to a least squares fit that is applicable to any mechanism. However, the condition equations may be incomplete and the procedure for analyzing the fit of the parameters to the data should be examined carefully by the user. The kinetic modeling computer program, Acuchem [4] is now widely used. It has been modified in the present work to: 1) perform "Monte Carlo" simulations, and 2) to analyze synthetic data (with noise) via the least squares method and to yield a best fit

to various kinetic parameters within the constraints of the experiment. The program can also serve for the analysis of laboratory data as well an aid in the optimization of experimental design.

The full program capabilities can be demonstrated through the application to the analysis of an important laboratory kinetics problem—which will be done in this paper. Here, the application of the program will be emphasized rather than its detailed construction. The details of the program will be published in near future. However, an interested reader wishing to implement methodology described here could request the program from authors.

2. Procedure

The Acuchem modeling program requires an input file containing a kinetic mechanism with initialized rate constants and initial species concentrations. An output file is generated which lists the concentrations of all of the species on a preselected time grid, and can be displayed as a user-directed graph. We have written an additional program that converts the Acuchem output file into a synthetic "laboratory" data file. The name of each species is printed separately and the user can enter the contribution of each species in the composite "experimental" absorption signal. In normal practice, the synthetic data would be used to determine the sensitivity of the parameter(s) whose values are being sought to other measured variables.

A new analysis program called Acufit has been devised. It reads the Acuchem input file, assumed to contain the correct mechanism or "model," and then either the synthetic "laboratory" or real laboratory data. This is fitted to the "model" in a prescribed way. Both rate constants and absorption coefficients (representing the contribution of each species to the signal) can be adjusted. An iterative adjustment procedure is employed. These problems are inherently nonlinear and one adjustment around initial "first guess values" (by taking only first derivatives) is usually not sufficient. Of course first guess values are necessary and, as long as they are not too divergent from the "correct" values, the iterations will converge (if a solution is possible, see below). Adjustments are made via solution of the "normal equations." Because the variance-covariance matrix is readily available, the quality of the fit can be assessed. Solving for all possible parameters in the system is usually not possible in that multiple (degenerate or near-degenerate) solutions can often fit the data equally well. Programs similar to the one described here are not fully automatic because operational decisions must be made. The possible variations in the analysis method are explored.

3. Mechanism (Model)

The specific kinetic problem we investigate here consists of determining the cross-combination rate constant for two radicals of atmospheric interest, HO_2 and CH_3O_2. Additional details of this system can be found elsewhere [5,6]. The experiments are complicated by overlapping absorptions from HO_2 and CH_3O_2, uncertainties in absorption cross sections, and the inability to perform the experiment under first-order conditions. The objective of this paper is not resolving the disagreement concerning the correct values for absorption cross sections or rate constant for $HO_2+CH_3O_2$ but to demonstrate the application, capabilities, and limitations of our current kinetic modeling program. To do so, we have chosen the initial conditions and results of earlier studies of this system in our laboratory. Primarily, because conditions of other studies are not very clearly outlined in the literature [5,6].

There are three dominant reactions, two combination reactions and the cross-combination reaction. The initial radical concentrations (or rather their ratio) are in the range of previously used experimental values [5,6]. The units below in Eqs. (1) and (2) are cm^3 $molecule^{-1}$ s^{-1} for k_x, molecules cm^{-3} for concentrations, nanometers for λ, and 10^{-20} cm^2 (base e) for absorption coefficient, ϵ_x.

$$\begin{aligned}
&HO_2+HO_2 \rightarrow H_2O_2+O_2, && k_1=1.86\times10^{-12}\\
&CH_3O_2+CH_3O_2 \rightarrow \text{products}, && k_2=3.60\times10^{-13}\\
&HO_2+CH_3O_2 \rightarrow CH_3O_2H+O_2, && k_3=2.90\times10^{-12}\\
&[HO_2]_0+[CH_3O_2]_0=10.8\times10^{13}, && \lambda(215)\\
&[HO_2]_0+[CH_3O_2]_0=11.8\times10^{13}, && \lambda(250)
\end{aligned} \qquad (1)$$

The parameters listed are used to synthesize a good surrogate to the "real" laboratory data, which can be used for test purposes. The objective here is to assess the optimum conditions for obtaining a best fit to the cross-combination rate constant k_3. The rate constants k_1 and k_2 and the ϵ's are best obtained in single component systems [7,8,9,10] containing only HO_2 or CH_3O_2.

Any complex experiment of this kind entails conditions that are characteristic of the experimental design. Those that apply to an earlier study from this laboratory [5] are given in Eq. (2).

$$\epsilon HO_2 \times [HO_2]_0 + \epsilon CH_3O_2 \times [CH_3O_2]_0 = 3.73 \times 10^{-4}, \quad \lambda(215)$$

$$\epsilon HO_2 \times [HO_2]_0 + \epsilon CH_3O_2 \times [CH_3O_2]_0 = 3.39 \times 10^{-4}, \quad \lambda(250) \qquad (2)$$

The conditions listed in Eq. (2) arise because, i) the sum of the initial concentrations, $[HO_2]_0$ and $[CH_3O_2]_0$, results from the titration of known number of precursor Cl atoms, and ii) for weak absorptions the measured absorption signal is linear in the sum of the product of the absorption coefficient and the concentration (and path length) for each respective species. The numbers given under Eq. (2) must always be consistent with those listed under Eq. (1). Also, for convenience, the program requires that the $t = 0$ concentrations be initialized and cannot be adjusted by the program. In the present work only dimensionless units are employed. This does not influence the analysis of errors.

4. Results of Experiments Performed at 250 nm

We have applied the Acufit program to the model defined by Eqs. (1) and (2) with a view towards: i) identifying the number of parameters that have to be fixed under various noise/signal (n/s) conditions; ii) specifying different parametric values (in groups) in order to identify those producing the least bias in the analysis of k_3; iii) fixing all parameters with the exception of k_3, the cross-combination rate constant, in order to provide an independent check on the error analysis obtained in a previous experimental study; and iv) identifying initial concentration ratios of reactants which produces the least bias on k_3 given variations of known parameters within their expected uncertainty. Results are presented in tabular and graphic form demonstrating the effects of these changes in the method of analysis.

4.1. Fixed Parameters, at "Perfect" Values

As stated earlier Acufit requires as input: i) a synthesized or a real laboratory data file, and ii) the Acuchem (model) input data file. In the example we used here the synthesized file was constructed using the values of k_1, k_2, k_3, ϵHO_2, ϵCH_3O_2, ϵH_2O_2, ϵCH_3O_2H, $[HO_2]_0$, and $[CH_3O_2]_0$, given under Eq. (1) for $\lambda = 250$ nm. The Acuchem (model) input file contains all of the information listed under Eq. (1), i.e., the mechanism, the initial concentrations (always assumed to be known) and the rate constants, k_1, k_2, and k_3 taken as initial first estimates. Acufit also requires specification of the parameters (k's or ϵ's) to be evaluated and their initial assignments. Parameters not to be evaluated (fixed) are held at their input values. Finally Acufit requests the value for the random (normally distributed) noise on the data and whether the noise distribution is to be always the same (unseeded) or randomly variable (seeded) from run to run. In the present study the "noise" or σ applied to the data is taken to be independent of the signal level, common for most absorption experiments.

Since the initial assignments for all of the parameters are similar to those used in the construction of the synthetic "laboratory" file, Acufit might return values very close to these, depending upon the entered level of noise. In most cases, however, the sums of residuals squared either increase with successive iterations or oscillate such that some of the adjusted rate constants or absorption coefficients become negative (the program returns negative k's as zero). This means that this problem is not sufficiently constrained so that a unique solution can be found. If this occurs one or more parameters must be fixed at some prescribed input value. If that value is the *same* as used in the construction of the synthetic "laboratory data" file, it is called a "perfect" value. If it is "fixed" at a different value it is called "imperfect." Only when "perfect" values are used for the *fixed* parameters will the analysis program return values for the *adjusted* parameters that are the same as those used in the construction of the synthetic file, i.e., within the precision given by the variance-covariance matrix. The precision, of course, depends on the noise level.

Table 1 was constructed to illustrate variations in the method of analysis. Column 0 labels all parameters that affect the outcome of the best-fit of the data to the model. Values used in creating the "synthetic laboratory" file are listed in column 1. Subsequent columns list results of the analysis with error limits obtained from the variance-covariance matrix. If a cell contains the symbol F, the exact value for that parameter as given in column 1 is employed. If the value is fixed at a value different from that in column 1 it is so designated (for example $F = 0$). All columns involve analysis of the same "synthetic" laboratory data file. This file contains the same noise distribution (at the same or different level as specified in the first row). That is, in running the program the random number generator that produces the distribution is

"not seeded." Figure 1 shows the best-fit to the synthesized signal at 0.01 and 0.05 *n/s* levels. It is noted that in spite of the different intensities, the distribution with regard to the noise is the same. The best-fit to the synthesized data, in Fig. 1, was obtained by fixing all parameters at their "perfect" values, (see column 1, Table 1). Most laboratory experiments are performed at *n/s* levels between these two extremes. In comparing the synthesized signal to a real lab signal it is important that the *n/s* levels be properly compared particularly if dimensionless units are employed.

Table 1. Different analysis fixing various parameters at their "perfect" values and adjusting those remaining

Parameters	Values	*n/s* = 0.01	*n/s* = 0.01	*n/s* = 0.01	*n/s* = 0.01	*n/s* = 0.01	*n/s* = 0.01	*n/s* = 0.01	*n/s* = 0.01	*n/s* = 0.05	*n/s* = 0.01	*n/s* = 0.05	*n/s* = 0.01	*n/s* = 0.05
0	1	2[a]	3[a]	4[a]	5[a]	6	7[a]	8[a]	9	10	11	12	13	14
ϵHO_2	60	57.2± 10	*F*	12.8± 84.	161± 178.	*F*	*F*	*F*	54.3± 11.3	38.1± 56.3	*F*	*F*	*F*	*F*
ϵCH_3O_2	365	*F*	364± 3.5	380± 27	330± 63.	365± 3.2	*F* *F*	*F* *F*	367± 2.7	372± 10.9	366± 2.2	369.± 9.3	*F* *F*	*F* *F*
ϵH_2O_2	8.3	*F*	*F*	*F*	*F*	*F*	*F*	*F* = 0.0	*F*	*F*	*F*	*F*	*F*	*F*
ϵCH_3O_2H	3.98	*F*	*F*	*F*	*F*	*F*	*F*	*F* = 0.0	*F*	*F*	*F*	*F*	*F*	*F*
k_1	1.86	1.25± 0.05	1.26± 1.03	0.97± 1.5	*F*	*F*	1.38± 0.97	1.31± 0.94	*F*	*F*	*F*	*F*	*F*	*F*
k_2	0.36	0.34± 0.02	0.34± 0.03	*F*	0.31± 0.09	0.36± 0.01	0.35± 0.02	0.34± 0.02	*F*	*F*	*F*	*F*	*F*	*F*
k_3	2.90	3.02± 0.17	3.01± 0.20	3.18± 0.23	2.59± 0.78	3.05± 0.20	3.05± 0.12	3.05± 0.12	3.08± 0.19	3.82± 1.12	3.08± 0.20	3.80± 1.07	3.00± 0.10	3.52± 0.63
$[CH_3O_2]_0$	0.88	*F*	*F*	*F*	*F*	*F*	*F*	*F*	*F*	*F*	*F*	*F*	*F*	*F*
$[HO_2]_0$	0.30	*F*	*F*	*F*	*F*	*F*	*F*	*F*	*F*	*F*	*F*	*F*	*F*	*F*

[a] The combination of parameters adjusted in this column cannot be uniquely determined if *n/s* = 0.05.

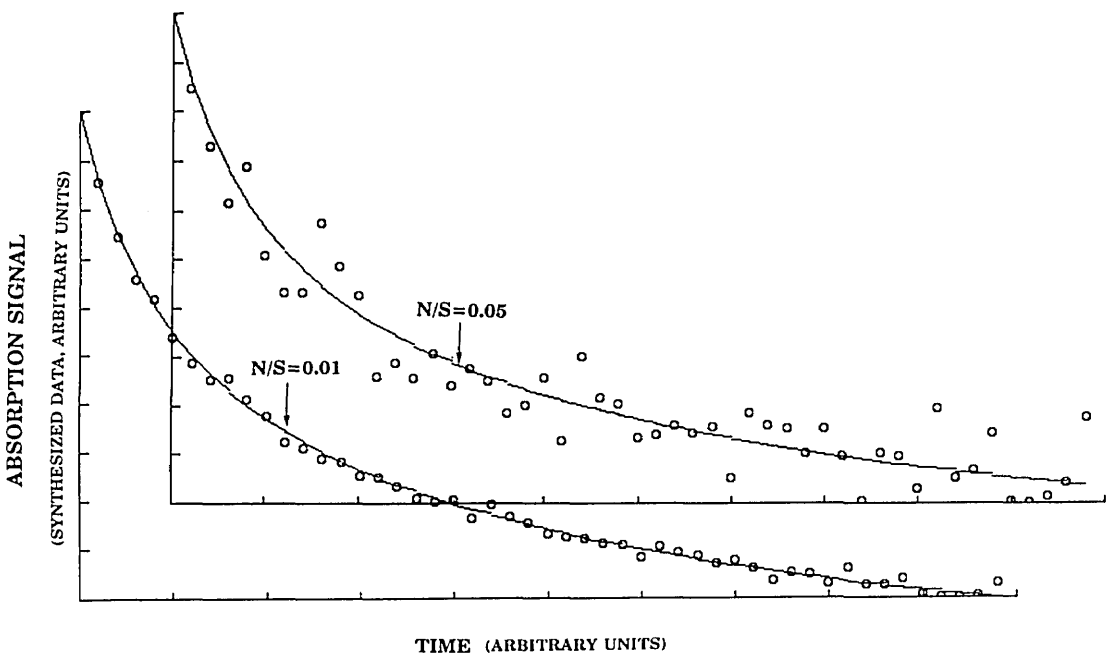

Fig. 1. Best fit to the data when the *n/s* ratios are 0.01 lower and 0.05 upper (insets). Parameters employed in synthesis and analysis are given in column 1, Table 1.

If a file is produced from a program in which the noise distribution is seeded, it is much the same as when a given experiment is re-run. Regardless of whether the noise distribution is seeded or not the error in fitting a parameter should usually fall within the error estimate given by the variance-covariance matrix. The error analysis may be checked by re-running in the seeded mode. Each experiment returns a slightly different value for the adjusted parameters and the standard deviation may be compared with the variance-covariance error estimates. Such checks demonstrate that the program performs properly.

For this mechanism or model, the program will not be able to adjust all parameters (Appendix A). There may be as many as nine parameters. It is unusual in such kinetic mechanisms for the adjusted parameters to be independent of one another. The variance-covariance matrix shows the degree of correlation or anti-correlation between them. Species concentrations are excluded from adjustment, a reasonable programming decision that can be relaxed at some later time. For this mechanism the maximum number of parameters that can be uniquely adjusted is four (Table 1). The number depends on the level of noise on the data.

To obtain the best fit to k_3 the question arises as to whether those parameters which contain considerable error should be fixed. Table 1 provides an answer to the question for at least one case. The analysis listed under column 5 shows a poor value for ϵHO_2, the error being as large as the value of the parameter. The error obtained for k_3 is ± 0.78. In column 6 the parameter for ϵHO_2 is fixed at its "perfect" value, $\epsilon HO_2 = 60$. As a result a better value of k_3 is obtained with an error of ± 0.20. In this case, provided that ϵHO_2 is known well enough, it would clearly be better to fix it than search for it. If for example, ϵHO_2 were fixed at an "imperfect" value of 30 while maintaining all of the other entries in column 6, $k_3 = 3.2 \pm 0.22$, would be obtained, a better value than that shown in column 5. We will explore in detail the effect of fixing parameters at "imperfect" values in the next section but emphasize here the well quoted rule that if a parameter is obtained with an error estimate comparable to its value it may be better to fix that parameter.

Table 1 shows, as expected, that the parameter of interest is obtained with better precision when a larger number of parameters are fixed. This advantage is offset by the fact that fixing parameters at "imperfect" values introduces a bias in the results. Table 1 shows further that the model is very insensitive to ϵH_2O_2 and ϵCH_3O_2H in that setting these absorption coefficients equal to 0 has little influence on the adjusted parameters (columns 7 and 8). Since all parameters cannot be adjusted simultaneously, the best strategy is to fix them at their "perfect" values. As shown in Table 1 the errors given by the variance-covariance matrix for the various parameters is closely linear in the *n/s* level (columns 9 and 10, as well as 13 and 14).

The main observations from the analyses listed in Table 1 are, i) a number of parameters must be fixed, ii) fixing some combination of parameters is superior to other combinations. Parameters that show the greatest error estimates should preferably be fixed, iii) the amenability of adjustment for certain parameters is a function of the noise level and initial conditions, and finally, iv) if all fixed parameters are entered at their "perfect" values the variance-covariance matrix error estimates are completely reliable.

4.2. Fixed Parameters at "Non-Perfect" Values

We now explore the consequence of not entering "perfect" values for the fixed parameters in the calculations. After all in an actual experiment, we do not usually know the exact value for a fixed parameter, only an average value with a plus and minus uncertainty. The conclusion is that fixing a parameter at a "non-perfect" value simply produces a bias on the values of the adjusted parameters yielded by the analysis. The strategy is to fix only those parameters causing the least bias on the parameter of interest, k_3 in the present example. When biases are present, estimates of errors (of the adjusted parameters) obtained from the variance-covariance matrix are likely to be too small. Such biases are best investigated by means of the present procedure through the use of synthetic data. The biases can then be determined, and only when they are added to the variance-covariance error estimate is there an appreciation of the real error in such a system.

In developing Table 2 a few observations are noted. The fixed parameters were generally chosen $\pm 10\%$ from their "perfect" values, column 1. This produces biases that are nearly symmetric. Since the program does not provide for adjustment of initial concentrations, when either $[HO_2]_0$ or $[CH_3O_2]_0$ is fixed at an "imperfect" value it is necessary to adjust one or both of the absorption coefficients, ϵHO_2 and ϵCH_3O_2 so that the implicit constraint, $[HO_2]\epsilon HO_2 + [CH_3O_2]\epsilon CH_3O_2 = \text{constant}$, applies. If ϵHO_2 and/or ϵCH_3O_2 are not

simultaneously adjusted a large bias occurs (columns 6 and 7, Table 2). In the next section the consequences of fixing ϵHO_2 and/or ϵCH_3O_2 at "imperfect" values are explored. In such cases the constraints of Eq. (2) must be take into account explicitly to properly set $[HO_2]_0$ and $[CH_3O_2]_0$.

A relatively small bias in k_3 develops regardless of which parameter is fixed at an imperfect value. If we were to conclude our error analysis at this point and analyze real "laboratory" data at the 1% *n/s* level we would expect an absolute error of about 0.19, Table 1, due entirely to the random noise and independent of any bias. If the initial concentrations of HO_2 and CH_3O_2 were uncertain to the extent of 10% we would expect a small bias of ± 0.07 (in k_3) due to CH_3O_2 (compare k_3 in columns 6 and 8, Table 2, with 2.90) and a bias of ± 0.23 due to HO_2 (compare columns 9 and 10, Table 2, with 2.90). Assuming the random errors and the biases can be combined through vector addition the combined error in k_3 would be: $\sigma^2(k_3) = (0.19)^2 + (0.07)^2 + (0.23)^2 = (0.31)^2$. Additionally if k_2 were fixed and its estimated error were also at the 10% level, the term $(0.44)^2$ would have to be added. If k_1 were fixed, a 10% estimated error in this parameter, according to Table 2, would require adding the additional term $(0.135)^2$ in order to obtain the combined error in $\sigma^2(k_3) = (0.55)^2$ (an error of 19% in k_3). This assumes that the errors in the fixed parameters can be properly estimated and they are not correlated. An error in both $[HO_2]_0$ and $[CH_3O_2]_0$ with no error in ϵHO_2 and ϵCH_3O_2 was assumed. The error estimates are associated with the product of the absorption coefficient and the initial concentration for each species. The errors in the initial concentration and the ϵ (for each species) are in fact distributed.

The principal conclusions are, i) that when one or more parameters are fixed, the bias on k_3 (the parameter of interest) that each fixed parameter produces must be determined, and ii) If the biases are small, as in the present case, errors given by the variance-covariance matrix are still valid. They encompass the correct or expected results (column 11, Table 2). If results fall outside of the error estimates obtained from the variance-covariance matrix the composite error can be obtained by vector addition of the random error, due to noise, and the bias engendered by fixing a parameter.

4.3. Fixing ϵHO_2 and/or ϵCH_3O_2 at "Non-Perfect" Values

We continue the analysis of Table 2 by fixing the two important absorption coefficients at "imperfect" values. This is equivalent to using a erroneous value for one or both of these coefficients in the analysis of real laboratory data. Here we are both compliant and noncompliant with the constraints of Eq. (2). Thus, ϵHO_2 and ϵCH_3O_2 are individually

Table 2. Bias produced on adjusted parameters by fixing selected parameters at "non-perfect" values

Parameters	Values	*n/s* = 0.0	*n/s* = 0.0	*n/s* = 0.0	*n/s* = 0.0	*n/s* = 0.0	*n/s* = 0.0	*n/s* = 0.0	*n/s* = 0.0	*n/s* = 0.0	*n/s* = 0.01
0	1	2	3	4	5	6	7	8	9	10	11
ϵHO_2	60	91.7	29.4	49.	163.	*F*	*F*	*F*	55.	66.	63. ± 11.0
ϵCH_3O_2	365	354.	375.	402.	330.	321.	*F*	407.	*F*	*F*	*F*
ϵH_2O_2	8.3	*F*	*F*	*F*	*F*	*F*	*F*	*F*	*F*	*F*	*F*
ϵCH_3O_2H	3.98	*F*	*F*	*F*	*F*	*F*	*F*	*F*	*F*	*F*	*F*
k_1	1.86	$F = 2.05$	$F = 1.67$	1.18	2.43	1.27	5.44	2.30	2.06	1.52	0.81 ±
k_2	0.36	0.35	0.37	$F = 0.40$	$F = 0.32$	0.32	0.44	0.39	0.35	0.37	0.35 ± 0.02
k_3	2.90	2.76	3.03	3.31	2.43	2.82	7.40	2.96	2.69	3.15	3.28 ± 0.19
$[CH_3O_2]_0$	0.88	*F*	*F*	*F*	*F*	$F = 1.0$	$F = 1.0$	$F = 0.79$	*F*	*F*	*F*
$[HO_2]_0$	0.30	*F*	*F*	*F*	*F*	*F*	*F*	*F*	$F = 0.33$	$F = 0.27$	$F = 0.27$

or simultaneously varied and the initial concentrations $[HO_2]_0$ and $[CH_3O_2]_0$ are fixed at values dictated by Eq. (2), or are fixed at values given in column 1 of Table 3. The results show that non-adherence to the conditional constraints of Eq. (2), will not adversely affect the bias on k_3 (compare columns 2 and 3, Table 3) if ϵHO_2 is fixed (10%) off its "perfect" value. A large bias does occur, however, if ϵCH_3O_2 is fixed $\pm 10\%$ off from its "perfect" value and the initial concentrations $[HO_2]_0$ and $[CH_3O_2]_0$ are not initialized in accord with Eq. (2) (see results of columns 4 and 5). Columns 9 and 10 show a significant bias on k_3 if ϵHO_2 is set $\pm 10\%$ and ϵCH_3O_2 is set $\pm 10\%$ off from their perfect values with both offset in the same direction.

4.4 Optimum $[HO_2]_0/[CH_3O_2]_0$ Condition for Obtaining k_3 at 250 nm

We explore here how the absolute error in k_3 varies with the ratio $[HO_2]_0/[CH_3O_2]_0$. It may be guessed that k_3 is best-fit under conditions where the cross-combination product builds up to its largest possible value, but at the same time it is desired to maximize the absorption signal. The noise level in the absorption signal is a function of the intensity of the analysis light beam (the signal to noise ratio improves linearly with the absorption signal). It is not known *a priori* which of these two optimization conditions most influences the minimization of error in k_3 or whether other factors also contribute.

Figure 2 shows the result of the error analysis obtained by varying the ratio $[HO_2]_0/[CH_3O_2]_0$. The absolute error in k_3 is obtained by first preparing a "synthetic" laboratory data file appropriate to the initial concentrations at the specified noise level, $\sigma = 3.66$ corresponding to a $n/s = 0.01$, with all of the other parameters given under Eq. (1). Then k_3 is adjusted (best-fit) fixing all other parameters at their "perfect" values.

The total absorption signal (S), the final cross-combination product ($P_{t=\infty}$) and the error in determining k_3 (E) are plotted in Fig. 2. Since (P) maximizes at about a 50/50 composition ratio of $[CH_3O_2]_0/[HO_2]_0$ and (S) maximizes well to the right (side of the figure) a minimum in the error in k_3 would be expected at a composition ratio greater than 50/50. In fact a minimum is obtained at about 40/60. The prediction indicates that factors other than the maximum signal and cross-combination product enter into the optimization analysis. The minimum error in k_3 occurs over a fairly extensive range of initial concentrations. Clearly the optimization of the composition condition must be made by minimizing the error in k_3.

Table 3. Bias produced on adjusted parameters by fixing absorption coefficients and concentrations at "non-perfect" values while maintaining constraints of Eq. (2)

Parameters	Values	n/s = 0.0	n/s = 0.0	n/s = 0.0	n/s = 0.0	n/s = 0.0	n/s = 0.0	n/s = 0.0	n/s = 0.0	n/s = 0.0
0	1	2	3	4	5	6	7	8	9	10
ϵHO_2	60	$F = 66.$	$F = 66.$	F	F	F	F	$F = 54.$	$F = 54.$	$F = 66.$
ϵCH_3O_2	365	F	F	$F = 400.$	$F = 400.$	$F = 474.$	$F = 328.$	F	$F = 328.$	$F = 400.$
ϵH_2O_2	8.3	F	F	F	F	F	F	F	F	F
ϵCH_3O_2H	3.98	F	F	F	F	F	F	F	F	F
k_1	1.86	F	F	F	F	F	F	F	F	F
k_2	0.36	F	F	F	F	F	F	F	F	F
k_3	2.90	2.71	2.96	2.20	5.70	1.80	4.90	3.20	5.00	2.00
$[CH_3O_2]_0$	0.88	$F = 0.87$	F	$F = 0.79$	F	$F = 0.65$	$F = 1.00$	$F = 0.89$	$F = 1.01$	$F = 0.78$
$[HO_2]_0$	0.30	$F = 0.31$	F	$F = 0.39$	F	$F = 0.53$	$F = 0.18$	$F = 0.29$	$F = 0.17$	$F = 0.40$

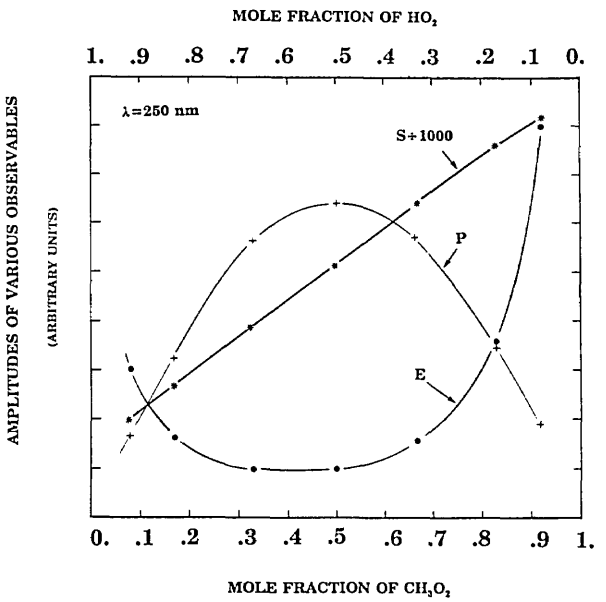

Fig. 2. Absolute error in k_3, E; Absorption signal at 250 nm, S; and cross-combination product plotted vs mole fractions of $[CH_3O_2]_0$ and $[HO_2]_0$. Parameters same as in column 1, Table 1; and $[CH_3O_2]_0+[HO_2]_0=1.2$.

5. Optimization of $[HO_2]_0/[CH_3O_2]_0$ to Obtain Several Parameters at 215 nm.

We extend the above analysis by optimizing $[HO_2]_0/[CH_3O_2]_0$ with respect to several of the parameters, taken one at a time. The experiment is at 215 nm and the appropriate parameters of Eq. (1) are used. The results of the analysis are shown in Fig. 3. It is noted that the analysis displayed in Fig. 2 (experiment at $\lambda=250$ nm) and 3 ($\lambda=215$ nm) can be directly compared with respect to the magnitude of the error on k_3, common to both figures.

The optimization conditions for obtaining the parameters k_1 and k_2 (also ϵHO_2 and ϵCH_3O_2) are obvious but it is instructive to examine the detailed shapes of the curves. Clearly for the self reactions the error in the determination of the k's is smallest when the associated radical concentration is dominant. The optimum ratio $[CH_3O_2]_0/[HO_2]_0=50/50$ producing the least error in k_3 is somewhat different from that found in the above case ($[CH_3O_2]_0/[HO_2]_0=40/60$) probably because at 215 nm ϵHO_2 is comparable in magnitude to ϵCH_3O_2. Again there is no way of guessing the outcome.

If the ratio of the two initial concentrations were to be optimized to obtain the least error in several parameters *combined*, a 50/50 mixture of $[HO_2]_0$ and $[CH_3O_2]_0$ would probably be the best compromise condition. We might expect to be able to solve for more than four parameters uniquely, as found previously using a nonoptimum $[HO_2]_0/[CH_3O_2]_0$ ratio. However, it is found that only four parameters can be assessed, regardless of how small the noise level is set. This means that some combination of parameters yield fits that are about as good as other combinations. The system must be further constrained by fixing some of them. Setting $[HO_2]_0/$

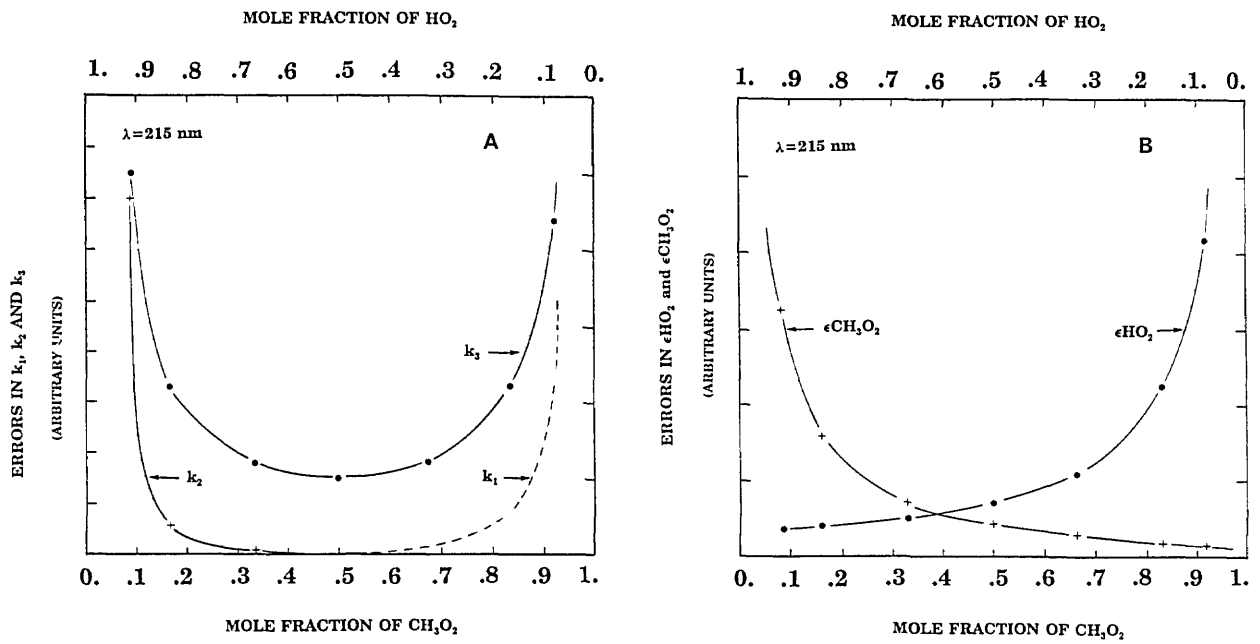

Fig. 3 Absolute errors in k_1, k_2, and k_3 vs mole fractions of $[CH_3O_2]_0$ and $[HO_2]_0$ at 215 nm. Rate parameters same as in column 1, Table 1; absorption coefficients (for $\lambda=215$.), Conditions as in Eq. (1); $[CH_3O_2]_0+[HO_2]_0=1.2$. B: Absolute errors in ϵCH_3O_2 and ϵHO_2 are similarly plotted.

$[CH_3O_2]_0$ significantly off center ($[HO_2]/[CH_3O_2]_0 = 50/50$, in Fig. 3) does have the expected effect of further restricting the number of parameters that can be varied simultaneously.

The combined error estimate in k_3 for a 50/50 mix of $[HO_2]_0/[CH_3O_2]_0$ (the optimum mixture) is recalculated. This is done as previously by determining the bias produced in k_3 by assuming a 10% error in both ϵHO_2 and ϵCH_3O_2 instead of in $[HO_2]_0$ and $[CH_3O_2]_0$. We also include the bias produced by 10% errors in k_1 and k_2, as well as the random error produced by a $n/s = 0.01$. A somewhat lower error estimate is obtained, $\sigma = \pm 0.30$ (an error of $\pm 10\%$) as compared to $\sigma = 0.55$ (an error of 19%) determined in Sec. 4.2 for nonoptimum mixtures. This error was evaluated by fixing all parameters and solving for k_3, thereby allowing a direct comparison with the estimated error of the previous Ref. [5]. Reevaluating the error in k_3 obtained in Ref. [5] where the percent error in both ϵHO_2 and ϵCH_3O_2 were chosen to be 30%, we find that at a 10% level and including the additional bias due to 10% errors in k_1 and k_2, we arrive at an error of about 20% in k_3, similar to the range of values obtained here. Even at the 2σ level, this error does not completely encompass the range of values reported in the literature [9]. Nevertheless, a proper accounting for each study would have to be performed separately under their unique set of boundary conditions, to ascertain whether the remaining differences are attributable to larger errors in the input parameters or other factors (such as secondary chemistry).

6. Conclusions

We have shown that the errors returned by the variance covariance matrix are reliable when certain parameters are adjusted and "perfect" values are used for the fixed parameters. Systematic errors introduced by employing "imperfect" values for the fixed parameters can be evaluated (and corrected for) if a small bias results in the adjusted parameter-of-interest (here k_3). The use of a generic least squares analysis program applicable to all kinetic mechanisms has been described, which can be used to optimize the conditions of an experiment. Monte carlo simulations are employed and the assumption has been made that they are reliable surrogates to real "laboratory" data.

7. Appendix A. Unique Solution

It is often difficult to ascertain if the parameters that are searched for (adjusted) are uniquely found. We define a unique fit purely operationally. If one or more parameters are initialized (guessed at) at different values we should arrive at the same ultimate best fit of the parameters (after several iterations). If this happens we define the fit to be unique. A second criterion involves employing two entirely different versions of Acufit. One program employs the general method outlined by Wentworth [11] which elaborates on Deming's text [2] and involves using the SVD method of matrix solution [12]. The second program employs the more recent Levenberg-Marquardt method [12] and involves using the Gauss-Jordan matrix solution. Both programs yield exactly the same values for the adjusted parameters (and variance-covariance matrix) when a unique solution is possible. They yield somewhat different results if a solution is not obtained; then both result in unrealistic variance-covariance matrices, the first program gives some (or all) matrix entries that are far too small, the other gives some entries that are much too high. Only when both programs yield the same answers do we operationally define that "the" solution exists. So far we have not encountered a problem where one program succeeds in finding a "unique" solution while the other does not.

Acknowledgments

The authors wish to acknowledge support for this work by NASA Upper Atmosphere (agreement W-18,119) and Planetary Atmospheres (agreement W-13,424) Research Programs.

8. References

[1] We are aware of the program "Opkine" by, F. Perez Pla, J. J. Baeza Baeza, B. Ramis Ramos, and J. Palou, J. Computat. Chem. **12**, 283 (1991), but have not compared it with our program.

[2] W. E. Deming, Statistical Adjustment of Data, John Wiley and Sons, Inc., New York (1943). Reprinted by Dover Publications, Inc., New York (1964).

[3] P. R. Bevington, Data Reduction and Error Analysis for the Physical Sciences, McGraw-Hill, New York (1969).

[4] W. Braun, J. T. Herron, and D. K. Kahaner, Int. J. Chem. Kinet. **20**, 51 (1988).

[5] P. Dagaut, T. J. Wallington, and M. J. Kurylo, J. Phys. Chem. **92**, 3833 (1988).

[6] M. J. Kurylo, T. J. Wallington, and P. A. Ouellette, J. Photochem. **39**, 201 (1987).

[7] M. M. Kurylo, P. A. Ouellette, and A. H. Laufer, J. Phys. Chem. **90**, 437 (1986).

[8] M. J. Kurylo and T. J. Wallington, Chem. Phys. Lett. **138**, 543 (1987).

[9] W. B. DeMore, et al., Chemical Kinetics and Photochemical Data for Use in Stratospheric Modeling, Evaluation no. 9, NASA Panel for Data Evaluation, JPL Pub. 90-1 (1990).

[10] P. Dagaut and M. J. Kurylo, J. Photochem. Photobiol. A: Chem. **51**, 133 (1990).
[11] W. E. Wentworth, J. Chem. Educ. **42**, 96 (1982).
[12] W. H. Press, B. P. Flannery, S. A. Teukolsky, and W. T. Vetterling, Numerical Recipes, Cambridge University Press, Cambridge (1986).

About the authors: *A. Fahr, W. Braun, and M. J. Kurylo are physical chemists with the NIST Chemical Kinetics and Thermodynamics Division. Walter Braun is currently retired, but continues to be active in research. The National Institute of Standards and Technology is an agency of the Technology Administration, U.S. Department of Commerce.*

Volume 98, Number 2, March-April 1993
Journal of Research of the National Institute of Standards and Technology

[J. Res. Natl. Inst. Stand. Technol. 98, 191 (1993)]

Measuring Low Frequency Tilts

Volume 98 | Number 2 | March-April 1993

M. L. Kohl

Joint Institute for Laboratory Astrophysics,
University of Colorado,
Boulder, CO 80309-0440

and

J. Levine

National Institute of Standards and Technology,
Boulder, CO 80303-3328

A borehole tiltmeter with a sensitivity of a few nanoradians is described. It is composed of two orthogonal horizontal pendulums with free periods of 1 s. The pendulums are insensitive to barometric pressure fluctuations, and the measured temperature coefficient is less than 30 nrad/°C. The range of the pendulums is about ±5 μrad, and their response is linear within 1% and stable over several years. The performance of the tiltmeter in the field was evaluated using tidal data obtained from a closely spaced array of boreholes in Southern California. The long-term stability of the tiltmeter is generally better than 1 μrad/yr. The data also indicate that instruments in boreholes at least 24 m deep are independent of surface effects. Several different capsules designed to couple the instrument to the surrounding material have been tested. In addition, an experimental method for estimating the magnitudes of local perturbation in the regional tilt field is described.

Key words: borehole tiltmeter; pendulum; tilt tides.

Accepted: October 22, 1992

1. Introduction

Measurements of the deformation of the surface of the earth can be used to deduce information about the earth's interior. One measure of the deformation is tilt which is defined as

$$\boldsymbol{\Omega}_D = \hat{z} \times (\boldsymbol{s} \times \hat{d}_0)/l, \tag{1}$$

where $\hat{z}$ is a reference direction and s is the relative displacement of a baseline of length l and direction $\hat{d}_0$ [1]. The reference direction, defined with respect to the earth's surface, is usually taken as the local vertical. The displacement vector is a function of the strain tensor $\mathbf{E}$ the rotation vector $\boldsymbol{r}$ and the baseline measuring the deformation:

$$\boldsymbol{s} = \boldsymbol{d} \cdot \mathbf{E} + \boldsymbol{r} \times \boldsymbol{d}. \tag{2}$$

Vertical tilt is the deflection of an originally vertical baseline ($\hat{d}_0 = \hat{z}$) while horizontal tilt is the vertical deflection of an originally horizontal baseline ($\hat{d}_0 \cdot \hat{z} = 0$). Near a horizontal free surface of an isotropic elastic body, normal stress vanishes and these two measurements are the same. There are two independent components of the tilt vector $\boldsymbol{\Omega}_D$, so measurements of the tilt along two orthogonal axes completely determine the tilt vector field.

The magnitude and frequency of tilt signals to be measured dictate the sensitivity and stability of instruments designed to measure them. Geophysical studies which use tilt data cover a broad frequency range. At one end of the frequency range are secular or long period tilts. This frequency range is of particular interest near fault zones where changes in the secular tilt rate could indicate changes in the status of the fault. Typical tectonic tilt rates for the western United States are on the order of 0.2 μrad/yr [11]. An example of another frequency range which is investigated using tilt data is the tidal band around a few cycles per day. Baker

[2] and Beaumont and Berger [3] predicted variations in earth tide amplitudes and phases due to changes in the elastic properties of surrounding material. Dilatancy near faults may lead to these changes. In order to measure the changes in tidal admittances and constrain models of the region, the tilt tides must be measured with a precision of a few percent. Typical amplitudes of the tidal components are on the order of 100 nrad. Therefore, the required sensitivity of a tidal tiltmeter is on the order of a few nanoradians.

2. The Instrument

The tiltmeter described here is a borehole instrument. It is composed of three parts—the sensor package, the electronics, and the frame. The sensor package contains the mechanical sensors which detect the tilt. The electronics quantify the movement of the sensor. The frame supports the sensor and the electronics so that the tiltmeter can be installed in a pressure-tight capsule which is lowered into a borehole.

2.1 Mechanical Parts

Since the tiltmeter was designed for borehole installations, the size of the sensor package is somewhat constrained, which in turn constrains the size of the pendulums. Because of this, the mechanical sensors used in the tiltmeter are horizontal pendulums. The advantages of using a horizontal pendulum are its compact size and mechanical amplification.

The amplification of a horizontal pendulum is calculated from its equation of motion. The equation of motion of an ideal horizontal pendulum with damping is

$$\ddot{\theta}+2\xi\omega_0\dot{\theta}+\omega_0^2\theta=\frac{g}{l}\Omega, \tag{3}$$

where θ is the angular displacement of the pendulum, ξ is the damping coefficient, ω_0 is the free period of oscillation of the pendulum, l is the length of the pendulum, and Ω is the tilt being measured (forced). (The expression changes slightly for a real pendulum because the radius of gyration is typically different than the distance from the pivot point to the center of the mass of the pendulum [1]). The amplification $A(\omega)$ of this pendulum is the ratio of the angular deflection of the pendulum to the applied tilt and is expressed as

$$A(\omega)=\frac{\theta}{\Omega}=\frac{g}{l\sqrt{(\omega_0^2-\omega^2)^2+(2\xi\omega_0\omega)^2}}. \tag{4}$$

For a horizontal pendulum, the free period of oscillation is related to the physical dimensions of the pendulum by $\omega_0^2=g\sin i/l$, where i is the inclination of the pendulum. Since the angular displacement of the pendulum is measured as a linear displacement of its free end, the mechanical sensitivity $G(\omega)$ of the pendulum is the ratio of the displacement of the pendulum to the applied tilt and depends on the length of the pendulum ($G(\omega)=A(\omega)l$, where l is the pendulum length).

The sensor package is composed of a mounting plate, two pendulums each with a pair of capacitor plates, and a cap which covers the mounting plate. It is nominally 7 cm in diameter and 6.5 cm in height. Boreholes with a 10 cm inner diameter are large enough to accommodate the package.

The plate on which the pendulums are mounted was designed to minimize the direct effects of temperature and barometric pressure (see Fig. 1a). It is machined from a single piece of stainless steel. The thick base of the plate provides good heat conduction. The mounting platform is machined above the base on a small pedestal. This configuration ensures that a pressure differential on the base results in an uplift of the mounting platform instead of a tilt. Two orthogonal pendulums (Fig. 1b) about 1 cm in length are each suspended between two capacitor plates attached to the mounting platform. The pendulums have a free period of 1 s and are approximately critically damped ($\xi=1$) with air dampers. The plane of rotation of the pendulums is inclined from horizontal by about 2.3°. A cap covers the plate and the sensor package is hermetically sealed. The final package is effectively independent of barometric effects. The measured temperature coefficient of the sensor package is less than 30 nrad/°C. This is sufficient for borehole installations where the temperature stability at the bottom of a 30 m deep borehole is a few m°C/yr [1].

Tilt signals with frequencies lower than about 0.05 Hz ($\omega\ll\omega_0$) have an amplification independent of their frequencies. This is the low frequency amplification factor, which is equal to the cosecant of the angle of inclination. Secular and tidal tilt signals are in this low frequency range so the amplification factor for these signals is roughly 25. This corresponds to a mechanical sensitivity of 0.244 μm/μrad. The amplification of signals with frequencies between 0.05 and 10 Hz varies with frequency. In this regime, the form of the amplification transfer function is necessary to interpret data.

In order for the sensitivity to remain the same, the angle of inclination of the pendulum must

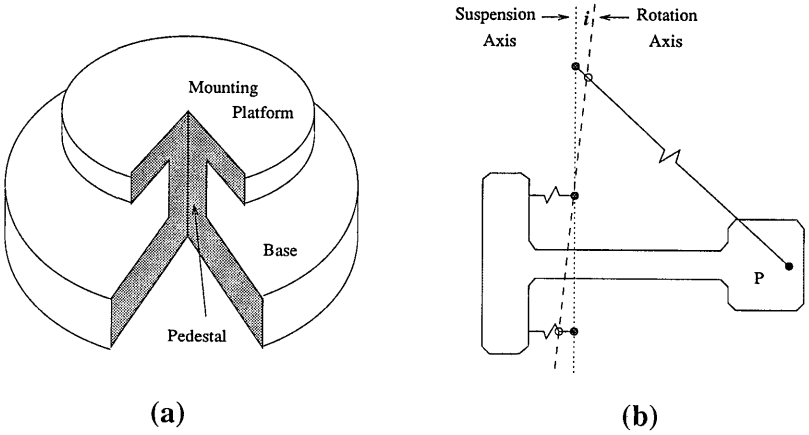

Fig. 1. a) Schematic drawing of the mounting plate composed of the base and the mounting platform, and b) schematic of the horizontal pendulum, P. The effective axis of rotation of the pendulum (dashed) is inclined from vertical suspension axis (dotted) by the angle $i = 2.3°$. The pendulum is suspended on three springy wires (solid).

remain constant. The range of the pendulums is about ± 5 μrad which indicates that the angle of inclination can change by that amount. However, 5 μrad is only a part in 10^4 of the nominal inclination angle of 2.3°. Therefore, the sensitivity changes by less than 1% for the possible inclination angles of the pendulum.

The sensor package is held onto three screws in the tiltmeter frame by a stiff spring (see Fig. 2). Stainless steel ball bearings on the screws orient the package on a kinematic mount. Two of the screws are adjustable ultrafine leveling screws (3.15 threads/mm) and the third screw is fixed. Small dc motors with a 500:1 gearing ratio drive the movable screws so that the sensor package can be leveled after installation. The range of the leveling screws is about $\pm 5°$.

2.2 Electrical System

The displacements of the pendulum are determined using a capacitive transducer. Changes in capacitance are interpreted as displacements of the pendulum, so it is necessary to have any stray capacitances remain constant. Therefore, all of the electronics except the filter and data logger are mounted directly above the sensor package to minimize the length of the leads between the sensor and the electronics.

Each pendulum is suspended between two fixed capacitor plates so that the separation between the pendulum and the plates is about 1 mm. The plates have roughly 1 cm^2 area, and the capacitance between the pendulum and either plate is about 2 pF. The displacement of the pendulum must be measured to about 0.5 nm to obtain the required sensitivity of a few nanoradians. This displacement will cause changes in capacitance of about five parts in 10^7 which is equivalent to a 1 aF capacitance unbalance.

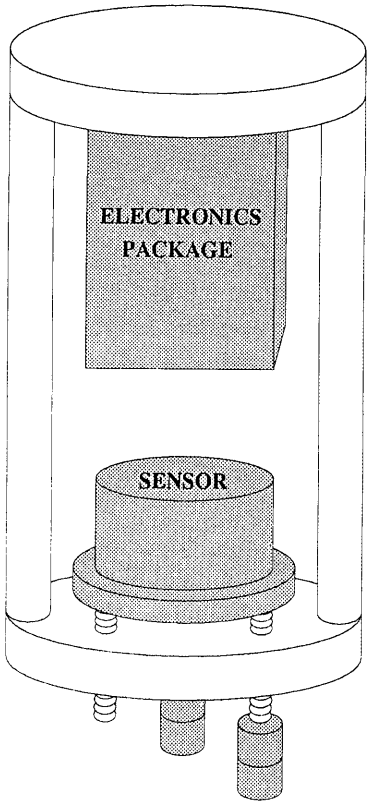

Fig. 2. Drawing of the tiltmeter. The sensor is held on to three screws by a stiff spring. Two of the screws are motor driven and one is fixed.

We use an ac bridge circuit to measure the capacitance changes between the pendulum and its capacitor plates. A schematic of the bridge is shown in Fig. 3. The secondary of a transformer drives two matched resistors (r) to ground. This supplies the two outer plates with ac signals out of phase with each other. The pendulum and its capacitor plates form two arms of the bridge, and the other two arms are formed by the precision resistors.

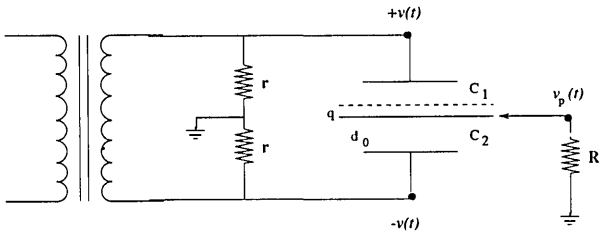

Fig. 3. Schematic of the capacitive transducer. The separation between the pendulum and each capacitor plate is $d_0 \simeq 1$ mm, and the displacement of the pendulum (center plate) from the center is q ($q_{max} \simeq 10^{-6}$m). R is the input impedance of the detector.

The choice of drive frequency is controlled by two factors. In order to minimize the effect of $1/f$ noise, a high frequency is desirable. However, transformers provide the best frequency stability when operated below about 30 kHz. Also, higher frequencies limit the gain of the amplifier. We chose to use a frequency of 12.5 kHz.

The amplitude of the drive signal determines the sensitivity of the measurements. The larger the voltage between the plates, the smaller the minimum measurable displacement, since the rms signal-to-noise ratio of the system is increased. However, larger voltages increase the force of attraction between the pendulum and the plates. Therefore, the drive amplitude must be chosen so that the electrostatic force on the pendulum produces an acceptable nonlinearity in the displacements.

The force between the plates of a simple two-plate capacitor is expressed as

$$f = \frac{1}{2} v^2(t) \frac{\partial C}{\partial d_0}, \tag{5}$$

where $v(t) = V_0 \sin \omega t$ is the drive voltage on the plates, C is the capacitance between the two plates, and d_0 is the separation of the plates. There are two components of $v^2(t)$, one at twice the frequency of the drive voltage and the other a constant. The capacitor plates do not respond to the high frequency component, so only the constant portion of the force is used to determine the displacing force on the plates. The electrostatic force between the plates of a simple capacitor becomes

$$f_E = \frac{1}{4} V_0^2 \frac{\partial C}{\partial d_0}, \tag{6}$$

where V_0 is the amplitude of the drive voltage. For the three-plate arrangement of the tiltmeter, the capacitances between the pendulum and each capacitor plate are expressed as

$$C_1 = C_0 \frac{1}{1 - \left(\frac{q}{d_0}\right)} \tag{7}$$

$$C_2 = C_0 \frac{1}{1 + \left(\frac{q}{d_0}\right)}, \tag{8}$$

where C_0 is the capacitance between the pendulum and each plate when the system is symmetric, and q is the displacement of the pendulum from this position. The electrostatic force on the pendulum from the two fixed plates driven out of phase with each other is

$$f_E = \left(\frac{V_0}{d_0}\right)^2 C_0 \frac{q}{\left(1 - \left(\frac{q}{d_0}\right)^2\right)^2}. \tag{9}$$

To prevent this force from becoming very large, the pendulum must have stops so that $q \ll d_0$. In this case, the displacement range of the pendulums is ± 1.22 μm corresponding to ± 5 μrad tilt.

The electrostatic force is balanced by the gravitational restoring force on the pendulum, so the energy balance equation for the system is

$$f_E(dx) = mgh, \tag{10}$$

where dx is the horizontal displacement of the pendulum, m is the mass of the pendulum, and h is the vertical displacement of the pendulum. The displacements of a horizontal pendulum of length l inclined by the angle i are

$$dx = l \cos i' \sin \rho \tag{11}$$

$$h = l \sin i - l \sin i', \tag{12}$$

where i' is the angle that the displaced pendulum makes with the horizontal. When the pendulum is displaced by the angle ρ, i' is related to i by

$$\sin i' = \sin i \cos \rho. \tag{13}$$

The maximum capacitor plate drive voltage V_0 is determined so that the additional displacement caused by the electrostatic force is less than one percent of the pendulum's deflection [$(dx)/q \leq 0.01$)]. The value for V_0 obtained by combining equations 9 and 10 is approximately

$$V_0 \simeq \sqrt{\frac{0.01\, mgd_0^2 \sin i}{2C_0 l}}. \tag{14}$$

Since the mass of the pendulum is 1 g, the maximum capacitor plate drive voltage which will provide linearity within 1% is about 10 V. In practice, any nonlinearity in the system using a 10 V amplitude signal on the plates is not noticeable in either the calibration of the instrument or in the data. Typical drift rates of the instrument are about 1 μrad/yr so most of the data are collected near the electrical center of the system where the effects of the nonlinearity are unmeasurable.

The output $v_p(t)$ of the capacitive transducer is an ac signal whose amplitude is dependent on the magnitude of the displacement of the pendulum from the electrical center of the bridge and whose phase with respect to the driving signal indicates the direction of the displacement. It is calculated from Fig. 3 by noting that

$$v + \frac{i_1}{j\omega C_1} + (i_1 - i_2)R = 0 \tag{15}$$

$$v - (i_1 - i_2)R + \frac{i_2}{j\omega C_2} = 0, \tag{16}$$

where i_1 is the current flowing through C_1 and i_2 is the current flowing through C_2. Using the definitions for the capacitances of the transducer with $q \ll d_0$, the transducer output is

$$v_p(t) = \frac{V_0 q}{d_0}\left(\frac{2R\omega C_0}{\sqrt{(2R\omega C_0)^2+1}}\right)\sin(\omega t + \phi), \tag{17}$$

where the phase angle ϕ is defined by

$$\tan \phi = -(2R\omega C_0)^{-1}. \tag{18}$$

For an ideal detector, the value of R is infinite, and the output amplitude would simply be $V_0 q/d_0$. In our case, R is 10 MΩ, so the amplitude of the signal is about 94% of the ideal amplitude, with a phase angle of roughly $-20°$. The part of the signal which is in phase with the drive voltage to the outer plates has an amplitude of

$$V_p = \frac{V_0 q}{d_0}\left(\frac{2R\omega C_0}{\sqrt{2R\omega C_0)^2+1}}\right)\cos\phi. \tag{19}$$

When the outer plates are driven with an amplitude of 10 V, V_p is about ± 10 mV for a capacitance unbalance of ± 1 fF ($q = \pm 1$ μm).

A source follower is connected directly to the pendulum. It decreases the signal by about a factor of 2. The signal is then amplified in two stages with a total gain of about 1440 before entering the phase sensitive detector. The available output from the amplifier is about ± 7.2 V corresponding to a capacitance unbalance of ± 1 fF, so that overloading of the amplifier is avoided.

The phase sensitive detector is composed of a JFET switch and an integrator. The switch is controlled by the same frequency that drives the outer plates of the transducer so that the integrator only works on the part of the amplified signal which is in phase with the drive frequency. The integrator has a dc gain of 10. The output of the phase sensitive detector is a dc voltage which is related to the transducer output by

$$V_{\text{out}} \simeq \frac{1}{2} V_p \times 14400 \div 2\pi, \tag{20}$$

and is about ± 11.5 V for ± 1 fF capacitance unbalance.

The remaining electronics are located at the top of the borehole. The dc voltage tilt signals are sent through a single stage unity gain low-pass filter with about a 100 s time constant to average out microseismic background noise, whose spectrum peaks around a period of 6 s. The filtered signals are recorded on a datalogger at the site.

Each datalogger has eight channel capability, so tilt signals from up to four tiltmeters can be recorded by a single datalogger. The additional channels alternatively can be used to record other local data such as temperature, etc. The filtered signal is digitized with a 12 bit analog to digital converter for the voltage range $\pm$ 10 V, making the least count of the digitizer about 2.4 nrad for the nominal sensitivity of 2 V/μrad. The digitized data are recorded every 6 min so that there are 10 data points per hour.

The datalogger is controlled with commands through the RS-232 interface which uses TTL protocol. This interface can be directly connected to a portable computer in the field, or to a modem for remote access. Data digitized and stored in RAM are retrieved each morning by an automatic dialing program on the computer in Boulder [6].

2.3 Calibration

The calibration of the tiltmeter is determined in the laboratory on a tilt table. It is conducted on a seismic pier in the basement of one of the buildings at the university. The pier is a large concrete block isolated from the building.

The calibration sweeps across the range of the tiltmeter sensor in approximately 1 μrad steps at a rate of one step per minute. Because the table is driven by a screw, the steps are not instantaneous. Each step is completed within 20 s so that the pendulum has at least 40 s to stabilize before the corresponding voltage is determined. The overall sensitivity of the channels is set to be about 2 V/μrad. Successive calibrations agree within 1% even when spaced several years apart [8]. The nominal calibration uncertainty is also about 1%.

Since changes in the amplifier circuits cause calibration changes, whenever any components fail in the field, the entire tiltmeter is replaced and the original tiltmeter is brought back to the lab for repair and calibration.

3. Installation and Alignment Methods

The boreholes are drilled by a conventional water well drill. They are lined with a steel casing as shown in Fig. 4. The holes are drilled slightly larger than the casing, since pressing the casing into the hole may lead to cracks in the casing. Because the tiltmeters have a leveling range of about $\pm 5°$, the lower section of the holes needs to be vertical within that range. When the drill is removed, concrete is poured down the hole so that the casing will be coupled to the surrounding material.

The lowest 2.4 m of the casing is stainless steel pipe with 10 cm inner diameter. A flat plate with a 1.3 cm diameter hemisphere in the center is welded to the bottom. The stainless steel instrument compartment is joined to 15 cm diameter carbon steel pipe. The joint is conical on the inside of the casing. As the casing is installed, additional lengths of 15 cm pipe are welded to form a continuous watertight pipe for the remaining depth of the borehole. Boreholes ranging from 15 to 120 m below the surface have been used.

Several different versions of the tiltmeter capsule have been designed. All versions are made from stainless steel pipe sections 2 m long. Their lids are pressure tight. The base of the tiltmeter frame is clamped in the capsule by three screws so that the sensor is located midway up the capsule. The differences between the versions is in the way that the capsule is located in the borehole.

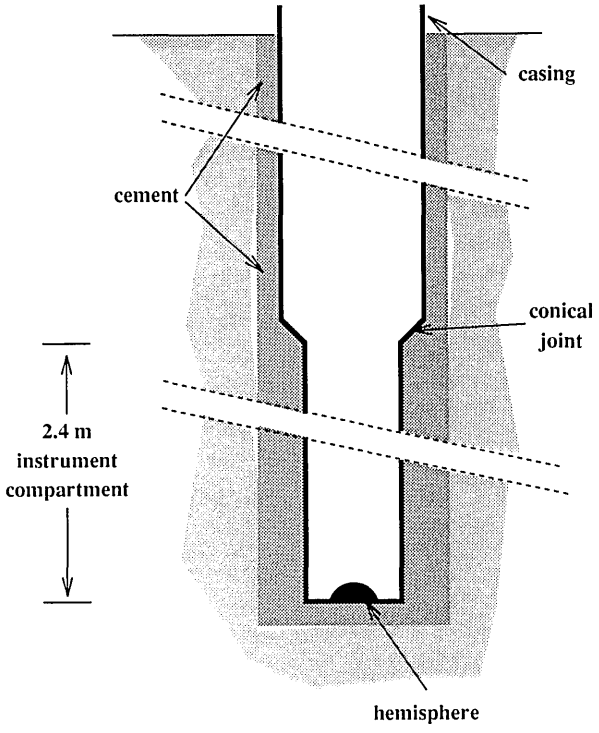

Fig. 4. Schematic drawing of the boreholes (not to scale).

The original design [5] locates the capsule by referencing only the sides of the borehole (Fig. 5a). A flat plate is welded to the bottom of the capsule so that the weight of the capsule rests on the hemisphere in the bottom of the borehole. Near the top and the bottom of the capsule are two contact points and a flat spring 120° apart. The flat springs press the contact points against the inside of the borehole casing to couple the instrument to the surrounding material.

The second design uses a different technique for centering the capsule in the borehole. The hemisphere not only supports the weight of the capsule but also centers the bottom. A plate with a cone cut into it is welded to the bottom of the capsule. The cone centers the bottom of the capsule on the hemisphere at the bottom of the hole. The top of the capsule is centered by three spring-loaded pins which are retracted by the weight of the capsule as it is being installed or removed. The capsule weighs approximately 133 N (13.5 kg mass), and each spring has about 26 N pressing against the casing when installed.

The third design is similar to the second, except that the bottom of the capsule is located on the conical joint above the instrument compartment. A plate with a spherical edge is welded to the bottom of the capsule. The top of the capsule is centered as

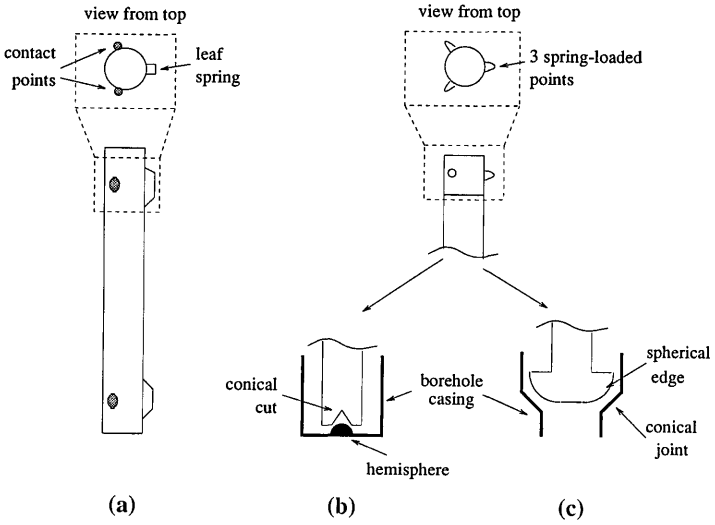

Fig. 5. Three different borehole capsule designs. The original design (a) has a set of two contact points and a flat spring located at the top and at the bottom of the capsule. The other designs have three spring loaded pins located at the top of the capsule. The second design (b) centers the bottom of the capsule on the hemisphere in the casing while the third design (c) locates on the conical joing above the instrument compartment.

before with three spring-loaded pins. Since the pins need a larger range of motion in order to press against the larger diameter casing, extra weight is added so that the pins retract completely during installation and removal. This capsule weighs about 267 N (27.2 kg mass), and the force on each spring is about 53 N.

The capsule is lowered into the borehole by a steel cable connected to the lid. Provided that the borehole is not too deep (less than 50 m), and the capsule is not too heavy, a capsule can be lowered by hand. For deeper holes and weighted capsules, a winch is used.

Once the capsule is lowered, it is important to know its azimuthal orientation. The drill bit wanders around the vertical direction when the boreholes are drilled, so direct observation is not possible except for very shallow holes (<10 m). Two different techniques were used to determine the orientation of the capsule depending on the depth of the borehole.

Holes less than 50 m deep use a series of lightweight aluminum rods [5]. The lowest rod slides onto a post welded on to the lid of the capsule (Fig. 6a). It fits in only one direction and is held on by a spring-loaded ball bearing, so that the rods can be removed after the orientation of the capsule is determined. As the capsule is lowered, additional rods are added. Each rod is about 2.5 m long and will attach in only one direction to the rod below it. In this way, the orientation of the capsule is translated to the surface where the azimuth is determined using a compass.

The rods were originally calibrated outside of the borehole so that the accuracy of the measurement was a few degrees. Using alignment rods to determine the orientation of a capsule has several disadvantages. First, the alignment rods must be used every time that a tiltmeter is installed. Second, the rods, being made of aluminum to minimize their weight, are relatively easily bent. This may cause degrading of the azimuth measurement for each successive installation. Finally, the system is feasable only for shallow boreholes—the rod stiffness decreases with length, and the additional weight becomes appreciable.

For deeper holes a different technique was developed. The lid of the capsule was modified to include an extension with a muleshoe attached to the top (Fig. 6b). The muleshoe is composed of two shovel-like pieces pointing down the borehole. As the capsule is lowered, the shovels reach two keys welded to the inside of the casing. The shovels guide the capsule into the hole by referencing the keys. When the capsule is at the bottom of the borehole, the keys fit into two notches in the muleshoe. The orientation of the keys was determined by attaching a gyroscope to the muleshoe. The gyroscope orientation was measured several times with a repeatability of 2°. In general, once

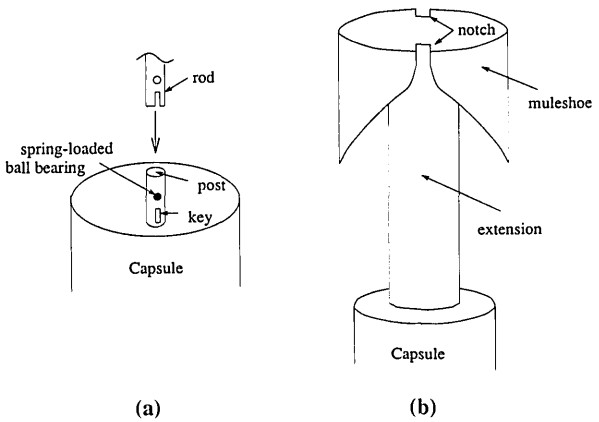

Fig. 6. Methods for determining the orientation of the tiltmeters. Shallow holes use a series of rods (a) while deeper holes use a muleshoe attached to the top of the capsule (b).

the orientation of the keys is known in a borehole, subsequent installations of that borehole need only note the orientation of the sensor with respect to the muleshoe. Since the muleshoe has two shovels, the amount of rotation of the capsule at the bottom of the borehole is reduced, however, there is a 180° ambiguity in the device. The ambiguity is easily resolved by looking at the tidal signals.

4. Performance in the Field

The tiltmeters have been installed in various locations during the past 12 years. The sites have included boreholes in Colorado [8], Wyoming [9], and California. All of the data presented here are from the California array, which consists of three closely spaced boreholes (within a radius of about 35 m) at different depths (24, 36 and 120 m).

Figure 7 shows a typical tilt time series recorded from the 24 m borehole. The time series shows a general trend (about 1 μrad/yr) as well as tidal components (amplitude about 10 nrad) with frequencies around one and two cycles per day. The trend in the data is a measure of the secular tilt present at the particular site combined with the instability of the instrument and the installation. For boreholes in Southern California, the expected secular tilt is less than 1 μrad/yr, so the recorded trend in Fig. 7 is unlikely to be entirely attributable to secular tilt. Drift rates as low as 0.2 μrad/yr have been observed.

Figure 8 is the power spectral density of a longer time series from the same borehole. The long period trend was removed from the time series before the spectrum was calculated. The signal to noise ratio at tidal frequencies is estimated by comparing the tidal amplitude to the inter-tidal noise amplitude. For these data, the signal-to-noise ratio for the larger components is 36–42 dB, which is typical of the data from California.

In order for geophysical interpretations of the tilt data to be accurate, it is important to understand how the measurements are affected by surface effects, cavity effects, and the existence of local inhomogeneities. Surface effects result from the measurement's being made near the surface of the earth. Cavity effects arise from the presence of the instrument itself. Inhomogeneities near the instrument cause strain field distortions which can affect the local tilt field. The influence of each of these effects on our borehole tiltmeters has been investigated.

The proximity of the earth's surface affects tilt measurements in several ways. Meertens and Wahr [10] showed that the local topography causes coupling of the strain field into the tilt field. The amount of coupling is dependent on the slope of the topography and can be calculated for any site. Temperature and barometric pressure may also affect the tidal tilt measurement due to thermal expansion and surface loading [7].

Data from the California array have been analyzed to estimate the size of each of these surface effects. The topography at the site is inclined by about 2.5° toward the southwest, so the topographic correction to the data is small and identical for each of the holes. The effect of the temperature and barometric pressure is estimated from the coherence spectra between the meteorological and tilt data. The data only show significant coherence amplitude for the barometric pressure and the tilt data from the 36 m deep hole. The coupling coefficient in this case is 7×10^{-3} nrad/Pa at nontidal frequencies. Assuming that the coupling is independent of frequency, and since the measured barometric pressure tides have maximum amplitudes of around 60 Pa, the modifications of tidal admittances due to barometric coupling are less than 5%. Because the sensor package is independent of atmospheric pressure changes, the pressure induced tilts are likely to be caused by indirect effects. These effects are true tilts that arise from the spatial variation in the barometric pressure load.

The measured tilt data can also be affected by the presence of the instrument itself. The existence of a cavity causes strain field distortions which may produce anomalous tilting of instruments inside the cavity. This anomalous tilting results from either tilting of the cavity walls or differential motion between the tiltmeter capsule and the cavity

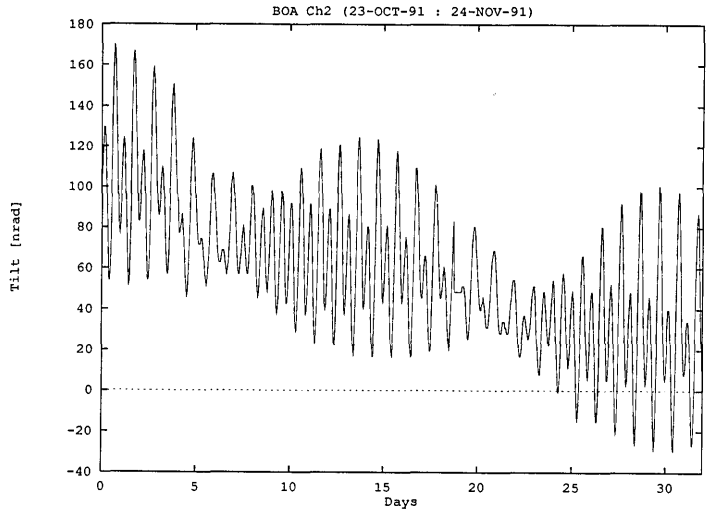

Fig. 7. Typical time series from a 24 m borehole.

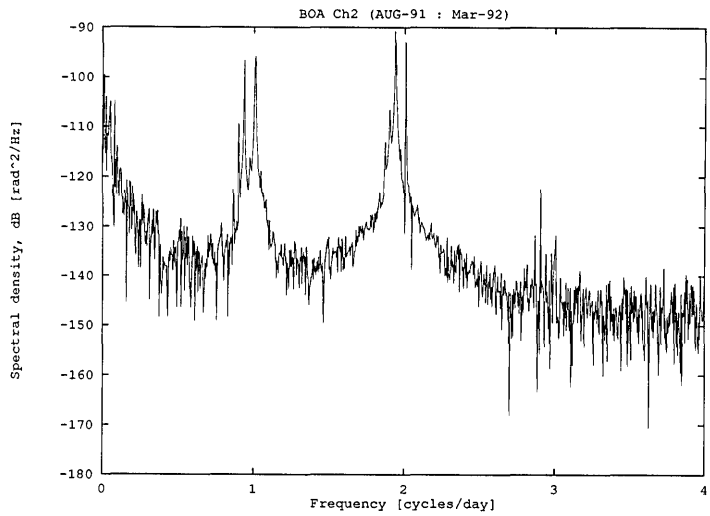

Fig. 8. Power spectral density of data from the 24 m borehole.

walls. Harrison [4] calculated the effect of distortions of the walls on tilt for several cavity shapes and found that a borehole tiltmeter will have no cavity effects when the sides of the borehole are referenced and only a small effect when the center of the bottom of the borehole is used as a reference. This result inspired the original capsule design which only references the sides of the borehole.

The size of the cavity effect arising from differential motion between the cavity and the capsule for the original capsule design is determined by comparing data obtained from multiple installations of a single borehole. Table 1 contains the amplitudes and phases along 0° and 90° azimuth of one of the largest tidal components, M_2 (frequency $\simeq$ 1.93 cycles/day), for different installations in a 24 m deep borehole. The phase is measured with respect to the local gravitational potential where a negative value indicates a phase lead. The values in parentheses are the uncertainties of the amplitudes and phases. Consecutive estimates of the tidal components during one installation are stable within 2% over several years. All of the data in this table were obtained with a single tiltmeter. The first two installations used the original capsule design installed along different azimuths. The first installation had the pendulums aligned with 15° and 105° azimuth, while the second installation was rotated to 314° and 440° azimuth. The differences between

the two installations is somewhat larger than expected from the performance of the tiltmeter during a single installation. Since measuring the tilt along any two orthogonal azimuths is sufficient to completely determine the local tilt field, these discrepancies indicate differential motion between the borehole and the capsule.

Subsequent study of the original capsule design revealed the source of this motion. Although the capsule references only the sides of the borehole, the reference points are asymmetric (two rigid contact points and one spring). This results in a cavity effect as shown in Fig. 9 because the lower set of reference points is located close the the bottom of the borehole. An applied strain field produces a tilt of the capsule, so the strain field is coupled into the tilt field along the spring azimuth. The magnitude of the coupling approaches 10% of the strain which is sufficient to account for the differences seen in the data. The second design (which eliminates the asymmetry of the reference points) was installed in the borehole in March 1992. At this point, there has only been one installation of the new capsule, so it is unclear whether the repeatability between installations has been improved.

The presence of local inhomogeneities near the tiltmeter can also influence the tilt data. This arises from the fact that the tiltmeters measure the tilt field using a relatively short baseline (2 m). Local disturbances in the tilt field with wavelengths shorter than 2 m will be averaged out while longer wavelength phenomenon will be recorded. The magnitude of this effect is estimated by comparing data from the different boreholes.

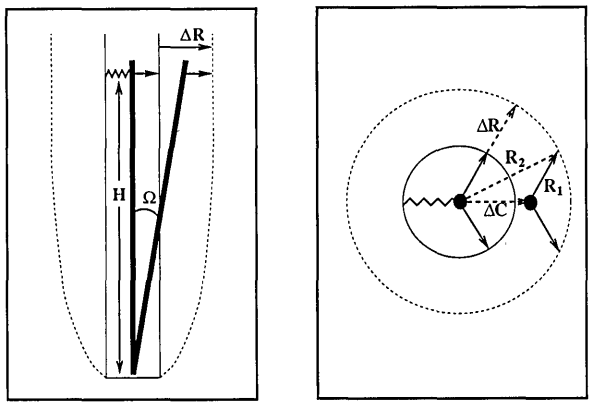

Fig. 9. Tilt caused by uniform expansion ΔR of a borehole for a (a) two dimensional and (b) three dimensional hole. The capsule references the sides of the hole by a spring and contact points (arrows). The contact points remain a fixed distance from the sides of the hole, while the spring expands.

Table 2 contains the M_2 amplitudes and phases along 0° and 90° azimuth for each of the three boreholes. The data show marked differences between the boreholes which exceed calibration

Table 1. M_2 data from multiple installations in a 24 m borehole. The phases are measured with respect to the local tidal potential (negative values are phase leads)

Data interval	Capsule type	0° azimuth Amplitude (nrad)	0° azimuth Phase (deg)	90° azimuth Amplitude (nrad)	90° azimuth Phase (deg)
Jun. 88–Aug. 91	original	18.44 (0.34)	124.5 (0.6)	18.48 (0.23)	−82.8 (0.6)
Aug. 91–Mar. 92	original	18.01 (0.28)	122.7 (0.9)	18.22 (0.29)	−85.7 (0.9)
Mar. 92–June 92	second	16.61 (0.82)	118.0 (2.9)	17.82 (0.63)	−91.1 (2.1)

Table 2. M_2 data from boreholes of various depths. The phases are measured with respect to the local tidal potential (negative values are phase leads)

Depth (m)	Data interval	0° azimuth Amplitude (nrad)	0° azimuth Phase (deg)	90° azimuth Amplitude (nrad)	90° azimuth Phase (deg)
24	Jun. 88–Aug. 91	18.44 (0.34)	124.5 (0.6)	18.48 (0.23)	− 82.8 (0.6)
36	Apr. 89–Aug. 91	21.42 (0.47)	96.5 (2.2)	14.05 (0.64)	−114.1 (2.1)
120	Dec. 89–Jul. 90	20.58 (0.81)	124.9 (2.3)	14.89 (0.82)	− 91.3 (3.2)

uncertainties (1–2%), the long-term stability (2%) and the expected differences from measuring at different depths (<1%). The material properties at the site change between a depth of 15 and 35 m due to the presence of a weathering layer associated with the water table [12]. Investigation of the effect of the weathering layer on tilt data shows that the regional strain field can become coupled into the tilt field. The magnitude of the tilt-strain coupling depends on several factors including the distance between the layer and the tiltmeter.

The third capsule design was installed in the 36 m borehole to experimentally determine if there is a variation of material properties near the bottom of the hole. Table 3 lists the measured M_2 admittances using the original capsule design and the third capsule design. The phase difference along 90° azimuth between the first two installations results from the asymmetry of the reference points as described earlier. Data from the third installation show a phase shift of about 26° along 0° azimuth from using symmetric reference points and changing the depth of the tiltmeter by only 2.4 m. This phase difference exceeds the maximum 10% strain coupling which could result from changing the reference points. Using reasonable estimates of the change in material properties, these measurements constrain the location and size of the weathering layer. The parameters obtained in this way are consistent with direct measurements using well logs and other data.

5. Conclusion

A geophysical borehole tiltmeter which has a sensitivity of a few nanoradians has been described. The stability of the calibration is less than 1% over several years. Consecutive estimates of the tidal admittances are stable to 2% for any installation of the tiltmeter. The long term drift of the tiltmeter in the field varies between 0.2 μrad/yr to more than 1 μrad/yr.

Several items can be noted from the analysis of the California data which should be considered carefully when planning future borehole tiltmeter installations. First, knowledge of the orientation of the tiltmeter is useful for comparisons between different boreholes. Of the two methods described here, determining the orientation using a gyroscope is more desirable, since the uncertainty in the measurement is about ±1° and does not degrade with time. Second, tiltmeters installed at depths of at least 24 m show no evidence of surface temperature effects. This is also true for barometric pressure loading, provided that the sensor is installed far from any boundary layers such as a water table. A drilling log can provide useful information for determining the optimal depth of installation of a tiltmeter in the borehole as well as for interpreting the tilt data. Once a borehole is drilled, changing the location of the tiltmeter in the borehole can be a very sensitive technique for determining the existence of a local perturbation in the tilt field. Finally, the design of the tiltmeter capsule determines the amount of tilt-strain coupling in the instrument itself. We have found that asymmetrically referencing the sides of the borehole near the bottom can produce almost 10% tilt-strain coupling.

Acknowledgments

This work was supported in part by the National Earthquake Hazards Reduction Program of the U.S. Geological Survey through grants 14-08-001-G1338 and 14-08-001-G1765.

Table 3. M_2 data from multiple installations in a 36 m borehole. The phases are measured with respect to the local tidal potential (negative values are phase leads)

Data interval	Capsule type	0° azimuth Amplitude (nrad)	0° azimuth Phase (deg)	90° azimuth Amplitude (nrad)	90° azimuth Phase (deg)
Apr. 89–Aug. 91	original	21.42 (0.47)	96.5 (2.2)	14.05 (0.64)	−114.1 (2.1)
Aug. 91–Mar. 92	original	21.30 (0.39)	96.6 (1.1)	13.36 (0.51)	−105.6 (2.3)
Mar. 92–June 92	third	21.72 (0.37)	123.5 (1.0)	14.93 (0.41)	− 93.9 (2.1)

6. References

[1] Duncan Carr Agnew, Strainmeters and tiltmeters. J. Geophys. Res. 24(3), 579–624 (1986).
[2] T. F. Baker, Tidal tilt at Llanwrst, north Wales: Tidal loading and earth structure. Geophys. J. R. Astron. Soc. 62, 269–290 (1980).
[3] Christopher Beaumont and Jon Berger, Earthquake prediction: Modification of the earth tide tilts and strains by dilatancy. Geophys. J. R. Astron. Soc. 39, 111–121 (1974).
[4] J. C. Harrison, Cavity and topographic effects in tilt and strain measurement. J. Geophys. Res. 81(2), 319–328 (1976).
[5] J. C. Harrison, Judah Levine, and Charles Meertens, Design of a deep borehole tiltmeter. In Proceedings of the Ninth International Symposium on Earth Tides, J. T. Kuo, ed., D-7000 Stuttgart, 1983. E. Schweizerbart'sche Verlagsbuchhandlung, pp. 273–280.
[6] Judah Levine, A study of secular tilt in Wyoming and Utah. Final report AFGL-TR-83-0247, Air Force Geophysical Laboratory, Hanscom A.F.B., MA, 1983.
[7] Judah Levine, J. C. Harrison, and Charles Meertens, Performance of a deep borehole tiltmeter. In Proceedings of the Ninth International Symposium on Earth Tides, J. T. Kuo, ed., D-7000 Stuttgart, 1983. E. Schweizerbart'sche Verlagsbuchhandlung, pp. 47–56.
[8] Judah Levine, Charles Meertens, and Robert Busby, Tilt observations using borehole tiltmeters. 1. Analysis of tidal and secular tilt. J. Geophys. Res. 94(B1), 574–586 (1989).
[9] Charles Meertens, Judah Levine, and Robert Busby, Tilt observations using borehole tiltmeters 2. Analysis of data from Yellowstone National Park. J. Geophys. Res. 94 (B1), 587–601 (1989).
[10] Charles Meertens and John Wahr, Topographic effect on tilt, strain and displacement measurements. J. Geophys. Res. 91 (B14), 14057–14062 (1986).
[11] W. H. Prescott, J. C. Savage, and W. T. Kinoshita, Strain accumulation rates in the western United States between 1970 and 1978. J. Geophys. Res. 84(B10), 5423–5435 (1979).
[12] Frank Wyatt, Displacements of surface monuments: Vertical motion. J. Geophys. Res. 94(2), 1655–1664 (1989).

About the authors: *Mary L. Kohl is a research assistant working on precision geophysical measurements in the Joint Institute for Laboratory Astrophysics (JILA). JILA is a joint institute which involves NIST and the University of Colorado at Boulder. Judah Levine is a physicist in the Time and Frequency Division of NIST and is a Fellow of JILA. The National Institute of Standards and Technology is an agency of the Technology Administration, U.S. Department of Commerce.*

Volume 98, Number 2, March–April 1993
Journal of Research of the National Institute of Standards and Technology

[J. Res. Natl. Inst. Stand. Technol. 98, 203 (1993)]

Optical Fiber Geometry: Accurate Measurement of Cladding Diameter

Volume 98 | Number 2 | March–April 1993

Matt Young, Paul D. Hale, and Steven E. Mechels

National Institute of Standards and Technology,
Boulder, CO 80303-3328

We have developed three instruments for accurate measurement of optical fiber cladding diameter: a contact micrometer, a scanning confocal microscope, and a white-light interference microscope. Each instrument has an estimated uncertainty (3 standard deviations) of 50 nm or less, but the confocal microscope may display a 20 nm systematic error as well. The micrometer is used to generate Standard Reference Materials that are commercially available.

Key words: critical dimensional measurements; gray scale measurement; interference microscope; micrometer; microscope; optical fiber; optical fiber geometry; scanning confocal microscope; Standard Reference Material; video microscope.

Accepted: November 25, 1992

1. Introduction

This paper reports the development of an artifact standard (a Standard Reference Material, or SRM) for video microscopes devoted to measuring optical fiber geometry [1]. Specifically, we have developed three devices, a contact micrometer [2], a scanning confocal microscope [3,4], and a white-light interference microscope [5], that are capable of absolute measurements with accuracy between 50 and 100 nm. Much of this material has been reported in various forums while it was in progress; this paper summarizes.

A video microscope dedicated to fiber geometry is called a gray scale system by the Telecommunications Industry Association (TIA) [6]. Gray scale systems are typically used to determine the outer, or cladding, diameter of a cleaved fiber end; the noncircularity of the cladding; and the decentering, or concentricity error, between the core and the cladding. Measurements of noncircularity and decentering do not require high absolute accuracy. Cladding diameter, by contrast, must be measured within 0.1 μm or less if we are to provide standards for the manufacture of efficient connectors that do not require manual adjustment.

Measurements made with video microscopes, unfortunately, may well suffer from a systematic error of a few-tenths micrometer [7]. The TIA subcommittee we work with wanted a transfer standard so that they could correct for this systematic error. It was, however, reluctant to accept an artifact standard other than an optical fiber because the measured result is a function of illumination and also because reflection from a metal film displays phase shifts that are not present in reflection from a glass edge. Indeed, the concern about phase shifts is not misplaced: we have measured widths of chromium-on-glass lines with a scanning confocal microscope and found the measured results to change by nearly 0.1 μm with polarization [4]. At any rate, even if a chromium-on-glass standard had been

adopted, it would have been necessary to measure a fiber very accurately to verify the relevance of the chromium standard. We therefore undertook to develop a fiber artifact standard for calibrating the gray scale systems. The National Physical Laboratory in the U. K. has a similar program [8].

In this paper, we will describe the contact micrometer, scanning confocal microscope, and white-light interference microscope that we have set up with the goal of measuring the cladding diameter within 0.1 μm or less. Because of the ease of using the micrometer, it is the instrument that we use regularly to prepare standards. Because of the need for accuracy (as opposed to precision or repeatability), however, we require the other methods to verify the accuracy of the micrometer.

2. Contact Micrometer

We acquired a contact micrometer from our colleague Theodore Doiron of the Precision Engineering Division in Gaithersburg, Maryland. The *anvil*, or stationary part, is a steel post about 3.8 mm in diameter (Fig. 1). The *spindle*, or moving part, rides horizontally on an air bearing and is pressed against the anvil with a known force; this force is developed by hanging a weight (not shown) over a pulley. The end of the spindle is a cylinder about 5 mm in diameter. A mirror is contacted to the opposite end of the spindle, and its position is measured by a commercial interferometer that has a least count of 1.25 nm. We estimate its accuracy to be a few nanometers owing to changes in barometric pressure, temperature, and humidity; cosine error; and so on. The reflecting surface of the mirror is perpendicular to the axis of the spindle, within less than 5′.

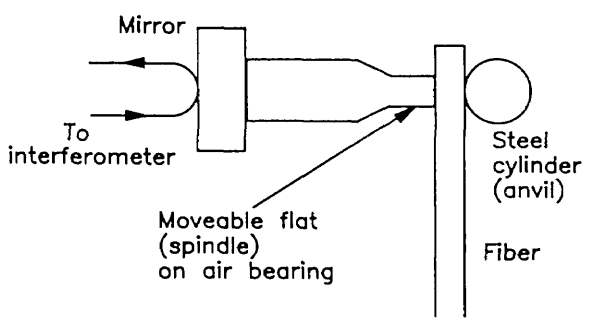

Fig. 1. A schematic drawing of the contact micrometer. The moveable spindle is pressed against the fiber with a known force, and the position of the spindle is monitored interferometrically.

2.1 Optical Polishing

We had both the spindle and the anvil polished with hard laps in an optical shop. The spindle must be flat, and the anvil must be cylindrical or conical, not barrel- or hourglass-shaped, or systematic errors will arise.

Measurements are performed by first pressing the fiber between the spindle and the anvil and using the interferometer to measure the position of the spindle. Then, the fiber is removed, and the spindle is brought into contact with the anvil. The difference between the two positions is the diameter of the fiber, apart from a correction for compression (below).

The anvil is epoxied under pressure to a vertical vee groove. The spindle and the end of the anvil may be made parallel by inserting a fiber and measuring its diameter both above and below the center of the spindle. The vee groove that holds the anvil may be shimmed for coarse adjustment. For fine adjustment, the end of the spindle has been polished flat but at an angle of a few minutes. The spindle may be rotated incrementally until the measurements above and below the center agree within a few nanometers.

A major problem is to ensure that there is no burr, or defect, projecting from the anvil. If there is such a defect, the micrometer will not close properly, and the measurements will be low, except rarely when the fiber seats on top of the burr. It is helpful, therefore, to have advance knowledge of the diameter of the specimen (apart from the correction for compression, below). This may be obtained by deliberately misaligning the spindle. Then, there is only one point of contact between the spindle and the anvil. (This point is comparatively hard to find, so it is not practical to design a micrometer in which the spindle and the anvil are not parallel.) With the spindle misaligned, we measure the diameter of the fiber at the point of contact. Next, we align the micrometer so that the spindle and the anvil are parallel, as outlined in the previous paragraph. If the anvil is free of burrs or contamination, the measured diameter is about the same as the diameter obtained when the parts were misaligned. In addition, the measurements above the center of the spindle and those below converge (as the spindle is rotated) to an unreasonably small value when there is a burr on the anvil. Thus, there are two clues that indicate the presence or absence of a burr; it is necessary to perform a great many alignments of the spindle, preferably at different locations on the anvil, to satisfy yourself that the

micrometer is accurate. We estimate that the error due to the presence of a burr is not larger than 10 nm.

To test the accuracy and parallelism of the surfaces, we next inserted a fiber and measured its apparent diameter at various points along the line of contact between the spindle and the anvil. Figure 2 shows the result. In the center of the plot, where the spindle is fairly flat, the total scatter of the data is about 32 nm and is partly the result of electronic noise and vibration but mostly the result of roughness in the surfaces. We presume, however, that the "correct" answer is the largest value, because the highest point on either surface is what actually makes contact when the fiber is removed. When the fiber is positioned anywhere else, the spindle moves less than one full fiber diameter when the second measurement is made. If we took, say, six measurements at different positions, the most probable result would be the mean of the relevant points in Fig. 2. But the presumed correct result is about 16 nm larger than this mean, so we add 16 nm to the measured value and assign an uncertainty equal to half that, or 8 nm.

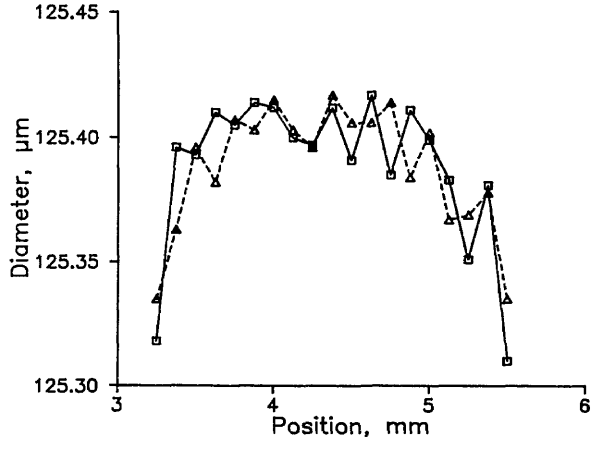

Fig. 2. Two consecutive sets of measurements of the diameter of the fiber as a function of position along the anvil.

2.2 Compression

The fiber and the anvil make a point contact, so there is measurable compression there. The compression depends on the elastic constants of the materials and can in principle be calculated from formulas developed by Puttock and Thwaite [9]. The spindle contacts the fiber in a line, not a point; the calculated compression is only a few nanometers. Similarly, when the fiber is removed, the spindle contacts the anvil in a line; the corresponding compression is also a few nanometers, but it has the opposite effect on the measurement. These last two compressions nearly cancel, so only the compression at the fiber-to-anvil contact ought to be significant. Unfortunately, as we will see, the situation is not so simple when the micrometer is applied to thin, flexible wires or fibers.

To test the formulas, we measured the diameter of different fibers and steel thread wires as a function of the force the spindle exerts on the fiber. If the formula is correct, the measured diameter will be a constant, independent of force. The formula for a cylinder-to-cylinder contact shows that the compression increases in proportion to the 2/3 power of the force, so we plotted both "raw" and "corrected" diameters as a function of the 2/3 power of the mass hanging from the thread and calculated least-squares lines of best fit. Figure 3 shows the results for one of the fibers: The corrected diameter is not independent of the force (or mass); that is, the line labeled "corrected" is not horizontal. The functional dependence is apparently correct, however, because the raw data lie on a line.

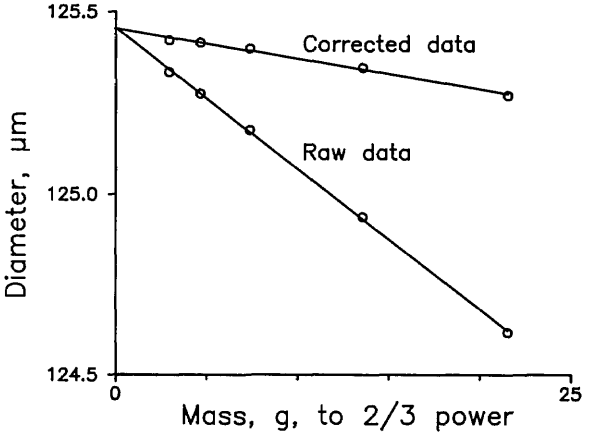

Fig. 3. Measured diameter as a function of mass (force) to the two-thirds power. The lines are least-squares lines of best fit. The slope of the line marked "Raw data" is used to determine the diameter of the fiber in the absence of force.

The y-intercept is presumably the correct value; therefore, the formalism of Puttock and Thwaite effected an undercorrection up to several tenths micrometer, depending on the force. This was so for both fibers and thread wires; as far as we know, [2] is the first published report of this result. Since ferrules are often characterized with the aid of steel thread wires, the result may be important to the measurement of the inside diameters of ferrules as well.

Our colleagues in the Precision Engineering Division have proposed the following explanation for the formulas' apparent breakdown: Thin steel wires or optical fibers are flexible. When they are pressed against the cylindrical anvil, they bend slightly, as if to wrap around the anvil. As a result, the pressure of the flat spindle against the fiber is greatest at the center of the spindle, directly opposite the point of contact between the fiber and the anvil. This pressure decreases in both directions away from the center of the spindle; as a result, the contact between the fiber and the spindle is not the uniform line contact assumed by the formulas. Since there is greater pressure on the fiber near the center of the spindle, the effective area of contact is reduced, and the deformation is greater than what is predicted by the formula.

Besides the fact that the formulas always undercorrect (never overcorrect), we have three bits of evidence in favor of this explanation. First, the Precision Engineering Division tested the formulas on steel wires that had increasing thickness and therefore increasing stiffness; the prediction of the formula improved as the thickness of the wire increased. Second, silica fibers are more flexible than steel thread wires of the same thickness, and we have found that the formulas are poorer predictors of the deformation of silica fibers than of steel wires. Finally, when we replace the steel spindle with a silica spindle and prepare a graph like Fig. 3, we find that the slope of the raw data line is different than when we use the steel spindle. This suggests that at least part of the discrepancy occurs at the spindle-to-fiber contact.

2.3 Calculation of Diameter and Its Uncertainty

We have made no attempt to calculate the deformation of the fiber-to-spindle contact. Rather, we use the measured slope of the line labeled "Raw data" in Fig. 3 to extrapolate from the measured diameter to the true diameter, or the diameter in the absence of deformation.

Because all the fibers we are interested in have approximately the same diameters and are made of the same materials, the slopes of the lines of best fit are in principle the same. Figure 4 shows raw or uncorrected data similar to those of Fig. 3. Fibers I, L, and J are different fibers made by different manufacturers. The slopes of the lines of best fit are, within statistical uncertainty, the same.

We can therefore use any mass to measure the diameter and then extrapolate to zero mass by using the measured slope instead of the formulas.

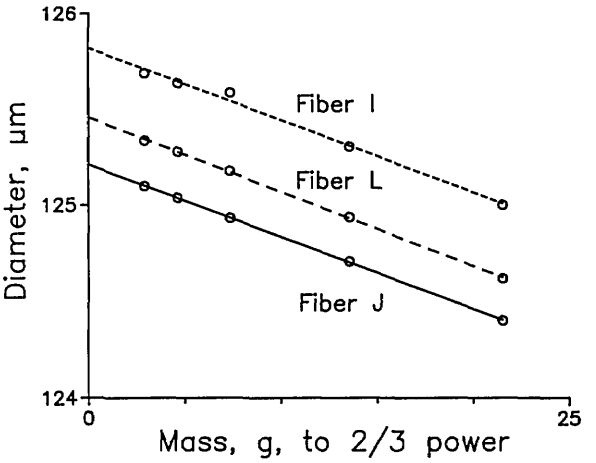

Fig. 4. Raw data for specimens of three different fibers as a function of mass and showing that the slope is invariant.

Table 1 shows the results of measurements on six specimens of the same three fibers as those labeled in Fig. 4. Uncertainties are calculated values, expressed as one standard deviation [10]. The overall uncertainty of the slope is given by the root-sum-of-squares (rss) average (0.0011) of the individual uncertainties divided by $\sqrt{6}$, or 0.0004. The y-intercept is not stated in the table because it is different for each specimen.

Table 1. Intercept uncertainty, slope, and slope uncertainty of six specimens

Fiber	Intercept uncertainty, µm	Slope, µm/g$^{2/3}$	Slope uncertainty, µm/g$^{2/3}$
I	23	−0.0377	0.0019
J	2.8	−0.0375	0.0002
L	5.5	−0.0386	0.0005
I′	14.4	−0.0380	0.0012
I″	9.4	−0.0369	0.0008
L′	10.8	−0.0378	0.0009
rss mean	14	−0.0378	0.0011

We chose a mass of 20 g because, with that mass, the deformation of the fiber is not great and there is little danger of damaging the spindle or the anvil, yet the force is enough to make a solid contact without causing the spindle to bounce. We used the slope given in Table 1 to extrapolate to the diameter of the fiber with zero mass (force). The statistical uncertainty of measuring that slope gives rise to a systematic uncertainty of the diameter of about 3 nm (1σ). Additionally, the random uncertainty of a single set of measurements is typically about 8 nm. An uncertainty of 8 nm results from the roughness

of the anvil; 10 nm from the possibility of a burr on the anvil; and an estimated 10 nm from taper or internal stress in the fiber (Sec. 5). A systematic uncertainty of our measurement of the force equivalent to 1/2 g gives rise to an uncertainty of 10 nm. Other uncertainties we have been able to identify are less than 2 nm (Table 2).

We follow the ISO formalism for propagating uncertainties and assume that measured (Type A) uncertainties display a Gaussian probability distribution, whereas inferred (Type B) errors display a rectangular probability distribution [11]. We combine uncertainties by adding their variances in quadrature (where the variance of a rectangular probability distribution is one-third the square of its half-width). In this way, we arrive at an estimated standard deviation of about 14 nm. We take the overall uncertainty of any diameter measurement to be ± 3 times this value, or ± 45 nm.

2.4 Control Chart

We prepared three fibers in retractable holders that allow us to preserve the ends indefinitely. We are therefore able to measure the diameter of the same specimens repeatedly in order to estimate stationarity and long-term drift. Figure 5 is a control chart, or a graph of measured diameter as a function of time, for nearly 2 years, beginning in March 1991, and continuing through January 1993.

From May through September 1991, the chart suggested a slight downward drift, though that drift was largely masked by the day-to-day uncertainty of the measurements. We attributed the drift to friction in the air bearing. We disassembled the bearing and cleaned it, and realigned and recalibrated the micrometer. In addition, the spindle is attached to an air supply by a soft plastic tube that can put a slight force on it. We balanced the spindle very carefully by adjusting the tube until the balance point of the spindle was just in front of the anvil; only then did we attach the mass to the spindle. This is a more accurate way of balancing the spindle than we had been using before the overhaul. Since the overhaul in late October 1991, we see no evidence of systematic changes in the control chart.

Table 2. Tabulation of uncertainties

Source of uncertainty	Criterion	Uncertainty, nm
	(a) Measured uncertainties	
Noise	Calculated standard deviation	8
Correction for deformation [1]	Standard deviation of calculated slope	3
	(b) Inferred uncertainties	
Correction for deformation [1]	Error of force equivalent to $\pm 1/2$ g	10
Surface roughness	$\pm 1/2$ of correction	8
Burr on anvil	Control chart	10
Deformation or taper	Stress analysis & interference microscope	10
Cosine	0.2°	1
Abbe offset	1 μrad (0.2") × 2 mm offset	2
Wavelength	Fluorescence linewidth	0.3
Index of refraction of air under average conditions	Uncertainty of calculation	<0.1
Variation of barometric pressure	±4 kPa	1
Variation of ambient temperature	±5 K	0.5
Variation of relative humidity	±50%	<0.1
Combined uncertainty	1σ	14
Expanded uncertainty	3σ	43

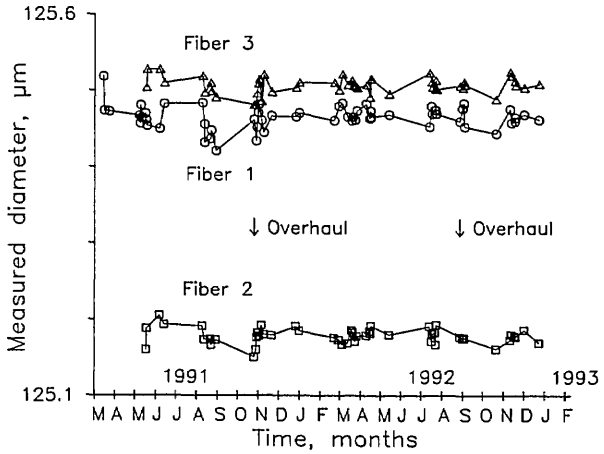

Fig. 5. A control chart for the contact micrometer: the measured diameter of three fiber ends as a function of time for nearly 2 years that began in March 1991. The micrometer was overhauled in October 1991, and August 1992.

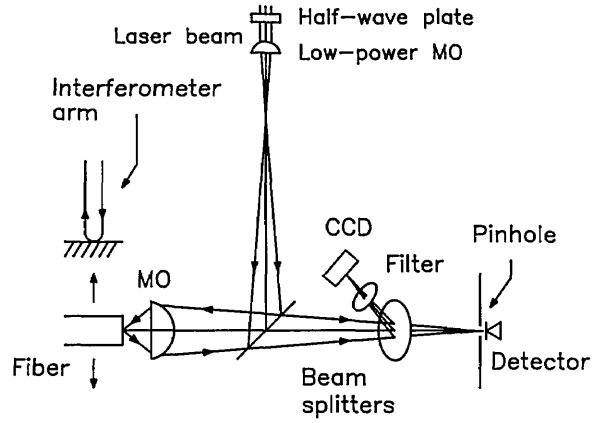

Fig. 6. A schematic drawing of the scanning confocal microscope. The fiber is scanned vertically and its position is monitored interferometrically.

3. Confocal Microscope

We built the scanning confocal microscope (SCM) because it permits direct inspection of the fiber endface, whereas most other systems operate at some point along the length of the fiber [2,12,13]. The light in the SCM is spatially and temporally coherent (a single-mode laser is used for illumination), so the image does not suffer from the systematic errors associated with partially coherent illumination [7]. For this reason, the SCM is more accurate than conventional microscopy or gray scale analysis, both of which use partially coherent illumination.

We designed the SCM to measure optical fiber diameters specifically, but we think the system has the potential to be applied to many objects of interest in video microscopy and critical dimensional measurements. In particular, because out-of-focus object points are invisible, the SCM is preferable to a conventional microscope for measurements of objects, such as ridge waveguides or features on integrated circuits, whose height exceeds the depth of field of the instrument [3], or a fraction of one micrometer.

Figure 6 is a schematic drawing of the SCM, which is discussed in more detail in [3] and [4]. The object, a fiber or a linewidth standard, for example, is mounted on a three-axis translator that has a nominal step size of 0.1 μm. The object is scanned vertically under computer control while the confocal microscope, illuminating laser, and detector remain stationary on the table. The position of the object is measured with a commercial interferometer, as above (Sec. 2).

To illuminate the specimen, we use a linearly polarized single-mode He-Ne laser with a wavelength of 633 nm. The beam is passed through a half-wave plate so that the plane of polarization can be rotated as necessary. The beam is chopped for phase-sensitive detection. It is focused to a point with a low-power microscope objective and then expands and reflects from a beam splitter. The beam that reflects from the beam splitter is focused by a 40×, 0.65 NA objective onto the object. That objective also focuses the beam reflected from the object onto a pinhole that precedes a detector. The pinhole is located so that the objective operates at the proper magnification (proper tube length) and is the same optical distance from the beam splitter as is the focal point of the low-power objective.

The beam reflected from the object is reflected by a second beam splitter onto a video camera that allows inspecting the quality of the fiber endface and locating the image point with respect to the scanning pinhole. The second beam splitter reflects the beam out of the plane of the page in order to help cancel the astigmatism of the first. This is necessary because we did not design the instrument with infinity-corrected objective lenses, or lenses whose long conjugate is infinite.

We position the specimen near the focal point of the objective by backlighting it with a ring illuminator (not shown) and exciting the core of the fiber by illuminating the far end. We then use the video monitor to superimpose the reflected laser light onto the core of the fiber. The filter that precedes the monitor has a central wavelength of about 550 nm and a passband of about 100 nm. By eliminating infrared radiation from the source, this filter reduces chromatic aberration and ensures that the

light from the white-light source and the laser light are parfocal. It also protects the video monitor from overexposure to the laser light.

We perform fine focusing manually by maximizing the photocurrent from the detector. To ensure sharp edge responses, the specimen is refocused near each edge just before the measurement scan across that edge. A scan across the fiber diameter takes approximately 1 min.

A silicon photodetector with a built-in operational amplifier is located behind the pinhole and measures the reflected light intensity. The output of the detector is synchronously detected by a lock-in amplifier. Data are obtained by moving the stepping motors in 0.1 μm steps. These stepping motors are controlled by a feedback loop that uses a linear encoder; the loop is evidently slightly underdamped, and the motors overshoot and then drift back and forth about 50 nm with a period of a few tens of seconds. The instrument is within specification, but the overshoot and drift cause noisy data near the edge. We could find no way to change the damping of the loop. If, however, we use the software to turn off the motors a specific time (about 0.1 s) after the command to step has been issued, we obtain stable data. Since we measure position with the interferometer, we have no need to rely on the encoder for position and would have been better off with a system that did not have a feedback loop.

After the stepping motor has completed its motion, we wait four time constants (0.4 s, altogether) of the lock-in amplifier before recording the detector output. The interferometer then determines the vertical position of the fiber by averaging three readings.

3.1 Theory

In [4], Mechels and Young showed that, in scalar theory, the geometrical image of an isolated dielectric edge is located at the inflection point of the electric field distribution in the vicinity of the edge. They used the inflection point of the electric field, rather than the point whose intensity is one-quarter of the peak intensity, to locate an edge because it is convenient, requires slightly less data acquisition, and is not affected if the reflectance of the specimen is not uniform.

They further showed experimentally that the inflection point can also be used to locate a metallic edge deposited on a glass substrate, provided that the light was polarized with its electric field vector parallel to the edge. They suggested that this was so because that polarization adheres to the same boundary conditions as a scalar wave, whereas the opposite polarization does not. Since then, we have calculated diffraction patterns of an edge as a function of polarization and distance from the edge. The two polarizations converge to the same diffraction pattern within a few hundred wavelengths of the plane of the edge, or far less than the distance between the edge and the aperture stop of our microscope objective. We therefore think that the polarization dependence of our measurements may have been the result of the oxide anti-reflection coating on the chromium lines, rather than of the boundary conditions at a metal edge. We plan to perform similar measurements with gold lines that are not coated with an oxide; preliminary results indicate that the measured widths of such lines either are independent of polarization or are more nearly so than the measured widths of the oxide-coated chromium lines.

We are interested primarily in the edges of an optical fiber, where there are neither standing waves nor phase shifts as might be caused by the reflection from a glass substrate. Further, the impulse response of the SCM is never less than 0 [14]. For these reasons, the edge response displays no zero crossings, there is no ambiguity in taking the square root of the measured data, and the electric field amplitude in the neighborhood of the edge is just the square root of the measured intensity. When examining a chromium-on-glass target, we contacted a cover slip to the substrate with an index-matching oil. (We use a microscope objective that is corrected for the spherical aberration of the cover slip and suspend the cover slip in air when we examine an object that is not contacted to a cover slip.) The index-matching fluid ensures that the reflectance from the glass substrate is very nearly 0. The same arguments hold, and we are able to calculate the edge response by calculating the square root of the data, as with a fiber.

3.2 Detector Aperture

In principle, the detector in the SCM should have a vanishingly small diameter [15]. More practically, we have used the sampling theorem to estimate that its *diameter* should be less than one-half the Airy disk *radius*. Using a larger diameter is mathematically equivalent to partially coherent imaging and guarantees a systematic error that we estimated in [4] to be a few tens of nanometers. Here we show experimental data regarding this systematic error.

We used the four widest lines on Standard Reference Material 475. This is a series of chromium lines deposited on a glass substrate; their widths have been measured by our laboratory in Gaithersburg with a total uncertainty of 60 nm. For this work, we used the parallel polarization only.

Figure 7 shows the electric-field amplitude (square root of the intensity) as a function of position for a 10.71 μm line. To save time, we take data only in the neighborhood of the edges. The curve is numerically differentiated, and parabolas (dashed curves) are fitted to the derivatives in the neighborhood of the peaks. The purpose of fitting the parabolas is both to smooth the data and to interpolate between pixels. The peaks of the parabolas are approximations to the true inflection points. The distance between the inflection points of the two edges is the width of the object.

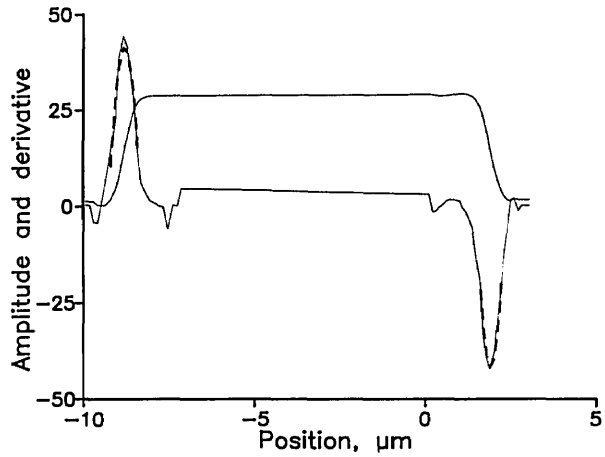

Fig. 7. Electric field amplitude (square root of the intensity) and its derivative. Scan of a 10.71 ± 0.06 μm chromium-on-glass line from SRM-475. The dashed curves are a nine-point parabolic fit to the derivative in the region of the edges.

We measured the widths of each of the four lines with a variety of pinholes in front of the detector. To reduce the effect of detector nonlinearity, we adjusted the intensity of the incident light so that the peak photocurrent was approximately the same in all the measurements. The results are shown in Fig. 8 (a–d), which plots measured width as a function of pinhole diameter for both reflecting lines and clear lines on a reflecting background. The Airy disk radius, for comparison, is about 24 μm.

Figure 9 is a composite of the four curves of Fig. 8 superimposed on Fig. 8 (a). Two of the curves have been inverted, and the vertical positions of the curves have been adjusted by eye for a sort of best fit. The data show a maximum systematic error of perhaps 40 nm with the 50 μm pinhole. As the pinhole radius approaches 0, random uncertainty obscures whether the curves approach an asymptote or not, but it is safe to say that using the 10 μm pinhole will result in a systematic error no larger than 5 or 10 nm. This systematic error will be positive for reflecting lines and negative for clear lines on a reflecting background. It is a curious quirk, incidentally, that the systematic error decreases somewhat when the pinhole diameter is increased to 100 μm. We do not know whether the systematic error would behave the same way if we had used the 25%-intensity criterion instead of the inflection point.

3.3 Linewidth Measurement

The 10 μm pinhole gave a substantially higher signal-to-noise ratio than the 5 μm pinhole, so we adopted 10 μm for subsequent measurements. Table 3 compares our measured data with Gaithersburg's results, which we call the canonical values. Our values agree well with the canonical values but show a possible systematic uncertainty whose sign depends on whether the line is clear or reflecting.

Table 3. Measured widths of chromium lines (SRM-475).[a] All measurements in micrometers. Parallel polarization

	Canonical value	Measured value	Difference
Reflecting lines	9.40	9.43	0.03
	10.71	10.72	0.01
Clear lines	9.63	9.59	−0.04
	10.97	10.93	−0.04

[a] Random uncertainty of SCM is $3\sigma = 40$ nm; total uncertainty of canonical values is 60 nm.

3.4 Fiber Diameter

To measure fiber diameters, we first estimated the location of the center of the cladding by finding the center of the core. Then we scanned five chords in a raster that surrounded the core center and measured the lengths of these chords. The chords were 0.6 μm apart, and, at most, only one of the chords is the diameter we seek. To estimate the true diameter, therefore, we plotted chord length as a function of the perpendicular distance from the core center and fitted the data to a parabola (Fig. 10). The peak of the parabola is the measured diameter. The random uncertainty of these measurements is approximately 40 nm (3σ); we discuss the systematic uncertainty below (Sec. 5).

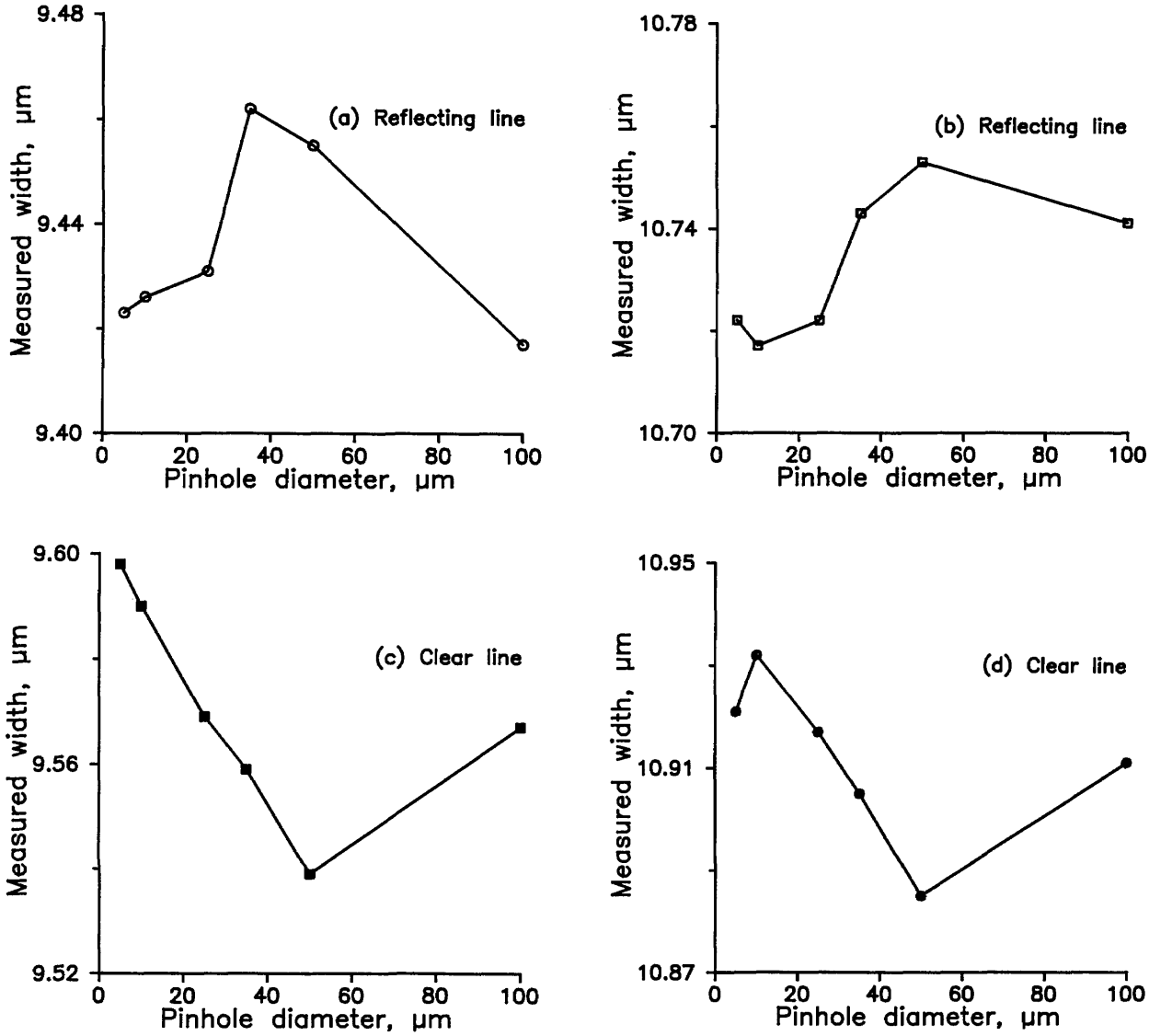

Fig. 8 (a–d). Widths of four SRM lines measured by the SCM and plotted as a function of the diameter of the pinhole in front of the detector.

4. Interference Microscope

We also constructed a white-light interference microscope which uses a Mirau interference objective [16] and a partial contact method for locating the fiber surfaces [5]. We chose a Mirau objective over the Michelson objective used in previous works [17,18] because of its stability, ease of operation, and higher magnification. We chose a partial contact method because, otherwise, we would have to know the index profile and material dispersion of a test fiber for absolute measurements [18].

We constructed the system from commercial metallurgical microscope parts; it uses bright-field illumination from a halogen lamp, a binocular eyepiece, and a CCD array video camera with 400× overall magnification (Fig. 11). The camera is connected to a video analyzer and monitor. An optical flat is held perpendicular to the optical axis with a high quality mirror mount on a precise three-axis translation stage. The position of the flat is monitored by a commercial interferometer with a least count of 1.25 nm. The interferometer, translation stage, and video analyzer are all controlled by computer, and repeated measurements can be made automatically.

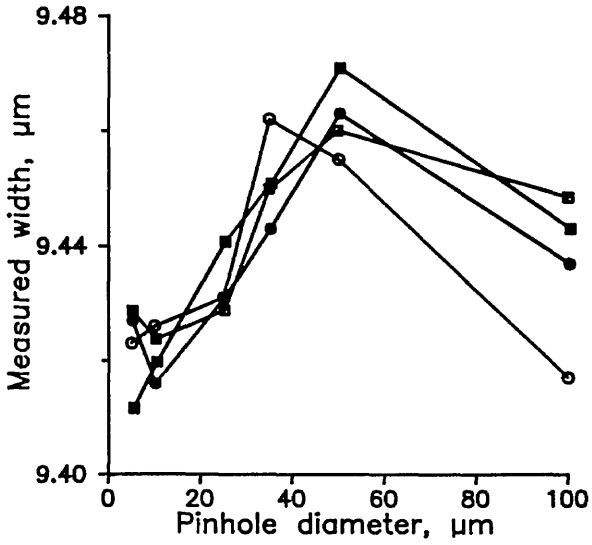

Fig. 9. A composite of the data of Fig. 8 superimposed on the axes of Fig. 8(a). Figures 8(c) and (d) are inverted. The vertical scale has no significance.

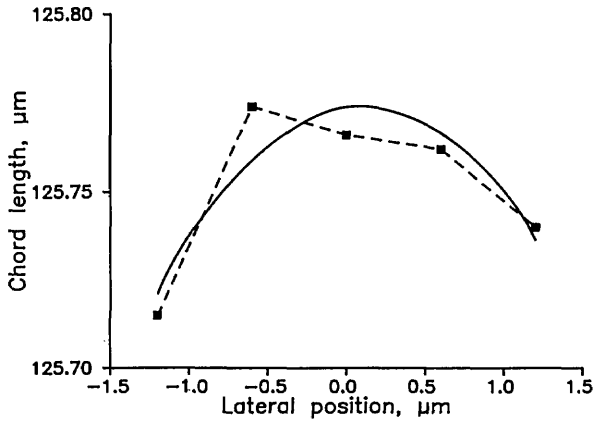

Fig. 10. Fiber diameter measured by the SCM as a function of lateral position. The peak of the best-fit parabola is assumed to give the true diameter.

The mirror mount has been modified to hold a fiber holder along with a cantilevered brass weight which holds the fiber against the optical flat. The fiber holder consists of a stainless steel vee groove, and the fiber is held into the groove by a wedge of silicone rubber. The holder fits into a fixture that positions the fiber on top of the flat. It can be interchanged among all three of our instruments. Before making a measurement, the mirror is aligned with the axis of the microscope by observing uniformly colored fringes from the flat across the entire field of view. When the eyepiece is used to observe the colored fringes, alignment within ±75 μrad can be achieved.

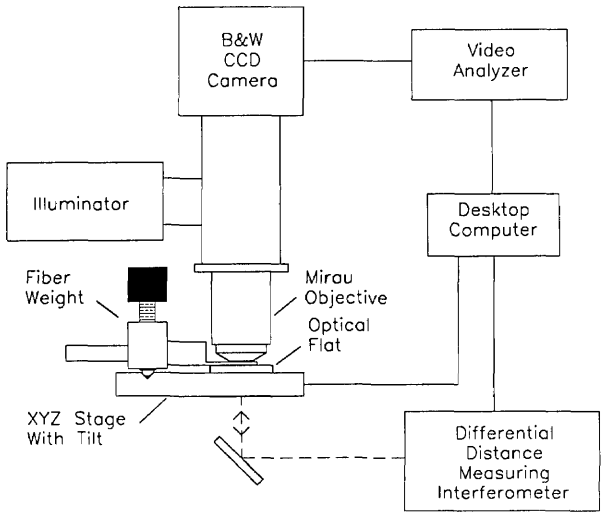

Fig. 11. A white-light interference microscope system based on Mirau objective.

The brass weight has a semi-circular cross section and is thin enough to fit between the fiber and objective with the curved side toward the fiber. It has a 0.76 mm slot through which the fiber and flat are viewed (Fig. 12). The weight can be oriented using two precise 1/4-80 screws so that even pressure is applied to the fiber from both contact points. The weight deforms the fiber by about 0.5 μm, but the deformation is localized to a region within 20 μm of the edge of the slot. Measurements of the fiber diameter are made 380 μm from both fiber-weight contacts.

Contact between fiber and flat is verified within 50 nm by viewing white-light interference fringes analogous to Newton's rings but linear because the fiber is cylindrical. To observe these fringes, the microscope is focused approximately 100 μm below

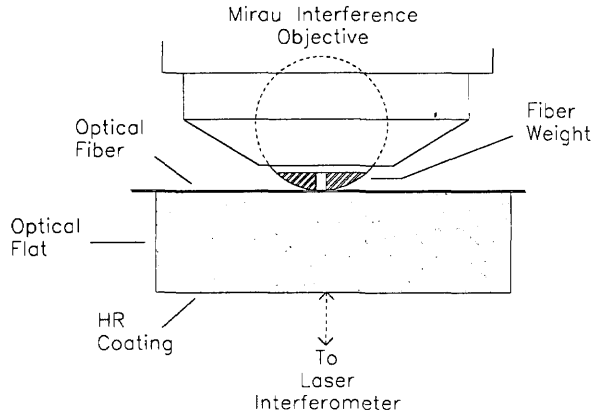

Fig. 12. A schematic drawing of the fiber held in contact with the optical flat.

the surface of the flat. The video analyzer verifies that the central dark fringe is as dark as the next outermost fringe, and all fringes are parallel and colorless. When slight pressure is applied to the brass weight, the central portion of the fiber rises away from the surface and the central fringe becomes hourglass-shaped. If one end of the fiber rises, the pressure is not uniform, and the weight needs to be rotated about its cylindrical axis using the precise screws.

Fringes from the top of the fiber should be colored uniformly along the length of the fiber and parallel (provided that the fiber diameter is uniform). Particulates larger than 25 nm in diameter on or adjacent to the fiber can be detected by a variation of the color of the fringes. Cleaning the fiber using spectroscopic grade methanol in an ultrasonic cleaner is effective in removing stray dirt. The flat is cleaned with spectroscopic grade methanol using the "drop-and-drag" method commonly used to clean optics with fragile coatings.

When the fiber is contacted to the flat and even pressure is applied, the fiber appears to wring onto the flat; that is, it makes optical contact and is held to the flat by a van der Waals force, which has a range of a few nanometers. We therefore think that the fiber is in intimate contact with the flat and that measurement of the distance between the flat and the top of the fiber is equivalent to measuring the diameter of the fiber with very small error; see the discussion of replacement uncertainty, below.

The top surface of the fiber or flat is located by scanning the stage and using the video analyzer to record the intensity of the white-light fringes while the position of the stage is monitored. The central fringe of the interferogram is then fitted to a parabola to average out random fluctuations in intensity and position tracking (Fig. 13). The region of the video image to be sampled is located using a set of cross hairs on the video monitor. Since the field of view is a few fiber diameters in extent, lateral motion of the translation stage is not required during a measurement. To measure the diameter of a fiber, the flat and the top of the fiber are located, and the distance between them is calculated. The flat is then relocated and the difference is again calculated. The average of these two measurements is one datum which has been corrected for linear drift. When this measurement is repeated without fiber replacement, the uncertainty of the measured mean diameter is about 3 nm (1σ). When the fiber is removed and replaced between measurements the uncertainty increases to 8 nm. The additional uncertainty may arise because the glass surface is rough (on a nanometer scale) and we cannot accurately reposition the fiber on the flat. That the uncertainty is only 8 nm is consistent with our assumption that the fiber is held to the flat by a van der Waals force.

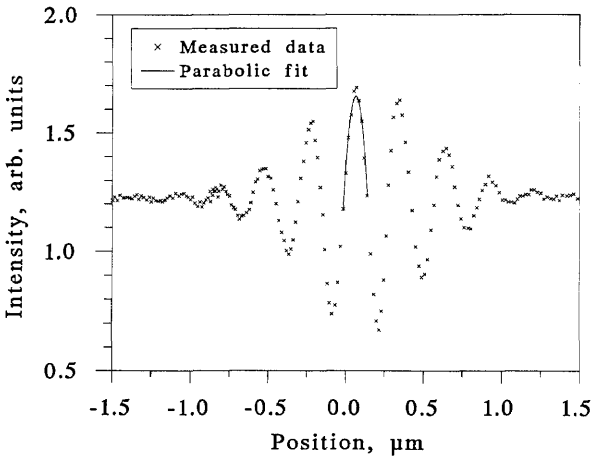

Fig. 13. A white-light interferogram with parabolic fit to central fringe.

The accuracy with which the cross hairs can be placed on top of the fiber is limited by quantization noise as well as random uncertainties. Slight offset of the cross hair makes the measured fiber diameter too small. To estimate the severity of the problem, we replaced the 20× Mirau objective with a 40× Mirau objective. We made six measurements on a control fiber and alternated them with measurements made with the 20× objective. The 40× objective gave values 6 ± 4 nm (1σ) larger than the 20× objective. If the probability distributions for placement of the cross hair are the same for both objectives, the mean offset of the measured diameter using the 40× objective is four times smaller than the offset for the 20× objective. That is, we require an additive correction of $(4/3) \times 6$ nm, or 9 ± 5 nm. All diameters quoted in this paper include this additive correction and its uncertainty. The overall uncertainty of 30 nm (3σ) is calculated by adding the uncertainty of 5 nm and the replacement uncertainty in quadrature.

5. Results

We measured the diameters of several fibers with all three instruments. We took care that each set of measurements was made by a different operator and that the operators did not discuss their

results until all measurements were completed. We measured two diameters of each of four fibers, for a total of eight diameters. The results are plotted in Fig. 14 as the arithmetic difference between measurements made by each of the two microscopes and those made by the micrometer as a function of the diameter measured by the micrometer. That is, the horizontal line represents the micrometer measurements, and the points represent differences from those measurements. The open squares are the measurements made by the confocal microscope, and the solid squares, by the interference microscope.

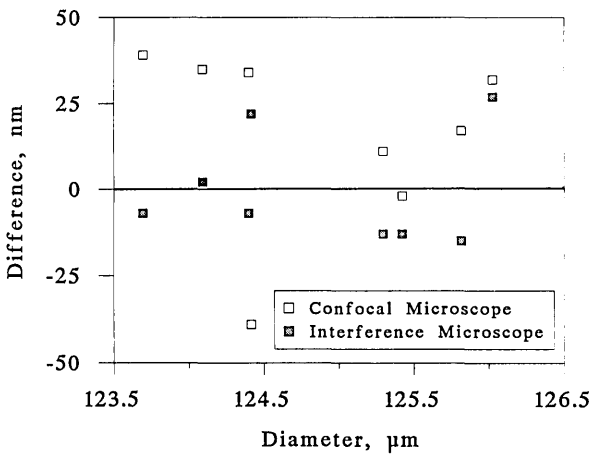

Fig. 14. Comparison of measurements by scanning confocal microscope and white-light interference microscope with measurements by contact micrometer. The micrometer measurements are represented by the horizontal line.

All three sets of measurements agree within their estimated experimental uncertainties. The arithmetic average of the confocal microscope measurements, however, exceeds the micrometer measurements by 16 nm, and the rss average exceeds the micrometer measurements by 29 nm. If there were a large systematic difference between the two instruments, then all the data points in Fig. 14 would have the same sign, and the arithmetic average would roughly equal the rss average. Similarly, if the arithmetic average were much less than the rss average, we could rule out a significant systematic difference between the two instruments. The arithmetic average of 16 nm is only slightly less than the rss average and is very roughly the increment by which the confocal microscope measurements differed from the Gaithersburg measurements of the metallic lines. Part of this discrepancy could be due to the finite width of the pinhole. Beyond that, we cannot explain it and do not know whether it represents a systematic error in the confocal microscope.

The single outlying point near the bottom of the graph in Fig. 14 is a measurement taken on a fiber that we think had very high stress and may have become deformed when it was cleaved; see below, at the end of this section. Without the outlying point, the arithmetic average difference between the two sets of measurements would be 24 nm, not 16, and the rss average difference would be 28 nm. The case that there is a real systematic difference between the two instruments could therefore be made more convincingly.

We used the interference microscope to measure the diameters of the same set of fibers. We had to remove the fibers from their holders and remount them, so we remeasured their diameters with the micrometer, in case there had been rotation when the fibers were remounted. (This is the reason that we show the data in relation to the micrometer, rather than present all three datasets in Fig. 14.) We show the results as the solid squares in Fig. 14. The arithmetic average difference between the two datasets is -1 nm, and the rss average is 15 nm. The agreement between the micrometer and the interference microscope is well within experimental error.

Finally, to ensure that fiber ends are not deformed by cleaving, we used the interference microscope with the 40× objective lens to visually examine a number of cleaved fibers, including the outlier in Fig. 14, at their ends. We could find no evidence for any deformation. Further, finite-element analyses of fibers with realistic axial stress distributions with magnitudes in the range of 20–50 MPa yielded radial deformations of a few nanometers at the end of the fiber. Since our SRM is a single-mode fiber with a homogeneous cladding and a low drawing tension, we do not think that internal stress is a factor. We caution, however, that certain high-stress fibers, such as polarization-maintaining fibers, might display enough internal stress that a measurement of a cleaved end will not be representative of the diameter of the fiber far from the end; this is a topic that may bear further investigation.

6. Discussion

We estimate the overall uncertainty (3 standard deviations of the mean) of the micrometer as 45 nm; of the confocal microscope as 40 nm; and of the white-light interference microscope as 30 nm.

The interference microscope and the micrometer agree remarkably well, whereas the confocal microscope may display an additional systematic error of the order of 20 nm. The microscopes are hard to use, so we use the micrometer to characterize Standard Reference Materials that are available from our offices in Gaithersburg [19].

These SRMs consist of a carefully cleaved fiber end in a retractable holder. The diameter of the end is measured at four angles with respect to a fiducial mark on the holder. All four diameters thus determined are reported, as well as their average. The individual diameter measurements are specified accurate within ±42 nm. For the convenience of the user, the SRM includes a short pigtail in case the core is to be illuminated. The SRM does not, however, include a specification of noncircularity or core-cladding decentering.

Acknowledgments

This work is based on a paper presented at the Conference on Precision Electromagnetic Measurements, Paris, France, June 9–12, 1992. Ted Doiron of the Precision Engineering Division in Gaithersburg, Maryland, designed and constructed the micrometer, and discovered why the mathematical correction failed. We thank John Baines of the National Physical Laboratory, U. K., for pointing out that the two beam splitters in the confocal microscope should be skew to one another and for other helpful suggestions, and Kenneth Raine and Dave Ferriss of NPL for providing us with finite-element analyses of cleaved fiber ends. We have benefited from discussions with Colin Sheppard of the University of Sydney; Robert Larrabee of NIST, Gaithersburg; Keith Emig and Jerry Parton of Corning; Andrew Hallam of York Industries; and Douglas Franzen and Gregory Obarski of NIST, Boulder. Jay Perkins of Meadowlark Optics and David Wilmering of NIST, Gaithersburg, polished the components of the micrometer, and Dale Thoele and Don Fulsos were always available for precise machining. Casey Shaar of Photon Kinetics supplied the design for the SRM holders. This work was supported in part by the Telecommunications Industry Association and the Naval Sea Systems Command.

7. References

[1] M. Young, Standards for optical fiber geometry measurements, Technical digest—Symposium on optical fiber measurements, 1990, G. W. Day and D. L. Franzen, eds., Natl. Inst. Stand. Technol. Spec. Publ. 792 (1990) pp. 129–133.

[2] M. Young, Fiber cladding diameter by contact micrometry, Digest, Optical fiber measurement conf., York, U. K. (1990) pp. 123–126.

[3] S. Mechels and M. Young, Scanning confocal microscope for accurate dimensional measurement, Proc. Soc. Photo-Optical Instrum. Engrs. **1660**, 542–550 (1992).

[4] S. Mechels and M. Young, Scanning confocal microscope for precise measurement of optical fiber diameter, Proc. Soc. Photo-Optical Instrum. Engrs. **1556**, 164–170 (1991).

[5] P. D. Hale and D. L. Franzen, Fiber cladding diameter measurement by white light interference microscopy, Technical digest—Symposium on optical fiber measurements, 1992, G. W. Day and D. L. Franzen, eds., Natl. Inst. Stand. Technol. Spec. Publ. 839 (1992) pp. 51–54.

[6] Fiberoptics Test Procedure FOTP-176, Measurement method for optical fiber geometry by automated gray-scale analysis, Telecommunications Industry Association-Electronic Industries Association, 2001 Pennsylvania Avenue, NW, Washington, DC 20006.

[7] S. Mechels and M. Young, Video microscope with submicrometer resolution, Appl. Opt. **30**, 2202–2211 (1991). M. Young and P. D. Hale, Off-axis illumination and its relation to partial coherence, Submitted to Appl. Opt., Jan. 1993.

[8] A. Collyer, K. W. Raine, and J. G. N. Baines, Investigation into the use of a scanning confocal microscope as a primary measurement method for determining optical fiber diameter, Digest, Optical fiber measurement conference, York, U. K. (1990) pp. 143–146. J. G. N. Baines, A. G. Hallam, K. W. Raine, and N. P. Turner, Fiber diameter measurements and their calibration, IEEE J. Lightwave Technol. **8**, 1259–1268 (1990).

[9] M. G. Puttock and E. G. Thwaite, Elastic compression of spheres and cylinders at point and line contact, Natl. Stand. Lab. Tech. Paper No. 25, Commonwealth Scientific and Industrial Research Organization, Melbourne, Australia (1969).

[10] J. R. Taylor, Introduction to error analysis, University Science Books (1982) p. 159.

[11] Anonymous, Guide to the expression of uncertainty in measurement, ISO/TAG4/WG3, International Organization for Standardization, 1, rue de Varembé, CH-1211 Genève 20, Switzerland (1992).

[12] M. S. O'Sullivan and D. W. Grandsen, A Fizeau fringe interferometer for fiber outside diameter measurements, Proc. Soc. Photo-Optical Instrum. Engrs. **841**, 287–290 (1987).

[13] M. J. Saunders, Non-contact, interferometric determination of the outside diameter of optical fibers, Technical digest—Symposium on optical fiber measurements, 1988, G.W. Day and D.L. Franzen, eds., Natl. Bur. Stand. (U. S.) Spec. Pub. 748 (1988) pp. 149–152.

[14] G. E. Obarski, T. J. Drapela, and M. Young, Scanning confocal microscopy for measuring diameter and linewidth: numerical modelling, in OE Lase 92—Biomedical Optics/Lasers, Sensors, and Spectroscopy, Proc. Soc. Photo-Opt. Instrum. Engrs. **1640**, in press.

[15] T. Wilson and C. Sheppard, Theory and practice of scanning optical microscopy, Academic Press, Orlando, Fla. (1984).
[16] H. Komatsu, Interferometry: Principles and applications of two-beam and multiple-beam interferometry, Technical Bulletin, Nikon Corporation, Tokyo, no date given.
[17] K. A. Emig, A comparison of interferometric techniques for fiber cladding diameter measurements, Technical digest—Symposium on optical fiber measurements, 1990, G. W. Day and D. L. Franzen, eds., Natl. Inst. Stand. Technol. Spec. Publ. 792 (1990) pp. 135–138.
[18] M. J. Saunders, Noncontact interferometric determination of the outside diameter of optical fibers, Technical digest—Symposium on optical fiber measurements, 1988, G. W. Day and D. L. Franzen, eds., Natl. Bur. Stand. (U. S.) Spec. Publ. 748 (1988) pp. 149–152.
[19] National Institute of Standards and Technology, Standard Reference Material Program, Room B311, Chemistry Building, Gaithersburg, Maryland 20899; 301 975-6776. Refer to SRM 2520, Optical Fiber Diameter Standard.

About the authors: *Matt Young is a Physicist with the Electromagnetic Technology Division in Boulder and chairman of the Boulder Editorial Review Board. Paul Hale is a Physicist with the Electromagnetic Technology Division. Earlier, he was a NIST Post-Doctoral Fellow. Steven Mechels is a Physicist with the Electromagnetic Technology Division. The National Institute of Standards and Technology is an agency of the Technology Administration, U.S. Department of Commerce.*

Volume 98, Number 2, March–April 1993
Journal of Research of the National Institute of Standards and Technology

[J. Res. Natl. Inst. Stand. Technol. 98, 217 (1993)]

Drift Eliminating Designs for Non-Simultaneous Comparison Calibrations

Volume 98 | Number 2 | March–April 1993

Ted Doiron

National Institute of Standards and Technology,
Gaithersburg, MD 20899-0001

The effects of drift on calibrations carried out by comparison have been studied at the National Institute of Standards and Technology for many years, and a number of strategies have been introduced to combat these effects. One strategy, the use of comparison designs which are inherently immune to linear drift, was developed specifically for mass comparison measurements. These techniques, developed for simultaneous comparisons, are extended to the case of non-simultaneous comparisons, such as gage block calibrations, where each artifact is measured separately, and the comparison is made mathematically from the individual measurements.

Key words: calibration design; comparison; drift eliminating; least squares analysis; metrology.

Accepted: October 28, 1992

1. Introduction

The sources of variation in measurements are numerous. Some of the sources are truly random noise, $1/f$ noise in electronic circuits for example. Usually the "noise" of a measurement is actually due to uncontrolled systematic effects such as instability of the mechanical setup or variations in the conditions or procedures of the test. Many of these variations are random in the sense that they are describable by a normal distribution. Like true noise in the measurement system, the effects can be reduced by making additional measurements.

Another source of serious problems, which is not random in nature is drift in the instrument readings. This effect cannot be minimized by additional measurement because it is not generally pseudo-random, but a nearly monotonic shift in the readings. In dimensional work the most important cause of drift is thermal changes in the equipment during the test. In this paper we will demonstrate techniques to address this problem of instrumental drift.

A simple example of the techniques for eliminating the effects of drift by looking at two different ways of comparing two gage blocks, one standard (A) and one unknown (B).

Scheme 1: A B A B

Scheme 2: A B B A

Now let us suppose we make the measurements regularly spaced in time, 1 time unit apart, and there is an instrumental drift of Δ. The actual readings (m_i) from scheme 1 are:

$$m_1 = A \quad (1a)$$
$$m_2 = B + \Delta \quad (1b)$$
$$m_3 = A + 2\Delta \quad (1c)$$
$$m_4 = B + 3\Delta \quad (1d)$$

Solving for B in terms of A we get:

$$B = A - \frac{1}{2}(m_1 + m_3 - m_2 - m_4) - \Delta \qquad (2)$$

which depends on the drift rate Δ.

Now look at scheme 2. Under the identical conditions the readings are:

$$m_1 = A \qquad (3a)$$
$$m_2 = B + \Delta \qquad (3b)$$
$$m_3 = B + 2\Delta \qquad (3c)$$
$$m_4 = A + 3\Delta \qquad (3d)$$

Here we see that if we add the second and third readings and subtract the first and fourth readings we find that the Δ drops out:

$$B = A - \frac{1}{2}(m_1 + m_4 - m_2 - m_3) \qquad (4)$$

Thus if the drift rate is constant—a fair approximation for most measurements if the time is properly restricted—the analysis both eliminates the drift and supplies a numerical approximation of the drift rate.

The calibration of a small number of "unknown" objects relative to one or two reference standards involves determining differences among the group of objects. Instrumental drift, due most often to temperature effects, can bias both the values assigned to the objects and the estimate of the effect of random errors. This paper presents schedules for sequential measurements of differences that eliminate the bias from drift and at the same time gives estimates of the magnitude of drift.

Previous works have [1,2] discussed schemes which eliminate the effects of drift for simultaneous comparisons of objects. For these types of measurements the difference between two objects is determined at one instant of time. Examples of these types of measurements are comparisons of masses with a double pan balance, comparison of standard voltage cells, and thermometers which are all placed in the same thermalizing environment. Many comparisons, especially those in dimensional metrology, cannot be done simultaneously. For example, using a gage block comparator, the standard, control (check standard) and test blocks are moved one at a time under the measurement stylus. For these comparisons each measurement is made at a different time. Schemes which assume simultaneous measurements will, in fact, eliminate the drift from the analysis of the test objects but will produce a measurement variance which is drift dependent and an erroneous value for the drift, Δ.

Calibration designs involve differences between measured items so that unless one or more of them are standards for which values are known, one cannot assign values for the remaining "unknown" items. Algebraically, one has a system of equations that is not of full rank and needs the value for one item or the sum of several items as the restraint to lead to a unique solution. The least squares method used in solving these equations has been presented [3] and refined [4] in the literature and will not be repeated in detail here. The analyses of particular measurement designs presented later in this paper conform to the method and notation presented in detail by Hughes [3].

The schemes used as examples in this paper are those currently used at NIST for gage block comparisons. In our calibrations a control (check standard) is always used to generate data for our measurement assurance plan [5]. It is not necessary, however, to use a control in every design and the schemes can be used with any of the objects as the standard and the rest as unknowns. Schemes of various numbers of unknowns and measurements are presented in the Appendix.

2. Calibration Designs

The term calibration design has been applied to experiments where only differences between nominally equal objects or groups of objects can be measured. Perhaps the simplest such experiment consists in measuring the differences between the two objects of the $n(n-1)$ distinct pairings that can be formed from n objects. If the order is unimportant, X compared to Y is the negative of Y compared to X, and there are only $n(n-1)/2$ distinct pairings. Of course only one measurement per unknown is needed to determine the unknown, but many more measurements are generally taken for statistical reasons. Ordinarily the order in which these measurements are made is of no consequence. However, when the response of the comparator is time dependent, attention to the order is important if one wishes to minimize the effect of time.

When this effect can be adequately represented by a linear drift, it is possible to balance out the effect by proper ordering of the observations. The drift can be represented by the series, ... −3, −2, −1, 0, 1, 2, 3, ... if there are an odd number of

comparisons and by ... $-5/2$, $-3/2$, $-1/2$, $1/2$, $3/2$, $5/2$, ... if there are an even number of comparisons.

As an example let us take $n=3$. If we make 12 measurements to obtain all possible $n(n-1)=6$ comparisons we get a scheme like that below, denoting the three objects by A, B, C.

Observation	Measurement
m_1	$A - 6\Delta$
m_2	$B - 5\Delta$
m_3	$C - 4\Delta$
m_4	$A - 3\Delta$
m_5	$B - 2\Delta$
m_6	$C - \Delta$
m_7	$A + \Delta$
m_8	$C + 2\Delta$
m_9	$B + 3\Delta$
m_{10}	$A + 4\Delta$
m_{11}	$C + 5\Delta$
m_{12}	$B + 6\Delta$

(5)

If we analyze these measurements by pairs, in analogy to the weighing designs of Cameron we see that:

		A	B	C	Δ
$d_1 = m_1 - m_2$	$= A - B - \Delta$	+1	−1		−1
$d_2 = m_3 - m_4$	$= C - A - \Delta$	−1		+1	−1
$d_3 = m_5 - m_6$	$= B - C - \Delta$		+1	−1	−1
$d_4 = m_7 - m_8$	$= A - C - \Delta$	+1		−1	−1
$d_5 = m_9 - m_{10}$	$= B - A - \Delta$	−1	+1		−1
$d_6 = m_{11} - m_{12}$	$= C - B - \Delta$		−1	+1	−1

(6)

The notation used here, the plus and minus signs, indicate the items entering into the difference measurement. Thus, d_2 is a measurement of the difference between object C and object A.

The difference between the above design and that of a design for simultaneous comparisons in Ref. [2] is that the drift column is constant. It is simple to see by inspection that the drift is balanced out since each object has two (+) and two (−) measurements and the drift column is constant. By extension, the effects of linear drift is eliminated in all complete block measurement schemes (those for which all objects are measured in all possible $n(n-1)$ combinations).

Although all schemes in which each object has equal numbers of (+) and (−) measurements is drift eliminating, there are practical criteria which must be met for the scheme to work. First, the actual drift must be linear. For dimensional measurements the instrument drift is usually due to changes in temperature. The usefulness of drift eliminating designs depends on the stability of the thermal environment and the accuracy required in the calibration. In the NIST gage block laboratory the environment is stable enough that the drift is linear at the 5 nm level over periods of 5 to 10 min. Our comparison plans are chosen so that the measurements can be made in this period.

Secondly, each measurement must be made in about the same amount of time so that the measurements are made at fairly regular intervals. In a completely automated system this is simple, but with human operators there is a natural tendency to make measurements simpler and quicker if the opportunity presents itself. For example, if the scheme has a single block measured two or more times in succession it is tempting to measure the object without removing it from the apparatus, placing it in its normal resting position, and returning it to the apparatus for the next measurement.

Finally, the measurements of each block are spread as evenly as possible across the design. Suppose in the scheme above where each block is measured four times block A is measured as the first measurement of d_1, d_2, d_3, and d_4. There is a tendency to leave block A near the measuring point rather than its normal resting position because it is used so often in the first part of the scheme. This allows block A to have a different thermal handling than the other blocks which can result in a thermal drift which is not the same as the other blocks.

3. Restraints

Because all of the measurements made in a calibration are relative comparisons, at least one value must be known to solve the system of equations. In the design of the last section, for example, if one has a single standard and two unknowns, the standard can be assigned to any one of the letters. (The same would be true of two standards and one unknown.) If there are two standards and one unknown, the choice of which pair of letters to assign for the standards can be important if all of the possible comparisons are not made. For full block designs (all possible comparisons are made) the uncertainty of the result does not depend on which letter is assigned to the standards or unknowns. For incomplete block designs the uncertainty of the results can depend on which letter the standard and unknowns are assigned. In these cases the customer blocks are assigned to minimize their variance and allow the larger variance for the measurement of the extra master (control).

This asymmetry occurs because every possible comparison between the four items has not been measured. For 4 objects there are 12 possible intercomparisons. If an eight measurement scheme is used all three unknowns cannot be compared directly to the standard the same number of times. For example, two unknowns can be compared directly with the standard twice, but the other unknown will have no direct comparisons. This indirect comparison to the standard results in a slightly larger variance for the block compared indirectly. Complete block plans, which compare each block to every other block equal number of times, has no such asymmetry, and thus removes any restriction on the measurement position of the control.

4. Example: 4 block, 12 comparison, Single Restraint Design for NIST Gage Block Calibration [4]

The gage block comparison scheme put into operation in 1989 consists of two standards blocks, denoted S and C, and two customer blocks to be calibrated, denoted Y and Z. In order to decrease the random error of the comparison process a new scheme was devised, consisting of all 12 possible comparisons between the four blocks. Because of continuing problems making penetration corrections, the scheme was designed to use either the S or C block as the restraint and the difference $(S-C)$ as the control parameter. The S blocks are all steel, and are used as the restraint for all steel customer blocks. The C blocks are chrome carbide, and are used as the restraint for chrome and tungsten carbide blocks. The difference $(S-C)$ is independent of the choice of restraint.

We chose a complete block scheme which assures that the design is drift eliminating and the blocks can be assigned to the letters of the design arbitrarily. We chose $(S-C)$ as the first comparison. Since there are a large number of ways to arrange the 12 measurements for a complete block design, we added two restrictions as a guide to choose a "best" design.

1. It was decided to avoid schemes which measured the same block two or more times consecutively. There are many possible schemes where one or more blocks are measured twice consecutively. There is a great temptation to not remove and replace the blocks under these conditions. The analysis assumes that each measurement is made with the same motion and that the measurements are evenly spaced in time. Consecutive repetition threatens both these assumptions.

2. We decided that schemes in which the six measurements of each block were spread out as evenly as possible in time would be less likely to be affected by small non-linearities in the drift. For example, for some schemes measurements of one block are completed by the 8th comparison, leaving the final 1/3 of the comparisons with no sampling of that block.

The new scheme is as follows:

$$
\begin{array}{lcccccc}
 & & S & C & Y & Z & \Delta \\
d_1 = S-C & & 1 & -1 & 0 & 0 & -1 \\
d_2 = Z-S & & -1 & 0 & 0 & 1 & -1 \\
d_3 = Y-Z & & 0 & 0 & 1 & -1 & -1 \\
d_4 = C-S & & -1 & 1 & 0 & 0 & -1 \\
d_5 = C-Y & & 0 & 1 & -1 & 0 & -1 \\
D = d_6 = Z-C & X = & 0 & -1 & 0 & 1 & 1 \\
d_7 = S-Y & & 1 & 0 & -1 & 0 & -1 \\
d_8 = C-Z & & 0 & 1 & 0 & -1 & -1 \\
d_9 = S-Z & & 1 & 0 & 0 & -1 & -1 \\
d_{10} = Y-C & & 0 & -1 & 1 & 0 & -1 \\
d_{11} = Y-S & & -1 & 0 & 1 & 0 & -1 \\
d_{12} = Z-Y & & 0 & 0 & -1 & 1 & -1
\end{array} \tag{7}
$$

When the S block is the restraint, with value L, the matrix equation to solve is:

$$
\begin{vmatrix} X'X & a \\ a' & 0 \end{vmatrix} \begin{vmatrix} A \\ \lambda \end{vmatrix} = \begin{vmatrix} X'Y \\ L \end{vmatrix} \tag{8}
$$

where $[A'] = [S\ C\ Y\ Z\ \Delta]$ is the vector to be estimated and $[a'] = [1\ 0\ 0\ 0\ 0]$ is the restraint vector.

$$
\begin{vmatrix} X'X & a \\ a' & 0 \end{vmatrix} = \begin{vmatrix} 6 & -2 & -2 & -2 & 0 & 1 \\ -2 & 6 & -2 & -2 & 0 & 0 \\ -2 & -2 & 6 & -2 & 0 & 0 \\ -2 & -2 & -2 & 6 & 0 & 0 \\ 0 & 0 & 0 & 0 & 12 & 0 \\ 1 & 0 & 0 & 0 & 0 & 0 \end{vmatrix} \tag{9}
$$

$$
\begin{vmatrix} B & h \\ h' & 0 \end{vmatrix} = \begin{vmatrix} X'X & a \\ a' & 0 \end{vmatrix}^{-1} = (1/24) \begin{vmatrix} 0 & 0 & 0 & 0 & 0 & 24 \\ 0 & 6 & 3 & 3 & 0 & 24 \\ 0 & 3 & 6 & 3 & 0 & 24 \\ 0 & 3 & 3 & 6 & 0 & 24 \\ 0 & 0 & 0 & 0 & 2 & 0 \\ 24 & 24 & 24 & 24 & 0 & 0 \end{vmatrix} \tag{10}
$$

The estimate for A can be written as

$$<A> = \begin{vmatrix} BX' & h \end{vmatrix} \begin{vmatrix} D \\ L \end{vmatrix} = 1/24 \begin{vmatrix} 0 & 0 & 0 & 0 & 0 & 0 & 0 & 0 & 0 & 0 & 0 & 0 & 24 \\ -6 & 3 & 0 & 6 & 3 & -3 & -3 & 3 & -3 & -3 & 3 & -3 & 24 \\ -3 & 3 & 3 & 3 & 3 & 0 & -6 & 0 & -3 & 3 & 6 & -3 & 24 \\ -3 & 6 & -3 & 3 & 0 & 3 & -3 & -3 & -6 & 0 & 3 & 3 & 24 \\ -2 & -2 & -2 & -2 & -2 & -2 & -2 & -2 & -2 & -2 & -2 & -2 & 0 \end{vmatrix} \quad (11)$$

This leads to estimated values for S, C, Y, Z, and Δ which can be written as a function of the comparison measurements:

$$<S> = L \quad (12a)$$
$$<C> = (1/8)(-2d_1 + d_2 + 2d_4 + d_5 - d_6 - d_7 + d_8 - d_9 - d_{10} + d_{11}) + L \quad (12b)$$
$$<Y> = (1/8)(-d_1 + d_2 + d_3 + d_4 - d_5 - 2d_7 - d_9 + d_{10} + 2d_{11} - d_{12}) + L \quad (12c)$$
$$<Z> = (1/8)(-d_1 + 2d_2 - d_3 + d_4 + d_6 - d_7 - d_8 - 2d_9 + d_{11} + d_{12}) + L \quad (12d)$$
$$<\Delta> = (-1/12)(d_1 + d_2 + d_3 + d_4 + d_5 + d_6 + d_7 + d_8 + d_9 + d_{10} + d_{11} + d_{12}) + L \quad (12e)$$

The deviations of the measured values from the estimated values, $\epsilon_1, \epsilon_2, \ldots, \epsilon_{12}$ can be determined from the equations above, or can be calculated directly using matrix methods. For example,

$$\epsilon_1 = (d_1)_{\text{observed}} - (<S> - <C>). \quad (13)$$

These deviations provide the information needed to obtain a value, s_w, which is the experimental estimate value for the short term process standard deviation, or within standard deviation σ_w.

$$s^2 = \sum_{i=1}^{n} \frac{\delta_i^2}{(n-m+1)} \quad (14)$$

The number of degrees of freedom, $(n-m+1)$, results from taking the number of observations $(n=12)$ less the number of unknowns $(m=5; S, C, Y, Z, \Delta)$, and then adding one for the restraint. Because of the complete block structure (all 12 possible combinations measured) the standard deviations of the predicted values for the three unknowns are the same:

$$s_C = s_Y = s_Z = (1/2)s. \quad (15)$$

The standard deviation of the predicted drift is

$$S_\delta = \sqrt{\frac{1}{12}}\, s. \quad (16)$$

5. Process Control

5.1 F–Test

Continued monitoring of the measurement process is required to assure that predictions based on the accepted values for process parameters are still valid. For gage block calibration at NIST, the process is monitored for precision by comparison of the observed standard deviation, s_w, to the average of previous values, σ_w. For this purpose the value of s_w is recorded for every calibration done, and this data set is periodically analyzed to provide an updated value of the accepted process σ_w for each gage block size.

The comparison is made using the F distribution, which governs the comparison of variances. The ratio of the variances s^2 (derived from the model fit to each calibration) and σ_w^2 derived from the history is compared to the critical value $F(8, \infty, \alpha)$, which is the upper α probability point of the F distribution for degrees of freedom 8 and ∞. For calibrations at NIST, α is chosen as 0.01 to give $F(8, \infty, .01) = 2.5$. The condition to be checked is:

$$F = \frac{s^2_{\text{obs}}}{\sigma_w^2} < 2.5. \quad (17)$$

If this condition is violated the calibration fails, and is repeated. If the calibration fails more than once the test blocks are re-inspected and the instrument checked and recalibrated. All calibrations, pass or fail, are entered into the history file.

5.2 *t*-Test

At NIST a control measurement is made with each calibration by using two known master blocks in each calibration. One of the master blocks is steel and the other chrome carbide. When a customer block is steel the steel master is used as the restraint, and when a customer block is carbide, the carbide master is used as the restraint. The use of a control measurement for calibrations is necessary in order to provide assurance of the continuing accuracy of the measurements. The *F*-test, while providing some process control, only attempts to control the repeatibility of the process, not the accuracy. The use of a control is also the easiest method for finding the long term variability of the measurement process [5].

While the use of a control in each calibration is not absolutely necessary, the practice is highly recommended. There are systems which use intermittent tests, e.g., measures a control set once a week [4]. This is a good strategy for automated systems because the chances of block to block operator errors is reduced greatly. For manual measurements the process variability, and of course the occurence of operator error is much higher.

The check for systematic error is given by comparison of the observed value of the difference between the standard and control blocks. If S is the standard it becomes the restraint, and if A is used as the control $(S-A)$ is the control parameter for the calibration. This observed control is recorded for every calibration, and is used to periodically update the accepted, or average value, of the control. The process control step involves the comparison of the observed value of the control to the accepted (historical) value. The comparison is made using the Student *t*-distribution.

The control test demands that the observed difference between the control and its accepted value be less than 3 times the accepted long term standard deviation, σ_t, of the calibration process. This value of the t-distribution implies that a good calibration will not be rejected with a confidence level of 99.7%. The condition to be checked is:

$$t = \frac{\left|(<S>-<C>-(S-C)_{acc}\right|}{\sigma_t} < 3 . \quad (18)$$

The value of σ_t is obtained directly from the sequence of values of $(<S>-<C>)$ arising in regular calibrations. The recorded $(<S>-<C>)$ as the restraint, and $<S>-<C>$ is again used as the control.

If both the precision (*F*-test) and accuracy (*t*-test) criteria are satisfied, the process is regarded as being "in control" and values for the unknowns, Y and Z, and their associated uncertainties are regarded as valid. Failure of either criterion is an "out-of-control" signal and the measurements are repeated.

The value for drift, (Δ), serves as an indicator of possible trouble if it changes markedly from its usual range of values. However, because any linear drift is balanced out, a change in the value does not of itself invalidate the result.

6. Conclusion

The choice of the order of comparisons is an important facet of calibrations, in particular if chosen properly the comparison scheme can be made immune to linear drifts in the measurement equipment. The idea of making a measurement scheme robust is a powerful one. What is needed to implement the idea is an understanding of the sources of variability in the measurement system. While such a study is sometimes difficult and time consuming because of the lack of reference material concerning many fields of metrology, the NIST experience has been that such efforts are rewarded with measurement procedures which, for about the same amount of effort, produce higher accuracy.

7. Appendix A. Selection of Other Drift Eliminating Designs

The following designs can be used with or without a control block. The standard block is denoted S, and the unknown blocks A, B, C, etc. If a check standard block is used it can be assigned to any of the unknown block positions. The name of the design is simply the number of blocks in the design and the total number of comparisons.

3 - 6 Design
(One master block, 2 unknowns 4 measurements each)

$$\begin{aligned} y_1 &= S-A \\ y_2 &= B-S \\ y_3 &= A-B \\ y_4 &= A-S \\ y_5 &= B-A \\ y_6 &= S-B \end{aligned}$$

3 - 9 Design
(One master block, 2 unknowns 6 measurements each)

$$\begin{aligned} y_1 &= S-A \\ y_2 &= B-A \\ y_3 &= S-B \\ y_4 &= A-S \\ y_5 &= B-S \\ y_6 &= A-B \\ y_7 &= A-S \\ y_8 &= B-A \\ y_9 &= S-B \end{aligned}$$

4 - 8 Design
(One master block,
3 unknowns
4 measurements each)

$y_1 = S - A$
$y_2 = B - C$
$y_3 = C - S$
$y_4 = A - B$
$y_5 = A - S$
$y_6 = C - B$
$y_7 = S - C$
$y_8 = B - A$

4 - 12 Design
(One master block,
3 unknowns
6 measurements each)

$y_1 = S - A$
$y_2 = C - S$
$y_3 = B - C$
$y_4 = A - S$
$y_5 = A - B$
$y_6 = C - A$
$y_7 = S - B$
$y_8 = A - C$
$y_9 = S - C$
$y_{10} = B - A$
$y_{11} = B - S$
$y_{12} = C - B$

5 - 10 Design
(One master block,
4 unknowns
4 measurements each)

$y_1 = S - A$
$y_2 = D - C$
$y_3 = S - B$
$y_4 = D - A$
$y_5 = C - B$
$y_6 = A - C$
$y_7 = B - S$
$y_8 = B - D$
$y_9 = C - S$
$y_{10} = A - D$

6 - 12 Design
(One master block,
5 unknowns
4 measurements each)

$y_1 = S - A$
$y_2 = D - C$
$y_3 = E - B$
$y_4 = E - D$
$y_5 = C - A$
$y_6 = B - C$
$y_7 = S - E$
$y_8 = A - D$
$y_9 = A - B$
$y_{10} = D - S$
$y_{11} = B - E$
$y_{12} = C - S$

7 - 14 Design
(One master block,
4 unknowns
6 measurements each)

$y_1 = S - A$
$y_2 = E - C$
$y_3 = B - D$
$y_4 = A - F$
$y_5 = S - E$
$y_6 = D - B$
$y_7 = A - C$
$y_8 = B - F$
$y_9 = D - E$
$y_{10} = F - S$
$y_{11} = E - A$
$y_{12} = C - B$
$y_{13} = C - S$
$y_{14} = F - D$

8 - 16 Design
(One master block,
7 unknowns
4 measurements each)

$y_1 = S - A$
$y_2 = E - G$
$y_3 = F - C$
$y_4 = D - S$
$y_5 = B - E$
$y_6 = G - F$
$y_7 = C - B$
$y_8 = E - A$
$y_9 = F - D$
$y_{10} = C - S$
$y_{11} = A - G$
$y_{12} = D - B$
$y_{13} = C - S$
$y_{14} = G - C$
$y_{15} = B - D$
$y_{16} = A - F$

9 - 18 Design
(One master block,
7 unknowns
4 measurements each)

$y_1 = S - A$
$y_2 = H - F$
$y_3 = A - B$
$y_4 = D - C$
$y_5 = E - G$
$y_6 = C - A$
$y_7 = B - F$
$y_8 = G - H$
$y_9 = D - S$
$y_{10} = C - E$
$y_{11} = H - S$
$y_{12} = G - D$
$y_{13} = C - S$
$y_{14} = A - C$
$y_{15} = F - D$
$y_{16} = S - H$
$y_{17} = E - B$
$y_{18} = F - G$

10 - 20 Design
(One master block,
9 unknowns
4 measurements each)

$y_1 = S - A$
$y_2 = F - G$
$y_3 = I - C$
$y_4 = D - E$
$y_5 = A - H$
$y_6 = B - C$
$y_7 = G - H$
$y_8 = I - S$
$y_9 = E - F$
$y_{10} = H - I$
$y_{11} = D - F$
$y_{12} = A - B$
$y_{13} = C - I$
$y_{14} = H - E$
$y_{15} = B - G$
$y_{16} = S - D$
$y_{17} = F - B$
$y_{18} = C - D$
$y_{19} = G - S$
$y_{20} = E - A$

11 - 22 Design
(One master block,
10 unknowns
4 measurements each)

$y_1 = S - A$
$y_2 = D - E$
$y_3 = G - I$
$y_4 = C - H$
$y_5 = A - B$
$y_6 = I - J$
$y_7 = H - F$
$y_8 = D - S$
$y_9 = B - C$
$y_{10} = S - E$
$y_{11} = A - G$
$y_{12} = F - B$
$y_{13} = E - F$
$y_{14} = J - A$
$y_{15} = C - D$
$y_{16} = H - J$
$y_{17} = F - G$
$y_{18} = I - S$
$y_{19} = B - H$
$y_{20} = G - D$
$y_{21} = J - C$
$y_{22} = E - I$

The choice of the order of comparisons is an important facet of calibrations, in particular if chosen properly the comparison scheme can be made immune to linear drifts in the measurement equipment. The idea of making a measurement scheme

robust is a powerful one. What is needed to implement the idea is an understanding of the sources of variability in the measurement system. While such a study is sometimes difficult and time consuming because of the lack of reference material concerning many fields of metrology, the NIST experience has been that such efforts are rewarded with measurement procedures which, for about the same amount of effort, produce higher accuracy.

Acknowledgment

I would like to acknowledge Mr. Chien-ming Wu of the Industrial Technology Research Institute and Ms. Carroll Croarkin of NIST for reading the draft paper and suggesting many useful changes and corrections.

8. References

[1] J. M. Cameron, M. C. Croarkin, and R. C. Raybold, Designs for the Calibration of Standards of Mass, Natl. Bur. Stand. (U.S.) Technical Note 952, 1977.
[2] J. M. Cameron and G. E Hailes, Designs for the Calibration of Small Groups of Standards in the Presence of Drift, Natl. Bur. Stand. (U.S.) Technical Note 844, 1974.
[3] C. G. Hughes, III and H. A. Musk, A Least Squares Method for Analysis of Pair Comparison Measurements, Metrologia 8, 109-113 (1972).
[4] C. Croarkin, An Extended Error Model for Comparison Calibration, Metrologia 26, 107-113 (1989).
[5] C. Croarkin, Measurement Assurance Programs, Part II: Development and Implementation, Natl. Bur. Stand. (U.S.) Special Publication 676-II, 1984.
[6] Further examples are presented in detail in a larger version of this work to be published as a NIST Technical Note.
[7] M. Priel, Automated Gage Block Calibration, Proceedings of the Measurement Science Conference, Anaheim CA, 1989.

About the author: Ted Doiron is a physicist in the Precision Engineering Division at NIST. The National Institute of Standards and Technology is an agency of the Technology Administration, U.S. Department of Commerce.

Volume 98, Number 2, March-April 1993
Journal of Research of the National Institute of Standards and Technology

[J. Res. Natl. Inst. Stand. Technol. 98, 225 (1993)]

A Three-Ratio Scheme for the Measurement of Isotopic Ratios of Silicon

Volume 98 | Number 2 | March-April 1993

Harry Ku

National Institute of Standards and Technology, Gaithersburg, MD 20899-0001

and

Frank Schaefer, Staf Valkiers, and Paul De Bièvre

Institute for Reference Materials and Measurements, Commission of the European Communities, JRC, B-2440 Geel, Belgium

This paper proposes a scheme of measurement sequences that has been used for the redetermination of the molar mass (atomic weight) of silicon at the Central Bureau for Nuclear Measurements (now Institute for Reference Materials and Measurements). This scheme avoids correlations among the measured ratios caused by normalizing all ion current measurements to that of the largest ion current. It also provides additional information for checking on the consistency of these ratios within a cycle of scans. Measurements of isotope abundance ratios of silicon are used as an illustration.

Key words: atomic weight of silicon; isotope ratios; mass spectrometer; measurement scheme; redundancy; symmetry.

Accepted: December 24, 1992

1. Measurement Scheme

In using mass spectrometers to measure abundance ratios of isotopes in an element, a general procedure is to relate all minor abundant isotopes to one major abundant isotope at the same point in time. Ion currents in a scan of the isotopic ion beams are either adjusted for time differences or normalized by a symmetrical arrangement of measurement sequence followed by averaging.

This paper proposes a scheme of measurement sequences that has been used for the redetermination of the molar mass (atomic weight) of silicon at the Central Bureau for Nuclear Measurements (CBNM).[1] This scheme avoids correlations among the measured ratios caused by normalizing all ion current measurements to that of the largest ion current. It also provides additional information for checking on the consistency of these ratios within a cycle of scans. Measurements of isotope abundance ratios of silicon are used below as an illustration.

Recalling that there are three stable isotopes of mass numbers 28, 29, and 30, with atomic masses $M(^{28}\mathrm{Si})$, $M(^{29}\mathrm{Si})$, and $M(^{30}\mathrm{Si})$ known almost exactly [3], the molar mass of a sample of silicon, M, can be determined as:

$$M(\mathrm{Si}) = \Sigma M(^{i}\mathrm{Si})\, f_i$$

where f_i is the fractional isotope abundance of isotope ^{i}Si, with $\Sigma f_i = 1$.

[1] The molar mass of a particular specimen of silicon thus determined was used in a project, in collaboration with the Physikalisch-Technische Bundesanstalt (PTB), Braunschweig, Germany, for the redetermination of the Avogadro Constant [1,2].

In our experiment, measurements were made on SiF_4 gas samples by means of a gas mass spectrometer equipped with a Faraday-cup collector. Ion currents were measured for $^{28}SiF_3^+$ (mass position 85), $^{29}SiF_3^+$ (86), and $^{30}SiF_3^+$ (87). Ion current ratios, $R(i/j)$, are formed from these measurements. These ratios, after corrections by proportionality factors, are estimates of ratios of fractional abundances, f_i/f_j. Denoting the corrected ratios as $r(i/j)$ and equating these to the f_i/f_j, it follows that

$$f_{28}=\frac{1}{1+r(29/28)+r(30/28)}, \quad (1)$$

and

$$f_{29}=r(29/28)f_{28},$$

$$f_{30}=r(30/28)f_{28}.$$

Scaling the conversion of ion-current ratios into isotope-abundance ratios, i.e., determining the proportionality factors is accomplished by means of accurately synthesized isotope mixtures with isotope abundance ratios close to those of the unknown silicon samples.

In previous work [1], a two-ratio scheme was used, because Eq. (1) requires only the measured values of $r(29/28)$ and $r(30/28)$, i.e., the ratios of minor abundant isotopes (3^+ to 4^+%) to the major abundant isotope ^{28}Si (92^+%) The sequence of measurements in a scan proceeds as depicted in Fig. 1. There is one average for each intensity measured: $I(1)$ for $^{28}SiF_3^+$, $I(2)$ for $^{29}SiF_3^+$, and $I(3)$ for $^{30}SiF_3^+$. Thus the ratios are:

$$R(86/85)=I(2)/I(1); \; R(87/85)=I(3)/I(1).$$

Eight to ten scans are measured during one cycle. A linear least squares fit of these measured ratios vs time would yield estimates of the ratios at t_0, the instant sample gas is introduced into the ionizing chamber, to calculate and to allow for mass fractionation effect. The residual standard deviation, and the relative standard deviations of the R's are also computed for each cycle.

The two-ratio scheme has been in use and appears to work well. However, two questions remain unanswered:

1. Since both $R(86/85)$ and $R(87/85)$ used the same value of $I(85)$ in the denominator, the two ratios are correlated. What is the effect of correlation on the resulting calculated f_{28}, f_{29}, and f_{30}? In addition, if the intensity of the major isotope is measured higher (or lower) than it should, because of minor nonlinearity in the instrumentation system, then the corresponding abundance will also be higher (or lower).
2. How do we know if the intensities measured in a scan, or in a cycle, are correct or consistent?

To answer these questions, a three-ratio scheme is devised such that all three ratios, $R(87/85)$, $R(85/86)$, and $R(86/87)$, are measured, using six independently measured averages of intensities. Thus 12 ion intensities are measured in a sequence in one scan as shown in Fig. 2. For the scheme shown, there are two average intensities for 85, $I(1)$ and $I(4)$, two averages for 86, $I(3)$, and $I(6)$,

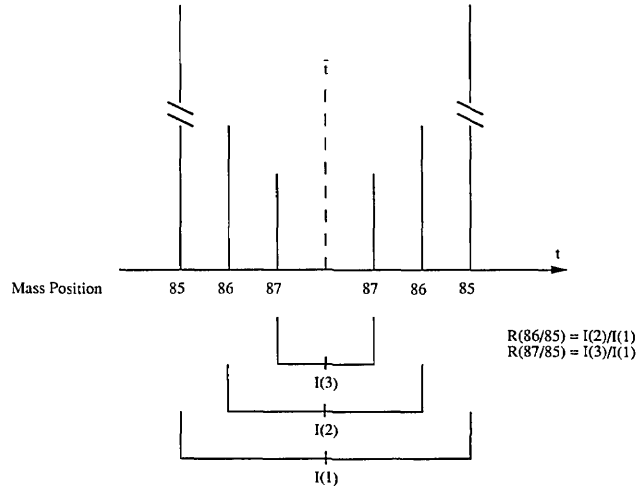

Fig. 1. Two ratio scheme. One scan of a two ratio scheme is shown here where two measurements of ion currents of each isotopic ion beam are made, centered about $\bar{t}$. Averages of those three pairs of measurements, $I(1)$, $I(2)$, and $I(3)$, are used to form the two ratios $R(86/85)$ and $R(87/85)$.

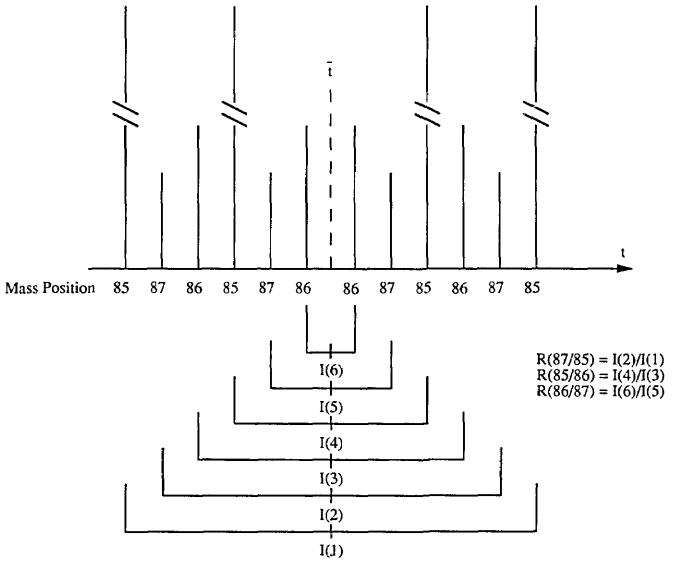

Fig. 2. Three ratio scheme. One scan of a three ratio scheme is shown in this diagram where four measurements of ion currents of each ion beam are made, all centered about $\bar{t}$. Averages of each two measurements equidistant about $\bar{t}$, $I(1)$ through $I(6)$, are used to form the three ratios $R(87/85)$, $R(85/86)$ and $R(86/87)$.

and two averages for 87, $I(2)$, and $I(5)$. The ratios may be formed as

$$R(87/85) = I(2)/\mathrm{I}(1),\ R(85/86) = I(4)/\mathrm{I}(3),\ \text{and}$$

$$R(86/87) = I(6)/\mathrm{I}(5).$$

Hence, there is no obvious correlation among the ratios to worry about because all ratios are formed with independently measured intensities. Furthermore, the "redundant" third ratio $R(86/87)$ can be used to form a "closure" to check on the consistency of the measured ratios [4], i.e.,

$$R(87/85)\,R(85/86)\,R(86/87) \equiv 1,$$

if there are no measurement errors. With measurement errors, we may formulate

$$R(87/85)\,R(85/86)\,R(86/87) = 1 + \epsilon,$$

and use the ϵ values as a control on the measured ratios. We note that

Average $\epsilon \approx 0$

Standard deviation of $\epsilon \approx \{\Sigma(\text{relative s.d. of } R\text{'s})^2\}^{1/2}$.

The relative standard deviations, computed from the residual standard deviations resulting from the linear fit of R's in a cycle, can be used in the above expression.

A control chart on ϵ can then be constructed to monitor measurements within a run. If ϵ's are predominately positive (negative), it is an indication of the presence of a systematic error at some, identifiable, point in the measurement procedure. Investigation as to its cause is in order.

The three-ratio scheme has been implemented in this laboratory (CBNM) for about 6 months now and seems to work well [2]. With computer controlled measurement and summary, the additional work is minimal once the software is prepared. A typical data summary sheet for the measurement of a silicon specimen is shown in Table 1, listing the three ratios measured in a cycle of ten scans, together with the ϵ's calculated for each scan, extrapolated values at t_0 and the relative standard deviations.

Table 1. Typical data summary sheet for a cycle of ten scans. Observed ratios of ion currents $R(86/85)$, $R(85/87)$ and $R(87/86)$ are listed in columns 2, 3, and 4, respectively, for the ten scans. The $(1+\epsilon)$ values area calculated for each scan and for the extrapolated values at t_0

Scan no.	$I(^{29}Si)/I(^{28}Si)$	$I(^{28}Si)/I(^{30}Si)$	$I(^{30}Si)/I(^{29}Si)$	$1+\epsilon$
1	0.050 597 5	29.880 0	0.661 443	1.000 005
2	0.050 597 1	29.871 2	0.661 547	0.999 860
3	0.050 606 0	29.864 9	0.661 637	0.999 961
4	0.050 615 4	29.858 5	0.661 706	1.000 036
5	0.050 617 5	29.849 7	0.661 798	0.999 922
6	0.050 622 9	29.842 2	0.661 888	0.999 913
7	0.050 628 5	29.834 4	0.661 954	0.999 862
8	0.050 636 2	29.826 7	0.662 056	0.999 910
9	0.050 642 7	29.819 4	0.662 123	0.999 895
10	0.050 645 7	29.812 9	0.662 238	0.999 910
Mean				0.999 927
Std. dev.				57
		Extrapolation		
Value ($t=t_0$)	0.050 574 5	29.906 7	0.661 149	0.999 998
Std. dev.	20	7	11	48
Rel. std. dev.	$3.9\cdot10^{-5}$	$2.3\cdot10^{-5}$	$1.7\cdot10^{-5}$	$4.8\cdot10^{-5}$

With the addition of the third ratio, there are also a number of features that can be used to check on the accuracy of the mass spectrometric measurements:

a. We note that in Fig. 2, the three ratios can be computed by different pairing of the intensities, e.g.,

$$R(87/85)=I(2)/I(4),\ R(85/86)=I(1)/I(6),$$
$$R(86/87)=I(3)/I(5),$$

and so on. Ratios computed from different pairings can be compared. If they differ consistently, the cause should be investigated.

b. If we denote 85 by A, 86 by B and 87 by C, then the sequence in Fig. 2 can be represented as

ACBACBBCABCA.

By permuting the positions of these isotopes, we could use also

ABCABCCBACBA
BACBACCABCAB
BCABCAACBACB
CBACBAABCABC
CABCABBACBAC.

The essential difference of these six sequences is the position of the major isotope A relating to the minor isotopes. If these six sequences yield ratios that are different beyond experimental errors, it is an indication that adjustments should be made on mass position, interference, or other factors.

c. The ratio of the minor isotopes, $R(86/87)$ is much more sensitive to small changes than the other two ratios where the major peak dominates the behavior of these ratios. For example, when a natural silicon sample is measured after an enriched ^{29}Si, the mass spectrometer seems to remember the last measurement (by adsorption to the walls or other reasons) and yields a higher 86 intensity than actually present in the natural silicon. This effect shows more clearly in the ratio (86/87) than the other two. Hence it can be used to check whether there has been enough flushing and cleaning of the ion source to erase the memory.

d. If we denote the three measured ratios by R_1, R_2, and R_3, then the least squares adjusted ratios are [5]:

$$r_1=\left(\frac{R_1^2}{R_2R_3}\right)^{1/3};\ r_2\left(\frac{R_2^2}{R_1R_3}\right)^{1/3};\ r_3\left(\frac{R_3^2}{R_1R_2}\right)^{1/3}.$$

r_1 and r_2 can be used in Eq. (1). The relative standard deviations of the r's is about 0.82 ($\sqrt{2/3}$) of those for the R's.

e. If a mass spectrometer has three Faraday cups to measure the three intensities separately (as is the case of the new spectrometer at CBNM), a similar scheme may be devised to yield three independent ratios as shown in Fig. 3. For each isotope,

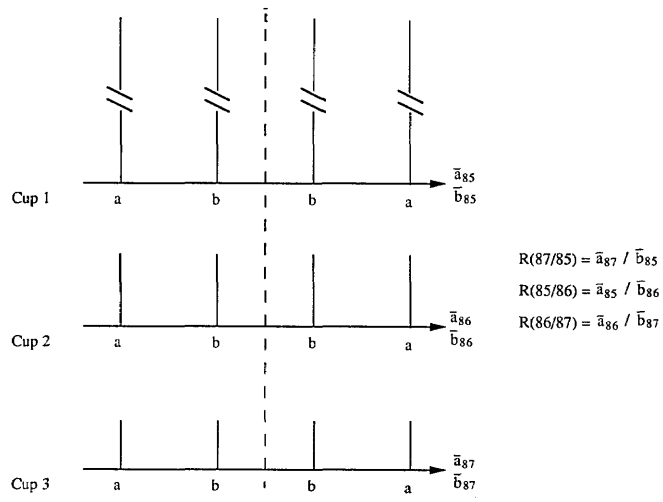

Fig. 3. Scheme for three Faraday cups. One scan of a scheme using three Faraday cups is shown in this diagram. Two averages of ion currents of each ion beam, $\bar{a}$ and $\bar{b}$, are used to form the three ratios $R(87/85)$, $R(85/86)$, and $R(86/87)$.

e.g., 85 using cup 1, four ion currents are measured at equal intervals in time in a scan. The two end ones are designated by a's, and the two middle ones by b's. Similarily, for 86 using cup 2, and 87 using cup 3, measured during the same time intervals as those of 85. Thus for each isotope, we have two averages, $\bar{a}$ and $\bar{b}$, both corresponding to time $\bar{t}$. Hence, three independent ratios can be computed, using the six averages $\bar{a}_{85}$, $\bar{b}_{85}$, $\bar{a}_{86}$, $\bar{b}_{86}$, $\bar{a}_{87}$, and $\bar{b}_{87}$, as follows:

$$R(86/85)=\frac{\bar{a}_{86}}{\bar{b}_{85}};\ R(85/87)=\frac{\bar{a}_{85}}{\bar{b}_{87}};\ R(87/86)=\frac{\bar{a}_{87}}{\bar{b}_{86}},$$

Here the ϵ's calculated from the three independent ratios would also check the consistency of the three cups.

With the objective to determine the molar mass of silicon accurate to one part in 10^7, thus requiring a precision in ratio measurements to parts in the 10^5 range, it is imperative to investigate all avenues of improvements. The three-ratio scheme provides symmetry and redundancy and appears to be a helpful step in this direction.

In the above, we have used the three isotopes of silicon as an example to illustrate the three-ratio scheme. It is obvious that any three- or more- isotopes of a polyisotopic element can be treated in the same manner. The selection of the particular set of three isotopes is, of course, a decision the experimenter must make to suit his objectives.

Acknowledgment

Our thanks to Steffen Peiser for his comments and encourgement.

2. References

[1] P. Seyfried, P. De Bièvre, et al., A Determination of the Avogadro Constant, Z. Phys. B Cond. Matter **87**, 289–298 (1992).

[2] P. De Bièvre, S. Valkiers, et al. High Accuracy Isotope Abundance Measurements for Metrology, submitted for publication.

[3] A. H. Wapstra and G. Audi, Atomic Data Nuclear Data Tables **39**, 281 (1988).

[4] Churchill Eisenhart, Realistic Evaluation of the Precision and Accuracy of Instrument Calibration Systems, J. Res. Natl. Bur. Stand. (U.S.) **67C** (2), 24 (1963).

[5] W. J. Youden, Uncertainties in Calibration, IRE Transactions on Instrument, **I-II**, (3-4), 64–65 (1962).

About the authors: *Harry Ku, mathematical statistician, retired in 1985 as Chief of the Statistical Engineering Division at the National Bureau of Standards (now the National Institute of Standards and Technology). Frank Schaefer, from Bremen University, was a visiting scientist at the Central Bureau for Nuclear Measurements. Staf Valkiers is a chemical engineer from HIK Technical College, Geel, Belgium. Paul De Bièvre, Ph. D. from Gent University, is Group Leader, Mass Spectrometry, and Advisor on Reference Materials at the Institute for Reference Materials and Measurements (formerly Central Bureau for Nuclear Measurements) of the Commission of the European Communities in Geel, Belgium. He is also Professor in Isotopic Mass Spectrometry at Antwerpen University. The National Institute of Standards and Technology is an agency of the Technology Administration, U.S. Department of Commerce.*

Volume 98, Number 2, March–April 1993
Journal of Research of the National Institute of Standards and Technology

[J. Res. Natl. Inst. Stand. Technol. 98, 231 (1993)]

"Wolf Shifts" and Their Physical Interpretation Under Laboratory Conditions

Volume 98 Number 2 March–April 1993

Klaus D. Mielenz

Alpine Lake Resort,
Terra Alta, WV 26764-0402

This paper attempts to reconcile conflicting points of view of laboratory physicists and coherence theorists on correlation-induced spectral changes arising from the partial coherence of primary and secondary light sources. It is shown that, under normal laboratory conditions and in the Fraunhofer approximation, the directional spectrum of light does not change on propagation in free space, and that each frequency component of the total spectrum is preserved in accordance with the principle of energy conservation. It is demonstrated, and illustrated by examples, that descriptions of diffraction by the theory of partial coherence and by classical wave optics are fully equivalent for incoherent primary sources. A statistical approach is essential, and coherence theory is required, for partially coherent primary sources.

Key words: classical optics; coherence theory; conservation of energy; correlation-induced spectral changes; diffraction; interference; propagation of light; radiometry; spectral invariance; spectral preservation; spectroscopy; Wolf shifts.

Accepted: March 3, 1993

1. Introduction

"The number of different optical phenomena has become in our time so great that caution must be taken so as to avoid being deceived, and also to refer the phenomena always to the simple laws. This is more necessary in the case of diffraction, as we shall see, than in all the other phenomena." This quote appeared in a classical memoir, "New Modification of Light by the Mutual Influence and the Diffraction of the Rays," which Fraunhofer published in 1821 [1]. It is still apropos today, as new issues concerning the modification of spectra by diffraction have arisen in the recent past.

In a paper published in 1986, Wolf [2] raised the interesting question "whether the normalized spectrum of light remains unchanged on propagation through free space." He considered this to be the case when the spectrum from a partially coherent source is emitted isotropically. He coined the term "invariance of the spectrum of light on propagation" to describe this isotropic propagation of a spectrum and noted that obviously there exist sources whose spectra are not emitted isotropically. The spectral properties of such sources have subsequently become known as "correlation-induced spectral modifications" or "Wolf shifts." In this context, the word "source" denotes either a "primary" (physical) source of radiation, or a "secondary" source such as a diffracting aperture.

Wolf has emphasized that he was concerned with physical mechanisms that produce spectral modifications of a still unknown nature. For example, in Ref. [2] he mentioned astrophysical measurements and posed the question "whether source correlations may perhaps not give rise to differences

between the spectrum of the emitted light and the spectrum of the detected light that originates in some stellar sources." In Ref. [3] he considered non-cosmological source correlations which "must clearly be manifestations of some cooperative phenomena. At the atomic level possible candidates may perhaps be superradiance and superfluorescence."

Wolf's papers prompted a large number of publications by himself and others on the subject of correlation-induced modifications. Regrettably, this literature includes papers which have led to misinterpretations of the physical nature of Wolf shifts. For the most part, these papers analyzed classical diffraction and interference experiments with incoherent sources within the context of coherence theory. It is likely that they were merely intended to convey illustrations of correlation-induced modifications, but nonetheless they have raised questions concerning the similarity and differences between statistical optics and classical wave optics. The present paper attempts to clarify these issues insofar as laboratory applications of optical theories are concerned.

2. Outline

There are three major questions that have been raised with respect to Wolf shifts encountered in the laboratory.

Does the spectrum of partially coherent light change on propagation in free space, and are such changes consistent with the principle of energy conservation? This question arises from repeated statements, e.g., Refs. [3–7] that the spectrum of light is not invariant on free-space propagation. For example: "It has been demonstrated in the last few years, both theoretically and experimentally that, in general, the spectrum of light generated by a partially coherent source changes on propagation, even in free space" [5]. The experiments cited here did not pertain to free-space propagation in a literal sense but were diffraction [8–10] or interference [11] experiments in which the spectra observed in different directions were found to be different, as might be expected in such experiments. In Sec. 4 of this paper, we address the issue of energy conservation from the point of view that "free-space propagation" means the unimpeded propagation of light outside of sources and in the absence of absorption, photoluminescence and similar mechanisms that can destroy or create spectral components. Diffraction at clear apertures is not regarded as free-space propagation, since apertures impede incident wave fronts by truncating them. The word "spectrum" is interpreted as the functional form of the spectral concentrations of measurable radiant quantities. We distinguish between "directional spectra" which are observed in a given direction, and "total spectra" which are obtained by (physical or mathematical) integrations of spectral radiant quantities over a specified space domain. A directional spectrum is considered "unchanged" if the relative spectral distribution of the pertinent spectral concentration does not change along the path of a ray. A total spectrum is considered "preserved" if it does not change within the boundaries of the specified domain. Our conclusion will be that coherence theory does *not* predict spectral modifications of directional spectra due to the free-space propagation of light in normal laboratory situations, and that total spectra obey the energy principle for each spectral component separately.

Do the theory of partial coherence and the classical Huyghens-Fresnel-Kirchhoff diffraction theory give different results in situations that involve incoherent physical sources? Which of them should be applied for solutions of practical problems? These questions arise from publications in which Fraunhofer diffraction [12] and Young's interference experiment [13,14] were reexamined by coherence theory for incoherent primary sources. The findings of these publications were consistent with classical results, but were presented in a manner so highly abstract that they could be mistaken as manifestations of hitherto unknown phenomena. In Sec. 5 of this paper, we will demonstrate that the theory of partial coherence and the Huyghens-Fresnel-Kirchhoff theory give identical results in the case of an incoherent primary source. We will emphasize that coherence theory is required if the primary source is partially coherent.

Are traditional radiometric practices afflicted by previously unknown errors due to the partial coherence of light? One of the above-mentioned papers [9] reported experimental results that conflicted with classical diffraction theory for incoherent primary sources such as those used, but was repeatedly cited [6,9,12] as evidence that radiometric measurements by national standardizing laboratories may be in error due to a lack of consideration of Wolf shifts. For example: "... the large scatter which exists in the spectroradiometry scales maintained by different national laboratories has up to now not been satisfactorily explained. ... The spectrum of the transmitted radiation undergoes fre-

quency shifts ... which were not taken into account in specifying the spectroradiometric scales" [6]. Nugent and Gardner [15] have since shown that, for an incoherent source and an optical system consisting of a series of thin apertures and lenses, diffraction is the only physical effect that can introduce spectral changes, and that diffraction effects are too small to be a significant source of error in spectroradiometric calibrations. As their paper has effectively addressed the issue of calibration errors, this question will not be pursued further in this paper except within the context of an example given in Sec. 5.2. However, most of the conclusions of the paper are pertinent to optical radiometry with partially coherent physical sources.

In Sec. 3, we define relevant terms which could otherwise be misunderstood or interpreted differently. Section 6 contains concluding remarks.

3. Definitions

To avoid the risk of misunderstandings due to poorly defined nomenclature, the most important terms and symbols used in this paper are summarized in the following. For a more detailed explanation of these terms, the reader is referred to pertinent review articles [16–19] and textbooks [20–22]. The following symbols will be used (see Figs. 1, 3, 5):

t denotes time, τ is a time delay, c is the speed of light in vacuum, λ is the wavelength, $\omega = 2\pi c/\lambda$ is the circular frequency, and $k = 2\pi/\lambda = \omega/c$ is the circular wavenumber of the light;

P and Q are points in space, $\boldsymbol{P}$ and $\boldsymbol{Q}$ are their position vectors with respect to the origin of a coordinate system, $d\boldsymbol{P}$ and $d\boldsymbol{Q}$ are area elements at these points, PQ is the distance and $\boldsymbol{PQ}$ is the vector from P to Q, $\boldsymbol{n}$ is a surface normal and $(\boldsymbol{n},\boldsymbol{PQ})$ is the angle enclosed by this normal and the vector $\boldsymbol{PQ}$.

Additional symbols will be introduced as needed. Lightface type is used for scalar quantities, and boldface for vectors and area elements. Multiple integral signs are avoided where possible so that, for example, $\int d\boldsymbol{P}\, d\boldsymbol{Q}$ ... denotes a four-fold integral.

The basic quantities of coherence theory used in this paper are the "mutual coherence function" $\Gamma(P_1,P_2,\tau)$ of two points in an optical radiation field (the point P_1 being considered at a time τ later than the point P_2) and its Fourier transform, the "cross-spectral density" $W(P_1,P_2,\omega)$:

$$\Gamma(P_1,P_2,\tau) = \langle V(P_1,t+\tau)V^*(P_2,t)\rangle$$

$$= \int d\omega\, e^{-i\omega\tau} W(P_1,P_2,\omega), \quad (1)$$

$$W(P_1,P_2,\omega) = (1/2\pi)\int d\tau\, e^{i\omega\tau}\Gamma(P_1,P_2,\tau), \quad (2)$$

where $V(P_i,t)$ is the complex wave amplitude (as defined in coherence theory) of the radiation field at the space-time point $(P_i,t)V^*$ is the complex conjugate, and $\langle ... \rangle$ denotes a finite power signal or an ergodic ensemble average. The cross-spectral density $W(P_1,P_2,\omega)$ has no negative-frequency components.

The following special forms of these functions are required for physical interpretations of theoretical results: The radiant flux density at a surface element $d\boldsymbol{P}_\perp$ perpendicular to the direction of light propagation at the point P,

$$E(P) = \Gamma(P,P,0) = d\Phi/d\boldsymbol{P}_\perp [\mathrm{N/m^2}], \quad (3)$$

and the spectral radiant flux density (spectral concentration of $E_\omega(P)$ with respect to frequency) at P,

$$E_\omega(P) = W(P,P,\omega) = d^2\Phi/(d\boldsymbol{P}_\perp d\omega)$$

$$= d\Phi_\omega/d\boldsymbol{P}_\perp [\mathrm{N/m^2/Hz}], \quad (4)$$

where Φ is the radiant flux, and $d\Phi_\omega$ is the spectral radiant flux incident on $d\mathbf{P}_\perp$. Radiant flux, radiant flux density, and spectral radiant flux density are often called "energy flux," "optical intensity" and "spectral power density," and are denoted by different symbols in theoretical optics. In this paper, the terms and symbols recommended in the *International Lighting Vocabulary* [23] will be used.

Spectral concentrations with respect to frequency, wavelength, etc., are denoted by subscripts, ω, λ, etc., and are also referred to by the adjective "spectral." The term "normalized spectrum" introduced by Wolf [2] refers to the spectral concentration of a radiant quantity divided by that quantity itself, so that the ratio Φ_ω/Φ represents the normalized frequency spectrum of radiant flux. This normalization appears to have no effect on the topics discussed in this paper.

The quantities defined by Eqs. (1) through (4) are often evaluated in a "far-field" approximation. In most papers on coherence this appears to be the Fraunhofer approximation of classical diffraction theory. To avoid confusion, we will specify all approximations made in this paper.

4. Free-Space Propagation of Cross-Spectral Density. Spectral Preservation

The propagation of cross-spectral density in free space is governed by two Helmholtz equations,

$$(\Delta_i + k^2)W(P_1,P_2,\omega) = 0, \quad i = 1,2, \tag{5}$$

which can be solved by means of Green functions in a manner analogous to that used in Kirchhoff's diffraction theory. According to Parrent [24], the general solution for the cross-spectral density at two space points P_1 and P_2, due to a plane polychromatic source, is

$$W(P_1,P_2,\omega) = 1/(2\pi)^2 \int d\mathbf{Q}_1 d\mathbf{Q}_2$$
$$\times \cos(\mathbf{n},\mathbf{Q}_1P_1)\cos(\mathbf{n},\mathbf{Q}_2P_2)$$
$$\times [(1 - ikQ_1P_1)(1 + ikQ_2P_2)/(Q_1P_1\, Q_2P_2)^2]$$
$$\times W(Q_1,Q_2,\omega)\exp[ik(Q_1P_1 - Q_2P_2)], \tag{6}$$

where Q_1 and Q_2 are two points inside the source domain and the other symbols are explained in Fig. 1. This equation is usually simplified by making two geometrical assumptions:

1. The distances Q_1P_1 and Q_2P_2 are large compared to the wavelength λ, so that

$$(1 - ikQ_1P_1)(1 + ikQ_2P_2)/(Q_1P_1\, Q_2P_2)^2$$
$$\sim k^2/(Q_1P_1\, Q_2P_2). \tag{7}$$

2. The angles $(\mathbf{n},\mathbf{Q}_1P_1)$ and $(\mathbf{n},\mathbf{Q}_2P_2)$ and the factor $1/(Q_1P_1\, Q_2P_2)$ do not vary appreciably within the source domain and are approximated by their values at the source center, so that

$$\cos(\mathbf{n},\mathbf{Q}_1P_1)\cos(\mathbf{n},\mathbf{Q}_2P_2)/(Q_1P_1\, Q_2P_2)$$
$$\sim \cos\theta_1\cos\theta_2/(r_1r_2). \tag{8}$$

This gives

$$W(P_1,P_2,\omega) = (\cos\theta_1\cos\theta_2)/(\lambda^2 r_1 r_2)$$
$$\times \int d\mathbf{Q}_1 d\mathbf{Q}_2\, W(Q_1,Q_2,\omega)\exp[ik(Q_1P_1 - Q_2P_2)]. \tag{9}$$

In the Fraunhofer approximation, the distances Q_1P_1 and Q_2P_2 in the argument of the exponential function are expressed by

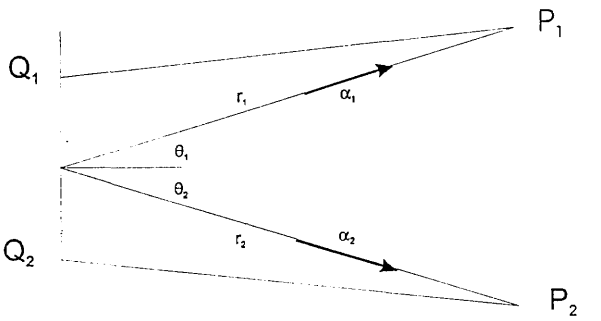

Fig. 1. Notation pertaining to free-space propagation of cross-spectral density. The points and light paths shown are not coplanar.

$$(Q_iP_i)^2 = (r_i\boldsymbol{\alpha}_i - \boldsymbol{Q}_i)^2, \quad Q_iP_i \sim r_i - \boldsymbol{\alpha}_i\cdot\boldsymbol{Q}_i. \tag{10}$$

Hence the spectral radiant flux $d\Phi_\omega$ defined by Eq. (4) may be evaluated by substituting $P_1 = P_2 = P$, $r_1 = r_2 = r$, $\theta_1 = \theta_2 = \theta$, and $\boldsymbol{\alpha}_1 = \boldsymbol{\alpha}_2 = \boldsymbol{\alpha}$ into Eq. (9). Thus,

$$d\Phi_\omega = d\boldsymbol{P}_\perp\, W(P,P,\omega) \sim \cos^2\theta\, \sin\theta\, d\theta\, d\phi$$
$$\times \int d\mathbf{Q}_1 d\mathbf{Q}_2\, W(Q_1,Q_2,\omega)\exp[-ik\boldsymbol{\alpha}\cdot(\boldsymbol{Q}_1 - \boldsymbol{Q}_2)], \tag{11}$$

where $d\boldsymbol{P}_\perp = r^2\sin\theta\, d\theta\, d\phi$, and $\boldsymbol{\alpha} = (\cos\phi\sin\theta, \sin\phi\sin\theta, \cos\theta)$ is the unit vector in the direction of light propagation at P. This shows that $d\Phi_\omega$ depends only on the angular position of the point of observation P, not on its distance from the source. Therefore, the directional radiant flux spectrum does not change on propagation in free space.

The total radiant flux spectrum emitted by the source into the positive hemisphere is obtained by integrating Eq. (11) over all directions: $0 \leq \theta \leq \pi/2$ and $0 \leq \phi \leq 2\pi$. Introducing sum and difference coordinates in the source plane,

$$\boldsymbol{Q}_+ = \tfrac{1}{2}(\boldsymbol{Q}_1 + \boldsymbol{Q}_2), \quad \boldsymbol{Q}_- = \boldsymbol{Q}_1 - \boldsymbol{Q}_2, \tag{12}$$

and reversing the order of integrations, we find

$$\Phi_\omega = \int d\Phi_\omega \sim \int d\boldsymbol{Q}_+ \{\int d\boldsymbol{Q}_-\, W(\boldsymbol{Q}_+ + \tfrac{1}{2}\boldsymbol{Q}_-, \boldsymbol{Q}_+ - \tfrac{1}{2}\boldsymbol{Q}_-, \omega)$$
$$\times \int d\theta \sin\theta\cos^2\theta \int d\phi\, \exp(-ik\boldsymbol{\alpha}\cdot\boldsymbol{Q}_-)\}. \tag{13}$$

The triple integral in curled brackets that appears in this expression depends on $\boldsymbol{Q}_+$ only. Therefore, Eq. (13) shows that the radiant flux spectrum, integrated over all directions, is equal to a single integral over the source plane. This implies preservation of the spectrum, as defined in Sec. 2. Equation (13) can be brought into a form more familiar to radiometrists,

$$\Phi_\omega = \int dQ_+ M_\omega(Q_+), \quad (14)$$

by defining

$$M_\omega(Q_+) = \{...\} = (2\pi/\lambda^2)\int dQ_- \times W(Q_+ + \tfrac{1}{2}Q_-, Q_+ - \tfrac{1}{2}Q_-, \omega) j_1(k|Q_-|)/(k|Q_-|) \quad (15)$$

as the "generalized spectral radiant exitance" of the source. Equation (15), where j_1 is the spherical Bessel function of the first kind and order, was derived by Marchand and Wolf [16].

Equations (11) and (13) constitute the laws of energy conservation, in the Fraunhofer approximation, for the free-space propagation of light from a planar source of any coherence. Equation (11) states that the directional spectrum does not change on propagation in free-space. Equation (13) states that energy is conserved for each spectral component separately. If the light propagation is anisotropic, the directional radiant flux spectrum will generally differ from the radiant exitance spectrum, but spectral components missing in any one direction of propagation will be present in other directions. This is reminiscent of Newton's famous *experimentum crucis* depicted in Fig. 2, which proved that the colors dispersed by one prism can be recombined by another. It is not difficult to imagine similar ways of recovering a source spectrum that propagates anisotropically. For example, if the "source" is a diffracting aperture illuminated by an incoherent physical source, then, the diffracted light will be spectrally anisotropic. It can, however, be collected by an integrating sphere so that under idealized conditions the spectral radiant exitance of the exit port of the sphere will be an exact duplicate of the spectral radiant exitance of the physical source. Under these circumstances, the total spectrum has been "preserved."

Wolf [2] expressed the belief that the tacit assumption of isotropy of spectral emission is "implicit in all of spectroscopy [but] does not appear to have been previously questioned because with light from traditional sources one has never encountered any problems with it." A different point of view is adopted in this paper. The isotropic propagation of a source spectrum may perhaps be an assumption dictated by necessity in astrophysical observations when it is not possible to study the light from stellar objects in different directions. However, this assumption would hardly be made tacitly by experienced spectrometrists dealing with man-made sources. There are probably no laboratory sources at all that emit strictly isotropic radiation. Physical realizations of blackbody sources incorporate apertures that diffract the isotropic thermal radiation generated inside the blackbody cavity, before it emerges into free space. The Planckian emission of metal-strip or coil lamps is modified by the spectral emissivity of the metal, which depends on wavelength as well as direction and can therefore cause spectrally dependent anisotropies. Additionally the finite size of the emitting strip or coil introduces diffraction and polarization effects, and coil lamps exhibit shadowing effects that cause a directionality of emission. In absorption spectrometry, spectral anisotropy can arise from the dichroism or pleochroism of samples. In photoluminescence spectrometry, the spectral anisotropy of polarized samples is a commonly known phenomenon. Accordingly, carefully performed spectrometric experiments usually involve a "mapping" of the radiation emitted or transmitted by sources and samples. That is, directional and spectral scans are performed to assess the magnitude of departures from the idealized case of angular and spectral isotropy. The tacit assumption that is made when such measurements are performed is, not that the spectrum is invariant in the sense defined by Wolf, but that it is preserved in the sense of Eq. (13).

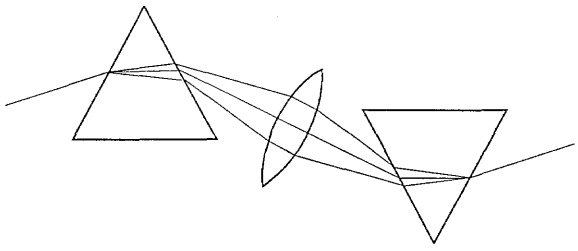

Fig. 2. Newton's *experimentum crucis* on spectral preservation.

Wolf and Gamliel [7] have cited an equation similar to Eq. (14) and, likewise, considered it to be a manifestation of energy conservation for each frequency component. However, they asserted that "there is no contradiction with the energy conservation law when the normalized spectrum changes on propagation." Their argument appears to be that generalized source quantities such as the spectral radiant exitance of Eq. (15) are defined in terms of the Fraunhofer approximation of the cross-spectral density $W(P_1,P_2,\omega)$, and that this approximation is not valid in the source plane. This is true. The evaluation of diffraction integrals in close proximity to a physical source is difficult and has been attempted only in special cases. For example,

Agrawal and Gamliel [4] have presented theoretical results for the paraxial propagation of partially coherent light at distances on the order of a few hundred wavelengths from a planar source. In one case considered they found that the spectrum, viewed at a fixed angle, first shifts towards the blue and then towards the red as the propagation distance increases. It is not within the purview of this paper to discuss these findings; the authors used a different mathematical approach and did not quantify the accuracy of their calculations. On the other hand, it should be noted that laboratory determinations of source parameters always involve measurements made at a distance. To determine the spectral radiant exitance of Eq. (15), a spectroradiometer would be used to measure the spectral radiant flux of Eq. (11) for specified geometrical conditions, and often the measurement would be performed under conditions that justify the Fraunhofer approximation. Thus, Eqs. (13) and (15) may suffice to demonstrate the invariance of light propagation in free space and spectral preservation under normal laboratory conditions. Because of various approximations made in deriving propagation equations such as Eq. (6), it may not even be possible at all to rigorously "prove" energy conservation. On the other hand, it seems safe to presume that conservation of energy, if not assumed explicitly in coherence theory, is implicit in the electromagnetic theory underlying it. The Helmholtz equations [Eq. (5)] apply to individual frequencies, and thus appear to imply that spectra do not change on free-space propagation and are preserved.

5. Similarities and Differences Between Coherence Theory and Classical Wave Optics

5.1 Propagation of Cross Spectral Density and the Huyghens-Fresnel-Kirchhoff Principle

Turning to the question how spectral modifications due to partial coherence differ from classical diffraction and interference effects, we note that the Helmholtz equations [Eq. (5)] for the free-space propagation of cross-spectral density were derived from the corresponding Helmholtz equation for classical wave amplitudes [24]. This suggests that Eq. (6) is, in fact, a straightforward generalization of classical diffraction theory.

There is, however, a practical difference in that Eq. (6) traces the propagation of cross-spectral density only from one pair of points to another, while the classical Huyghens-Fresnel-Kirchhoff diffraction integral traces the propagation of wave amplitudes from a source to an aperture and on to a point of observation in one sweep (Fig. 3). In order to eliminate this difference, we can apply Eq. (6) twice; first, from a pair of source points (P_1,P_2) to a pair of points (Q_1,Q_2) in the aperture plane,

$$W(Q_1,Q_2,\omega)=(\cos\theta_1\cos\theta_2)/(\lambda^2 r_1 r_2)$$

$$\times\int dP_1 dP_2\, W(P_1,P_2,\omega)\exp[ik(P_1Q_1-P_2Q_2)]; \quad (16)$$

and then from (Q_1,Q_2) to a pair of points (P'_1,P'_2) in the diffracted wave field,

$$W(P'_1,P'_2,\omega)=(\cos\theta'_1\cos\theta'_2)/(\lambda^2 r'_1 r'_2)\times$$

$$\int dQ_1 dQ_2\, W(Q_1,Q_2,\omega)\times\exp[ik(Q_1P'_1-Q_2P'_2)]. \quad (17)$$

Substituting the first equation into the second, we find

$$W(P'_1,P'_2,\omega)=(1/\lambda^4)(\cos\theta'_1\cos\theta'_2/r'_1 r'_2)$$

$$\times\int dP_1 dP_2(\cos\theta_1\cos\theta_2/r_1 r_2)\, W(P_1,P_2,\omega)$$

$$\times\int dQ_1 dQ_2\exp[ik(P_1Q_1+Q_1P'_1-P_2Q_2-Q_2P'_2)]. \quad (18)$$

Therefore, from Eq. (4) for $P'_1=P'_2=P'$, $r'_1=r'_2=r'$, $\theta'_1=\theta'_2=\theta'$,

$$E_\omega(P')=W(P',P',\omega)=(1/\lambda^4)(\cos^2\theta'/r'^2)$$

$$\times\int dP_1 dP_2(\cos\theta_1\cos\theta_2/r_1 r_2)\, W(P_1,P_2,\omega)$$

$$\times\int dQ_1 dQ_2\exp[ik(P_1Q_1+Q_1P'-P_2Q_2-Q_2P')]. \quad (19)$$

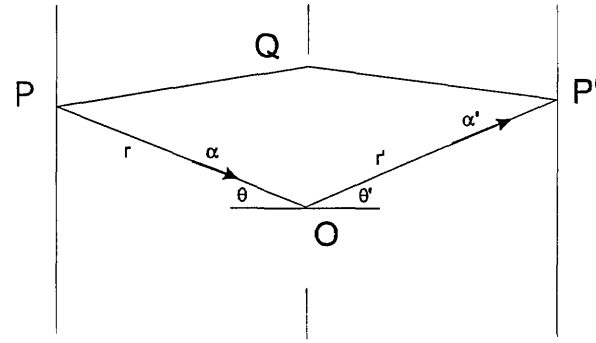

Fig. 3. Notation pertaining to diffraction at an aperture. The points and light paths shown are not coplanar. The points P, Q, and P' represent either of the points P_i, Q_i, and P'_i mentioned in Sec. 5.1.

These equations are valid in the geometrical approximations of Eqs. (7) and (8), without approximations made with respect to the argument of the exponential functions in the integrands.

If the primary source is planar and incoherent, Eq. (19) can be simplified further by expressing the cross-spectral density inside the first integral by an expression given by Marchand and Wolf [16],

$$W(P_1,P_2,\omega)=(\lambda^2/\cos\theta_1)\,L_\omega(P_1,\alpha)\,\delta(P_2-P_1), \quad (20)$$

where $L_\omega(P_1,\alpha)$ is the spectral radiance at the source point P_1 and in a direction α, and δ is a delta function. Letting $P_1=P$, $r_1=r$, $\theta_1=\theta$, we obtain

$$E_\omega(P'_1)=(1/\lambda^2)(\cos^2\theta'/r'^2)\int(\mathrm{d}P\cos\theta/r^2)\,L_\omega(P,\alpha)$$

$$\times\int\mathrm{d}Q_1\mathrm{d}Q_2\exp[ik(PQ_1+Q_1P'-PQ_2-Q_2P')]$$

$$=(1/\lambda^2)(\cos^2\theta'/r'^2)\int\mathrm{d}\Omega\,L_\omega(P,\alpha)\Big|$$

$$\times\int\mathrm{d}Q\exp[ik(PQ+QP)]\Big|^2, \quad (21)$$

where $\mathrm{d}\Omega$ is the solid angle element subtended at the aperture center O by a source area element at P, and α is the unit vector in the direction PO.

Since Eq. (21) can be recognized as the classical Huyghens-Fresnel-Kirchhoff diffraction formula for an extended incoherent source, we may conclude:

> Classical optics and the theory of partial coherence give precisely the same results when applied to diffraction problems that involve an incoherent primary source. It is immaterial which approach is used in practice. Laboratory physicists appear to prefer the Huyghens-Fresnel-Kirchhoff formula, perhaps because they are more familiar with it or because the partial coherence of the radiation incident upon the aperture is already built into the formula. Coherence theorists apparently prefer to think of apertures as secondary sources, and use the van Cittert-Zernicke theorem to describe their coherence properties. The results are the same.
>
> Classical diffraction theory is not applicable if the primary source is partially coherent. In this case, a statistical treatment is required and coherence theory must be used. Simple optical systems, such as a single aperture or lens, can be analyzed by single formulae such as Eqs. (18) and (19). However, for more complicated systems involving multiple apertures or lenses, a stepwise approach may be more practicable because multiple combinations of Eq. (6) quickly lead to unwieldy expressions.

It should be noted that the equations of this section no longer describe the free-space propagation of light and, therefore, no longer imply spectral preservation. There are two cases to be distinguished when light is diffracted at an aperture:

1. If the incident light is spectrally isotropic, the spectral concentration of radiant flux will be uniform inside the aperture and the total spectrum of the diffracted light will differ from the total source spectrum only by a constant (frequency-independent) factor. The *relative* ("normalized") source spectrum will be preserved.
2. If the incident is spectrally anisotropic, the truncation of wavefronts at the aperture will be spectrally selective. The total spectrum of the diffracted light will be different from the source spectrum by a frequency-dependent factor. The *absolute* and *relative* source spectra will *not* be preserved.

These cases occur irrespective of the state of coherence of the primary physical source. Because spectral isotropy has generally been attributed to incoherent sources only, an important result of Wolf's original paper [2] is that he has postulated the existence of partially coherent isotropic sources whose relative spectra will also be preserved upon diffraction, and that he has rigorously defined the properties of such sources. This is likely to have a significant impact on laboratory spectrometry. For example, the development of new imaging devices [8,11] which obey the conditions formulated by Wolf may be expected to reduce diffraction errors in optical radiometry.

5.2 Example: Axial Diffraction Loss Due to a Circular Aperture

The first assertion that "the large scatter found in the intercomparison of spectroradiometric scales is attributed to the spectral shifts" may be found in the above-referenced paper by Kandpal, Vaisha, and Joshi [9]. These authors stated that "apertures make the incoherent light partially coherent and a source correlation is introduced which along with the optics involved violates certain scaling law thereby modifying the spectral distribution of the source in the far zone."

Diffraction errors in radiometry are, of course, well understood [25–34] by laboratory physicists.

The phenomenological interpretation of these errors is that, on account of the scale factor $1/\lambda^2$ in the Huyghens-Fresnel diffraction integral Eq. (21), the different spectral components of light incident on an aperture are diffracted differently. If observations are made on axis the spectral radiant flux will be found to be "blue-shifted," because diffraction at an aperture spreads red light farther into the off-axis region than blue light (Fig. 4). For a circular aperture illuminated by a point source this is described, in the Fraunhofer approximation, by the Airy diffraction formula found in textbooks of optics. By reciprocity, the same treatment applies for an extended, incoherent circular source and a point detector on axis [26]. The result is a classical formula which was originally derived by Rayleigh [35],

$$\epsilon(0)=J_0^2(kaw)+J_1^2(kaw), \tag{22}$$

where $\epsilon(0)$ is the axial diffraction loss, J_0 and J_1 are Bessel functions of the first kind, a is the radius of the aperture, and w is the angular radius of the source.

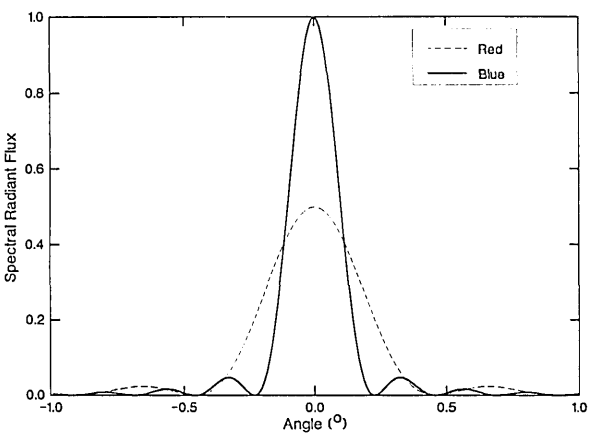

Fig. 4. Diffraction patterns for red and blue light.

Foley [12] used the theory of partial coherence to derive the same result in a different form,

$$S(z,\omega)=(af/a_s z)^2\, S^{(0)}(\omega)\,\{1-J_0^2[3.832a/L(\omega)] -J_1^2[3.832a/L(\omega)]\}, \tag{23}$$

where $S(z,\omega)$ is the axial "spectrum" observed at a distance z from the aperture, a and a_s are the respective radii of the aperture and source, f is the focal length of a lens illuminating the aperture, $S^{(0)}(\omega)$ is the "source spectrum" and $L(\omega)=3.832f/ka_s$. Foley's explanation of Eq. (23) was "that the spectrum of the light at an on-axis observation point in the far zone differs from the spectrum in the aperture by a simple geometrical factor and a frequency dependent factor ... that depends only on the ratio ... of the aperture to the effective correlation length of the light in the aperture at frequency ω. Hence the difference between the spectrum of the light at an on-axis observation point in the far zone and the spectrum of the light in the aperture is determined by whether the light in the aperture is effectively spatially coherent over it, i.e. whether the light in the aperture is globally coherent."

Apart from confirming that classical optics and coherence theory give identical results for incoherent sources such as assumed here, this example also points to a communications gap between laboratory physicists and coherence theorists. The word "diffraction" is not mentioned once in the Kandpal, Vaisha and Joshi and Foley papers. It is hoped that the above discussion will help bridge this gap.

5.3 Example: Spectral Changes Produced in Young's Interference Experiment

In a paper referenced above, James and Wolf [13] considered the optical setup depicted in Fig. 5, in which an incoherent, plane, polychromatic source with angular radius $\alpha=R/a$ is used to illuminate a screen containing two circular pinholes of area A which are located at distances $\pm d/2$ from the source normal. The source and pinhole planes are parallel to one another, are separated by a distance which is large enough to justify the Fraunhofer approximation, and the interference effect is observed at a similarly large distance from the aperture. The point of observation P_0 is located on axis and at equal distances r from the two pinholes, so that "colour effects, which are usually produced in interference experiments with broadband light, are absent." James and Wolf found the following expression for the spectrum observed at P_0,

$$S(P_0,\omega)=2\,S^{(i)}(\omega)\,(A/2\pi cr)^2\,\omega^2\,[1+2J_1(\omega\alpha d/c)/(\omega\alpha d/c)]. \tag{24}$$

The conclusion of their paper was that the spectral effects produced by the experiment are two-fold: a blueshift due to diffraction which is described by the factor ω^2 in Eq. (24), and a redshift due to the finite size of the source which is described by the Bessel function in the same equation.

James and Wolf expected an achromatic fringe in the center of the interference pattern. Quite the opposite is true. The central blueshift due to diffraction is to be expected for the same reason as previously illustrated in Fig. 4. It represents a classical phenomenon which is described by the $1/\lambda^2$ scale factor of the Huyghens-Fresnel-Kirchhoff diffraction formula Eq. (21).

The central redshift due to the finite size of the source can likewise be explained by classical reasoning. In the notation of Fig. 5, the contribution of a source point Q to the interference pattern at P_0 is given by $[1+\cos(\omega\Delta/c)]\ \mathrm{d}Q$, where $\Delta=(QS_2+S_2P_0)-(QS_1+S_1P_0)=QS_2-QS_1$ is the path difference of the interfering light. Referred to polar coordinates with the origin at the center O of the pinhole screen, we have $Q=(\rho\cos\chi,\rho\sin\chi, -a)$, $S_{1,2}=(\pm d/2,\ O,\ O)$, $(QS_1)^2-(QS_2)^2=2\rho d\cos\chi$, $QS_1+QS_2\sim 2a$, so that

$$\Delta=[(QS_1)^2-(QS_2)^2]/(QS_1+QS_2)\sim(\rho\mathrm{d}/a)\cos\chi. \quad (25)$$

Hence, the spectral radiant flux produced at P_0 by the source as a whole will be proportional to

$$\int\rho\mathrm{d}\rho\int d\chi\{1+\cos[(\omega\rho d/c)\cos\chi]\}$$

$$=2\pi\int\rho\mathrm{d}\rho[1+J_0(\omega\rho d/ac)]$$

$$=\pi R^2[1+2J_1(\omega\alpha d/c)/(\omega\alpha d/c)], \quad (26)$$

which is in agreement with Eq. (24). The physical interpretation of the redshift is that each point of the primary source produces its own interference pattern, the width of the fringes increasing with wavelength so that the outer portions of the source contribute more red than blue light to the central fringe.

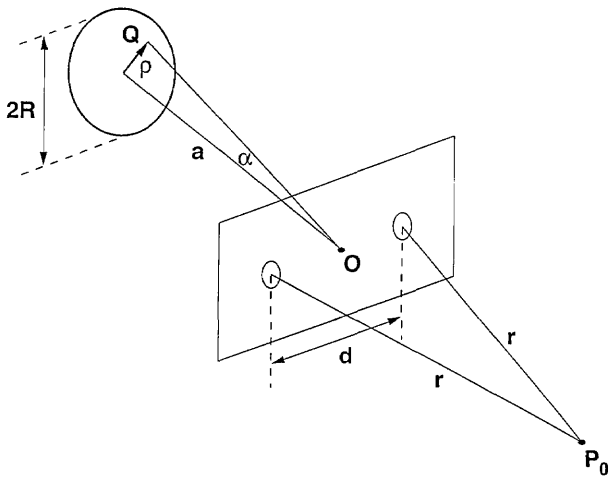

Fig. 5. Young's interference experiment.

In a subsequent paper [14], James and Wolf considered the off-axial spectral effects produced by Young's experiment in a paraxial approximation. They obtained, instead of Eq. (24),

$$S(x,\omega)=2S^{(i)}(\omega)\,(A/2\pi cr)^2\,\omega^2$$

$$\times\{1+2|J_1(\omega\alpha d/c)/(\omega\alpha d/c)|\cos(\beta+\omega xd/rc)\}, \quad (27)$$

where x is the lateral distance of the point of observation from the central point P_0, and $\beta=0$ or π according to whether $J_1(...)$ is positive or negative. James and Wolf stated that they were dealing with "new aspects" of Young's experiment.

Since an incoherent primary source was assumed, the spectral modifications described by Eq. (24) are classical effects. They were first investigated by Fraunhofer [1] and are explained in textbooks, including those by Jenkins and White [36] and Strong [37]. Briefly stated, although white-light interference may not be visible to the unassisted eye, it still takes place in Young's experiment and can be observed with a spectroscope. The spectroscope reveals "channeled spectra" in the form of dark bands in the neighborhood of wavelengths for which destructive interference takes place, and enhanced colors near wavelengths that interfere constructively. This is shown in the various figures of Ref. [14], and also by colored drawings in the 1897 edition of Müller-Pouillet's "Lehrbuch" [38]. Nonetheless, the elucidation of channeled spectra by coherence theory is interesting and offers a novel point of view.

6. Concluding Remarks

We have attempted to reconcile conflicting points of view of laboratory physicists and coherence theorists on correlation-induced spectral changes arising from the partial coherence of primary and secondary light sources. We have shown that, under normal laboratory conditions and in the Fraunhofer approximation, the directional spectrum of light does not change on propagation in free space and that the total spectrum is preserved in accordance with the principle of energy conservation. We have demonstrated that descriptions of spectral phenomena by the theory of partial coherence and by classical wave optics theory are fully equivalent for incoherent primary sources. We have emphasized that a statistical approach is essential, and coherence theory is required, for partially coherent primary sources.

We have also pointed out that the theoretical description of light propagation in the proximity of sources is, by and large, still an unsolved problem. Most publications on partial coherence (this one included) use the Fraunhofer approximation, whereas optical radiometry often requires at least the Fresnel approximation. Theorists could make valuable contributions to optical radiometry by turning to this issue.

The essence of Wolf's original paper [2] on correlation-induced spectral changes should not be misconstrued as a contradiction or modification of the classical wave theory of incoherent physical sources. Rather, it should be regarded as a generalization and extension of classical optics that allows the description of phenomena arising from the properties of existing or newly developed partially coherent sources. Wolf's formulation of the conditions under which the spectrum of a partially coherent source is propagated isotropically may lead to the development of new imaging devices that could reduce the magnitude of diffraction errors in optical radiometry.

Acknowledgments

The author is grateful for constructive suggestions and comments on an earlier version of this manuscript by Professor Emil Wolf (University of Rochester, Rochester, NY), Dr. John B. Shumaker (retired from NIST), Dr. William R. Blevin (CSIRO Division of Applied Physics, Linfield NSW, Australia), Dr. L. P. Boivin (NRC/CNRC, Ottawa, Canada), and Dr. Albert C. Parr (NIST). It is also a privilege to acknowledge help and advice received from Dr. Christopher L. Cromer, Dr. B. Carol Johnson, and Mr. R. D. Saunders, Jr. (all of NIST).

7. References

[1] J. von Fraunhofer, Denkschr. kgl. Akad. Wiss. München 1821/22. (Translated in The Wave Theory of Light and Spectra, Sec. 2, Arno Press (1981) p. 14.)
[2] E. Wolf, Phys. Rev. Lett. **56**, 1370 (1986).
[3] E. Wolf, Nature **326**, 363 (1987).
[4] G. P. Agrawal and A. Gamliel, Optics Comm. **78**, 1 (1990).
[5] E. Wolf and J. R. Fienup, Optics Comm. **82**, 209 (1991).
[6] E. Wolf, Trends in International Optics, J. W. Goodman, ed., Academic Press (1991) pp. 221–223.
[7] E. Wolf and A. Gamliel, J. Mod. Optics **39**, 927 (1992).
[8] G. M. Morris and D. Faklis, Optics Comm. **62**, 5 (1987).
[9] H. C. Kandpal, J. S. Vaishya, and K. C. Joshi, Optics Comm. **73**, 169 (1989).
[10] G. Indebetouw, J. Mod. Optics **36**, 251 (1989).
[11] F. Gori, G. Guattari, C. Palma, and C. Pandovani, Optics Comm. **67**, 1 (1988).
[12] J. T. Foley, Optics Comm. **75**, 347 (1990).
[13] D. F. V. James and E. Wolf, Optics Comm. **81**, 150 (1991).
[14] D. F. V. James and E. Wolf, Phys. Letters A **157**, 8 (1991).
[15] K. A. Nugent and J. L. Gardner, submitted to Metrologia Nov. 1991.
[16] E. W. Marchand and E. Wolf, J. Opt. Soc. Am. **64**, 1219 (1974).
[17] W. H. Carter and E. Wolf, J. Opt. Soc. Am. **67**, 785 (1977).
[18] E. Wolf, J. Opt. Soc. Am. **68**, 6 (1978).
[19] M. J. Beran and G. B. Parrent Jr., Theory of Partial Coherence, Prentice-Hall (1963).
[20] M. Born and E. Wolf, Principles of Optics, 4th ed., Pergamon Press (1970).
[21] J. B. Shumaker, Introduction to Coherence in Radiometry, Natl. Bur. Stand. (U.S.) Tech. Note 910-6 (1983).
[22] J. W. Goodman, Statistical Optics, Wiley & Sons (1985).
[23] International Lighting Vocabulary, 4th Ed., International Commission on Illumination/International Electrotechnical Commission (1987).
[24] G. B. Parrent Jr., J. Opt. Soc. Am. **49**, 787 (1959).
[25] J. Focke, Opt. Acta **3**, 161 (1956).
[26] W. R. Blevin, Metrologia **6**, 39 (1970).
[27] W. H. Steel, M. De, and J. Bell, J. Opt. Soc. Am. **62**, 1099 (1972).
[28] L. P. Boivin, Appl. Optics **14**, 197 (1975).
[29] L. P. Boivin, Appl. Optics **14**, 2002 (1975).
[30] L. P. Boivin, Appl. Optics **15**, 1204 (1976).
[31] L. P. Boivin, Appl. Optics **16**, 377 (1977).
[32] L. P. Boivin, Appl. Optics **17**, 3323 (1978).
[33] L. P. Boivin, Metrologia **17**, 19 (1981).
[34] L. P. Boivin, Environmental Corrections in Absolute Radiometry in Absolute Radiometry, F. Hengstberger, ed., Academic Press (1989) pp. 170–192.
[35] Lord Rayleigh, Phil. Mag. (5) **11**, 214 (1881).
[36] F. A. Jenkins and H. E. White, Fundamentals of Optics, McGraw-Hill (1957).
[37] J. Strong, Concepts of Classical Optics, Freeman & Co. (1958).
[38] Müller-Pouillet's Lehrbuch der Physik und Meteorologie, 4th Ed., Vol. 2, Part 1, L. Pfaundler, ed., F. Vieweg & Sohn (1897).

About the author: Klaus D. Mielenz is a physicist and retired Chief of the Radiometric Physics Division of NIST. The National Institute of Standards and Technology is an agency of the Technology Administration, U.S. Department of Commerce.

Volume 98, Number 2, March–April 1993
Journal of Research of the National Institute of Standards and Technology

Conference Report

ACCURACY IN POWDER DIFFRACTION II: A REPORT ON THE SECOND INTERNATIONAL CONFERENCE Gaithersburg, MD May 26–29, 1992

Report prepared by

Judith K. Stalick

Reactor Radiation Division,
National Institute of Standards and Technology,
Gaithersburg, MD 20899-0001

1. Introduction

The purpose of this conference was to assess the progress that has been made in the theory, techniques, and applications of powder diffraction data since the first highly successful symposium on Accuracy in Powder Diffraction held at NIST (then the National Bureau of Standards) in 1979, as well as to define problem areas where further work is needed. The proceedings of the first symposium, published as *Accuracy in Powder Diffraction* (NBS Special Publication 567), have been widely cited in the literature, testifying to their importance as resources for active researchers in powder diffraction. However, the 13 intervening years have seen further major advances in the practice of this technique.

This conference was organized by the Commission on Powder Diffraction of the International Union of Crystallography (IUCr), and was sponsored jointly by NIST, the IUCr, and the JCPDS–International Centre for Diffraction Data (ICDD). The meeting was attended by 177 registrants, representing 18 countries and five continents. The international program committee, chaired by R. J. Hill (CSIRO, Australia), selected the 26 invited speakers, and another 11 oral presentations were chosen from the 70 contributed abstracts. The program was divided into six topics: phase identification and quantification; accuracy and standards; new developments in software and data analysis; profile fitting, decomposition, and microstructural effects; novel applications and structural science; and new developments in hardware, including detectors, and studies under non-ambient and time-resolved conditions. The program for the last session was designed to interface smoothly with the Workshop on X-Ray and Neutron Diffraction at High Pressure, organized by the High Pressure Group of the IUCr, which was held immediately after the conference at the Geophysical Laboratory of the Carnegie Institution in Washington, DC. In addition, two tutorial workshops, organized by the ICDD, were conducted as part of the conference, one on powder diffractometer sensitivity and one on indexing methods.

The sessions opened with a tribute to the late William Parrish detailing his contributions to powder diffraction, delivered by T. C. Huang of IBM. Bill Parrish was responsible for developing many of the instruments and analytical methods that are used for powder diffraction analysis; his pioneering efforts will make possible even further advances.

2. Phase Identification and Quantification

The first keynote presentation by B. L. Davis (South Dakota School of Mines and Technology) discussed the development and application of quantitative phase analysis with reference intensity ratios (RIR). He included in his presentation helpful experimental techniques as well as applications to mineralogical samples. L. Zevin (Ben-Gurion University, Israel) then discussed standardless methods of phase analysis, in which a system of n phases can be determined provided that at least n mixtures of these phases are available. In the second keynote talk, R. L. Snyder (Alfred University) led the participants through the mathematical relationships developing a consistent set of notation for each of the RIR-based methods for quantitative analysis, including the standardless methods as well as the whole-pattern fitting and Rietveld techniques. J. K. Stalick (NIST) then discussed phase analysis with the Rietveld method in further detail; using neutron diffraction data, minor impurity phases were quantitatively determined even when there were no apparent peaks observable. A statistical approach to microabsorption corrections was presented by H. Hermann (Institute of Solid State Research, Dresden, Germany), based upon particle-size distributions and surface roughness. M. S. Nakhmanson (Comphys Lab Enterprise, St. Petersburg, Russia) discussed theory and techniques for phase identification using the PDF database. The organization of the database into clusters of materials with similar structure can result in broadened as well as more efficient database uses. Additional presentations were made by R. G. Marquart (Fein-Marquart Associates) on the user-assisted autocalibration process in the μPDSM micro powder diffraction search/match, D. K. Smith (Penn State University) on the limiting effect of crystallite size on accuracy in quantitative powder diffraction analyses, and H. Oettel (Technical University of Freiberg, Germany) on x-ray phase analysis in textured materials.

3. Accuracy and Standards

In the opening address for this session, P.-E. Werner (University of Stockholm, Sweden) discussed the relative merits of cameras and diffractometers for x-ray diffraction measurements, presenting detailed experimental comparisons. Although the diffractometer is clearly to be preferred for accurate intensity measurements, the high angular resolution of a Guinier camera results in very accurate position measurements. J. F. Bérar focused on data optimization and propagation of errors, with particular application to the Rietveld method using x-ray data. He showed that the details of peak shapes and sample effects can result in systematic errors. J. P. Cline (NIST) described the characterization and use of XRD standard reference materials, and H. Toraya (Nagoya Institute of Technology, Japan) discussed the accurate determination of unit-cell parameters using an internal standard reference material and whole-pattern fitting.

4. New Developments in Software and Data Analysis

The exciting emergence of techniques for *ab initio* structure solution from powder data was the focus of two keynote talks and an additional oral presentation. L. B. McCusker (Institute of Crystallography, ETH-Zentrum, Switzerland) reviewed the available software, and presented some examples of structures solved from powder data. She emphasized the importance of minimizing the degree of peak overlap by improving sample crystallinity and instrumental resolution. J. M. Newsam (Biosym Technologies Inc.) described direct space methods of structure solution, utilizing model-building methods coupled with interactive simulation of data with comparison against experiment. The simulated annealing method has been successfully applied to 90% of known zeolite structures. M. Estermann (Institute of Crystallography, ETH-Zentrum, Switzerland) gave details of the fast iterative Patterson squaring (FIPS) method, an improved treatment of severely overlapping reflections in a powder pattern for the application of direct methods. The third keynote talk of this session was a review of the procedures and applications of automatic indexing by D. Louër (Université de Rennes, France). He stressed the importance of high precision in the measurement of peak positions, and surveyed the different computer-based approaches. B. H. Toby (Air Products and Chemicals, Inc.) discussed recent advances in the determination of atomic pair distribution functions for the analysis of short-range order in crystalline and non-crystalline materials, and J. Schneider (Universität München, Germany) showed how short-range order effects could be combined with standard Rietveld refinement.

5. Profile Fitting, Decomposition, and Microstructural Effects

The first keynote presentation of this session by J. I. Langford (University of Birmingham, UK) reviewed the use of the Voigt function in determining microstructural properties from diffraction data by means of pattern decomposition, including all formulas and codes necessary for the analysis. Again, high resolution and good counting statistics are necessary to obtain reliable information. The second keynote address by V. Valvoda (Charles University, Czechoslovakia) discussed both experimental techniques to reduce preferred orientation effects and various methods of correcting the model. Finally, T. M. Holden (Chalk River Laboratories, Canada) reviewed residual stress measurements with neutrons, and A. Le Bail (Université du Maine, France) discussed the current status of modelling anisotropic line-broadening effects in Rietveld analysis.

6. Novel Applications and Structural Science

The applications of powder data analysis to structure problems now extend beyond the Rietveld refinement of positional parameters. D. L. Bish (Los Alamos National Laboratory) described in a keynote address how the traditional Rietveld method could be applied to structure solution when used, for example, in conjunction with distance least-squares constraints and crystal-chemical principles or with high-resolution TEM data. Several examples of zeolites and clay mineral structures were given. H. Boysen (Universität München, Germany) showed how anharmonic thermal parameters could be determined using the Rietveld method, with examples of diffusion paths in fast-ion conductors. A high resolution synchrotron x-ray powder diffraction and molecular modelling study of the structural changes accompanying absorption of trans-stilbene into H-ZSM-5 zeolite was described by J. B. Parise (SUNY at Stony Brook). The second keynote talk by J. P. Attfield (University of Cambridge, UK) reviewed recent advances in the use of anomalous dispersion in powder diffraction studies, including the use of synchrotron x-ray wavelengths that are close to an elemental absorption edge. He showed that using this technique one could determine cation distribution and oxidation states. R. W. Cheary (University of Technology, Sydney, Australia) then discussed how line broadening effects could be employed to study intergrowths and antiphase domains in barium hollandite compounds, and R. Vargas (IVIC, Caracas, Venezuela) described a physical model for x-ray analysis of order-disorder in lamellae of myelinated nerve sheaths.

7. New Developments in Hardware, Including Detectors, and Studies Under Non-Ambient and Time-Resolved Conditions

In the keynote address of this session, Y. Fujii (University of Tokyo, Japan) reviewed the utility of the diamond-anvil cell for investigations of powders under high pressure using synchrotron x-ray radiation, and described the high-pressure facilities available at the Photon Factory in Tsukuba. Of particular interest was the use of imaging plates to provide data suitable for Rietveld refinement. Synchrotron radiation was also used by L. W. Finger (Carnegie Institution of Washington) in the study of sub-micron single crystals of bismuth, and by M. Sutton (McGill University, Canada) for time-resolved x-ray diffraction studies of crystallization in metallic glasses. The high temperature x-ray determination of phase transitions in large grain alloys was discussed by O. B. Cavin (Oak Ridge National Laboratory). J. S. Loveday (Rutherford Appleton Laboratory, UK) reviewed two important new developments in the field of neutron diffraction at high pressure: a large-volume cell which allows Rietveld refinement above pressures of 10 GPa, and the development of a new detector at a Russian reactor. J. A. Fernandez-Baca (Oak Ridge National Laboratory) described the new multidetector powder diffractometer at Oak Ridge. Finally, crystal structure analysis by pattern fitting of energy-dispersive powder diffraction data, using synchrotron radiation at high pressure, was described by T. Yamanaka (Osaka University, Japan).

8. Summary

This conference made it quite clear that the renaissance in powder diffraction has continued at an even greater pace since the first meeting on Accuracy in Powder Diffraction in 1979. The variety and quality of information that can be extracted from a powder pattern has greatly increased, particularly with the application of whole-pattern or Rietveld

methods; the ability to study materials under non-ambient conditions has also been expanded. In a summary statement, R. J. Hill and D. E. Cox have stated, "Diffraction patterns previously collected only for phase identification or unit cell determination are now used to study such things as the subtleties of electron density distribution, the mechanism of phase transformations, and the distribution of cation oxidation states. We can look forward eagerly to APD-III, but perhaps we should recognize the pace of change is now so great that we should not wait another 13 years for this!"

Proceedings from this conference have been published as NIST Special Publication 846. You may contact either of the conference co-chairmen (J. K. Stalick and E. Prince, both of the Reactor Radiation Division) for further information.

Volume 98, Number 2, March–April 1993
Journal of Research of the National Institute of Standards and Technology

Conference Report

METROLOGICAL ISSUES IN PRECISION-TOLERANCE MANUFACTURING: A REPORT OF A NIST INDUSTRY-NEEDS WORKSHOP Gaithersburg, MD August 11–12, 1992

Report prepared by

Dennis A. Swyt

Precision Engineering Division,
National Institute of Standards and Technology,
Gaithersburg, MD 20899-0001

1. The Goal of the Workshop

The purpose of this NIST-initiated workshop was to provide an opportunity for U.S. discrete-part manufacturing companies which see potential benefit from improved NIST research and services in areas of interest to them to make needs known such that NIST can address them, in particular to identify specific needed measurement-and-standards support from NIST which is not currently being provided or is being provided in forms or with accuracies insufficient to those needs.

2. The Motivation of the Workshop

When Congress changed the name of this Federal agency from NBS—the National Bureau of Standards—to NIST, it kept the NBS measurement-and standards function and added a new, principal mission: to assist U.S. industry to develop and deploy the new technology it deems it requires to achieve international competitiveness. Pursuing this mandate, the Director of NIST—who came to NBS from industry—is focusing on support which will assist U.S. manufacturers to achieve higher quality, lower costs, and increased speed to market. The Precision Engineering Division further focuses on providing to U.S. manufacturing industries practical access to national and international standards of length at levels of accuracy which they need.

The basis for the workshop—that is, its motivation, content, and structure—was the recent report by the Precision Engineering Division, entitled Challenges to NIST in Dimensional Metrology: The Impact of Tightening Tolerances in the U.S. Discrete-Part Manufacturing Industry, which identified a variety of industry needs within its mission area [1].

This report showed an on-going trend to tighter dimensional tolerances in manufactured parts with: 1) the dimensions and tolerances of state-of-the-art precision-tolerance products shown in Fig. 1; 2) the decrease in the size of such tolerances an average of a factor of three every 10 years shown in Fig. 2; 3) the multiples by which accuracies of industry's production control measurements are expected to be better than tolerances and the multiples by which accuracies of NIST measurements are expected by industry to be better than those of their production control shown in Table 1; and 4) the lag of NIST laboratory capabilities behind these changes in industry needs shown in Table 2.

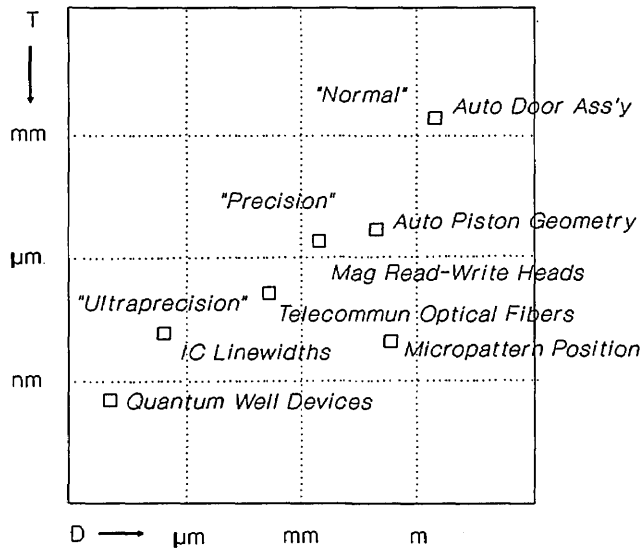

Fig. 1. Log-log plot of tolerance versus dimension for discrete-part products in normal, precision, and ultraprecision regimes.

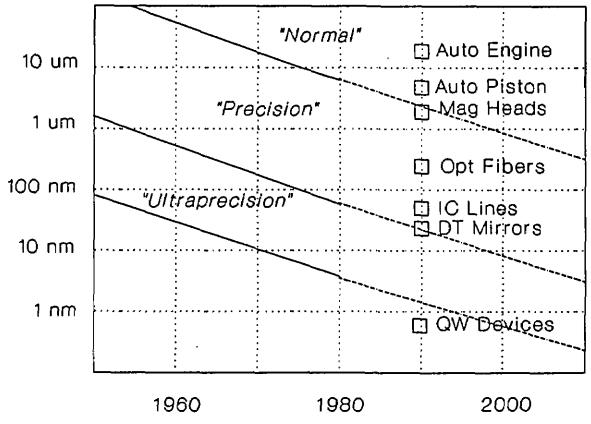

Fig. 2. Semilog plot of trends in limiting values of tolerances in normal, precision and ultraprecision regimes with examples of state-of-art today.

Table 1. Effect of two of the most commonly used ratios on accuracies of inspection and reference measurements: 1) the gage maker's rule (factor of 10); and 2) the minimum ratio (factor of 4)

	Gage maker's rule	Minimum ratio
Manufacturing tolerance	T	T
Inspection accuracy	$M = T/10$	$M = T/4$
Expected NIST accuracy	$N = M/10 = T/100$	$N = M/4 = T/16$

Table 2. NIST accuracy relative to that required to support design tolerances and production measurements at limit of normal-tolerance regime over the period of years 1970 to 2000

Measurement	Relations	1970s	1980s	1990s	2000
Manufacturing design tolerance	T	20 μm	7.5 μm	2.5 μm	1 μm
Production measurement accuracy	$M = T/4$	5 μm	1.75 μm	0.625 μm	0.25 μm
Req'd NIST measurement	$N = M/4 = T/16$	1.25 μm	0.5 μm	0.15 μm	0.05 μm
Realized NIST measurement accuracy	U	1.0 μm	Same		?

3. The Scope of the Workshop

Manufacturing industries served by this workshop included those with products whose function, quality, cost and availability depend on parts or part features specified in terms of length-based tolerances.

Invited industry participants included those from firms in industries such as automotive, aerospace, farm-and-construction equipment, machine tool, electronics, semiconductor equipment, computers and instrumentation which have measurement problems associated with assuring that dimensional features of the product as made conform to those of the product as designed.

Attendees were company, industry, or agency representatives able to address specifics of measurement needs in terms of design tolerances, manufacturing deviations, production-control measurement accuracies, and required reference standards and in the context of their business or mission goals and needs. Among the 80 industry attendees were representatives of, for example, AT&T, Boeing, Caterpillar, Cummins Engine, Eastman Kodak, Ford, General Motors, Hewlett Packard, IBM, Ingersoll Milling, Northrup, Texas Instrument, the machine tool and gear manufacturers associations, and an array of instrument and gage manufacturers. A complete list of firms represented at the workshop is shown in Appendix A.

4. The Structure of the Workshop

The 2 day workshop included plenary and parallel working sessions organized to address the range of industries, measurement technologies and problems suggested by the "Challenges" report which defined the three tolerance regimes shown in Table 3.

Following welcoming remarks by Dr. John W. Lyons, Director of NIST, were three theme-setting presentations by representatives of Boeing commercial aircraft company (illustrating issues of close-tolerance manufacturing of large-scale discrete-parts in the aerospace industry), Cummins Engine company (illustrating issues of the close-tolerance manufacturing of medium-scale discrete-parts in the automotive industry), and IBM (illustrating issues of close-tolerance manufacturing of small-scale discrete-parts in the advanced microelectronics industry). Similar plenary-session presentations on the metrological issues in discrete-part manufacturing in their lines of business were made by representatives of 11 other firms.

During the course of the workshop, participants received briefings on NIST laboratory capabilities, the research and services it provides, and the new means by which it aims to support domestic manufacturing industries, including: Cooperative Research and Development Agreements (CRDAs), under which NIST can work jointly with industry on problems of mutual interest; Regional Manufacturing Technology Centers, the system of technology-transfer centers being funded and administered by NIST; and the Advanced Technology Program (ATP), the new grants program to help high-tech companies or consortia of companies improve their competitiveness. Attendees were also asked what effect on their operations NIST's proposed adoption of the BIPM-recommended means of expressing measurement uncertainty would have (Appendix B).

Individual firm's needs were presented to NIST in the form of worksheets. For developing common points of view on industry needs, attendees self-selected into one or more of five working groups topically devoted to:

1) Larger-Scale Parts, Coordinate Measuring Machines and Theodolites;
2) Complex-Shape Parts, Including Gears and Screw Threads;

Table 3. Tightening of realizable dimensional tolerances in normal, precision, and ultraprecision tolerance regimes of machining from 1980 to 2000

Machining	Production and measuring	Accuracy	Accuracy
Normal	Conventional milling and turning coordinate measuring machines	7.5 μm	1 μm
Precision	Diamond turning machines interferometer systems	0.075 μm	0.01 μm
Ultraprecision	Atom and ion-beam machining scanning tunneling microscopes	0.005 μm	<0.001 μm

3) Medium-Sized Parts, Including Small-Bore Features (such as microwave airlines);
4) Figure/Finish, Including Diamond Machining; and
5) Ultrasmall Features, Microelectronic Lithographies, and Scanning-Probe Microscopies.

5. Specific Working-Group Recommendations

The following is a summary of the industry needs and desired NIST actions related to those needs which the working groups produced and industry spokespersons presented in plenary sessions.

5.1 Working Group on Larger-Scale Features

This working group included a large contingent of users of coordinate measuring machines and their summary-report statement of needs consisted of: 1) improved NIST calibration accuracy, especially of meter-size standards, with a base calibration by NIST or DoE; 2) standards-committee support by NIST, especially ISO, where NIST should lead the U.S. delegation; 3) development of a long-term strategy to learn the accuracy achieved on real workpieces on 3D coordinate measuring systems; 4) for probing, provision of application documents on performance characterization and calibration methodology, covering also thermal properties and especially long-stylus properties; and 5) calibrations of thermal-expansion coefficients of CMM calibration artifacts to accuracies of one to three percent. For emphasis, this group concluded its presentation of needs by reading a letter from a Vice President of the Caterpillar Company to NIST, quoted in the "Challenges" report, saying:

> *"Five years ago our company embarked on a major factory modernization program with the purpose of maintaining, if not increasing the competitive edge that has historically been ours. A vital component of our overall program was modernization of our metrological equipment. Central to the metrology upgrade was increased use of coordinate measuring machines (CMMs) on our factory floor. Obtaining length standards of adequate accuracy, certified by NIST, for use in certification and ongoing verification of our new CMMs is a problem of ongoing concern. For the past three years we have been unable to obtain certification of step gages from NIST... Our current solution is to use PTB (German Standards Bureau) for certification of step gages ... The current situation is unacceptable. We cannot afford the cost and time of continuing to send reference artifacts to Europe for certification. For both competitive and strategic reasons, we must have a metrologically strong partner at NIST..."*

5.2 Working Group on Complex-Shape Parts

This working group included a large contingent of manufacturers of gears and gear-measuring equipment and their summary-report statement of needs consisted of: 1) establishing a calibration service for gear involute/lead masters for which none now exists, potentially including a round-robin measurement exercise coordinated by NIST; 2) publishing a report addressing the propagation of uncertainties down through the "hierarchies" of measurement/calibration processes; 3) doing something about the problem that "calibration" is a vague term with different meanings in different applications; 4) conducting round-robins, correlating data, and working with industry in developing measurement techniques because methods are needed to correlate measurement techniques for complex shapes; 5) with small manufacturers needing certification of outside measurement services, address the accreditation of organizations providing measurements of complex shape; and 6) step up research, including cooperative research with industry, in the area of on-line measurement techniques for processes producing parts of complex shape.

5.3 Working Group on Mid-Scale Features

This working group included representatives of a number of companies and groups within a single company who indicated measurement issues for part and feature sizes "below what can be reliably measured on a CMM," a region which they showed graphically by amending Fig. 1, originally of the NIST "Challenges" report, to produce Fig. 3. The figure so presented illustrates three points: 1) state-of-the-art tolerances for manufacturing processes used by Hewlett-Packard Santa Rosa — from sheet-metal radio-frequency enclosures through diamond-turned microwave parts to e-beam and molecular-beam-epitaxy fabricated features—agree with those shown in the NIST "Challenges" report; 2) there is a region of industrial demand below that delivered by coordinate measuring machines and above that achieved in

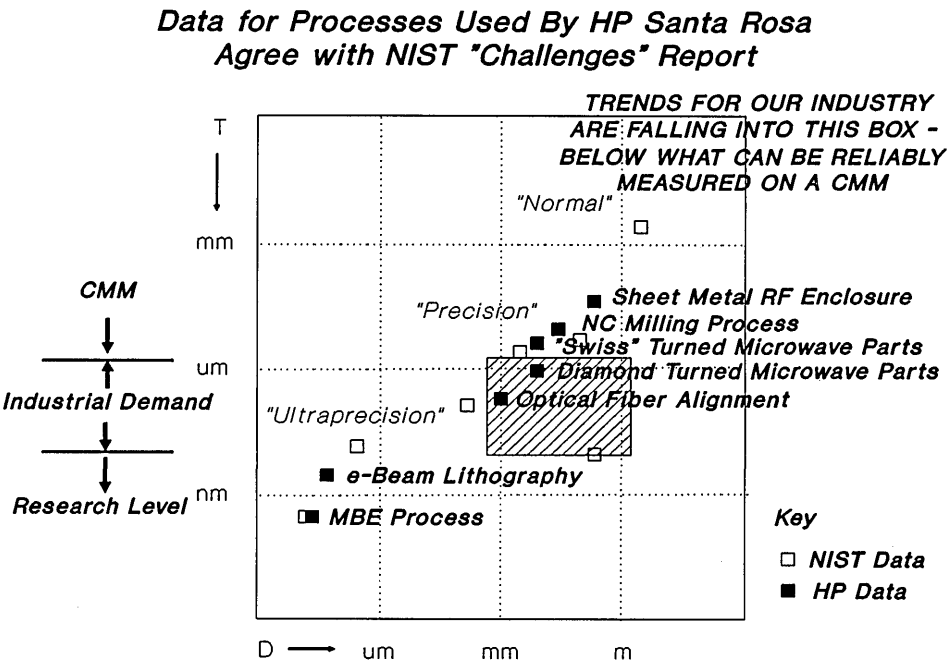

Fig. 3. Graphical representation of industry measurement needs presented by working group 3.

research; and 3) the trend of this industry's needs lies in this region which is bounded by dimensions from sub-millimeter to above one meter and tolerances from about 20-50 nm to about 2 μm.

A summary of 18 specific types of artifact standards needed to support unique or non-general purpose measurement solutions for particular types and sizes of manufactured part features which was presented is shown as Table 4. In addition to those artifact standards, this working group also indicated industry need for educational/training information from NIST, including NIST-lead development of industry-useable calibration procedures, for precision-tolerance applications when production tolerances are less than 16 times NIST capabilities, i.e., measurement accuracies, including better documentation of NIST procedures.

Table 4. Artifact standards needed for unique or non-general purpose solutions

Dimensional feature type	Typical size	Improved standards needed
Outside diameter	1–1000 mm	CMM ball plates, step gages, gage blocks
Inside diameter	1–1000 mm	Master rings, step gages
Step height	0.1–100 μm	Amplification standards for step height
Distance between lines	0.001 mm–20 m	Laser interferometers, digital and line scales
Out-of-roundness	0.01–100 μm	Amplification standards for roundness
Layer thickness	0.01–100 μm	Foils test specimens
Angle, subdivision of circle	0–360 degrees	Levels, index tables
Angle—materialized	0–360 degrees	Right angles, polygons, angle blocks, cone angle
2D/3D dimensions	0.001–1000 mm	Two- and three-dimensional standards
Geometrical properties of involutes	Module 0.4–10 mm Diameter 5–500 mm	Master wheels, Involute standards
Geometrical properties of screw threads	Diameter 1–200 mm	Thread masters, plugs, rings
Roughness, waviness	0.01–1000 μm	Parameter standards, comparison specimens
Straightness	0.01 μm	Straightness standards, straight edges
Flatness	0.01 μm	Flatness standards, surface plates
Roundness	0.01–100 μm	Roundness standards, CMM reference balls
Cylindricity	0.01 μm	Plugs, rings
Shape of curves	0.01 μm	Curve standards
Shape of surfaces	0.1 μm	Surface standards

5.4 Working Group on Figure/Finish

This working group included representatives of manufacturing companies with principal interests in characterization of surface roughness, surface figure (e.g., curvature of aspherical forms), and specialized production processes associated with them, such as single-point diamond machining and ductile regime grinding.

In the area of surface finish, the major concerns were that NIST should: 1) send NIST technical staff to participate in development of international (ISO) and national (ANSI) documentary standards dealing with surface roughness; 2) develop a set of artifacts and standard protocols for instrument evaluation, for example, sinsuoidals with spatial wavelengths from 200 mm on down and "realistic" (e.g., quasi-random) surfaces; 3) provide standard data sets for software evaluation; and develop better step-height standards. A specific surface-finish standard needed is one with standard data sets for known sinusoidal, triangular, and square-wave forms (for instrument adjustment) plus a random wave form with an RMS roughness of less than 10 nm (for instrument correlation).

In the area of figure, the present NIST program should be encouraged, with its good approach of progressing from successively developing state-of-the-art capabilities to measure first flat, then sphere, then asphere forms. In the area of ductile regime grinding, NIST needs to develop the means for measurement of sub-surface damage, including determination of the transfer function between instruments, and developing definitions and standard tests, all supported by educational services including tutorials and giving of hands-on experience.

5.5 Working Group on Ultrasmall-Scale Features

This working group included representatives of manufacturing firms that either use or produce scanning-probe-microscope instruments for the characterization of ultrasmall features of discrete-part manufactured goods such as nanoelectronic devices. The principal needs from NIST identified were those for: 1) Standard Reference Materials—with certification of sub-micrometer artifacts in all the dimensions (2D plus height) and 2D in distance (with field characterization and pattern placement); 2) Technology Development—especially STM probe tip development, which is a key enabling technology for small high-tech companies facing heavy foreign competition but having difficulty getting support from the NIST Advanced Technology Program; and 3) Road Maps—with a 5 year plan from NIST in response to the workshop's requests, indicating what is feasible and how it will conform to other roadmaps in industry, e.g., Sematech.

6. Principal Findings of the Workshop

The principal recurring theme of needs, broadly shared among the industry representatives—whether from commercial aircraft, heavy equipment, automobiles, engines, computers, instrumentation or microelectronics was an urgent request that NIST provide new or improved accuracy physical artifact dimensional standards applicable to industry specific needs, including those for coordinate measuring machines, involute gears, small bore microwave devices, x ray optical surfaces and nanometer scale microelectronics.

The most frequently stated basis of the need of companies for more high-accuracy artifact standards from NIST is the "new traceability" required to meet ISO-9000-type quality requirements for products to be sold both in the European Economic Community and Pacific-rim nations. The next most frequently stated basis is the need for fixed reference points to support development of innovative products being strongly competed by Japan.

Finally, the sense of the closing plenary session was that this group of representatives of U.S. discrete-part manufacturing urged NIST to immediately respond to these stated needs for higher-accuracy artifact standards across the range of applications indicated in this workshop, including developing a documented operational plan spelling out how over the next few years it will do so.

7. Appendix A. Manufacturing Companies Represented at Workshop

AALA
American Gear Mfrs
AT&T
AT&T Bell Labs
Automated Precision
Baxter Associates
Boeing Aircraft
Boeing Defense
Brown & Sharpe
Caterpillar
Cummins Engine
Detroit Center Tool
Diffracto
Digital Instruments
Eastman Kodak
Edge Technologies
EDM
Federal Products
Ford Motor Co.
General Motors
Giddings & Lewis
GKS Inspection
GM Powertrain
Hewlett Packard
IBM
Industrial Tectonics
Ingersoll Milling Machine

ITW Zero Systems
Leica
Lion Precision
M&M Precision
Martin Marietta
Moore Special Tool
Moore Products
NMTBA
Newport Klinger
Northrup
Optodyne
OPTRA
Precise Inspection
R.E.Smith
SAMI
Tencor
Texas Instruments
Timken
TopoMetrix
Ultratech Stepper
Van Keuren
VLSI Standards
Zygo

8. Appendix B. Results of Representation of Uncertainties Survey

Also as part of the formal workshop, industry attendees were queried on the issue of NIST adoption of the CIPM recommendation on representation of uncertainties in measurement [2], specifically:

> *"What is your view of NIST changing the basis of its 'accuracy' statements from the old system of 'random-and-systematic added linearly' to the new system of 'type A and type B added sum-of-squares', in particular from the predominantly used $U_T = 3\sigma + se$ to a proposed $U_T = 2\sigma$."*

Eighteen firms of the 75 which attended the workshop responded. Results are summarized in Table 5 according to the legend shown with it.

In sum, 100% of the 18 respondees said it would pose no substantial problem (also, in effect, given the opportunity to do so none of the 75 attendees said it would pose a problem); 22% (4 respondees representing three firms and a DoD facility: Boeing Aircraft, Precise Inspection, Ingersoll Milling again and the Naval Aviation Depot at Pensacola) said the change would involve some transition problems. The only "transition problems" specified were "some problems with documentation" (Boeing). Five gaging companies, including Detroit Tool, Federal Products, Lion Gage, Moore Products, Precise Inspection, suggested that there is a special problem associated with how uncertainty of measuring gages is handled when assessing whether gaged parts are in or out of tolerances or when assessing whether the gage itself is in or out of tolerance.

Five respondees representing four firms (Cummins Engine, Eastman Kodak, General Motors, and Ingersoll Machine Tool) said the change to the CIPM recommended system of representing uncertainty would provide a positive advantage. Advantages noted were: "Financial and international political criteria" (Eastman Kodak);

Table 5. Responses of workshop attendees on question of what effect would NIST changeover to CIPM system of representing measurement uncertainty would have on manufacturing firm[a]

Company	Effect[a]	Using	Comment
Automated Precision	o	$3\sigma + se$	
Boeing Aircraft	t	(2 or 3)$\sigma + se$	Some documentation problems
Cummins Engine	+	2σ	Meaningful use in uncertainty budgets
Cummins Engine	+	2σ	Align NIST with foreign national laboratories
Detroit Center Tool	o	$3\sigma + se$	Use precision in gage acceptance
Eastman Kodak	+	(2 or 3)σ	Criteria are cost, international political; need standard
Federal Products	o	$3\sigma + se$	In some cases it may be an advantage
GKS Inspection	o		Uses what customers want
GM Powertrain	+	3σ	
Ingersoll Mach Tool	+,t		Common method good
Lion Precision Gage		2σ	Not considered problem in depth
Moore Products		$3\sigma + se$	Not sure of customer response
Naval Aviation Depot	t	$3\sigma + se$	Should use only ISO Type A
Optra	o		Seems like good idea
Oak Ridge Natl Lab	o	$3\sigma + se$	Positive step
Precise Inspection	t	$A = 2R$	Any change important
Tencor Instruments	o	(1 or 3)σ	Used with appropriate reference
Timken	o	3σ	

[a] Key to symbols:
+ = The NIST changeover will provide an advantage to my firm.
o = The NIST changeover will pose no problem.
t = The NIST changeover will pose some transition problems.
− = The NIST changeover will pose substantial problems.

"Align NIST with other major foreign national laboratories" (Cummins); "Allow meaningful use of uncertainties in firm's uncertainty budgets" (Cummins); "Provides common method to state/interpret 'accuracy' statements" (Ingersoll); and "Positive step toward internationally consistent measurements" (ORNL).

8. References

[1] D. A. Swyt, Challenges to NIST in Dimensional Metrology: The Impact of Tightening Tolerances in the U.S. Discrete-Part Manufacturing Industry, NISTIR 4757, Natl. Inst. Stand. Technol., Jan 1992.

[2] ISO/IEC/OIML/BIPM, Guide to the Expression of Uncertainty in Measurement, International Standards Organization, Technical Advisory Group 4, Working Group 3, June 1992.

Volume 98, Number 2, March–April 1993
Journal of Research of the National Institute of Standards and Technology

Conference Report

SYMPOSIUM ON OPTICAL FIBER MEASUREMENTS Boulder, CO September 15–17, 1992

Report prepared by

Douglas L. Franzen and Gordon W. Day

Electromagnetic Technology Division, National Institute of Standards and Technology, Boulder, CO 80303

The seventh Symposium on Optical Fiber Measurements was held on September 15–17, 1992 at NIST in Boulder, CO. Over 220 people attended the two and a half day meeting and heard a program consisting of 11 invited and 43 contributed papers with over half the papers coming from outside the United States. In addition, 10 committees associated with standards organizations like the Telecommunication Industry Association (TIA) and International Electrotechnical Commission (IEC) met in conjunction with the Symposium. The meeting covered metrology aspects of lightwave communications. While optical fiber measurements were emphasized, other lightwave components were also addressed including sources, detectors, integrated optic advices, passive filters, splitters, and connectors. The meeting scope covered metrology in both laboratory and field environments.

Important technical topics of the meeting included optical time domain reflectometry (OTDR), single-mode fiber geometry, polarization effects in fiber, and optical fiber amplifiers. OTDRs have unique measurement capabilities and represent the largest market segment of fiber optic test equipment. They therefore continue to be a topic of interest at the Symposia. T. Horiguchi and other workers from Nippon Telegraph and Telephone (NTT) reported on an OTDR operating at 1600 nm. Usual OTDRs operate at typical system wavelengths of either 1300 or 1550 nm. By operating at longer wavelengths, where single-mode fiber bending loss is higher, the new OTDR has improved sensitivity for locating potential faults caused by excessive bending. Operation at 1600 nm is accomplished by using a Q-switched erbium fiber laser to pump a fiber Raman laser. A dynamic range of 24.5 dB is achieved with a resolution of 20 m.

Future fiber networks may contain several fiber splitters for distribution. F. Kapron and J. Berardinelli from Bellcore described an algorithm for determining branch fault loss and reflectance when the OTDR "looks" through a splitter. To better quantify OTDR signatures, A. Judy from AT&T Bell Laboratories developed an expression which relates fiber backscatter and reflectance. J. Clayton and others from AT&T Bell Laboratories performed statistical analysis to determine the limitations of OTDRs when predicting fiber uniformity.

Low coherence reflectometry is closely related in function to OTDR. It is an interferometric technique for obtaining very high resolution on short lengths of fiber. K. Takada from NTT reviewed the method in an invited paper. W. Sorin and D. Baney of Hewlett Packard described a method for improving the accuracy of reflectance measurements in the presence of fiber chromatic dispersion.

Geometrical dimensions of single-mode fiber continue to be an important issue. Low loss splices and connectors depend on dimensional integrity. The common measurement method of near-field video analysis requires a standard for absolute calibration. In an invited paper, J. Baines and K. Raine of the National Physical Laboratory (NPL) reviewed recent developments in fiber geometry measurements and concluded standards laboratories need to determine cladding diameter with uncertainties of 0.1 μm (nominal cladding diameter is 125 μm). Measurement methods in use at NPL include a Michelson white light interferometer, an image inverting microscope, and a scanning confocal microscope.

M. Young, P. Hale, and S. Mechels described geometry measurements at NIST where a contact micrometer, scanning confocal microscope, and white light interference microscope are used to determine cladding diameter. They estimate overall uncertainty for the three methods as 50, 40, and 30 nm, respectively. Of the three methods, the micrometer is most efficient to use; therefore, it will be the method employed by NIST in dispensing standard reference fibers. In a separate paper, P. Hale of NIST described the interference microscope in more detail. The partially automated system is based on a Mirau interference objective and a specially designed fixture for holding the fiber on an optical flat. A comparison of the micrometer and confocal microscope to the interference microscope, on eight fiber diameters, yielded average rms differences of 15 and 29 nm.

The geometry of the plastic buffer coatings surrounding the fiber is also important. Buffer coatings protect the fiber from the environment and should be concentric to provide good centering in ribbon cable. A. Hallam and J. Shaw described a conventional gray scale near-field system which is modified to measure coating thickness and concentricity. The modification is an oil filled cell which uses dark-field illumination and views the fiber from the side. Typical repeatabilities for coating diameter and concentricity are 0.2 and 0.25 μm. Hermetic fiber coatings of thinly deposited carbon (tens of nanometers) are frequently used to improve fiber strength and suppress hydrogen induced loss. Y. Ishida and others from Furukawa Electric make use of the electrical properties of the carbon to measure the coatings during draw. By measuring the complex impedance, they are able to measure coating thickness with a resolution of ±1 nm for thicknesses over 17 nm.

Polarization effects in fiber can be useful for sensor applications; however, they can also be detrimental to communications systems where polarization mode dispersion (PMD) reduces system bandwidth. In an invited paper, B. Hefner of Hewlett Packard described a polarimeter and summarized the progress in polarization measurements. Y. Gu and L. Poyntz-Wright from York Technologies discussed methods for measuring extinction ratios in polarization-maintaining fiber, while L. Stokes of Hewlett Packard presented accurate measurements of polarization dependent loss of fiber components as a function of wavelength. Unwanted polarization mode dispersion in conventional fiber arises from core deformation and external stress. While the effects are small in kilometer lengths, fibers in future undersea systems using erbium fiber amplifiers are likely to be hundreds of kilometers long, so distortion could result at high bit rates. Y. Namihira and J. Maeda from KDD of Japan compared several methods for measuring PMD, and concluded that the interferometric method is best for measuring small PMD values. L. Thevenaz, M. Nikles, and P. Robert from the Swiss Federal Institute of Technology described a novel PMD measurement method based on an interferometric loop of fiber. The method is very easy to implement in the laboratory and gives the probability distribution of the PMD.

Five papers were concerned with optical fiber amplifiers. This new technology promises to revolutionize long fiber systems. D. Hall of Corning, in an invited paper, discussed the characterization of erbium fiber amplifiers. Measurements requiring immediate attention include gain, noise, and distortion. Reflections within the measurement system are potential sources of error in gain measurements. Gain measurements at specific wavelengths in the presence of power at other wavelengths have not been addressed; those types of measurements will be necessary for wavelength-division-multiplexed systems. Analog cable TV signals require low distortion; measurements need to be developed to characterize erbium fiber amplifiers for this requirement. R. Hickernell and others from NTT reported on chromatic dispersion measurements in erbium doped fiber. By using techniques of Fourier transform spectroscopy, they concluded the dispersion resulting from resonant gain or loss can be significant compared to background fiber dispersion. M. Artiglia and other CSELT of Italy colleagues addressed measurements of noise figure. They concluded that excess

noise from the source can affect the results; a procedure to correct data for excess noise is given. T. Kashiwada and others from Sumitomo evaluated potential sources of error in noise figure measurement; improved results were obtained through the use of a bandpass filter and a method of polarization control. There is a significant market for erbium fiber amplifiers. Automated measurements are therefore cost effective. D. Cole and M. Vance from Corning evaluated an automated system for measuring gain, output power, amplified spontaneous emission (ASE), and unabsorbed pump power as a function of input power and wavelength.

Four page summaries of papers given at the Symposium are contained in a 245 page meeting digest. The *Technical Digest—Symposium on Optical Fiber Measurements, 1992* is available as NIST Special Publication 839. A copy can be obtained by contacting either D. L. Franzen (303) 497-3346 or G. W. Day (303) 497-5204; copies are free of charge as long as supplies last. Alternatively, the Digest can be purchased from the Superintendent of Documents, U.S. Government Printing Office, Washington, DC 20402 or the National Technical Information Service (NTIS), Springfield, VA 22161.

Volume 98, Number 2, March–April 1993
Journal of Research of the National Institute of Standards and Technology

Conference Report

NORTH AMERICAN INTEGRATED SERVICES DIGITAL NETWORK (ISDN) USERS' FORUM (NIUF) Gaithersburg, MD October 26–30, 1992

Report prepared by

Elizabeth B. Lennon

Computer Systems Laboratory,
National Institute of Standards and Technology,
Gaithersburg, MD 20899-0001

1. Introduction

The Computer Systems Laboratory (CSL), National Institute of Standards and Technology, sponsored the sixteenth North American ISDN Users' Forum (NIUF) at its Gaithersburg, Maryland site on October 26-30, 1992. About 250 users, implementors, and service providers of ISDN technology attended the meeting. CSL collaborated with industry in 1988 to establish the NIUF to ensure that emerging ISDN applications meet the needs of users. A Cooperative Research and Development Agreement (CRDA) with industry was established in 1991 to govern the management of the forum; the CRDA now has 36 signatories from industry and academia. CSL serves as chair of the forum and hosts the NIUF Secretariat. NIUF membership is open to all interested users, product providers, and service providers; meetings are held three times a year at various locations throughout North America.

2. The ISDN Standards Process

International standards for ISDN support worldwide communications for the exchange of voice, data, and image information among users, independent of any manufacturer, service provider, or implementation technology. ISDN standards are developed by the International Telephone and Telegraph Consultative Committee (CCITT) and, for North America in particular, by the Exchange Carriers Standards Association (ECSA) accredited standards committee, T1, under the umbrella of the American National Standards Institute (ANSI).

ISDN standards provide a broad variety of options and parameters to meet many potential needs and applications. To ensure interoperability and terminal portability within the ISDN network and its attendant equipment, a uniform subset of options and parameters must be selected for implementation. Each application usually requires only a subset of total functionality available in the standards; for ISDN products and services to work together in a multi-vendor environment, common sets of options must be selected.

To cope with this proliferation of choices and to provide practical products and services which meet the needs of users, the standards specification process must be extended to include the development of Application Profiles, Implementation Agreements, and Conformance Criteria which will promote interoperability. The NIUF addresses all of these areas.

3. NIUF Goals and Organization

The NIUF seeks to achieve three principal objectives:

- To promote an ISDN forum committed to providing users the opportunity to influence developing ISDN technology to reflect their needs;
- To identify ISDN applications, develop implementation requirements, and facilitate their timely, harmonized, and interoperable introduction; and
- To solicit user, product provider, and service provider participation in the process.

The actual work of the NIUF is accomplished in two workshops: the ISDN User's Workshop (IUW) and the ISDN Implementor's Workshop (IIW). The IUW produces Application Requirements which describe potential applications of ISDN and the features which may be needed. The IIW develops Application Profiles, Implementation Agreements, and Conformance Criteria which provide the detailed technical decisions necessary to implement an application requirement in an interoperable manner. The NIUF Executive Steering Committee coordinates the activities of the two workshops.

4. Accomplishments of the NIUF

Since its inception in 1988, the NIUF has achieved the following:

- 133 active applications for development of Application Profiles have been accepted;
- Application Profiles have been completed for 14 applications;
- 12 Implementation Agreements have been completed; and
- 8 Conformance Tests have been completed.

CSL established the NIST Special Publication 823 series, Integrated Services Digital Network Technology Publications, to publish the approved Implementation Agreements, Conformance Tests, and other NIUF documents. Copies of these documents are available for sale by the Government Printing Office, (202) 783-3238 or the National Technical Information Service, (703) 487-4650.

5. October 1992 NIUF Focuses on TRIP '92

The October NIUF focused on finalizing plans for the Transcontinental ISDN Project 1992 (TRIP '92) on November 16-20, 1992, which marked the advent of National Integrated Services Digital Network (National ISDN-1). Cosponsored by the NIUF and the Corporation for Open Systems (COS), TRIP '92 involved 74 user organizations in 149 locations across North America as well as several international sites. National ISDN-1 is based on national and international standards and is consistent with Implementation Agreements developed by the NIUF.

TRIP '92 Open Houses across the nation featured demonstrations of ISDN applications available to government and industry such as video/multimedia conferencing, desktop conferencing and screen sharing, LAN-to-LAN bridging, medical imaging, Group 4 facsimile, and image and large data file transfer. NIUF industry partners participating in the demonstrations at the NIST Open House site included AT&T Bell Laboratories, COMSAT, Bell Atlantic, and Northern Telecom. Also featured was a special session for about 170 government and industry executives. Speakers at this session included Robert M. White, Under Secretary for Technology, who presented a government view of national ISDN, and Irwin Dorros, Executive Vice President, Bellcore, who gave the industry perspective.

6. Highlights of October 1992 NIUF

Other highlights of the October meeting included a demonstration of Remote Message Retrieval Over ISDN by the Messaging and Answering Group and completion, subject to final approval at the NIUF February 1993 meeting, of two significant NIUF documents: *A Catalog of National ISDN Solutions for Selected NIUF Applications* and *A Generic Model for ISDN Cost Analysis*. Both documents resulted from a cross-industry team effort by NIUF members. The catalog focuses on demonstrating solutions for those applications identified as most important by an NIUF survey; most applications are satisfied with basic rate ISDN access and can be implemented using NI-1 solutions. The cost analysis document contains an ISDN checklist of both hard and soft costs and benefits. The document also includes a spreadsheet available in Microsoft Windows and MAC-based

Excel, from which users can form the basis for their own customized spreadsheet for an ISDN cost analysis.

7. For More Information

For more information about the NIUF and its publications or to obtain conference proceedings, contact the NIUF Secretariat: Dawn Hoffman, Computer Systems Laboratory, National Institute of Standards and Technology, Building 223, Room B364, Gaithersburg, MD 20899-0001; telephone (301) 975-2937 or Fax (301) 926-9675.

News Briefs

General Developments

Inquiries about News Briefs, where no contact person is identified, should be referred to the Managing Editor, Journal of Research, National Institute of Standards and Technology, Administration Building, A635, Gaithersburg, MD 20899; telephone: 301/975-3572.

NIST/PRIVATE COMPANY RESEARCH MAY INCREASE LASER POWER

NIST and a private company have signed a two-year Cooperative Research and Development Agreement to develop an improved design for an external laser stabilizer. Private company researchers will team on the project with a NIST physicist who, while at Stanford University in 1984, designed an external stabilizer that reduces frequency noise without requiring optical modification of the laser. This allows the laser to operate at virtually full power. He has worked on several versions of his original design since then. Pooling their expertise, the researchers hope to improve the design even further and develop a stabilizer prototype that eventually may be licensed. The private company plans to use external stabilizers on lasers that probe spectral hole-burning effects in rare-earth, ion-doped crystals. Other potential benefits of the CRADA research include information storage applications, optical frequency standards using sharp resonances in special crystals and ulta-high resolution spectroscopy.

1993 DATES SET FOR ISDN USERS' FORUM

The North American ISDN Users' Forum has set its meeting dates for the remainder of calendar year 1993. They are June 21-25 and Oct. 18-22 (all sessions will be at NIST's Gaithersburg, MD, facility). NIUF is a cooperative industry and government activity formed by NIST in 1988. Its goal is to create a strong voice for users of the Integrated Services Digital Network—the futuristic information highway that allows users to send and receive voice, data and images simultaneously. As ISDN is developed and implemented, participation in the NIUF and attendance at its meetings can enable ISDN users to influence ISDN products to reflect user needs and identify ISDN applications. The NIUF also develops technical agreements and tests that promote uniform use of ISDN standards and help ensure interoperability of ISDN products. Last November, the NIUF co-sponsored Transcontinental ISDN Project (TRIP) '92, which inaugurated a national ISDN network based on standards and implementation agreements.

ISDN "SOLUTIONS CATALOG" NOW AVAILABLE

The North American Integrated Services Digital Network Users Forum has developed a national ISDN solutions catalog that is now available through the National Technical Information Service. Though the version being offered is still in draft form, forum officials anticipate that few, if any, changes will be made when the final edition is printed later this year. The catalog explains 38 solutions for ISDN applications that NIUF members identified as most important in a recent survey. Some of the solutions detailed include video conferencing, screen sharing, facsimile, caller ID, telecommuting and file transfer. Also listed are 116 products that 55 suppliers have identified as part of these solutions. Catalog of National ISDN Solutions for Selected NIUF Applications is available for $44.50 (print) or $17.50 (microfiche) from NTIS, Springfield, VA 22161, (703) 487-4650. Order by PB 93-124642.

NCWM PUBLISHES FIRST METRIC SIZE ANNUAL REPORT

In support of the Federal Government's metric transition program, the report on the 77th Annual Meeting of the National Conference on Weights and Measures has been printed on metric standard paper, size A5 (148 by 210 mm). It contains NCWM committee reports and general session speeches. International addresses were: "1993-Fortress Europe or Free-Trade Opportunity?" by the director of the National Weights and Measures Laboratory, U.K.; "Weights and Measures in Canada," by the chief of Canadian Weights and Measures; and "Legal Metrology in Europe," by the director of Technical and Scientific Services, Physikalisch-Technische Bundesanstalt, Germany. NCWM, an organization of more than 3000 weights and measures officials, and representatives of industry, consumer groups, and federal agencies, establishes uniform laws, regulations, device specifications, and tolerances that are adopted by federal, state, and local government agencies. The Report of the 77th National Conference on Weights and Measures, 1992 (NIST SP 845), is available from NCWM, P.O. Box 4025, Gaithersburg, MD 20855, (301) 975-4012, fax: (301) 926-0647.

LATEST BALDRIGE QUALITY AWARD CRITERIA RELEASED

Themes being emphasized in the 1993 criteria for the Malcolm Baldrige National Quality Award include a company's "investment in its people" and companies as good "corporate citizens." The 1993 criteria also emphasize the important role of information and analysis in decision making. Almost 700,000 copies of the criteria have been distributed since the award's beginning. Thousands of organizations use the criteria for self-assessment, training and education. Many state and international awards are based on the Baldrige Award criteria. Established by Congress in 1987, the award program promotes quality awareness, recognizes quality achievements of U.S. companies and publicizes successful quality strategies. NIST manages the award, in conjunction with the private sector. Applications for the award are due April 1. Single copies of the 1993 Award Criteria are available free of charge from the Malcolm Baldrige National Quality Award office, (301) 975-2036, fax: (301) 948-3716.

CRADA GOAL: ASSESSING BREAST CANCER RISK

NIST and an Ithaca, NY, biotechnology company are collaborating on an analytical system that could provide measurements to help doctors assess a woman's risk for contracting breast cancer. The Private company and NIST recently entered a cooperative research and development agreement to develop a commercial flow injection immunoassay system (FIIA), speeding transfer of this NIST-invented technology to the medical community. The FIIA approach uses specially designed liposomes, coated with antibodies, to detect very small quantities (10^{-12}g/g) of female estrogen hormones indicative of cancer risk. This new technique could potentially be used for routine screening in an automated and inexpensive clinical test. Furthermore, reliable risk assessment measurements could aid doctors in early cancer diagnosis and treatment, as well as help researchers evaluate cancer prevention strategies.

NEW METAL ALLOY SHOWS UNEXPECTED WEAR POTENTIAL

Preliminary tests of a new biocompatible alloy of zirconium, palladium and ruthenium show the material has extraordinary resistance to fracture and wear. The alloy was invented by a NIST physical metallurgist in the Paffenbarger Research Center. The patent is held by the American Dental Association Health Foundation, sponsor of the center at NIST. The alloy is strong enough for dental and medical devices and holds significant potential as an industrial coating where high-performance materials are required for bearing surfaces and mechanical joints. The material has proven strongly resistant to wear, corrosion and crack propagation, and none of the elements are known to involve toxic reactions. The metal could meet a need for a wear-resistant system for total hip and knee implants. Tests show that under applied stress normally large enough to produce a permanent change in shape, the alloy undergoes internal changes that actually increase its ability to resist further deformation and fracture. For information, contact Richard M. Waterstrat, B148 Polymer Building, NIST, Gaithersburg, MD 20899-0001, (301) 975-6831.

TWO FED LABS TO PURSUE "MANUFACTURING QUALITY"

Formalizing and expanding a long-standing relationship, NIST and the Department of Energy's Oak Ridge National Laboratory have launched a "manufacturing quality" initiative addressing measurement needs and other technology issues facing U.S. industry. The two labs agreed "to pursue all avenues of collaboration that can help improve the nation's 'technological standing.' " The joint initiative—signed by NIST, DOE and the private company that manages the Oak Ridge Y-12 plant—will begin with NIST assisting Oak Ridge in characterizing the accuracy of high-performance coordinate measuring machines at the Y-12 plant. Plans also call for joint development of a NIST-DOE gear metrology center at the Tennessee facility. Services spawned by the NIST-Oak Ridge collaboration will help U.S. manufacturers of precision parts and products satisfy the ISO 9000 international market quality standards.

NEW SYSTEM HELPS DIAGNOSE, SOLVE CONCRETE PROBLEMS

Getting advice from many of the world's concrete experts on fixing cracks and other highway problems soon will be as easy as turning on a personal computer thanks to a new "expert" system being developed by NIST researchers. The system, called HWYCON, is an interactive computer program and knowledge base. It will help highway inspectors and engineers diagnose problems, select materials for new construction or reconstruction, and repair highways and highway structures such as concrete pavements and bridge columns. HWYCON contains facts and accepted practices, as well as "rules of thumb" from concrete experts at NIST and organizations such as the American Concrete Institute. HWYCON also includes explanations of terms, a list of references, and photographs and drawings. The National Research Council's Strategic Highway Research Program sponsored the design of HWYCON. It is expected to be available at a later date from SHRP.

GETTING THE COLD FACTS ON LOW-COST CRYOCOOLERS

Present equipment for cooling superconducting magnets and electronics tends to be large, expensive and less reliable than desired. This restricts most of the market to magnetic resonance imaging and a few large scientific installations such as particle accelerators. If expected advances in high-temperature superconductor technology occur in the near future, a potentially large market will develop for small, inexpensive and reliable cooling equipment in the 30 to 80 K temperature region. A recent article in Superconductor Industry (Fall 1992) by a NIST researcher describes five main types of small cryocoolers (recuperative Joule-Thompson and Brayton cycles, and regenerative Stirling, pulse-tube, and Gifford-McMahon cycles), detailing their operating principles, advantages, disadvantages and relative costs. The article concludes with some observations on future trends and development needs in the field. For a copy of paper 45-92, contact Sarabeth Moynihan, MC 104, NIST, Boulder, CO 80303-3328, (303) 497-3237.

NIST, OIL COMPANY STUDY "GREEN" WASTE DISPOSAL

Scientists from NIST and a U.S. oil company are teaming up to study environmentally acceptable ways to dispose of wastes. NIST and the oil company recently signed a cooperative research and development agreement to investigate the destruction of various toxic compounds in near-supercritical water. At high temperatures (above 374 °C) and high pressure (above 22.1 MPa, or 3250 lb/in^2), water exists in a "supercritical" state with properties of both a liquid and a gas. Oxidation (that is, combustion) in supercritical water is known to convert a variety of hazardous wastes into relatively benign compounds, such as carbon dioxide and inorganic salts. NIST and the oil company plan to study chemical reactions inside a reactor at near-supercritical conditions and analyze in what manner beneficial waste destruction takes place. The U.S. military and private industry eventually may use the process to turn hazardous wastes into harmless compounds.

NIST AND INDUSTRY TEAM FOR MMIC PACKAGING

NIST and a private company have signed a cooperative research and development agreement whereby NIST will characterize packaging for monolithic microwave integrated circuits. Specifically, NIST will use a microwave network analyzer to characterize the interconnections in ceramic electronic packages under terms of the one-year agreement. The private company will provide NIST with test wafers, including calibration structures specified by NIST and test structures of interest to

the company. The test wafer will include three types of transmission line: stripline, microstrip, and coplanar waveguide, each usable over a frequency range of 0.045 to 40 GHz. The test wafer also will include transmission lines of varying line widths. Results of the measurements will be published. For more information, contact Roger B. Marks of NIST at (303) 497-3037 or Martin Goetz of StratEdge at (619) 569-5000.

NIST SEEKS ALTERNATIVE SUPPRESSANTS TO HALON 1301

As part of an interagency program to screen potential alternatives to halon 1301 for in-flight fire suppression, NIST is seeking candidate chemicals, or mixtures of chemicals, for review. Submitted candidates would be in addition to the 12 already being evaluated: HFC-32, HFC-32/HFC-125 (azeotrope), HFC-227, HCFC-22, HFC-134a, FC-116, HCFC-124, HFC-125, FC-218, FC-31-10, FC-318, and $NaHCO_3$. Suppressants submitted for review must meet specific criteria and either be currently in commercial production or expected to be so by September 1994. NIST will not necessarily perform any laboratory tests on the submitted products. Contact Richard G. Gann, B250 Polymer Building, NIST, Gaithersburg, MD 20899-0001, fax: (301) 975-4052.

RESPONSE GROUP FORMED TO PREVENT SECURITY PROBLEMS

Government and private organizations in North America and Europe have formed a coalition to help combat and prevent the world's escalating computer and network security problems. Called the Forum of Incident Response and Security Teams, or FIRST, the group joins together various computer security incident response teams from the public and private sectors, as well as from universities. Incident response teams generally augment an organization's overall computer security efforts by focusing on computer security incidents. FIRST aims to foster cooperation and coordination in incident prevention, prompt rapid reaction to incidents, and promote information sharing among members. Response teams typically are set up to serve a defined constituency. In many cases, a team serves a single organization's computer network users. Computer vendors operate other teams and deal primarily with their specific operating systems. For more information, contact the FIRST secretariat, Dennis Steinauer, A216 Technology Building, NIST, Gaithersburg, MD 20899-0001, (301) 975-3359.

DATES SET FOR 1993 OSE IMPLEMENTORS' WORKSHOPS

The Open System Environments Implementors' Workshop (OIW) has scheduled its meetings for the remainder of calendar year 1993. They are June 7–11, Sept. 13–17 and Dec. 6–10. All meetings will be held at NIST headquarters in Gaithersburg, MD. The OIW was formed in 1983 as an open international forum with participation of more than 200 computer manufacturers, word processing vendors, semiconductor companies, communication carriers and various users from the United States and other countries. Co-sponsored by NIST and the Institute for Electrical and Electronics Engineers Computer Society, the workshop is organized into special interest groups that develop agreements for various functional and applications areas of open system environments such as electronic mail, file transfer, and network management. Workshop agreements are published and available to the public. For more information or to register, contact Brenda Gray, B217 Technology Building, NIST, Gaithersburg, MD 20899-0001, (301) 975-3664.

CRADA YIELDS EXPERT ADVICE FOR SMALL MANUFACTURERS

NIST and a private company have agreed to incorporate NIST's decision-support software package Automan in an expert system to facilitate technology transfer to small manufacturers. Under a Phase II Small Business Innovation Research grant from the U.S. Department of Agriculture, the private company is developing Production Advisor, an expert system for helping manufacturing managers analyze their production systems, establish key technology improvement goals, identify candidate technologies to meet these goals, evaluate solutions, and implement the selected technology. Originally developed for the U.S. Navy's MANTECH program, Automan implements the analytical hierarchy process, a mathematical decision tool that allows several options to be compared based on multiple, complex and not necessarily quantifiable criteria. Under the cooperative research and development agreement, Automan will be used by Production Advisor in the initial analysis of a production system and the final evaluation of technology alternatives. Although Production Advisor initially will target circuit-board assembly, the private company expects to extend the expert system easily to other small manufacturing operations.

FOR ACCURATE LAB THERMOMETERS, CALL NIST

Hospital and clinical laboratories rely on precise temperature measurements to ensure accurate results for many of the medical tests they perform daily. For example, changes in temperature can affect enzyme rate analyses, pH and blood gas analyses, as well as many other measurements. To help the medical community achieve the necessary accuracy, NIST offers for sale Standard Reference Material 934, a clinical laboratory thermometer calibrated at four points. Certified at NIST, the standard reference thermometer is a 300 mm long, mercury-in-glass instrument that is calibrated at 0, 25, 30, and 37 °C. SRM 934 comes in a wooden case with a Report of Calibration and a detailed publication, Description and Use of a Precision Thermometer for the Clinical Laboratory. It is available for $637 from the Standard Reference Materials Program, Room 204, Building 202, Gaithersburg, MD 20899-0001, (301) 975-6776, fax: (301) 948-3730.

NEW SCANNER ACCURATELY MEASURES MAGNETIC DOMAINS

Thin-film magnetic read head performance depends in part on controlling magnetic domain formation. Domains can cause irreversible magnetoresistive (MR) response and Barkhausen noise. NIST researchers have developed a scanning four-probe resistance measurement system for studying and measuring the formation and movement of magnetic domains in thin-film magnetic read heads. The voltage probes have tip radii of about 0.1 μm and can be independently positioned to within 0.05 μm under video-microscope observation. Applying two orthogonal magnetic fields measures the MR response as a function of field magnitude and angle. These features provide a unique dynamic picture of the MR response of extremely small areas. The researchers found that magnetostatic interactions and nontransverse applied field components lead to the formation of domains and subsequent Barkhausen noise. Domain formation can be suppressed by reducing the magnetostatic interactions with flux closure schemes or by exchange biasing the film.

AUTOMATED FREQUENCY MEASUREMENT AT YOUR SERVICE

Calibration managers in the electronic equipment, defense, aerospace, automotive and computer industries will be interested in NIST's automated frequency measurement service that increases productivity and reduces cost. Each subscriber receives a computer-controlled device that fits easily on a desktop or small table. All calibration results are displayed using high-resolution, full-color graphics, and the data are transferred simultaneously back to NIST via modem for traceability. Certification of the traceability is reported monthly to subscribers. Measurements are accurate enough to calibrate quartz, rubidium or cesium oscillators; up to four oscillators can be calibrated at one time. Since the system is completely automatic, it does not require any operator attention. For more information or to subscribe to the service, contact George Kamas, (303) 497-3378, or Michael Lombardi, (303) 497-3212, Div. 847, NIST, Boulder, CO 80303-3328.

STEP GETS "GREEN LIGHT" TO BECOME STANDARD

The U.S.-led drive to create a universal system for the exchange of manufacturing product data moved closer to reality on Feb. 26 when the initial release of STEP (Standard for Exchange of Product Model Data) was approved as a draft international standard. The International Organization for Standardization (ISO) Technical Committee 184/SC4 unanimously approved the STEP release addressing drafting and mechanical design applications. Following a 6 month comment period, the draft standard will become official and will be known as ISO 10303. "This vote reflects a broad consensus across Europe, Japan and the United States that the initial release of STEP is now technically complete and that production-quality software implementations may now begin," says a NIST engineer who serves as chair of the ISO committee. Seventeen additional applications of STEP are under way. NIST coordinates much of the U.S. effort in STEP and hosts an industry-government sponsored National Initiative for Product Data Exchange at its Gaithersburg, MD, headquarters.

NIST, NTTC TEAM UP TO BOOST U.S. COMPETITIVENESS

The National Technology Transfer Center—the "information gateway" to the technologies and expertise existing in more than 700 federal laboratories—and NIST have announced a new partnership to help U.S. manufacturers become competitive internationally. Specifically, NTTC and NIST will seek to:

- cross train personnel on each organization's mission, expertise and activities;
- establish methods for maintaining close working relationships between staffs;
- coordinate and link electronic databases and bulletin boards;
- share information on program evaluation criteria and techniques; and
- ensure that NIST's seven Manufacturing Technology Centers have the opportunity to serve as field technical experts for NTTC.

CRADA PARTNERS TO SEEK ALTERNATIVE REFRIGERANT

The Electric Power Research Institute—the research and development arm of the electric utility industry" and NIST have signed a cooperative research and development agreement to help industry find environmentally friendly replacements for R22, a refrigerant used widely in home air conditioners and heat pumps. R22 contains hydrochlorofluorocarbons, chemicals believed to be damaging the Earth's ozone layer and scheduled for phase out starting in 2015. Engineers at NIST will test two mixtures of refrigerants—R32/R134a and R32/R125/R134a—to determine their boiling properties and assess how well they will perform in equipment. EPRI will use the NIST data to advance its development of new heating and cooling technologies that are more efficient than existing systems, have zero ozone depletion potential and minimize greenhouse gas emissions.

COMMENT PERIOD BEGINS FOR OPEN SYSTEMS STANDARD

A coalition of government and industry organizations is seeking comments through NIST on a proposed specification that, when adopted, will become common to a variety of open systems users. The Industry Government Open Systems Specification is designed to provide common requirements for Open Systems Inter-connection products and services, enabling the computer industry to develop products that meet the needs of a broad user market. IGOSS will eliminate the separate OSI profiles that coalition participants now use. Participants—which include NIST, the Canadian government and the electric power industry—plan to use IGOSS as the primary reference for functional profiles to be issued by individual IGOSS organizations in the future. Written comments on IGOSS's technical content should be sent to Gerard Mulvenna, B217 Technology Building, NIST, Gaithersburg, MD 20899-0001, (301) 975-3631 by May 15.

BIOTECH FIRM ESTABLISHES CARB FELLOWSHIP

A private company has established a $100,000 fund for a graduate fellowship in structural biology at the Center for Advanced Research in Biotechnology. The Maryland Biotechnology Institute will use the fund to award fellowships to students entering the Molecular and Cell Biology Program of the University of Maryland College Park, and who intend to carry out their graduate research at the CARB. CARB was established in 1984 by NIST, the University of Maryland and Montgomery County, MD, as a unique center for government, academic, and industry scientists. The private company, one of Maryland's largest biotechnology employers, develops laboratory products for biological research in medical diagnostics, tissue culture, cell biology, immunology, and molecular biology; and manufactures and markets related reagents. Beginning September 1993, the $100,000 fund for the graduate research fellowships will be paid over a 5-year period at the rate of $20,000 a year. In consideration of this commitment, the University of Maryland has agreed to waive tuition for fellowship recipients.

NEW PAPERS ADDRESS LAB USES FOR DIODE LASERS

NIST has been a pioneer in the scientific applications of diode lasers, devices better known for their use in CD players and laser-jet printers. Two new papers are available from the institute on diode lasers: one discussing their ability to measure frequency and length, and the other detailing how to overcome technical problems with their use. In the first paper, the authors describe the development

of diode lasers that operate in the visible portion of the electromagnetic spectrum and the opportunities this offers for frequency measurements and frequency/length standards. Also highlighted is an anti-reflection coated red diode laser operating on a calcium transition at 657 nm. Among the technical difficulties discussed in the second paper are tuning problems (eliminated by using wavelength selective optical feedback) and amplitude fluctuation of the detected laser light (the authors recommend the use of electronic feedback). For copies of the two papers (designated by no. 93-6), contact Sarabeth Moynihan, Div. 104, NIST, Boulder, CO 80303-3328, (303) 497-3237.

VIDEO HIGHLIGHTS 1992 BALDRIGE AWARD WINNERS

What is quality management? Why is it important to U.S. competitiveness? How is it achieved? In a new 19 minute video, representatives from the five 1992 winners of the Malcolm Baldrige National Quality Award answer these questions and others on quality and quality management. The 1992 winners are AT&T Network Systems Group/Transmission Systems Business Unit, Morristown, NJ; Texas Instruments Inc. Defense Systems and Electronics Group, Dallas, TX; AT&T Universal Card Services, Jacksonville, FL; The Ritz-Carlton Hotel Co., Atlanta, GA; and Granite Rock Co., Watsonville, CA. The 1992 winners video is available from the American Society for Quality Control for $20. Order item TA512 in ASQC's inventory by calling (800) 248-1946. Videos highlighting Baldrige winners from the previous 4 years also are available from ASQC.

U.S./CANADA MUTUAL TYPE EVALUATION RECOGNITION

As a result of meetings sponsored and organized by NIST, Canadian and U.S. representatives agreed to mutual recognition of type evaluation tests conducted by and for both nations. In partnership with the National Conference on Weights and Measures, state weights and measures agencies, federal agencies, and device manufacturers, NIST manages the National Type Evaluation Program, using six "participating laboratories" around the nation and four other field evaluation sites to evaluate prototype designs of commercial measuring equipment against national standards. Such varied equipment includes retail, truck, in-motion railroad and shipping scales, motor fuel dispensers, point-of-scale systems, load cells, digital indicators, computer software, and fluid meters.

Representatives from these laboratories, the NCWM, and NIST will now work with Canada's type evaluation laboratory to compare requirements and test protocols so that manufacturers may submit commercial devices to laboratories in either or both nations. Further steps will be necessary to permit manufacturers to design to a single set of performance criteria; however, this agreement to work with Canada's legal metrology group represents the first step toward harmonization of national requirements as a means of removing barriers to trade with our largest trading partner in commercial devices.

1992 CONFERENCE OF LEGAL METROLOGY IN GREECE

A NIST scientist headed the U.S. delegation to the 9th Quadrennial Conference of Legal Metrology in Athens, Greece, Nov. 2–6. Another NIST scientist and a representative of the Department of State were members of the official U.S. delegation, which also included observers representing the NIST Weights and Measures Program, the National Conference on Weights and Measures, and a private company. Representatives of 41 of the 49 member nations of the International Organization of Legal Metrology (OIML) participated.

The conference establishes overall policy for OIML, sanctions (ratifies) the OIML recommendations approved during the previous 4 years, and establishes a budget for the International Bureau of Legal Metrology for the next 4 years. Eighteen recommendations on the performance requirements of measuring instruments were sanctioned. The United States was directly responsible for four of these recommendations (load cells, atomic absorption spectrometers for measuring metal pollutants, electronic weighing instruments, and direct mass flow measuring systems for liquids) and strongly influenced the development of four other recommendations (instruments for measuring vehicle exhaust emissions, non-automatic weighing instruments, automatic rail-weighbridges, and discontinuous totalizing automatic weighing instruments). The status of the technical work, the long-range policy, the program for developing countries, and liaison reports of cooperation with other international organizations were also discussed.

The 27th Meeting of the International Committee of Legal Metrology (CIML) was held in conjunction with the conference. A NIST scientist is

the U.S. member of CIML, which develops policy for the technical activities of OIML, establishes the work structure, and approves work projects and official OIML publications (recommendations and documents). Significant decisions were made for new work procedures for developing and approving the technical work, new committee structures and associated work projects, and assignment of some new committee secretariats to member nations. The United States was assigned responsibility for five of the 18 new technical committees (metrological control; prepackaged products; instruments for measuring mass and density; instruments for measuring pressure, force, and related quantities; and instruments for measuring pollutants).

NIST SCIENTISTS ABLE TO OBSERVE ONE ELECTRON IN 10 BILLION

A NIST scientist and a guest researcher have performed an experiment that indicates the presence of a single excited electron above a condensed ground state of 10^{10} superconducting electrons. At the very low temperature of the experiment (0.035 K), electrons are bound together in pairs, the usual picture of the superconducting state which allows the dissipationless flow of electrical current. Prior to the invention of the single-particle electrometer, little consideration had been given to what would happen if there happened to be an odd number of electrons in the sample. Obviously the last one could not be paired.

The experimenters used a Coulomb-blockade electrometer composed of two ultra-small tunnel junctions fabricated by electron-beam lithography and a double-angle evaporation process. Earlier work at NIST had demonstrated that this configuration of electrometer has the capability of making the required observations, with noise levels of only 0.0001 electrons at 10 Hz. The electrometer used in this experiment differs from that reported by other workers in that it has two normal-state outer electrodes and a submicrometer superconducting central electrode, or island, a configuration designated N-S-N. The dimensions of the island give rise to the 10^{10} figure for the number of superconducting electrons involved. The use of normal-state outer electrodes in the electrometer prevents them from being a source of superconducting tunneling electrons, a problem that has confused the results from S-S-S electrometers (all electrodes superconducting) used by others. The results of this experiment have been submitted to Physical Review Letters.

FAST PULSE TEST SERVICES RE-ESTABLISHED AT NIST

Special-test services for measurements of fast electrical pulse waveforms are now operational at NIST. These services include: Impulse Generator Spectrum Amplitude (NIST Calibration Services Users Guide (SP250) Test No. 65100S), Fast Repetitive Baseband Pulse Parameters (65200S), Network Impulse Response (65300S), and Pulse Time Delay through Coaxial Transmission Lines (65400S). All of these special tests are performed "at cost"; experience suggests that a typical customer incurs fees on the order of a few thousand dollars for measurements on a single transfer standard. The NIST Automatic Waveform Analysis and Measurement System, which is the heart of the apparatus used to perform these measurements, has been installed in an electromagnetically shielded enclosure having a floor area of 5 by 5 m, ambient temperature controlled to about ± 0.5 °C, and incoming ac line power both filtered and dynamically regulated.

Initial measurement results obtained under these improved environmental conditions indicate that the measurement uncertainties are now generally smaller, in some cases by a factor of two or more. In 1993, the goals for the service are to reduce time and amplitude errors and to reflect all improvements in the services' advertised uncertainties, which are to be expressed in accordance with the International Standards Organization 9000 guidelines.

SUBMICROMETER-RESOLUTION SCANNER DEVELOPED FOR DYNAMIC MEASUREMENTS OF DOMAINS IN MAGNETIC READ HEADS

NIST scientists have developed a scanning four-probe resistance measurement system for studying and measuring the formation and movement of magnetic domains in thin-film magnetic read heads. This development responds to a need to control domain formation, which degrades device performance, leading to irreversibility in the magnetoresistive (MR) response and to Barkhausen noise, also detrimental to head performance. The upcoming generation of magnetic recording media has bit densities that challenge the capabilities of existing inductive reading methods; in response to this limitation, the cutting-edge head technology is based on MR effect in soft ferromagnetic materials.

The voltage taps are microprobes fabricated from beryllium copper with a tip radius on the order of 0.1 μm. Each probe can be moved independently of the other with a step resolution of 0.05 μm. Microprobe placement and movement are monitored by both a horizontal and vertical microscope-camera viewing system. Two orthogonal magnetic fields can be applied to the device being studied so that the MR response can be studied as a function of field magnitude and angle. The scanning system is used to measure local MR responses of the device, from which the local magnetic structure is inferred. This information indicates where and under what field conditions domains are formed. The team has found that magnetostatic interactions, along with a nontransverse applied field component, lead to the formation of domains and subsequent Barkhausen noise. Domain formation can be suppressed by reducing the magnetostatic interactions with flux closure schemes or by exchange biasing the film. The scanning microprobe system is unique in that local areas of the MR device can be measured dynamically as a function of applied field with submicrometer resolution.

NEW PROCESS PRODUCES NIST 10 V ARRAY STANDARDS WITH INDUSTRY COLLABORATION

A NIST scientist has developed a new process for fabricating 10 V Josephson-junction voltage array standards. Working jointly in the context of a cooperative research and development agreement with a private company, the process uses an SiO_2 insulating layer deposited by the company together with niobium trilayer Josephson junctions fabricated at NIST. The resulting yield of 50 percent for the process of making the 20000 junction chips, each of which constitutes an array standard and is available only from NIST, is sufficiently good that NIST has eliminated its backlog of orders for the standards and has a number in reserve. Delivery of a new deposition system for SiO_2 insulators in the spring of 1993 will return full in-house fabrication capability to NIST for the 10 V chips, and serious consideration is being given to discontinuing the fabrication and sale of the simpler 1 V, 3000 junction chips at that time. NIST anticipates that the success of the new process should make commercial production of voltage array standards possible.

NIST SCIENTIST CHAIRS WORKSHOP RESPONDING TO INDUSTRY NEEDS FOR MCT CHARACTERIZATION

A NIST scientist recently organized and chaired the Workshop on Measurement Techniques for Characterization of Mercury Cadmium Telluride (MCT) Materials, Processing, and Detectors, held in response to industry needs for enhancing the manufacturability of infrared focal plane arrays. Problems encountered have led to increasing concern that the ability to grow and fabricate device structures has outgrown the ability to provide the characterization methods needed to advance infrared detector technology. In addition, a lack of understanding of the materials-, processing-, and device-related theory underlying the use of both routine and state-of-the-art characterization methods interferes with interpretation of results.

Interest in these issues drew 117 participants for the workshop's nine invited review and 10 poster papers. Topics covered by the invited papers included how silicon materials characterization has evolved and what has been learned with silicon to improve the manufacturing of other devices based on different materials; the impact of characterization methods on MCT infrared detector technology; in-situ characterization methods for monitoring and control of vapor-phase epitaxial growth of MCT; test structures used in semiconductor electronics with applications to infrared detector materials and processes; and magneto-transport, minority-carrier-lifetime, and scanning-laser-microscopy characterization methods. The poster papers presented newly available methods, including a lifetime screening technique using transient millimeter-wave reflectance and characterizations by photo-induced microwave reflection, far-infrared photoluminescence, pulsed infrared synchrotron radiation, direct Zeeman atomic absorption spectroscopy, and Faraday rotation. The NIST scientist will serve as editor of the workshop proceedings, to be published in 1993 as an issue of Semiconductor Science and Technology.

NAVY PRODUCTIVITY IMPROVED WITH FASTENER WORKCELL

Since the advanced fastener workcell was installed at the Portsmouth Naval Shipyard, it has been producing level-1 fasteners. The workcell is a direct technology transfer to the U.S. Navy from the NIST Automated Manufacturing Research Facility, which is the Navy Center of Excellence for automated discrete-part manufacturing technology.

Based on a General Accounting Office study issued in its 1991 report, military safety-critical fastener products have a rejection rate of 40 percent or higher. The failure of these fastener products has caused a number of helicopter accidents. Production data of the fastener workcell for the last few months received by NIST indicate that the median production time for a fastener is about 10 min (50 percent better than the design goal of 20 min) as compared to 90 min with conventional means. Employing a variable thread measurement system and error compensation technique, safety-critical fastener production at Portsmouth, thus far, is running with 99 percent of the manufactured parts meeting specifications and a rejection rate of only 1 percent.

INFORMATION TECHNOLOGY VISION FOR THE U.S. FIBER/TEXTILE/APPAREL INDUSTRY

A NIST scientist has published a report entitled, Information Technology Vision for the U.S. Fiber/Textile/Apparel [FTA] Industry.

The ideas presented in the report were developed through interactions with the FTA industry while working on the Apparel Product Data Exchange Standard project. The goal of the project is to develop manufacturing data standards, based on the Standard for the Exchange of Product Model Data, for integrating the information needed to operate an apparel manufacturing enterprise.

The scientist's report describes the importance of the FTA industry to America's economic well-being, the threat to the industry due to imports, opportunities for the use of information technology to advance the industry and counter the import threat, and the roles the organizations involved with the industry can play. Information technology is described as the "linchpin" for the research and development required.

NIST plans to convene a workshop with FTA industry leaders to explore more fully the information technology needs of the industry and develop a plan to satisfy those needs. The scientist's report will provide a straw man for such a plan.

NIST SCIENTIST TO CHAIR NEW ISO TECHNICAL COMMITTEE ON SURFACE CHEMICAL ANALYSIS

The International Organization for Standardization (ISO) recently formed a new Technical Committee on Surface Chemical Analysis, which is designated ISO/TC 201. A NIST scientist was nominated by the Japanese standards body (the host of the ISO/TC 201 Secretariat) to be chairman of the new technical committee, and his appointment was confirmed recently by the ISO technical board. The new technical committee was formed following a proposal from Japan and currently has 10 full participating members (the national standards bodies of Austria, Belgium, China, Germany, Japan, Russia, Sweden, Turkey, the United Kingdom, and the United States) and 15 observer members (the national standards bodies of Australia, Egypt, Finland, France, India, Ireland, Korea, Norway, Philippines, Poland, Romania, Singapore, South Africa, and Switzerland).

The official scope of ISO/TC 201 is "standardization in the field of surface chemical analysis, which uses electrons, ions, neutrals or photons both as an incident beam and a detecting signal." With current techniques of surface chemical analysis, compositional information is obtained for regions close to a surface (generally within 20 nm) and composition-versus-depth information is obtained with surface analytical techniques as surface layers are removed.

ISO/TC 201 plans to create a variety of subcommittees. One will work to promote the harmonization of requirements concerning instrument specifications, instrument operations, specimen preparation, data acquisition, data processing, qualitative analysis, quantitative analysis, and reporting of results. Others will establish consistent terminology, and develop recommended procedures and promote the development of reference materials and reference data to ensure that surface analyses of the needed precision and accuracy are made. ISO/TC 201 will also prepare draft international standards.

STOP-ACTION MEASUREMENTS OF ENERGY TRANSFER PROCESSES

In a joint research effort involving scientists at NIST, picosecond lasers are being used to determine the rates and mechanisms for energy flow from metal substrates to the vibrational modes of chemisorbed molecules. Such information is critically important to understanding chemical reactivity at surfaces since sticking, desorption, surface mobility, and chemical reactions are activated by vibrational excitation. The coupling of optical radiation to surface reactions is receiving attention in catalysis, semiconductor processing, and solar energy conversion.

In these first experiments, carbon monoxide (CO) chemisorbed at monolayer coverage on a clean Pt(lll) crystal was studied because it is the adsorbate/substrate system best characterized by traditional non-time-resolved methods. The experiments have revealed a fascinating series of snapshots of a warp-speed world where changes can occur in the time that it takes light to travel a mm or so. Two laser pulses of about 0.9 ps (1 ps = 10^{-12} s) duration hit the crystal; one is a visible pump pulse, the other an infrared probe pulse which determines the energy content of the Pt and CO vibrational modes by absorption spectroscopy as a function of pump/probe time delay. The pump pulse excites the Pt substrate (initially at T = 150 K) creating hot electrons near the surface (penetration depth = 15 nm). These hot electrons initially have an elevated electronic temperature $T_e \approx 250$ K. In 1.6 ps the hot electrons equilibrate with the Pt lattice vibrations (phonons) giving $T_{lat} = T_e = 200$ K. The hot electrons and phonons then energize one of the four vibrational modes of the chemisorbed CO, specifically the frustrated translation mode at a frequency $\nu = 1.8$ THz (60 cm^{-1}). The temperature T_{ads} of this mode comes into equilibrium with T_e and T_{lat} in 2 ps. If the mode is excited only by the hot electrons, then T_e and T_{ads} have a coupling time of 2 ± 1 ps. If instead the mode couples only to the Pt phonons, then T_{lat} and T_{ads} have a coupling time less than 1 ps. On a longer timescale of 100 ps, the three coupled temperatures return to the initial value as heat diffuses away from the surface into the Pt crystal.

These experiments provide the first useful estimates of these energy transfer rates, which are quite fast and comparable to the 0.6 ps vibrational period of the excited mode. The NIST group is now starting experiments on other systems (e.g., CO/Cu) in order to test theories being developed by colleagues in private industry.

NEW DETECTOR-BASED PHOTOMETRIC SCALES AND IMPROVED PHOTOMETRIC CALIBRATION SERVICES

The candela scale recently was established using standard photometers calibrated against a high-accuracy cryogenic radiometer, the basis of the NIST detector spectral responsivity scale. The measurement chain was shortened significantly compared with the traditional candela scale based on a fixed temperature blackbody. This resulted in an improvement of the scale uncertainty of a factor of 2 to 0.5 percent (3σ). Eight photometers are now maintained as the primary standards for the illuminance and the luminous intensity scales, rather than groups of lamps of different wattage.

This change makes photometric calibration services at NIST more versatile and flexible than ever before. Luminous intensity of light sources, ranging from 10^{-3} to 10^{4} cd, can be calibrated directly with the standard photometers because they have a linear response over this range and an illuminance sensitivity as low as 10^{-7} lx. Users' illuminance and luminance meters can be calibrated directly against the NIST standard photometers or a calibrated integrating sphere source. The total flux of incandescent lamps, with outputs ranging from 10^{-1} to 10^{5} lm, can be calibrated by direct substitution with NIST total luminous flux standard lamps—providing industry with an improved basis for measuring the performance of lamps and photometers, such as measuring the lighting efficiency (lm/W) of miniature lamps used in automotive applications.

NIST ASSISTS THE STATE OF MARYLAND IN RADIATION DOSE RECONSTRUCTION FOR AN INDUSTRIAL ACCELERATOR ACCIDENT

In December 1991, a radiation overexposure occurred at an industrial radiation facility in Maryland. An operator violated safety procedures and placed his hands, feet, and head in a high-energy electron beam resulting in severe disability. At the request of state of Maryland officials and the attending physician, a team of NIST scientists conducted post-accident radiation measurements at the facility. Radiation dosimeters were mounted in strategic locations in the accident area, and the accident conditions were reproduced according to personal accounts. The results were used by the physician to assess the degree of the exposure. In follow-up studies, bone samples from the victim were examined at NIST to measure directly the absorbed radiation dose received by the victim. A paper describing the reconstruction dosimetry for this accident has been accepted by the journal Health Physics. The details of the NIST and state of Maryland measurements will assist the health physics community in designing improved safety procedures to prevent future accidents and in formulating measurement protocols for accelerator accident victims.

STRUCTURAL STUDIES OF LANGMUIR-BLODGETT FILMS USING NEUTRON REFLECTIVITY

A collaborative research effort between NIST scientists and guest scientists from the Institute of Crystallography, Moscow; the Max Planck Institute for Polymer Research, Germany; and the University of Akron, Ohio, is under way to understand the microscopic structures of organic Langmuir-Blodgett (LB) film systems. The principal probe in these investigations is neutron reflectivity in which the large difference in neutron scattering power for hydrogen and deuterium isotopes, makes it possible to determine the chemical composition profile normal to the plane of the film with near nanometer resolution.

LB films, created by forming a monomolecular layer of surfactant molecules on a water surface and then transferring onto a solid substrate (and repeating several times to form multilayers), may consist of fatty acids, polymers, polymerizable compounds, and lipids, as well as proteins and nucleic acids. The applications of LB films are many. LB films are used in liquid crystal displays, resists for electrons and photon lithography, optical lens coatings, molecular lubricants, capacitors and other microelectronic devices, and biosensors. Biologically important molecules that do not crystallize, such as proteins, also can be incorporated in LB films with an artificial periodicity and specific orientations, which makes it possible to obtain unique structural information from diffraction or reflectivity measurements.

Despite all of the above-mentioned existing and potential applications, relatively little is known about the detailed, microscopic structure of the LB films themselves. Such knowledge is essential for a proper understanding of their basic properties and is the principal goal of the present research.

MAGNETIC SENSOR FOR MECHANICAL PROPERTIES

NIST is undertaking a project to develop magnetic sensors for mechanical properties. The project is scheduled to begin in CY 1993 and, if successful, the sensors could be used to monitor the properties of sheet steel on-line and, thereby, facilitate the implementation of intelligent processing systems for the steel industry. Such systems are both cost effective and energy efficient.

It has long been known that Barkhausen noise, magnetoacoustic emission, residual magnetization, hysteresis, permeability, coercive force, and flux leakage are all sensitive, in some degree, to mechanical properties. The challenge in using magnetic measurements to monitor mechanical properties is to select that measurement, or combination of measurements, which can be made rapidly in a production environment and which will be effective in detecting changes in the properties of most interest. In preparation for this project, preliminary studies on sheet steel have been carried out at NIST. These studies showed that conditioning of the sheet, i.e., whether it was cold or hot rolled, and some of the resulting mechanical properties could, indeed, be discerned by magnetic measurements. Differences in yield strength and other mechanical properties that are strongly dependent upon ferrite grain size, and residual stresses, could be correlated with Barkhausen magnetic measurements.

FIRST DIRECT OBSERVATION OF PHOTOREFRACTIVE GRATINGS IN A NONLINEAR OPTICAL MATERIAL

The lattice deformation due to photorefractive space charge fields in a nonlinear optical material has been observed directly for the first time in recent x-ray diffraction imaging of barium titanate. The work was performed by NIST at the National Synchrotron Light Source at Brookhaven National Laboratory.

Two beams split from a 50 mW frequency-doubled YAG laser at 532 nm were used to form high-contrast fringe patterns (modulation 96 percent) with fringe periods between 7 and 50 μm. X-ray diffraction images were obtained for the piezoelectric strain pattern induced by the resulting charge redistribution. In this work, interior 180 degree crystal domains also were observed directly for the first time and identified unambiguously through their phase shift of the fringe pattern.

Direct observation both of the optically induced grating and of the 180 degree crystal domains is expected to provide guidance for improving the performance of devices made from this material for high-capacity optical information processing.

MEASUREMENTS FOR POLYMER PROCESSING CONSORTIUM

Members of the Measurements for Polymer Processing Consortium attended a semi-annual consortium review meeting at NIST in Dec. 1992. This was the first review meeting of this NIST/

industry consortium since its inauguration in June 1992. Industry representatives participated in discussions regarding industry requirements for real-time measurements of polymer processing parameters, particularly temperature and viscosity. The NIST measurement program, which is based on optical methods of measurement, utilizes optical fiber probes to monitor the state of polymer resins at specific positions in the process stream of polymer processing machinery. Introductory presentations by NIST staff included a summary of previous NIST experience of instrumenting a polymer injection molding machine and a twin screw extruder with optical fibers. Discussions of current work focused on measurement methods to monitor temperature and viscosity using fluorescence spectroscopy. The fundamental science underlying the measurement concepts was thoroughly discussed. A request from industry representatives to develop a method to measure temperature gradients (the temperature profile through a thickness of polymer resin) during processing was unanimously supported by those present. Industry representatives agreed that accurate knowledge of temperature, temperature gradients, and viscosity are needed to understand the physics of polymer processes and to optimize productivity and product performance.

NIST CONDUCTS ASSESSMENT OF VENTILATION MEASUREMENT TECHNIQUES

NIST staff conducted a study of ventilation and ventilation measurement techniques in the Bonneville Power Administration Building in Portland, OR. This project involved an assessment of outdoor air-ventilation measurement techniques for use in mechanically ventilated commercial buildings. These techniques were evaluated for the practicality of their use in the field and their reliability. The following measurement techniques were compared: tracer gas decay measurement of whole building air change rates, the determination of air change rates based on peak carbon dioxide concentrations, the determination of percent outdoor air intake using tracer gases, and direct airflow rate measurements within the air handling system using traditional engineering approaches. Airflow rates were measured in the air-handling system ductwork using pilot tube, hot-wire anemometer, and vane anemometer traverses. Good agreement was obtained between the different techniques. While accurate determinations of percent outdoor air intake were achieved using tracer gas techniques, the use of carbon dioxide detector tubes yielded unreliable results. Reliable determinations of ventilation rates per person were made based on sulfur hexafluoride decay and direct airflow rate measurements, but the use of peak carbon dioxide concentrations led to inaccuracies, e.g., the overprediction of ventilation rates by as much as 100 percent.

NIBS PROVIDES NIST WITH RESEARCH RECOMMENDATIONS

In Dec. 1992, the National Institute of Building Sciences (NIBS) held its Research Recommendations Subcommittee meeting to discuss and prioritize building and fire research needs. Private-sector and federal agency members participated. Requests for building and fire research recommendations were polled from more than 3500 members of private and public construction and fire-related organizations. The poll seeks to determine what areas of research are most important to these organizations. Over 50 research recommendations were evaluated by four subcommittees: structures, materials, environment, and fire. Priority recommendations will be provided as input to creating the NIST program plan. The recommendations are solicited and evaluated following the criteria: national need and relevance to NIST mission, expertise, and facilities.

Since 1986, NIBS has provided NIST with recommendations for building and fire research. This NIBS activity was initiated in response to the House Committee on Science and Technology's request that NIST consult with NIBS for research recommendations. A memorandum of understanding exists between NIST and NIBS to facilitate the development of these research recommendations.

NIBS was authorized by the U.S. Congress in 1974 to improve the building regulatory environment, facilitate the introduction of new and existing products and technology into the building process, and disseminate nationally recognized technical and regulatory information. NIBS is a non-profit, non-governmental organization bringing together expertise from a representative sample of the public and private building- and fire-related organizations to focus on approaches to reduce barriers for improved building design and construction practices.

NIST DELIVERS HOME FIRE SAFETY INFORMATION TO USERS

NIST recently has completed work on a 20-page booklet entitled Protecting Your Family from Fire. It will be produced both in English and Spanish. The booklet includes information on home fires and how to use smoke detectors, fire alarm systems, and residential sprinklers to protect families, especially those including young children or older persons (who are disproportionately victims of fires). The booklet also provides guidance on the use of flashing lights for alerting hearing impaired persons. Numbers and locations of devices needed, as well as how to test and maintain the devices, are covered. The booklet was developed with the support of the U.S. Fire Administration, which will be handling printing and distribution.

NIST TRAINS BATF AGENTS

NIST recently conducted a 3 day workshop to introduce agents of the Bureau of Alcohol, Tobacco, and Firearms (BATF) to the use of fire models in investigating and reconstructing fire incidents. Fifteen agents, who conduct fire investigations as part of BATF's National Response Teams, participated in the workshop. BATF headquarters staff have been distributing NIST-developed software tools like FPEtool, CFAST, and HAZARD I to their field offices to enhance the technical foundation of their investigations and to improve their performance in obtaining convictions in criminal arson cases.

NEW FEDERAL INFORMATION PROCESSING STANDARDS (FIPS) APPROVED

The Secretary of Commerce has approved three new FIPS for federal agency use. FIPS 177, Initial Graphics Exchange Specification, which adopts ASME/ANSI Y14.26M-1989, will enable federal agencies to use more effective and productive computer-aided design and computer-aided manufacturing techniques.

FIPS 178, Video Teleconferencing Services at 56 to 1920 kb/s, supports the design and development of video teleconferencing systems. The referenced specifications for FIPS 178 are the CCITT Recommendations H.320, H.221, H.242, H.261, and H.230 developed by CCITT with federal government assistance. Systems developed under this standard will facilitate the interoperability of products and services from different suppliers.

FIPS 179, Government Network Management Profile, which adopts Version 1.0 GNMP, specifies the common management information exchange protocol and services, specific management functions and services, and the syntax and semantics of the management information required to support monitoring and control of the network and system components and their resources.

OPEN SYSTEMS ENVIRONMENT (OSE) IMPLEMENTORS' WORKSHOP (OIW) MEETS

On Dec. 14–18, NIST and the IEEE Computer Society co-sponsored the OIW, part of a continuing series of workshops to develop implementation specifications for computer network protocols. About 260 participants attended the meeting.

The OIW Plenary voted to use the Common Programming Interface—Communications (CPI-C) Specification as a reference in the Transaction Processing implementation agreements; the specification has recently been made publicly available. CPI-C is a application programming interface for program-to-program communications and was designed to eliminate incompatibilities between LU 6.2 variations. CPI-C is independent of the underlying transport layer protocols. This marks the first use of public specifications in implementors agreements by a regional workshop. The OIW also adopted the IEEE P1003.0 Open Systems Environment Reference Model for use in their work program.

NEW PUBLICATION FOCUSES ON AUTOMATIC INDEXING

Automatic indexing is becoming a critical technology as more full-text data become available online. NISTIR 4873, Automatic Indexing, provides a tutorial on the single-term indexing of "real world" text and describes advances in automatic indexing beyond the single-term indexing done in most operational retrieval systems. Whereas traditional indexing enables reasonable searching of large full-text documents, more advanced techniques raise the retrieval performance beyond the mediocre level. The document underscores the importance of continuing research in retrieval technologies and the timely acceptance of proven methodologies as standard automatic indexing techniques by the information retrieval community.

STANDARD CLASSIFICATION FOR BUILDING ELEMENTS

NIST scientists have written and NIST is distributing SP 841, entitled UNIFORMAT II: A Recommended Classification for Building Elements and Related Sitework. It provides a standard format for collecting and evaluating costs in the economic evaluation of buildings and building systems. It also provides a standard framework for other design and construction-related activities such as project descriptions and scheduling. The report responded to requests from the building community for a comprehensive standard classification based on building elements rather than building products or materials. At present no such standard exists in North America. The NIST report is the technical basis for the ongoing development by ASTM of a standard classification for building elements and related sitework. It is also the basis for the Construction Specifications Institute's (CSI's) in-press publication entitled Uniformat: A Uniform Classification of Construction Systems and Assemblies. Adoption by ASTM and CSI of NIST's UNIFORMAT II classification will assure its widespread acceptance and use in North America.

WORKSHOP ON EXPERIMENT DESIGN FOR SCIENTISTS AND ENGINEERS

NIST recently held the workshop "Experiment Design for Scientists and Engineers." NIST instructors presented the latest statistical experiment design techniques for improving product and process quality to 24 engineers from regional industries. The engineers had primarily research and development responsibilities and represented a wide spectrum of small to medium-size companies dealing in electronics, communications, chemicals, materials, food, and paper.

The workshop covered comparative designs, full and fractional factorial designs, response surface methods, and Taguchi's approach to reducing variability. The concepts underlying designed experiments were reinforced through hands-on experiments—the students found this feature of the workshop very effective. Students felt the techniques presented would be particularly useful for improving their own product and process quality. NIST plans to offer this workshop on the west coast in the summer of 1993.

U.S. AND CANADA PUBLISH HARMONIZED PERFORMANCE STANDARDS ON PLYWOOD SHEATHING

Harmonized national performance standards for plywood and other wood-based panels (oriented strand board, waferboard, and particleboard) recently have been published as DoC Voluntary Product Standard PS 2-92 Performance Standards for Wood-Based Structural-Use Panels in the United States and as CAN/CSA-0325.0-92 Construction Sheathing in Canada. The U.S. standard was developed and published under DoC procedures at NIST and approved on Aug. 27, 1992.

The standards were developed at the request of a special Binational Committee on Plywood (BNC), appointed by the U.S. and Canadian governments, to resolve issues that were delaying the implementation of the United States-Canada Free Trade Agreement of 1987 (CFTA) with regard to plywood sheathing. The United States was concerned that certain U.S. plywood sheathing was not permitted to be sold in Canada.

An official from the Standards Management Program at NIST represented NIST as an observer in the BNC deliberations and served as secretary of the Standard Review Committee that developed the DoC Voluntary Product Standard for which the American Plywood Association provided financial support.

The Canadian standard now has been incorporated into the National Building Code of Canada, and the U.S. standard has been incorporated into National Evaluation Report NER-108 of the four U.S. model building code organizations (SBCCI, BOCA, CABO, ICBO). With the incorporation of the performance standards into the national building codes, a presidential proclamation was issued in December 1992 that approved staged U.S. reductions in duties on certain plywood originating in Canada on Jan. 1, 1993, in accordance with the provisions of the CFTA.

NIST DISCOVERS "SAND" ON YBCO THIN FILMS

NIST scientists have discovered the hitherto unsuspected existence of insulating nanometer-scale particles on thin films of various specimens of high-critical-temperature yttrium/barium/copper oxide (YBCO). Since the presence of the "sand" affects the film's properties, this discovery is an important

contribution to improved understanding of the films and to their successful exploitation in practical electronic devices, particularly devices using multilayer structures.

The NIST team also suggests that the particles may be the natural pinning sites responsible for the high critical currents observed in YBCO thin films, to date an unresolved issue. The scientists used both scanning tunneling microscopy (STM) and atomic force microscopy (AFM) to examine the surface morphology of specimens prepared by NIST colleagues and by a private company. These methods have the capability of resolving nanometer-scale features, such as individual growth steps on the surface of submicrometer grains, difficult if not impossible to image by other means.

The scientists found that the AFM images revealed the presence of a high density of individual particles, 10 to 50 nm across and 5 to 20 nm high. The STM images did not show these particles, presumably because they are insulating (STMs sense a tunneling current and thus only "see" conducting surfaces). However, subsequent AFM images showed that the STM tip breaks off the particles during scanning and moves them to the edges of the scanned area. AFM images of films from 12.5 to 400 nm in thickness, prepared over a range of deposition temperatures, and on substrates including buffered sapphire, lanthanum aluminate, magnesium oxide, and neodymium gallium oxide were all found to show the nanometer-scale particles (not to be confused with much larger particles commonly observed on laser-ablated YBCO thin films).

NIST APPLIES FOR PATENTS ON ADVANCED TEST STRUCTURES FOR NANOMETER-SCALE MEASUREMENTS

NIST scientists have applied for patents on two test structures having nanoscale capabilities. Test structures are special devices fabricated as an integral part of an integrated-circuit wafer (typically along with product devices) and widely used to measure various parameters associated with the fabrication process, including materials properties and dimensions. Instruments known as wafer probers make electrical contact with test structures through pads on the structures and conduct electric signals from measurement circuits in the probers to and from the structures. Test structures provide means for implementing the large number of measurements required for process control and diagnosis in modern integrated-circuit manufacturing. The employment by the semiconductor industry of increasingly smaller feature sizes requires the development of test structures having capabilities to match.

The first patent covers a line-width micro-bridge test structure. This test structure uses four-terminal bridge resistance measurements to determine the width of a conducting line. An interference in this measurement traditionally has been the shunting effect of the voltage taps. The new test structure contains additional dummy voltage taps and allows the width to be extracted even when the active region of the bridge is short and the voltage taps are arbitrarily wide. The second patent covers a method and structure for eliminating the effects caused by imperfections in electrical test structures utilized in submicrometer feature metrology. This structure also uses four-terminal bridge resistance measurements, in this case employed to determine the separations of pairs of conducting features. By canceling errors caused by asymmetries in, and current shunting at, the voltage taps, the test structure permits feature placement to be determined to within 15 nm.

NIST RECOMMENDS NIJ RESTRICT COMPLIANCE TESTING OF POLICE BODY ARMOR TO LARGE SIZES

The NIST Office of Law Enforcement Standards (OLES) recently completed an experimental evaluation that resulted in a recommendation to the National Institute of Justice (NIJ) to restrict compliance testing of police body armor to physically large specimens, corresponding to shirt or jacket sizes of 46 to 48. NIJ has responded to the recommendation with a statement requesting large-size specimens, with provision for special exceptions in which the armor supplier formally accepts that no retests will be allowed on the basis of size. Body armor is claimed to have saved lives over 1300 times to date; thus its performance is a vital issue to police officers. Under the NIJ program of compliance testing, more than 800 models of body armor have been impacted by bullets under controlled conditions (including bullet type and size, bullet velocity, and pattern of bullet impacts) to determine if the armor models met the NIJ armor standard. In some instances, companies and police departments have submitted small-size specimens, and the law-enforcement community has become concerned that the ballistic test results could be influenced in some unknown way by the size of individual specimens or by minimally spaced shot patterns.

Accordingly, in consultation with NIST scientists, OLES designed and conducted a pilot experiment, with an intentionally limited number of specimens, to investigate these issues. The data obtained from the experiment were analyzed using a statistical model that allowed for estimation of the possible effects of three factors: armor size, the spacing of impact points, and the difference between front and back panels. None of these factors was found to have a statistically significant effect. Because the number of specimens was limited, confidence intervals for the estimated effects were wide, and it was not possible to rule out the existence of subtle, or even not-so-subtle, long-term effects. Calculations demonstrated that a very large experiment would be required to produce acceptably reliable estimates of any possible effects resulting from shot-pattern spacing and armor size. NIST concluded that the expense of such experiments would not be warranted and recommended that NIJ sanction compliance testing of only larger armor sizes.

VIDEOTAPE DEMONSTRATES NIST MODEL FOR SIMULATING FLAT-PANEL DISPLAYS

The NIST Digital Imaging Project has produced a videotape that demonstrates vividly what NIST has accomplished to date in the modeling of flat-panel displays. Among other applications, flat-panel displays are used widely in lap-top and notebook computers, are key elements of advanced aircraft cockpits and vehicle dashboards, are equally key elements in situational displays for both defense and civilian applications, and are beginning to appear as replacements for cathode-ray tubes in television sets and electronic instrumentation. Effective exploitation and improvement of flat-panel displays will depend on a better understanding of the mechanisms underlying their operation and an ability to characterize their performance. The videotape is intended to be used in support of discussions between representatives of the Digital Imaging Project and members of other laboratories in industry, government, and academia.

Having a running time of about 15 min, the tape opens by demonstrating the effect of viewing angle for an active-matrix liquid-crystal display as an introduction to the developmental NIST model for a display having pixels which modulate light by exploiting the electro-optical Kerr effect (not actually used for displays). The tape shows visually how such a display would work and the results of implementing the model on the NIST Princeton Engine videocomputer to investigate the effects of viewing angle, cross talk between pixels, and resistance between the connections of the elements that form the screen. The Kerr-effect model was chosen for its mathematical and conceptual simplicity. However, since it exhibits artifacts generic to electro-optic displays, it serves as a prototype upon which more complicated and realistic models of liquid-crystal and other flat-panel display technologies can be based.

NIST/INDUSTRY CRADA

A major producer of heavy equipment has signed a CRADA with NIST to develop artifacts for the interim testing of coordinate measuring machines (CMMs). The private company will be participating in a program designed to create equipment and methodologies for the rapid assessment of CMM performance. The company's technology center in Peoria, IL, will be testing prototypes developed at NIST and assisting in developing factory floor versions of the technology.

NEW CRADA TARGETS KEY MACHINE FOR MAKING FUTURE CAR ENGINES

A new cooperative research project has been initiated between NIST, private Industry, and the National Center for Manufacturing Sciences to enhance the accuracy of one of the participating companies' piston turning machine. The machine produces high-precision pistons for today's automobile engines. Next-generation engines will require complex-shaped pistons that must meet dimensional tolerances much more stringent than those for today's simpler, slightly oval versions. Consequently, the machine accuracy has to be improved by about a factor of five.

NIST researchers have been working on machine-tool accuracy enhancement by real-time software error compensation for the last 10 years. With this cooperative research project, they will apply their expertise in the piston-turning machines which also require high-speed, high-precision actuation systems, another major research focus at NIST. The NIST researchers will evaluate the machine's performance over a range of operating conditions, characterize the thermal and geometric errors, and modify actuator design to improve the actuation system's speed by a factor of two.

CALIBRATION OF PROFILOMETER FOR GEOMETRIC CHARACTERIZATION OF ROCKWELL C HARDNESS INDENTERS

During the past fiscal year, staff members at NIST have evaluated alternative instruments for measuring the microform shape of Rockwell C indenters. A profilometer was procured for this purpose; and fixtures, artifacts, and procedures for instrument calibration have been developed. The calibration is based upon measurement of both circular arc and spherical form (400 μm diameter) and conical form for rotational symmetry about the indenter axis. The instrument calibration has required several unique manufacturing and assembly tasks to obtain calibrated artifacts representative of indenter geometry and form. Future work will focus upon measurement of working indenters to establish procedures and documentation requirements.

This work is one part of the National Hardness Standardization Program headed by NIST. Other aspects of the program include the development of Standard Reference Materials for hardness and the certification of hardness measuring machines.

NEW AMERICAN STANDARD FOR ROBOT PERFORMANCE

The American National Standards Institute has approved a new American standard for industrial robots and robot systems for "Path-Related and Dynamic Performance Characteristics Evaluation." This standard is intended to be used for the evaluation of the general dynamic performance of robots and, in particular, their ability to move their end effector on a continuous path.

This standard was developed by a committee consisting of members who came from the robot manufacturers industry, robot users, academia, and NIST. The main objective of the committee was to come up with a standard that is practical and can be used to facilitate comparisons of like robots, in order to make possible the easy selection of robots by users. This became a very important condition for the development of this standard since the robot users felt that relevant International Organization for Standardization (ISO) standards do not help them when it comes to the crucial decision of robot selection.

NIST played an important technical advisory role in the development of this standard. The NIST member pointed out to the committee that a relevant path-related performance characteristics evaluation standard, proposed by ISO, is not practical from a robot metrology point of view and cannot be performed with currently available metrology equipment. A different approach to this evaluation standard was proposed to the committee. This approach was accepted and became the basis for the American standard.

CERTIFICATION OF CADMIUM AND LEAD IN ALUMINUM

Scientists at NIST have collaborated with the Aluminum Association and the primary aluminum manufacturers in the United States (under the auspices of the American Society for Testing and Materials) in the production of a series of aluminum Standard Reference Materials (SRMs). These standards are certified for cadmium and lead content.

Increased concern about toxic metals in the environment has resulted in legislation in 13 states and proposed legislation at the federal level. The legislation is aimed at eliminating cadmium and lead from packaging materials. Lead and cadmium can be introduced into these materials during certain recycling processes. The toxicity of these elements, coupled with the increased amount of recycled aluminum used today, has resulted in the need for these standards to provide an effective benchmark for the requisite chemical measurements.

Certification measurements were made at NIST using the highly accurate technique of isotope dilution mass spectrometry. Two alloy types (nominal Cd content 8, 20, and 50 parts per million and nominal Pb content 20, 60, and 150 parts per million) were analyzed. The Standard Reference Materials Program will issue these materials (SRMs 1710-1715) as solid disks.

WORKSHOP ON SUPERCRITICAL WATER OXIDATION

The proceedings of a recent Workshop on Federal Programs Involving Supercritical Water Oxidation, held in July 1992 at NIST in Gaithersburg, have been published in NISTIR 4920. The workshop, sponsored by NIST, brought together project leaders and program coordinators of federal efforts to use the process of supercritical water oxidation (SCWO) in the treatment of waste streams. Supercritical water oxidation has been described as a technology of high promise for safe and economical processing of a wide variety of environmentally dangerous waste streams.

Several military programs were discussed, including U.S. Army and Air Force programs for

demilitarization of weapons stockpiles and a DARPA program to develop a transportable 3800 L/d SCWO pilot plant for destruction of chemical agents, propellants, and other hazardous or toxic substances. U.S. Navy efforts to develop a pilot plant for treatment of shore-side industrial wastes and a compact shipboard waste-water treatment system also were described.

Other programs described included the use of SCWO by NASA for space life-support applications and a number of projects being developed by the Department of Energy involving SCWO treatment of mixed radioactive wastes and applications to site clean-up.

THIN-FILM THERMOCOUPLE RESPONSE DETERMINED TO 100 kHz

Thin-film thermocouple (TFTC) devices are ideally suited as probes of temperature and heat flux transients in the high-temperature, reactive environments characteristic of internal combustion and jet engines. There are several advantages to these devices. One is that the low physical profile of the devices makes them essentially nonintrusive. A second is that thin-film devices have the potential for high-speed response. A third advantage is that when fabricated of appropriate materials, these devices can maintain robustness to chemical, thermal, and mechanical stresses. However, because of their multilayered structure, the response of TFTC devices is very nonlinear with respect to the frequency of the heat flux. Therefore, the calibration of such a device must include validation of a model for the frequency-dependent response of the structure and determination of the material-dependent thermal parameters inherent to the model.

Scientists at NIST have developed a system based on pulsed and sinusoidally modulated laser heating which allows the measurement of TFTC gauges over a wide range of frequencies, from 0.01 Hz (i.e., essentially dc) to over 100 kHz. This system has been used to make measurements on a TFTC heat flux gauge employed in the development of a prototype ceramic-lined diesel engine. The gauge consists of a thin-film metal thermocouple (a 4 μm film consisting of Pt on Pt-10% Rh) sputter-deposited on a thick ceramic layer (1 mm zirconia) with low thermal conductivity which was deposited by the plasma spray technique on a metal engine plug (a semi-infinite heat sink). The thermal response of this device is accurately described by a heat-transfer model for over 7 decades in frequency. Additionally, the scientists have determined thermal conductivities and diffuasivities for the various layers and studied the sensitivity and the stability of the response as a function of temperature from 300 to 900 K.

LASER COOLING AND TRAPPING OF XENON

Laser-cooling metastable rare gas atoms such as xenon offers a number of unique opportunities. Laser-cooled metastable xenon has been identified as an ideal candidate for an optical frequency standard, with potentially unprecedented stability. In addition, such systems are interesting in numerous areas: ultra-cold collision physics, highly forbidden transition rate measurements, quantum collective effects, novel surface probes, and atom interferometry.

Researchers at NIST have succeeded in decelerating and magneto-optically trapping metastable xenon for the first time, using light from a single titanium:sapphire laser. Each of the nine stable isotopes has been trapped, including those with an abundance of less than 0.1 percent. The extremely high isotopic selectivity of the laser cooling and trapping has been used to improve greatly the accuracy of isotope shifts and hyperfine structure constants. Results also were obtained on collision processes that affect trap performance.

The primary loss mechanism out of the magneto-optical trap is a collision process known as Penning ionization, in which two metastable atoms collide and exchange excitation energy. If an atom receives enough energy to ionize, it leaves the trap. Preliminary measurements have shown a Penning ionization rate substantially less than that for lighter metastable rare gas atoms. The researchers have observed both Penning ionization from the metastable state and from the optically excited state used in the laser cooling. Experiments are under way to look for the predicted, but never observed, quantum statistical suppression of ionization in a spin-polarized sample of fermions.

CHARACTERIZATION OF A NEW CLASS OF COMPOUNDS BEING CONSIDERED FOR USE AS ALTERNATIVE REFRIGERANTS

The phasing out of the chlorofluorocarbons (CFCs) commonly used as refrigerants, solvents, and propellants for the last 50 years is causing the search for environmentally acceptable alternatives to be accelerated. One of the families of compounds that are being considered for use as

alternative refrigerants is a class of partially fluorinated ethers. In the search for new refrigerants, no one compound has been found to be satisfactory in all respects. Therefore, mixtures of various compounds are being considered. Mixtures offer the potential of tailoring refrigerants in a variety of ways: modifying vapor pressure, changing lubricant solubility characteristics, changing specific heat, and altering flammability ranges. However, the number of mixtures possible is so large that measurement of all possibilities is impractical. One must rely on a small number of wisely chosen measurements and combine these with the best theoretical modeling techniques to predict the necessary properties.

The properties of hydrocarbon and halogenated hydrocarbon mixtures have been found to have strong correlations with the permanent electric dipole moments and the molecular polarizabilities of the constituent compounds. The electric dipole moment has been used for predicting the mixture equation of state, a feature that has been incorporated into NIST Standard Reference Database 23, "NIST Refrigerant Properties Data Base." However, when a compound has the possibility of existing as several steric conformations (as is the case with the partially fluorinated ethers), dielectric measurements are insufficient to determine the dipole moments and relative abundances of the various conformers. Unique interpretation of the dielectric measurements is possible only if the dipole moments and the relative abundances of the various conformers present can be obtained independently.

To establish some benchmarks to aid these modeling calculations, NIST scientists studied two members of the family of fluorinated ethers in detail, namely CF_2HOCF_2H and $CF_2HOCH_2CH_3$, and determined the lowest energy conformation and measured the electric dipole moments of the lowest energy conformer for both compounds. This is important information for use in modeling the mixture equations of state for this series of compounds since each conformer makes an individual contribution, which is strongly dependent on the dipole moment, to the free energy of the mixture. With these additional data, obtained only from the high-resolution rotational spectrum, predicting the equations of state that treat these materials as a mixture of components will be more accurate than could be obtained from measurements of the average dipole moment.

UNCERTAINTY STANDARD ON RADIATION PROCESSING DOSIMETRY DEVELOPED

NIST scientists have made significant contributions to the development of a new draft E10.01 American Society for Testing and Materials (ASTM) standard on the statement of uncertainty in measurements of absorbed dose in industrial radiation processing. Dose measurements are required to assure that the dose delivered to the product meets the requirements of the process, whether for regulatory needs such as the sterility of medical products or food processing, or for materials' property modification such as polymer cross linking. It is critical that an appropriate statement of the uncertainty in these dose measurements be developed and made consistent with the terminology and basic concepts of ISO/TAG 4 Guide to the Expression of Uncertainty in Measurement. The ASTM document will be used as a model for other ASTM documentary standards relating to radiation dosimetry, will help them conform with accepted international guidelines, and will provide a uniform format for the statement of measurement uncertainties.

NVLAP ACCREDITS FIRST SECONDARY CALIBRATION LABORATORY FOR IONIZING RADIATION

The NIST National Voluntary Laboratory Accreditation Program (NVLAP), in coordination with the NIST Office of Radiation Measurements has accredited the first laboratory under the Secondary Calibration Laboratory for Ionizing Radiation LAP. The Food and Drug Administration's Center for Devices and Radiological Health (CDRH) has been accredited in accordance with NIST Special Publication 812, Criteria for the Operation of Federally Owned Secondary Calibration Laboratories for Ionizing Radiation, to perform calibrations of diagnostic, survey, and reference class instruments for the measurement of x-ray fields. Instruments calibrated by CDRH are used by state radiological inspectors to assure that diagnostic x-ray machines in all hospitals and doctors' offices are operated in a safe and effective manner.

NIST-7 REPLACES NBS-6 AS U.S. PRIMARY FREQUENCY STANDARD

NIST-7, an optically pumped cesium-beam frequency standard developed by NIST researchers,

has officially replaced NBS-6 as the U.S. primary frequency standard. The standard, designed to ultimately operate with an accuracy of 1×10^{-14} already is performing at a level of 4×10^{-14}. At this level it is two times more accurate than NBS-6. Further study of systematic effects will be needed to attain the design accuracy, and additional electronic development is needed to increase automation of its operation. The development of the standard was led by NIST scientists with input on the design from many other quarters. The design of the microwave system, for example, was done in large part by colleagues in Italy and invaluable design review was provided by colleagues in private industry.

This is the most accurate optically pumped standard to be used as a primary standard. All previous cesium standards have been based on magnetic-state selection and detection. One key advantage of the technique is greatly enhanced signal-to-noise performance, which allows for more rapid evaluation of accuracy. In fact, this standard has the best short-term performance of any cesium-beam standard ever built. When it achieves its full-design accuracy, it will be the most accurate primary frequency standard in the world.

"GIANT CATALYSTS"—A NEW GENERATION OF MESOPOROUS MATERIALS

A collaborative research effort has been initiated between scientists at NIST, the University of California (Santa Barbara), and private industry to characterize, by neutron scattering techniques, a new generation of "giant catalysts" containing mesopores. The discovery of this revolutionary new class of mesoporous materials was recently reported by industry (Nature, vol. 359, p. 710, 1992).

The new mesoporous molecular sieves are unique in that they contain hexagonally arranged and uniformly sized channels whose size can be varied in diameter within the range 1.3 to 20 nm by controlled density synthesis, and are up to an order of magnitude larger than previously existing zeolite catalysts which are at the heart of our chemical production petroleum industries. These new materials are being studied intensively for their potential in many applications, including large-molecule catalysis and chemical separation, as well as their possible role as hosts for semiconductors or "quantum wires," which may be constructed by chemical reactions in the channels. NIST has a unique collection of neutron research facilities for studying the processing, structure, and molecular behavior of these exciting new materials.

STRESSES IN CERAMICS MEASURED BY RAMAN SPECTROSCOPY

Residual stresses due to processing, phase transformations, etc., are a significant factor in the reliability of ceramics used in both structural and electronic applications. Microfocus Raman spectroscopy, which can have a lateral resolution on the order of a micrometer, is an ideal tool for residual stress measurements, since these stresses frequently vary dramatically over distances comparable to the size of the microstructure. A diamond pressure cell and an *in situ* biaxial stress apparatus have been used to obtain calibration curves of stress vs. Raman peak position for polycrystalline alumina in a microfocus Raman spectrometer. The diamond pressure cell provides a curve relating peak shift to hydrostatic stress while the biaxial apparatus provides a similar curve for directionally applied stresses. Such calibration curves are essential for quantitative measurements of residual stresses using Raman peak shifts. This methodology now is being used at NIST to evaluate residual and applied stresses in monolithic and composite ceramics.

TEMPERATURE SENSING IN ALUMINUM PROCESSING

A significant step in the development of a non-contact electromagnetic temperature sensing system for on-line monitoring of high-speed rolling of aluminum sheet has been accomplished in a test performed at an industrial research center. The demonstration was carried out under a cooperative research and development program shared by NIST and The Aluminum Association, Inc., a consortium of processing and manufacturing companies. The electromagnetic sensing system operates by measuring the induction of eddy currents in the moving test material and thereby obtaining the electrical resistivity which depends upon the temperature in a known way. The results of the electromagnetic (or eddy current) measurements were compared with readings from a thermocouple which contacted the moving material. The test demonstrated that one can compensate for variations in the electrical resistivity of the test material arising from variations in alloy composition.

GAS-COUPLED ACOUSTIC MICROSCOPE

The feasibility of a new gas-coupled acoustic microscope has been demonstrated by NIST scientists. Traditionally, acoustic microscopy relied on liquid couplants, which impose several operational

restrictions in high-speed quality-control applications. The new microscope functions in both through-transmission and pulse-echo modes, and appears to exhibit better spatial resolution characteristics than similar liquid-coupled devices. Images have been obtained in the 3 to 20 MHz frequency region. Potential applications include quality control in the microelectronics industry and materials characterization.

ADVANCED SMARTCARD DEVELOPED

NIST scientists have developed an Advanced Smartcard Access Control System (ASACS), which implements the proposed Digital Signature Standard on a device with the same dimensions as a standard credit card. Easily carried in a wallet or purse, the smartcard provides users with a secure means for generating and verifying digital signatures. Digital signature technology, which provides a replacement for the handwritten signature, is a crucial element in the processing of electronic documents. The smartcard also contains the Data Encryption Standard algorithm and supports unitary log-in authentication using cryptographic techniques. Several federal agencies are initiating programs which will take advantage of the technology developed for the ASACS project.

NIST AND INDUSTRY JOIN FORCES IN PARALLEL PROCESSING RESEARCH

NIST successfully fabricated its MultiKron very large scale integration (VLSI) instrumentation chip and transferred the technology to private industry for its supercomputer parallel system. NISTIR 4737, Operating Principles of MultiKron Performance Instrumentation for Multiple-Instruction Multiple-Data (MIMD) Computers, describes the single-chip VLSI design, which replaces earlier performance instrumentation chip sets. In addition, researchers redesigned and refabricated a faster MultiKron version in a smaller-sized VLSI reticle, resulting in reduced costs. Also designed and implemented was a prototype of a local collection network for captured performance data.

GUIDELINES FOR EVALUATING VIRTUAL TERMINAL IMPLEMENTATIONS PUBLISHED

NIST Special Publication 500-205, Guidelines for the Evaluation of Virtual Terminal Implementations, assists users in determining which implementation, among several candidates, best meets their functional requirements. The document is one of a series of evaluation guidelines for Open Systems Interconnection (OSI) applications. NIST has issued guidance for message handling systems and file transfer, access and management implementations and plans evaluation guidelines for other OSI applications, such as directory services. These documents help users implement Federal Information Processing Standard 146-1, Government Open Systems Interconnection Profile, which facilitates the interoperability of dissimilar computer systems in the federal government.

NIST ISSUES STUDY OF OPEN SYSTEMS INTERCONNECTION (OSI) KEY MANAGEMENT

For communications between computer systems to be useful in many environments, the systems and their communications must be secure. One prerequisite is the management of keying material needed by the underlying cryptographic mechanisms that provide security. NISTIR 4972, A Study of OSI Key Management, addresses key management as it applies to communications protocols based on the OSI architecture. The report contains criteria and a model of OSI key management incorporating both secret key and public key cryptography. A guest researcher at NIST authored the study.

GUIDANCE ON COMPUTER SECURITY TOOLS AND TECHNIQUES PUBLISHED

Two new NIST publications assist users in the selection of appropriate tools and techniques for protecting computer systems and the information they process. NIST Special Publication 800-5, A Guide to the Selection of Anti-Virus Tools and Techniques, provides criteria for judging the functionality, practicality, and convenience of anti-virus tools. NIST Special Publication 800-6, Automated Tools for Testing Computer System Vulnerability, analyzes factors affecting the security of a computer system. Using automated tools, a system manager can identify common vulnerabilities stemming from administrative errors and take corrective action to reduce significantly the security exposure of their system.

Volume 98, Number 2, March–April 1993
Journal of Research of the National Institute of Standards and Technology

Standard Reference Materials

STANDARD REFERENCE MATERIALS 1400 AND 1486—BONE ASH AND BONE MEAL

Research that relates human and animal nutrition to a number of diseases often depends on linking nutritional intake of minerals with the concentration of those same minerals in bone. The bone matrix presents a severe challenge to analytical methodology in the decomposition of samples prior to atomic spectrometric and other analyses. It is, therefore, helpful to have SRMs available in which the concentration of minerals in a bone matrix have been certified.

The Standard Reference Materials Program announces the availability of SRM 1400, Bone Ash, and SRM 1486, Bone Meal, to meet this research need. Certified values are given for Ca, Mg, P, Fe, K, Sr, and Zn in the two materials. Additionally, information values are provided for Al, As, Cd, Cu, Fe, Mn, Se, Si, Na, and C (total). The SRMs are issued in units of 50 g and are composed of powdered material.

STANDARD REFERENCE MATERIALS 3171A, 3172A, AND 3179—MULTIELEMENT SPECTROMETRIC SOLUTION MIXES

The U.S. EPA and state regulatory bodies have been monitoring a number of toxic metals in the environment under the Resource Conservation and Reclamation Act and the Solid Waste Program, among others. Most laboratories performing the needed analyses through the Contract Laboratory Program are using spectrometric techniques such as flame atomic absorption, inductively coupled plasma atomic emission, and inductively coupled plasma mass spectrometry for the analyses. These methods require the use of instrumental calibration solutions and interference check solutions.

The Standard Reference Materials Program announces the availability of three multielement solutions to meet these requirements, in addition to the full 3100 series of single-element calibration solutions. The multielement solutions SRM 3171a and 3172a are renewals of earlier SRMs to which antimony, molybdenum, thallium, and vanadium have been added. With these additions, the two solutions now contain all toxic metals important to Toxicity Characteristic Leaching Protocol (TCLP) and other environmental analyses. Most elements in these SRMs occur in ratios between 1:1 and 1:10, which are typical of natural waters, but not of solid environmental sample leachates.

SRM 3179 is a set of three solutions to be combined on dilution to provide not only the TCLP toxic metals, but also matrix elements (e.g., Al, Fe, and others), in ratios which are more characteristic of solid sample leachates prepared using the EPA Method 3050 leaching protocol.

SRMs 3171a and 3172a are issued in units of 50 mL. SRM 3179 is a set of three 50 mL solutions to be combined on dilution into a single multielement mix. Chemical incompatibilities of some elements prelude premixing as a single solution by NIST. All three SRMs are prepared in 5 percent (V/V) nitric acid.

STANDARD REFERENCE MATERIALS 2108-2109—CHROMIUM (III) AND CHROMIUM (VI) SPECIATION SOLUTIONS

Chromium is a metal that occurs in the environment in both dissolved and solid phases and in a variety of chemical forms. It is the concentration of individual chromium species in a sample, rather than total chromium concentration, which is most useful in determining biological availability, toxicity, or potential as a nutrient. Therefore, reference samples having species-specific, certified concentrations are needed for calibration and to assure interlaboratory comparability of data in studies on the beneficial and/or harmful effects of chromium in the biosphere.

The Standard Reference Materials Program announces the availability of SRMs 2108 and 2109 to meet these needs. SRM 2108 is a solution containing 1.000 mg/mL of chromium only in the plus-three oxidation state. It was prepared by the dissolution of high-purity metal in hydrochloric acid. The absence of chromium plus-six was established spectrophotometrically.

SRM 2109 is a solution containing 1.000 mg/mL of chromium only in the plus-six oxidation state, prepared by the dissolution of high-purity potassium dichromate (SRM 136e) in deionized water. The absence of chromium plus-three in SRM 2109 was measured by an ion-exchange separation of the two states, and measurement of total chromium in the eluent, which would indicate chromium plus-three, if present. The two SRMs are issued in units of 50 mL each.

Volume 98, Number 2, March–April 1993
Journal of Research of the National Institute of Standards and Technology

Calendar

June 21–25, 1993
NORTH AMERICAN ISDN USER'S FORUM (NIUF)

Location: National Institute of Standards and Technology Gaithersburg, MD

Purpose: To develop user-defined applications, implementation agreements for existing standards, and tests needed for a transparent, ubiquitous and user-driven integrated services digital network (ISDN).
Topics: Broadband, small business issues, customer premise equipment, ISDN applications and other ISDN-related subjects.
Format: Tutorials, users' and implementors' workshops, and working group meetings.
Audience: ISDN users, implementors and service providers.
Sponsor: NIST.
Contact: Dawn Hoffman, B364 Materials Building, NIST, Gaithersburg, MD 20899-0001, (301) 975-2937.

July 12–16, 1993
THIRD INTERNATIONAL CONFERENCE ON CHEMICAL KINETICS: REACTIONS IN GAS AND CONDENSED MEDIA

Location: National Institute of Standards and Technology Gaithersburg, MD

Purpose: To bring together scientists interested in gas and condensed phase chemical kinetics to facilitate the interchange of concepts and data and to apply this knowledge to the solution of applied problems.
Topics: Rates and mechanisms of gas and condensed phase reactions of: carbon-centered radicals including carbenes; peroxyl radicals; hydroxyl radicals; halogen and hydrogen atoms; nitrogen-containing radicals; sulfur-centered and other radicals; metal-containing radicals; and ozone and its reaction products. These reactants are of considerable interest for industrial and environmental processes.
Format: Seven non-parallel sessions consisting of invited lectures, contributed lectures, contributed poster sessions and general discussions.
Audience: Industry, government agencies and academia.
Sponsor: NIST.
Contact: Robert Huie, A260 Chemistry Building, NIST, Gaithersburg, MD 20899-0001, (301) 975-2559.

October 18–22, 1993
1993 PRECISION THERMOMETRY SEMINAR

Location: National Institute of Standards and Technology Gaithersburg, MD

Purpose: To present the fundamentals of thermometry, discuss the latest temperature scale and share the latest advances in the field.
Topics: Temperature scales, resistance thermometry with emphasis on platinum resistors, thermocouple thermometry, liquid-in-glass thermometry, gas thermometry, and radiation thermometry.
Format: Tutorials and laboratory workshops.
Audience: Laboratory staff from industry, government agencies and academia.
Sponsor: NIST.
Contact: Audrey Engstrom, B128 Physics Building, NIST, Gaithersburg, MD 20899-0001, (301) 975-4800.

October 26–28, 1993
GAGE BLOCK CALIBRATION WORKSHOP

Location: National Institute of Standards and Technology Gaithersburg, MD

Purpose: To emphasize the concepts, techniques and apparatus used in gage block calibration.
Topics: Gage block specifications, statistics, process control parameters, measurement corrections, drift eliminating measurement designs, procedures, interferometry, and error budgets.
Format: Lecture sessions, slide presentations and a laboratory session.
Audience: Metrology managers and laboratory technicians.
Sponsor: NIST.
Contact: John Stoup, A107 Metrology Building, NIST, Gaithersburg, MD 20899-0001, (301) 975-3471.

October 27–29, 1993
XXV BOULDER DAMAGE SYMPOSIUM, ANNUAL SYMPOSIUM ON OPTICAL MATERIALS FOR HIGH-POWER LASERS

Location: National Institute of Standards and Technology Boulder, CO

Purpose: To exchange information on the technology and physics of materials for high-energy/high-power lasers.
Topics: New materials, bulk, surface and thin-film damage phenomena and levels, measurements of properties of materials, design and degradation considerations for high-output systems, experimental design, data reduction and standards of laser-induced damage, fundamentals and modeling of laser interaction with optical materials.
Format: Symposium, both oral and poster. Abstracts (150 words) due by AUG. 16, 1993. Internal mini-symposium, "The Quest for the Invincible Laser Coating—A Critical Review of Pulsed Laser-Induced Damage to Optical Coating: CAUSES AND CURES," chaired by Karl Guenther, CREOL.
Audience: Industry, government agencies and academia.
Sponsors: NIST, CREOL, LANL, LLNL, SN DoD and SPIE.
Contact: Donna Wilson/Arthur Guenther, c/ CREOL, University of Central Florida, 1242 Research Pkwy., Suite 400, Orlando, FL 3283((407) 658-6834, fax: (407) 658-3966, E-MAI DONNA@ADMIN.CREOL.UCF.EDU.

June 27–July 1, 1994
CONFERENCE ON PRECISION ELECTROMAGNETIC MEASUREMENTS—CPEM '94

Location: Clarion Harvest House Hotel Boulder, CO

Purpose: To exchange information on a wid range of problems in the area of precise electro magnetic measurements. A number of specia sessions on the fundamental constants will be held in anticipation of a new adjustment of the constants scheduled for 1995.
Topics: Direct current and low-frequency measurements; fundamental constants and special standards; time and frequency; rf, microwave and millimeter-wave measurements; lasers, optical fibers and optical electronics; superconducting and other low-temperature systems; dielectrics and antennas; automated measurement methods; and advanced instrumentation, including new sensors and novel measurement methods.
Format: General sessions, plenary sessions and poster sessions.
Audience: Industry, government agencies and academia. Emphasis is on standards activities and measurement methods.
Sponsors: NIST, IEEE Instrumentation and Measurement Society and Union Radio Scientifique Internationale.
Contact: Donald B. Sullivan, Div. 847, NIST, Boulder, CO 80303-3328, (303) 497-3772.